



HAL
open science

Breakable silica nanoparticles for the in vitro and in vivo delivery of biomolecules

Mike Dentinger

► **To cite this version:**

Mike Dentinger. Breakable silica nanoparticles for the in vitro and in vivo delivery of biomolecules. Other. Université de Strasbourg, 2018. English. NNT : 2018STRAF057 . tel-03270816

HAL Id: tel-03270816

<https://theses.hal.science/tel-03270816>

Submitted on 25 Jun 2021

HAL is a multi-disciplinary open access archive for the deposit and dissemination of scientific research documents, whether they are published or not. The documents may come from teaching and research institutions in France or abroad, or from public or private research centers.

L'archive ouverte pluridisciplinaire **HAL**, est destinée au dépôt et à la diffusion de documents scientifiques de niveau recherche, publiés ou non, émanant des établissements d'enseignement et de recherche français ou étrangers, des laboratoires publics ou privés.

ÉCOLE DOCTORALE DES SCIENCES CHIMIQUES
Institut de Science et d'Ingénierie Supramoléculaires

THÈSE présentée par :

Mike DENTINGER

soutenue le : **12 Décembre 2018**

pour obtenir le grade de : **Docteur de l'université de Strasbourg**

Discipline/ Spécialité : Chimie

**Breakable silica nanoparticles for the *in vitro* and
in vivo delivery of biomolecules**

THÈSE dirigée par :

M^{me} DE COLA Luisa

Professeur, Université de Strasbourg

RAPPORTEURS :

M^{me} LICANDRO Emanuela

Professeur, Università degli Studi di Milano (Italie)

M^{me} NEVES Isabela

Professeur, Universidade do Minho (Portugal)

AUTRES MEMBRES DU JURY :

M. INNOCENZI Plinio

Professeur, Università degli Studi di Sassari (Italie)

M. SAILOR Michael J.

Professeur, University of California, San Diego (USA)

*« J'ai pas eu besoin d'enlever la mer de la côte d'azur
Je m'assiérais plutôt au bord en l'admirant c'est sûr
J'envie à l'être d'avoir avec lui ce qu'il a de plus cher
Sans chercher à lui prendre car je sais ce que ça vaut
L'absence est à l'amour ce qu'est au feu le vent attiseur
Eteint le petit allume le grand tu me manques
J'ai cherché à comprendre : on m'a dit "c'est ça la vie"
Envie de toi, envie d'émois parfois je me sens trahi
Je suis cet arbre sans feuilles ce stylo sans encre
C'est la sécheresse en moi, même en saison de pluie
Je ne peux rien cultiver d'autre si ce n'est la tristesse
Christ, est-ce une manière de me dire
Que je n'ai pas le droit à tout ?
C'est le cœur qui parle, la main qui tremble
Sur des feuilles mortes
Et une tête qui pense toujours si t'étais en vie
Si t'étais en vie »*

Pit Bacardi, Si loin de toi,

To my father,

But also to all the colleagues and friends who make everything much easier

Abbreviations

ROS: Reactive Oxygen Species
GSH: glutathione
CTAB: cetyltrimethylammonium bromide
TEOS: tetraethyl orthosilicate
BTSPD: bis(triethoxysilyl-propyl)disulfide
TMB: trimethylbenzene
DNA: Deoxyribonucleic acid
siRNA: small interfering ribonucleic acid
APTES: 3-(aminopropyl) triethoxysilane
PBS: Phosphate Buffer Saline
TEM: Transmission Electron Microscopy
PLK1: Polo-like kinase 1
HCC: Hepatocellular Carcinoma
CLSM: Confocal Laser Scanning Microscopy
SEM: Scanning Electron Microscopy
DOX: Doxorubicin
PDT: Photodynamic Therapy
DLS: Dynamic Light Scattering
STEM: Scanning Transmission Electron Microscope
EPR effect: Enhanced and Permeability Retention effect
BBB: Blood Brain Barrier
PEG: Polyethylene glycol
PET: Positron Emission Tomography
CT: Computed Tomography
MRI: Magnetic Resonance Imaging
RISC: RNA Induced Silencing Complex
FDA: US Food and Drugs Administration
PMO: Periodic Mesoporous Organosilica
PEI: Polyethylenimine
GFP: Green Fluorescent Protein
MSN: Mesoporous Silica Nanoparticles

BET: Brunauer-Emmet-Teller method
SAXS: Small Angle X-ray Scattering
XPS: X-ray Photoelectron Spectroscopy
TGA: Thermogravimetric analysis
MES: 2-(N-morpholino)ethanesulfonic acid
 D_h : Hydrodynamic diameter
FACS: fluorescence-activated cell sorting
MFI: Mean Fluorescence Intensity
ALAT: Alanine aminotransferase
ASAT: Aspartate aminotransferase
RITC: Rhodamine Isothiocyanate
TEA: Triethylamine
PFA: Paraformaldehyde
BSA: Bovine Serum Albumin
DMEM: Dulbecco's Modified Eagle's Medium
FBS: Fetal Bovine Serum
HFE: Hydrofluoroether
RB: Rose Bengal
FITC: Fluorescein isothiocyanate

Table of contents

Abbreviations.....	5
Résumé de thèse.....	13
Summary of the thesis.....	31
Chapter 1: General Introduction.....	49
1.1 Nanoparticles for biomedical applications	50
1.2 Drug, gene, and protein delivery	56
1.3 Mesoporous Silica Nanoparticles	59
1.4 Hybrid stimuli-responsive mesoporous silica nanoparticles for specific drug delivery and bioapplications.....	70
1.5 Objective of the thesis	76
1.6 References	78
Chapter 2: Large pore breakable mesoporous silica nanoparticles for PLK1 siRNA delivery.....	87
2.1 Introduction	88
2.2 Synthesis of large pore breakable mesoporous silica nanoparticles.....	91
2.2.1 <i>Synthesis of small pore breakable mesoporous silica nanoparticles.....</i>	<i>91</i>
2.2.2 <i>Post synthetic treatment and the formation of large pore mesoporous silica nanoparticles (LP-ssNPs).....</i>	<i>91</i>
2.2.3 <i>Material characterizations.....</i>	<i>92</i>
2.2.4 <i>Breakability test of LP-ssNPs towards the presence of glutathione (GSH).....</i>	<i>97</i>
2.2.5 <i>Surface functionalization of LP-ssNPs with 3-aminopropyltriethoxysilane (APTES)</i>	<i>98</i>
2.2.6 <i>siRNA loading and jetPEI covering of LP-ssNPs</i>	<i>100</i>
2.3 <i>In vitro</i> behavior of LP-ssNPs	105
2.3.1 <i>Cytotoxicity</i>	<i>105</i>
2.3.2 <i>Rhodamine B grafting on LP-ssNPs for cellular uptake studies</i>	<i>106</i>

2.3.3	<i>FACS analysis</i>	107
2.3.4	<i>Cellular uptake followed by confocal microscopy</i>	108
2.3.5	<i>Lysosomes co-localization</i>	110
2.3.6	<i>Uptake and degradability determined by means of TEM</i>	110
2.3.7	<i>Delivery and release of siRNA</i>	111
2.4	<i>In vivo efficacy of jp-PLK1@NH₂-LP-ssNPs.</i>	112
2.4.1	<i>1st experiment</i>	112
2.4.2	<i>2nd experiment</i>	113
2.4.3	<i>Blood analyses</i>	114
2.5	<i>Loading optimization</i>	117
2.6	<i>Conclusion</i>	118
2.7	<i>Acknowledgments</i>	119
2.8	<i>Materials and Methods</i>	119
2.8.1	<i>Chemicals</i>	119
2.8.2	<i>Synthesis of breakable disulfide mesoporous silica nanoparticles (ssNPs):</i>	120
2.8.3	<i>Post synthetic pore expansion treatment (LP-ssNPs):</i>	120
2.8.4	<i>Grafting of 3-(aminopropyl)triethoxysilane (NH₂-LP-ssNPs):</i>	121
2.8.5	<i>Breakability of LP-ssNPs and NH₂-LP-ssNPs:</i>	121
2.8.6	<i>Grafting of Rhodamine B isothiocyanate for confocal imaging (r-LP-ssNPs):</i>	121
2.8.7	<i>siRNA loading and jetPEI® coating (jp-siRNA@LP-ssNPs):</i>	121
2.8.8	<i>Grafting of N¹-(3-trimethoxysilylpropyl)diethylenetriamine (polyNH₂-LP-ssNPs):</i>	122
2.8.9	<i>Cell culture experiments</i>	122
2.8.10	<i>Cell viability</i>	122
2.8.11	<i>Flow cytometry</i>	122
2.8.12	<i>Confocal microscopy</i>	123
2.8.13	<i>siRNA labelling and cellular uptake</i>	124

2.8.14	<i>In vitro</i> breakability test by means of TEM.....	124
2.8.15	Animal experimentation.....	125
2.8.16	Cell-Derived Xenograft tumor model.....	125
2.8.17	Experimental protocol.....	125
2.8.18	Blood analysis.....	126
2.8.19	Instruments.....	126
2.9	References.....	128
Chapter 3: Loading of a neutral peptide on breakable silica nanoparticles..... 133		
3.1	Introduction.....	134
3.2	Syntheses and characterizations.....	135
3.3	Peptide labelling with a cyanine 5 dye (PepCy5).....	136
3.4	Peptide loading.....	138
3.5	Killing effect of the Pep@LP-ssNPs on larvae.....	141
3.6	Synthesis of breakable organo-hybrid nanocapsules (PepCy5@ssBS).....	144
3.7	Conclusion.....	145
3.8	Materials and Methods.....	146
3.8.1	<i>Materials</i>	146
3.8.2	<i>Synthesis of the disulfide doped breakable mesoporous silica nanoparticles (ssNPs):</i>	146
3.8.3	<i>Pore expansion treatment (LP-ssNPs):</i>	146
3.8.4	<i>Synthesis of non breakable mesoporous silica nanoparticles (MSNs) :</i>	146
3.8.5	<i>Peptide coupling with a Cy5 dye (PepCy5):</i>	147
3.8.6	<i>Incubation with the peptide:</i>	147
3.8.7	<i>Killing effect of the Pep@LP-ssNPs on larvae</i>	147
3.8.8	<i>Synthesis of the breakable nanocapsules (PepCy5@ssBS)</i>	147
3.8.9	<i>Instruments</i>	148
3.9	References.....	149

Chapter 4: Intracellular pharmacokinetics of chemotherapeutics delivery within 50 nm disulfide doped breakable silica nanoparticles 150

4.1	Introduction	151
4.2	Synthesis and characterization of 50 nm disulfide-doped breakable silica nanoparticles.....	152
4.2.1	<i>Synthesis of the 50 nm disulfide doped silica nanoparticles (ssNPs50)</i>	152
4.2.2	<i>Material characterizations</i>	153
4.2.3	<i>Breakability of ssNPs50</i>	155
4.3	Loading of Doxorubicin within ssNPs50 (DOX@ssNPs50).....	155
4.4	<i>In vitro</i> experiments.....	156
4.5	Conclusion	162
4.6	Acknowledgments	163
4.7	Materials and Methods	163
4.7.1	<i>Chemicals</i>	163
4.7.2	<i>Synthesis of 50 nm disulfide-doped silica nanoparticles (ssNPs50)</i>	163
4.7.3	<i>Breakability test of ssNPs50</i>	164
4.7.4	<i>Loading of Doxorubicin within ssNPs50 (DOX@ssNPs50)</i>	164
4.7.5	<i>Cell culture</i>	164
4.7.6	<i>Raman spectroscopy</i>	164
4.7.7	<i>Microspectrofluorimetry</i>	165
4.7.8	<i>Fluorescence imaging</i>	165
4.7.9	<i>Instruments</i>	165
4.8	References	167

Chapter 5: ROS breakable silica nanoparticles 168

5.1	Introduction	169
5.2	Synthesis of the ROS-responsive linker	173
5.3	Synthesis and characterization of ROSNPs.....	176
5.3.1	<i>Synthesis of ROSNPs</i>	176

5.3.2	<i>Material characterizations</i>	176
5.4	Breakability tests	179
5.4.1	<i>Breakability by Potassium superoxide (KO₂)</i>	179
5.4.2	<i>Breakability with a photosensitizer (Rose Bengal)</i>	181
5.4.3	<i>Rose Bengal functionalization on the surface of ROSNPs</i>	183
5.5	<i>In vitro</i> experiments.....	185
5.5.1	<i>Cytotoxicity</i>	186
5.5.2	<i>Synthesis of FITC-ROSNPs</i>	187
5.5.3	<i>Cellular uptake followed by confocal microscopy</i>	187
5.6	Conclusion	192
5.7	Materials and Methods	192
5.7.1	<i>Chemicals</i>	192
5.7.2	<i>Synthesis of the linker: 4,4,14,14-tetraethoxy-9,9-dimethyl-3,15-dioxo-8,10-dithia-4,14-disilaheptadecane (ROS-linker)</i>	192
5.7.3	<i>Synthesis of the ROS breakable nanoparticles (ROSNPs)</i>	193
5.7.4	<i>Synthesis of FITC doped ROS breakable nanoparticles (FITC-ROSNPs)</i>	193
5.7.5	<i>Breakability test with potassium superoxide (KO₂)</i>	194
5.7.6	<i>Breakability test with Rose Bengal</i>	194
5.7.7	<i>Synthesis of Rose Bengal ω-carboxypentyl Ester (RBHA)</i>	194
5.7.8	<i>Synthesis of Rose Bengal-NHS ester (RBHAOSu)</i>	194
5.7.9	<i>Grafting of RBHAOSu on the ROSNPs (ROSNPs-RBout)</i>	195
5.7.10	<i>Synthesis of Rose Bengal-doped ROSNPs (ROSNPs-RBin)</i>	195
5.7.11	<i>Breakability test with the grafted Rose Bengal ROS-NPs</i>	195
5.7.12	Cell culture experiments	196
5.7.13	<i>Cell viability</i>	196
5.7.14	<i>Confocal experiments</i>	196
5.7.15	<i>Instruments</i>	197

5.8	References	198
Chapter 6: Instrumental techniques.....		201
6.1	SEM.....	202
6.2	TEM.....	203
6.3	Confocal laser scanning microscope	204
6.4	UV-Vis Spectroscopy	205
6.5	Fluorescence spectroscopy	206
6.6	Dynamic Light Scattering (DLS)	207
6.7	Zeta Potential	208
6.8	TGA	209
6.9	References	210
General conclusions and Perspectives		211
Acknowledgments		213
Curriculum vitae		219

Résumé de thèse

Depuis quelques décennies, les nanomatériaux ont accompagné notre quotidien avec une utilisation pour les cosmétiques, le craquage pétrolier, l'électronique *etc.*^[1,2] Grâce à leurs propriétés intéressantes, qui pourraient mener à la prochaine révolution industrielle,^[3,4] les nanoparticules ont créé une niche très importante dans le domaine médical, constamment en train d'explorer de nouvelles technologies pour le développement d'outils efficaces.^[5] Leur capacité à contourner les différentes barrières biologiques leur ont permis de trouver des applications dans la livraison de médicaments et de gènes, en imagerie, en biocaptage et en détection. Ces nanoconteneurs peuvent être divisés en trois principales catégories (organique, inorganique et hybride) et sont très versatiles, ce qui leur permet d'avoir une longue circulation dans le sang, une biodistribution spécifique ainsi que la capacité de relargage de molécules sur demande.

Plusieurs matériaux ont déjà effectué une percée dans le monde de la nanomédecine,^[6,7] grâce notamment à des particules virales,^[8] liposomales,^[9] polymériques,^[10] peptidiques,^[11] métalliques (or, argent et points quantiques),^[12] de silice,^[13] de silicium,^[14] et de carbone.^[15] Afin de délivrer des chargements dans des tissus spécifiques, la taille, la forme, la charge à la surface ainsi que les différentes fonctionnalisations possibles sont des paramètres importants et le développement de nanoparticules efficaces requièrent des années d'études entre la synthèse et leur potentielle commercialisation.

Parmi tous les matériaux étudiés, les nanoparticules de silice mésoporeuses ont suscité un grand intérêt de la part des chercheurs, de par leur facile modification,^[16-19] la possibilité de fonctionnaliser de manière sélective la surface ou l'intérieur des pores,^[20] leur grande capacité de stockage^[21] ainsi que leur biocompatibilité (**Figure 1**). Elles offrent donc, par leur structure robuste, une protection des molécules chargées contre une dégradation prématurée mais permettent également une internalisation cellulaire.^[22,23] De plus, la fonctionnalisation des pores ou de la surface crée des interactions spécifiques avec certains types de molécules,^[24] augmentant ainsi leur chargement et/ou l'implémentation de molécules capables de cibler directement certains types de cellules.^[25] Malgré leurs très nombreux avantages, leurs applications cliniques sont toujours très limitées du fait de leur tendance à s'accumuler dans les tissus, ainsi que d'un relargage trop prématuré du chargement, qui les rendent

incompatibles à la chimiothérapie, où de fréquentes injections sont nécessaires.^[26–28] Une des possibilités pour contrer le relargage trop prématuré du chargement est de bloquer l'entrée des pores une fois la nanoparticule chargée. Ces systèmes, appelés nanoportes, sont capables de réagir à certains stimuli tels que le pH, une réaction d'oxydo-réduction, la lumière *etc.* afin de relarguer leurs chargements dans l'environnement intracellulaire.^[29–31]

Grâce aux travaux pionniers de Shea et Brinker^[28,32] sur le développement de nanoparticules d'organosilice mésoporeuses périodiques, les chercheurs ont réussi à contrer les problèmes d'accumulation en insérant dans la structure même de la nanoparticule, des liens clivables en présence d'un stimulus précis. Ces composés organiques sont capables de se rompre en présence d'un stimulus particulier, brisant la particule en fragments suffisamment petits, permettant ainsi une excrétion par voie rénale.^[33–36] Quelques exemples ont récemment été publiés par notre laboratoire, basés sur des systèmes redox ou se clivant en présence d'enzymes et ont démontré des résultats très prometteurs.^[37–39]

Le titre de cette thèse est : « **Nanoparticules de silice cassables pour le relargage *in vitro* et *in vivo* de biomolécules** » et porte sur la modification de nanoparticules de silice mésoporeuses cassables comportant des liens disulfures pour le relargage de médicaments, de gènes et de peptides. Elle présente également le développement d'un nouveau type de nanoparticules de silice mésoporeuses cassables capables de se briser en présence de dérivés réactifs de l'oxygène (ROS). Ces nanoparticules peuvent ensuite être fonctionnalisées avec des molécules photosensibles capables de générer des oxygènes singulet sous irradiation afin d'améliorer la cassabilité du matériau.

Le glutathion (GSH), un tripeptide capable de réduire les ponts disulfures, a attiré beaucoup d'attention pour le développement de nanomatériaux répondant à un stimulus, grâce à la différence en concentration entre le milieu intra (2-10 mM) et extracellulaire (2-5 μ M) de la cellule.^[40] Dans notre laboratoire, nous avons développé des nanoparticules de silice comportant dans la structure interne du matériau, des ponts disulfures pouvant être réduits en présence du tripeptide. Cette réaction, qui induit la cassabilité de la nanoparticule permet ainsi la destruction progressive du matériau en petits fragments, permettant ainsi le relargage de médicaments anti-cancéreux dans le cytoplasme ainsi qu'une excrétion de ces morceaux en dehors du corps humain.^[37,39]

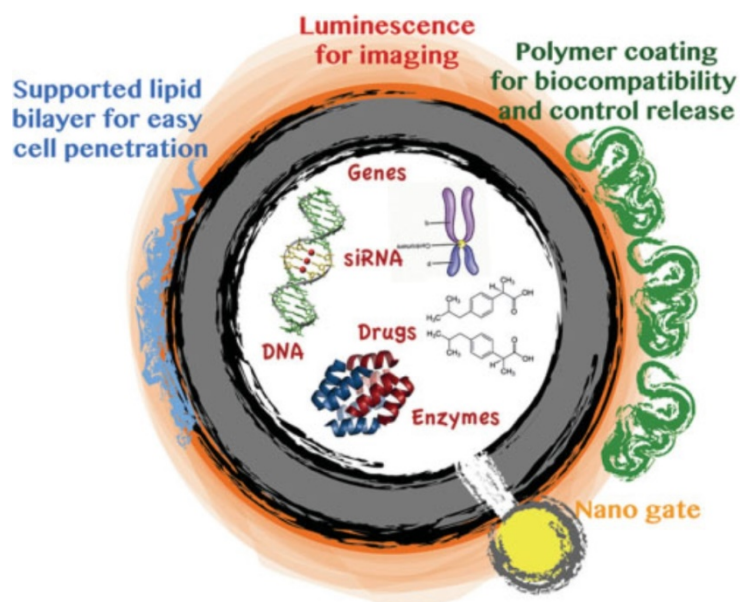


Figure 1: Représentation schématique de nanoparticules de silice pour des applications biomédicales. Il représente le chargement de molécules ainsi que la fonctionnalisation du matériau afin d'obtenir des propriétés ciblantes et imperceptibles. Réimprimé avec l'autorisation de Lülfi H., Devaux A., Prasetyanto E.A., De Cola L., Porous nanomaterials for biomedical applications, in *Organic Nanomaterials: Synthesis, Characterization, and Device Applications*, Wiley, Ch22 (2013). Copyright 2013, WILEY-VCH Verlag GmbH & Co. KGaA, Weinheim.

Le matériau a été synthétisé en utilisant la méthode de Stöber en présence de cetyltriméthylammonium bromide (CTAB) afin de créer la porosité. Les particules ont été formées en utilisant comme précurseurs, de l'orthosilicate de tétraéthyle (TEOS) et du bis(triéthoxysilyl-propyl)disulfide (BTSPD) avec un ratio molaire de 70:30 et du NaOH comme catalyseur basique. Les nanoparticules de silice cassables en résultant ont été caractérisées et présentent une taille de 100 nm ainsi qu'une taille de pore d'environ 2 nm. Cependant, pour le chargement de molécules plus grosses, tels que des oligonucléotides comme l'ADN ou du siRNA, de plus grosses pores sont requises. Pour cela, un traitement post-synthétique avec du triméthylbenzène (TMB) a été effectué permettant une distribution de la taille des pores centrée autour de 12 nm (LP-ssNPs). Une représentation schématique de la synthèse des nanoparticules est démontrée sur la **Figure 2**.

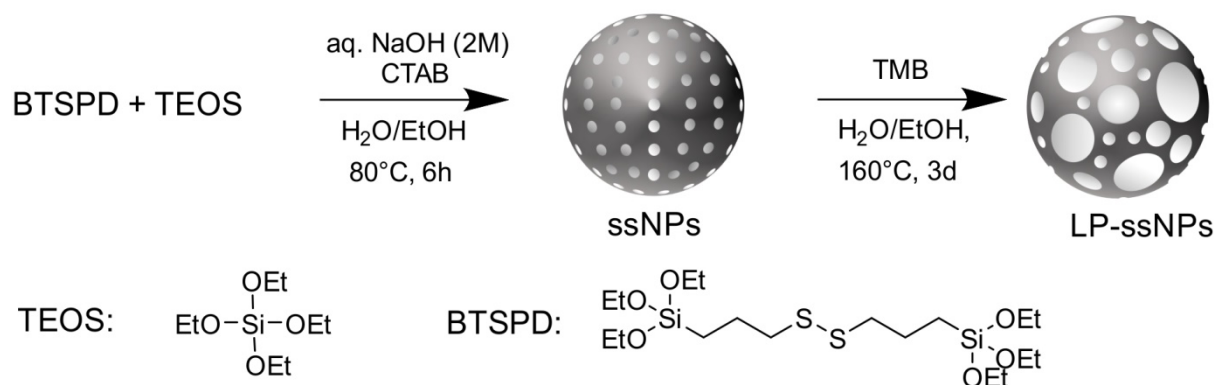


Figure 2: Représentation du schéma de synthèse des LP-ssNPs.

Les LP-ssNPs, chargées négativement, ont ensuite été fonctionnalisées avec du 3-(aminopropyl)triéthoxysilane (APTES) afin d'obtenir une nanoparticule chargée positivement (NH₂-LP-ssNPs), permettant ainsi une liaison électrostatique avec un oligonucléotide chargé négativement. Un test de cassabilité a été effectué, en imitant la concentration intracellulaire en GSH. Les nanoparticules ont été dispersées dans une solution de GSH (10 mM) dans du PBS et agitées pendant 7 jours à 37 °C. La **Figure 3** représente les images par microscopie électronique à transmission (MET) et démontre une cassabilité avancée après 3 jours d'incubation et la présence de très petits fragments après 7 jours. D'un autre côté, les nanoparticules n'ont présenté aucune cassure pendant le même temps d'incubation sans glutathion.

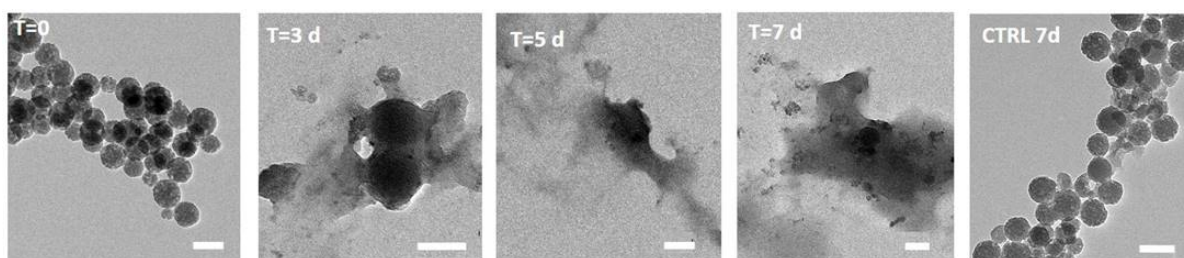


Figure 3: Analyse MET d'une suspension de a) LP-ssNPs and b) NH₂-LP-ssNPs à 0.1 mg/mL, PBS, 37 °C en présence de GSH (10 mM) (0-7 d). A droite, une image contrôle de nanoparticule cassable dans une solution de PBS sans GSH pendant 7 jours. Echelle = 100 nm.

Le chargement d'un petit ARN interférant (siRNA) double brin polo-like kinase 1 (PLK1) a été effectué. Ce siRNA a été choisi pour sa capacité à inactiver le gène exprimant la protéine PLK1, représentant une cible intéressante pour la thérapie contre le cancer.^[41] Les protéines PLK font partie de la famille des serine/threonine kinases, capables de phosphoryler

différentes protéines, régulant ainsi la progression du cycle cellulaire. Le chargement du siRNA polo-like kinase 1 a été effectué. Il a été choisi pour sa capacité à éteindre le gène exprimant la protéine PLK1, qui est une cible intéressante pour la thérapie contre le cancer. De telles propriétés, combinées à la prolifération rapide des cellules cancéreuses, ont démontré la grande expression de PLK1 dans les tissus cancéreux par rapport aux tissus sains.^[42] Sun W. *et al.* ont démontré également la grande concentration de PLK1 dans les cellules hépatocytaires carcinomales. De plus, ils ont prouvé que cette concentration était directement associée au développement de cellule hépatocytaires carcinomales.

Pour bloquer l'expression du gène PLK1, des séquences spécifiques de siRNA doubles brins peuvent être relarguées dans les cellules grâce à des systèmes tels que les nanoparticules.^[43] Pour cela, les NH₂-LP-ssNPs ont été chargés avec un siRNA double brin PLK1 et un siRNA double brin contrôle avec un chargement de 182 µg de siRNA par mg de nanoparticules (PLK1@NH₂-LP-ssNPs et control@NH₂-LP-ssNPs).

Le nanoconteneur a finalement été recouvert d'un polymère de polyéthylèneimine linéaire (jetPEI®) afin de protéger le chargement contre les nucléases, permettant ainsi une meilleure internalisation cellulaire grâce à sa charge positive et enfin améliorant la rupture endosomale (jp-PLK1@NH₂-LP-ssNPs and jp-control@NH₂-LP-ssNPs). L'assemblage couche par couche du système est illustré dans la **Figure 4**.

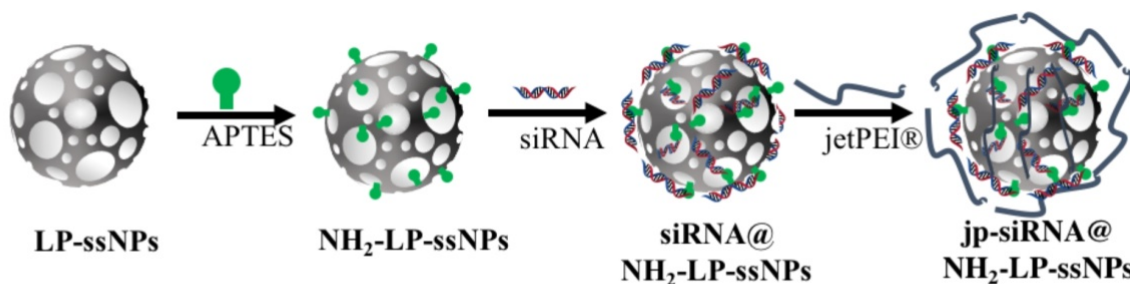


Figure 4: Représentation schématique de l'assemblage couche par couche pour aboutir au matériau final.

Les expériences *in vitro* ont ensuite été conduites dans les cellules hépatocytaires Huh-7. Les LP-ssNPs n'ont démontré aucune toxicité pour les concentrations testées après 48 h d'incubation. La microscopie confocale et la cytométrie de flux ont également démontré une importante internalisation des nanoparticules seulement après 3 h d'incubation et une augmentation après 48 h. Les particules et le siRNA PLK1 ont respectivement été marquées avec de la Rhodamine et de la Cyanine 5 pour démontrer un relargage efficace de l'oligonucléotide. Le matériau a ensuite été incubé pendant 3 h dans les cellules Huh-7. La

Figure 5 démontre un relargage efficace du siRNA comme il peut être observé par la diffusion du signal de la Cyanine 5 par rapport à la Rhodamine dans le cytoplasme.

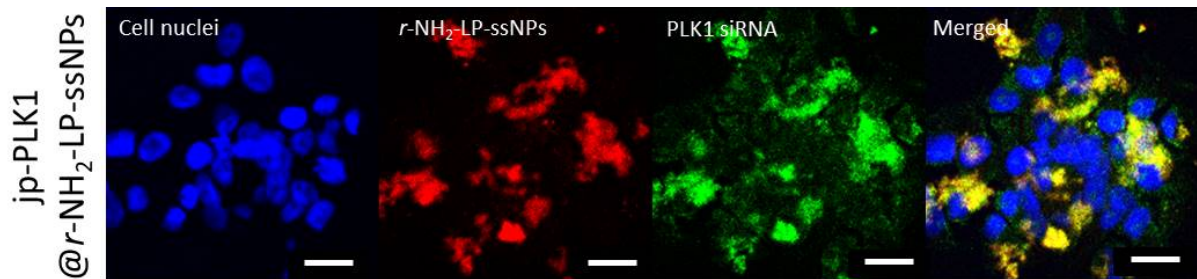


Figure 5: Internalisation cellulaire des jp-PLK1@r-NH₂-LP-ssNPs. Les images confocales ont été prises après 3 h d'incubation avec les particules. Les noyaux cellulaires ont été colorés avec de l'Hoechst 33342 (bleu) et les particules ont été fonctionnalisées avec de la Rhodamine (rouge). Le siRNA PLK1 a été couplé à une Cyanine 5 (vert) avec un Cy5Label IT[®] siRNA Tracker Intracellular Localization Kit (Mirus) et chargé sur les nanoparticules. Les images de droite correspondent à la superposition des signaux. Les longueurs d'excitations sont : 355, 488 et 633 nm. Echelle = 20 µm.

L'effet antitumoral a ensuite été testé *in vivo* par injections intra-tumorales de nanoparticules dans des souris xéno greffe (**Figure 6**). Des injections de jp-PLK1@NH₂-LP-ssNPs et de jp-control@NH₂-LP-ssNPs ont été effectuées tous les deux jours pendant 2 semaines. Comme démontré dans la **Figure 6.b**, les injections de PBS et de siRNA contrôle ont démontré une rapide croissance tumorale tandis que le traitement avec les jp-PLK1@NH₂-LP-ssNPs présentait une croissance beaucoup plus lente prouvant l'effet thérapeutique de notre système.

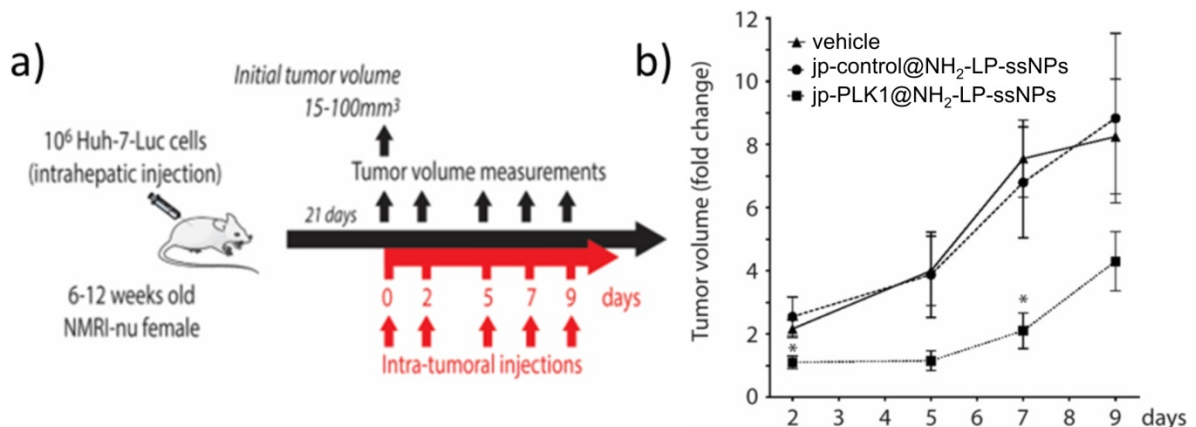


Figure 6: L'injection intratumorale de jp-PLK1@NH₂-LP-ssNPs réduit drastiquement la croissance tumorale dans des modèles de souris xéno greffe. a) Schéma démontrant l'expérience. b) jp-siRNA@NH₂-LP-ssNPs réduit et repousse la croissance tumorale. Les cellules Huh-7 Luc ont été injectées de façon orthotopique dans le foie de souris NMRI-nu et la croissance tumorale a été analysée par imagerie de bioluminescence. Une fois que le volume de la tumeur a atteint 15-100 mm³, le véhicule (n=5), jp-control@NH₂-LP-ssNPs (n=4), ou jp-PLK1@NH₂-LP-ssNPs (n=4) a été injecté de façon intra-tumorale et la taille de la tumeur a été mesurée aux jours 0, 2, 5, 7 et 9. Les résultats (moyenne ± s.e.m.) sont reportés par rapport à la taille initiale. *p<0.05 Fisher's t-test.

Les LP-ssNPs ont ensuite été utilisées afin de charger un peptide capable d'induire une toxicité chez les insectes. De tels peptides ont trouvé un grand intérêt pour l'industrie agro-alimentaire. La population mondiale augmente de 70 millions de personnes chaque année et devrait atteindre 9.2 milliards d'humains d'ici 2050, ce qui implique que l'agriculture devra faire face à une demande constante en nourriture, fibres, *etc.* et la disponibilité de nouveaux champs d'exploitation est limitée.^[44] Parmi les différentes stratégies employées, l'utilisation de pesticides permettrait de réduire de 35 % la perte de ressources due aux infestations. Certaines recherches ont mené à l'utilisation de certains peptides qui pourraient potentiellement tuer les insectes.^[45] Parmi elles, les venins d'araignées ont démontré une grande efficacité pour tuer spécifiquement les insectes. Ici, nous présentons l'utilisation des LP-ssNPs pour charger le peptide.

Le peptide a d'abord été marqué avec une Cyanine 5 avant d'être chargé dans les cavités des LP-ssNPs. Les analyses thermogravimétriques ont présenté une perte de 23 % en poids, attribué aux ponts disulfures présents dans la structure du matériau. D'un autre côté, les nanoparticules chargées avec le peptide (PepCy5@LP-ssNPs) ont montré une perte de 41 %, correspondant à un chargement de 18 % de peptide (**Figure 7**).

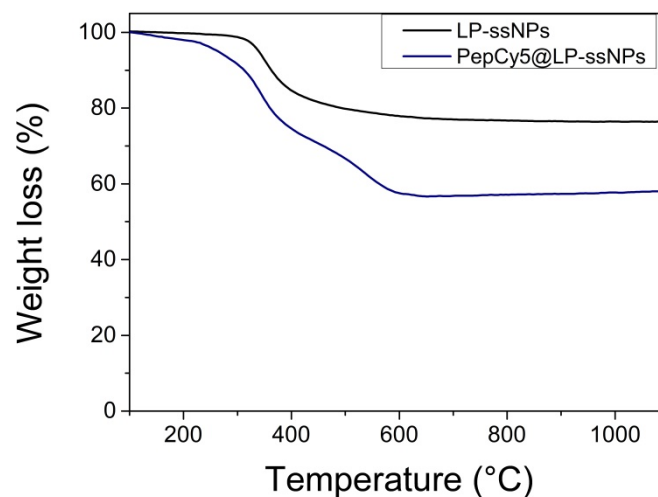


Figure 7: Chargement de PepCy5 dans les pores de LP-ssNPs.

Comme mentionné précédemment, la modification des nanoparticules de silice est relativement directe et simple et permet ainsi une utilisation dans plusieurs domaines médicaux. Par exemple, le traitement des glioblastomes requiert généralement des nanomatériaux de tailles inférieures ou égales à 50 nm, autorisant ainsi le passage de ces dernières à travers la barrière hémato-encéphalique (BBB) par différents mécanismes. Le plus

commun étant peut être la transcytose au travers des cellules endothéliales même si le passage à travers les jonctions serrées à également pu être observé.^[46]

Dans ce but, des nanoparticules de silice de 50 nm, incorporant des ponts disulfures (ssNPs50), ont été synthétisées en utilisant de la triéthanolamine (TEA) comme catalyseur. Cette base permet ainsi un contrôle de la nucléation grâce à ces propriétés chélatantes qui influencent la condensation de la silice.^[47] Les nanoparticules obtenues ont été caractérisées par Microscope Electronique à Balayage (MEB) et ont démontré un matériau sphérique avec une taille de 49 ± 5 nm (**Figure 8**).

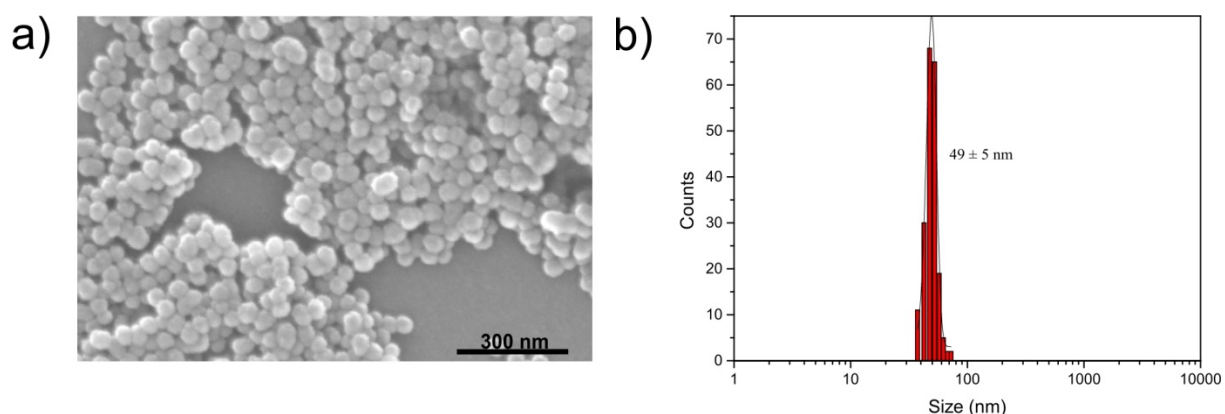


Figure 8: a) Image MEB des ssNPs50. Echelle = 300 nm. b) Distribution granulométrique basée sur le comptage de 200 nanoparticules.

Le matériau a ensuite été chargé avec de la Doxorubicine, un agent anticancéreux capable de s'insérer entre les brins d'ADN, et qui de plus, est facile à tracer grâce à ses propriétés lumineuses. Un chargement final de 50 mg de Doxorubicine par g de ssNPs50 a été déterminé par mesure spectroscopique UV-Vis du surnageant après incubation.

Des études *in vitro* ont ensuite été effectuées dans des cellules de glioblastome humaines U87 au Luxembourg Institute of Health par le Dr. Valérie Palissot. Les signaux de la Doxorubicine et d'un de ces dérivés liposomaux (Caelyx[®]) ont été déterminés par microspectroscopie Raman, qui comme présenté dans la **Figure 9.a**, présentent deux pics caractéristiques à 1210 et 1241 cm^{-1} . Ces signaux ont également été observés *in vitro* après incubation dans le cytoplasme ainsi que dans le noyau (**Figure 9.b and c**).

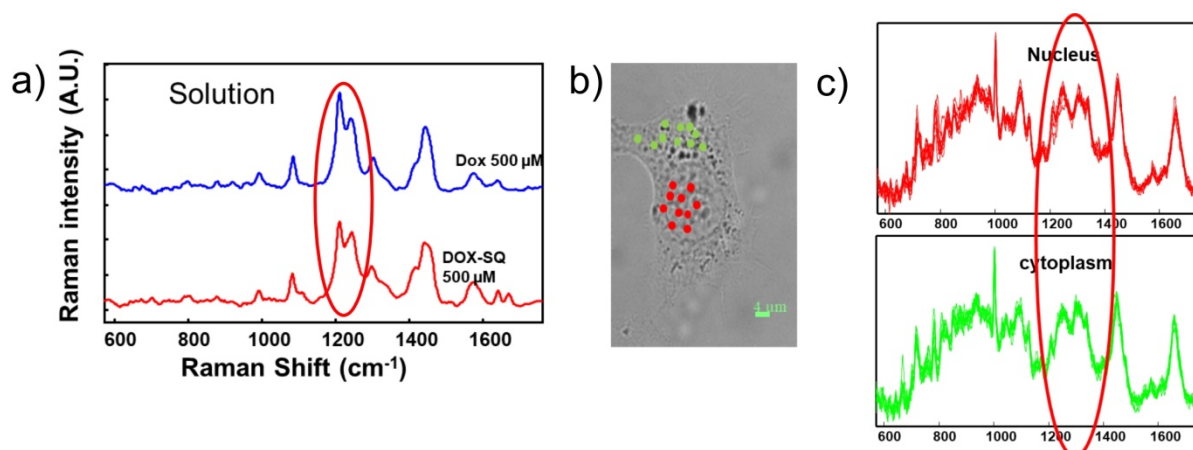


Figure 9: a) Spectroscopie Raman de la Doxorubicine et de sa forme liposomale permettant de caractériser 2 signaux distincts (encerclés en rouge). b) Microspectroscopie Raman d'une unique cellule. Les points représentent les scans mesurés dans le cytoplasme (en vert) et dans le noyau (en rouge). Echelle = 4 μm . Scan Raman fait dans le cytoplasme et le noyau permettant de déterminer la présence de Doxorubicine.

La cinétique de relargage de la Doxorubicine des pores des ssNPs50 a ensuite été étudiée et comparée à la forme liposomale Caelyx[®] qui est présente sur le marché. Après 3 h d'incubation, les expériences confocales ont démontré que la Doxorubicine était piégée dans les endosomes et qu'aucun signal n'était aperçu dans la région périnucléaire. Le même constat a été fait avec les DOX@ssNPs50, avec tout de même un léger signal dans le noyau, suggérant un relargage lent de la Doxorubicine des nanoparticules. Un contrôle positif a été effectué avec de l'Adriblastina[®] composant la Doxorubicine sous sa forme libre. Cette fois-ci, un signal intense a pu être constaté dans le noyau, suggérant une accumulation de la molécule entre les brins d'ADN. La microspectroscopie Raman a par contre démontré une accumulation de la Doxorubicine dans le noyau après 4 h d'incubation avec une solution à 10 μM en agent thérapeutique (**Figure 10.a**). La **Figure 10.b** démontre une augmentation de la concentration dans le noyau au fur et à mesure et atteint une concentration locale de 250 μM pour les DOX@ssNPs50 alors que Caelyx[®] présente un relargage plus lent avec seulement 100 μM pour le même temps d'incubation.

L'étude de nouvelles possibilités pour livrer des agents anticancéreux de manière contrôlée a constitué l'un des plus grand défis de la dernière décennie. Les matériaux répondant à des stimuli, qui interagissent avec des caractéristiques spécifiques du milieu cellulaire, ont été largement étudiés puisqu'ils permettent un relargage contrôlé de médicament dans les tissus ciblés. Parmi les liens répondant à des stimuli, les dérivés réactifs de l'oxygène (ROS) ont suscité beaucoup d'intérêt,^[48-50] et en comparaison avec les systèmes redox, ils offrent une spécificité plus importante à l'égard de la tumeur, en raison de la production importante de ROS dans les cellules cancéreuses (pouvant atteindre 100 μ M) par rapport aux cellules saines (2 nM).^[51]

En suivant cette ligne directrice, des nanoparticules de silice mésoporeuses contenant des liens répondant au ROS ont été développées (ROSNPs). Ces nanoparticules contiennent des liens thioacétale (**Figure 11**) capables de se rompre en présence d'oxygène singulet. De plus, la concentration de ces derniers peut facilement être augmentée localement à l'aide de photosensibilisateurs attachés sur la surface du matériau. Sous irradiation, ils produisent des oxygènes singulets, détruisant ainsi la nanoparticule, créant un contrôle spatiotemporel pouvant être utilisé pour la thérapie photodynamique.

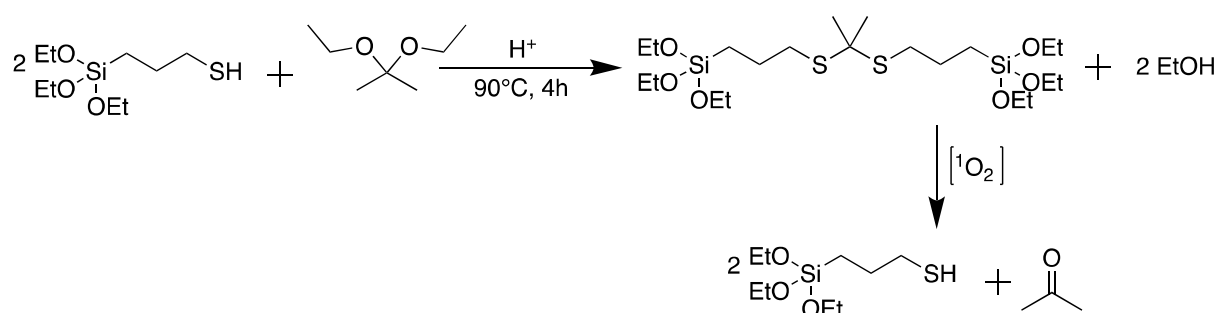


Figure 11: Synthèse du lien thioacétale. En présence d'oxygène singulet, la molécule s'oxyde formant ainsi deux molécules de 3-(mercaptopropyl)triéthoxysilane et une molécule d'acétone.

Le lien clivable a été synthétisé de manière quantitative suivant une réaction en une étape. Le pont répondant à des stimuli a directement été mélangé ensuite à du TEOS en présence de CTAB dans un processus modifié de Stöber pour former les ROSNPs. Un schéma du design du matériau est représenté dans la **Figure 12**.

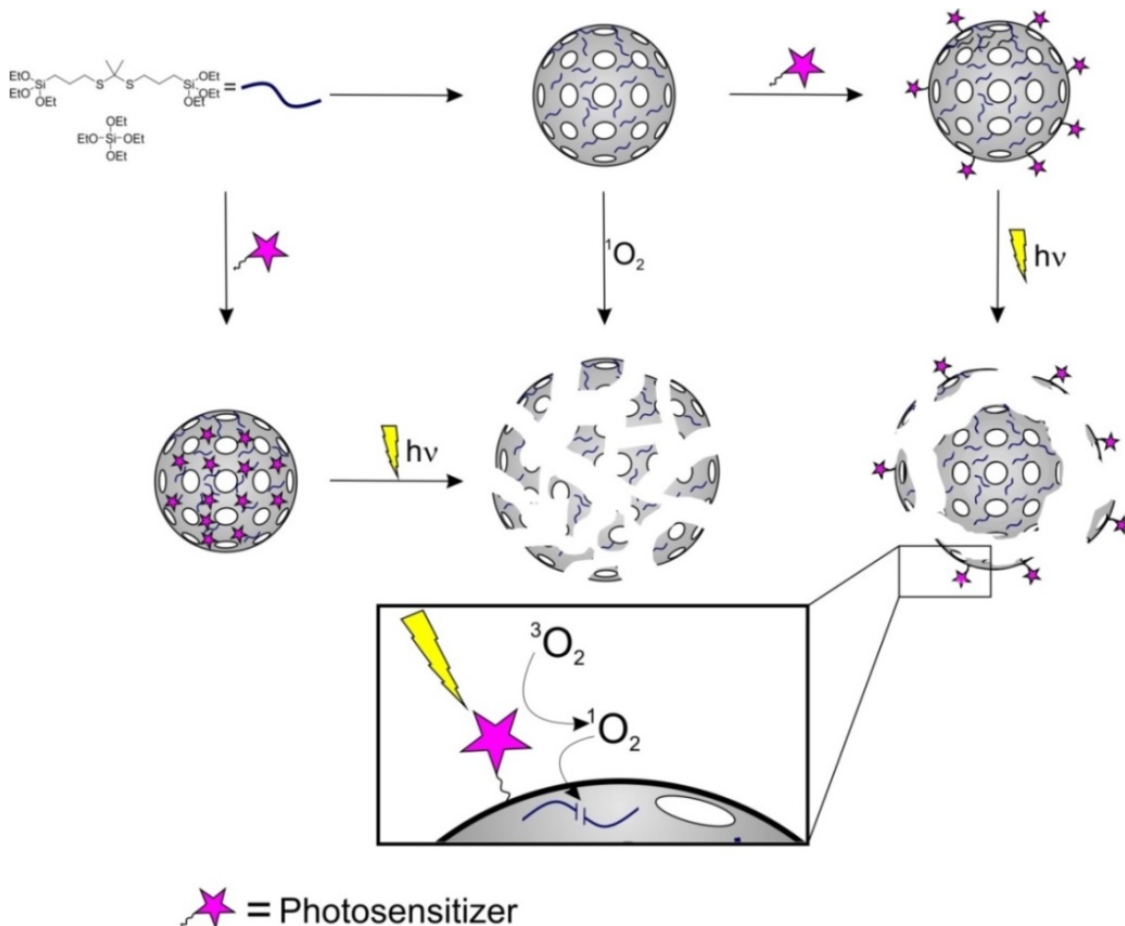


Figure 12: Représentation du schéma de synthèse des différentes ROSNPs.

Les ROSNPs ont été caractérisées par MEB (**Figure 13.a**) et MET (**Figure 13.b**) et présentent une morphologie sphérique ainsi qu'une taille de 105 ± 12 nm déterminée par le comptage de 200 nanoparticules. Ces données ont ensuite été confirmées par diffusion dynamique de la lumière (DLS) présentant une valeur de 131 ± 28 nm.

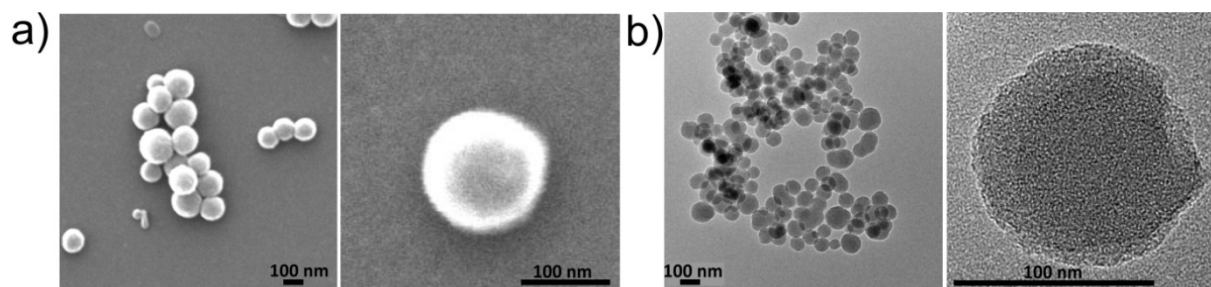


Figure 13: Images a) MEB et b) TEM des ROSNPs. Sur l'image de gauche, plusieurs particules sont représentées et l'image de droite montre un zoom sur une particule unique. Echelle = 100 nm.

Des tests de dégradation des nanoparticules ont été effectués en incubant les ROSNPs ($0.1 \text{ mg}\cdot\text{mL}^{-1}$) dans une solution de superoxyde de potassium (KO_2 , 10 mM) dans du PBS. Après 3 h d'incubation, les images STEM présentaient déjà une cassure avancée des nanoparticules tandis qu'après 48 h, seulement de petits fragments ont pu être détectés (**Figure 14.a**). Un contrôle négatif a été effectué en incubant les particules dans du PBS. Ces dernières ne présentaient aucune cassure après 48 h d'incubation, démontrant la stabilité du système en milieu aqueux (**Figure 14.b**).

La lumière, plus précisément possédant des longueurs d'onde se trouvant entre 600 – 1200 nm (fenêtre optique pour les tissus), pénètre profondément et de manière précise à travers la peau et est, pour cette raison, utilisée pour le diagnostic ou la thérapie.^[52] Parmi elles, la thérapie photodynamique a été la première à être approuvée par la US Food and Drug Administration et est souvent employée en clinique.^[53] Elle consiste en l'utilisation d'un laser qui irradie un tissu jusqu'à atteindre la tumeur, où un photosensibilisateur, qui a été injecté, s'accumule et réagit avec son environnement proche pour produire des oxygènes singulet sous l'effet de la lumière. Ces photosensibilisateurs présentent généralement une absorbance entre 600 et 800 nm afin de fournir suffisamment d'énergie pour promouvoir l'excitation de l'oxygène de son état triplet à son état singulet.^[53,54]

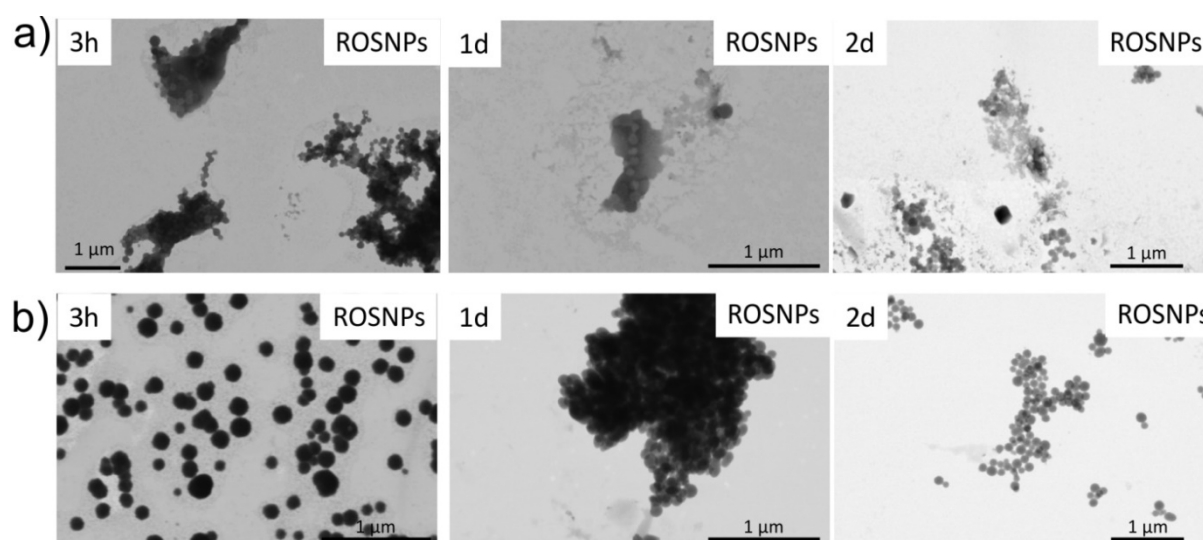


Figure 14: Tests de cassabilité d'une dispersion de ROSNPs ($0.1 \text{ mg}\cdot\text{mL}^{-1}$). a) ROSNPs incubées pendant 3 h, 1 j et 2 j dans une solution de KO_2 (10 mM). b) ROSNPs incubées pendant 3 h, 1 j et 2 j dans de l'eau milliQ (contrôle). Echelle = $1 \mu\text{m}$.

Le Rose Bengal est un analogue de la fluorescéine comportant des Cl et des I et possèdent un rendement quantique de $^1\text{O}_2$ de 0.75 et est couramment sous essai clinique pour le traitement du mélanome et du cancer du sein et porte le nom de PV-10.^[55] En tant que

grand producteur d'oxygène singulet, le Rose Bengal a été utilisé pour démontrer la cassabilité des nanoparticules. La **Figure 15** montre les images STEM prises après l'exposition des ROSNPs incubées avec différentes concentrations de Rose Bengal sous irradiation de la lumière pendant 4 h. Comme prévu, ces différentes concentrations ont eu un impact considérable sur la dégradation du nanomatériau. Une incubation à 10^{-2} M démontrait une cassure très avancée des nanoparticules après seulement 4 h d'irradiation. En réduisant la concentration à 10^{-3} M, une dégradation importante est toujours observée. A 10^{-4} M par contre, très peu de nanoparticules semblent se briser et une concentration à 10^{-5} M ne présente aucun changement.

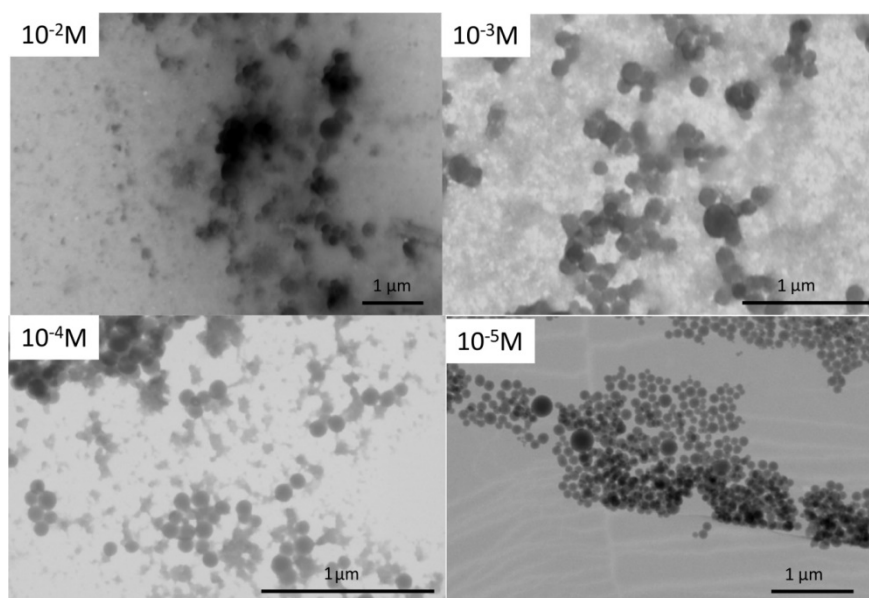


Figure 15: Analyse STEM d'une suspension de ROSNPs a $0.1 \text{ mg}\cdot\text{mL}^{-1}$ en présence de différentes concentrations de Rose Bengal (de 10^{-2} M à 10^{-5} M). Les échantillons ont été irradiés pendant 4 h avec une lampe Hg. Echelle = $1 \mu\text{m}$.

Afin de créer une production d'oxygène singulet proche du nanomatériau et de promouvoir ainsi la cassure du matériau sous irradiation de la lumière, le photosensibilisateur a été couplé de façon covalente sur la surface du matériau. Pour cela, le Rose Bengal a été modifié de manière à posséder une chaîne aliphatique dotée d'un acide carboxylique qui a ensuite été couplé à la particule à l'aide d'APTES par un couplage de type peptidique (ROSNPs-RB). Les images MET après 4 h d'irradiation ont démontré une dégradation partielle de la surface et des pores de la nanoparticule (**Figure 16.a**). Ceci peut être expliqué par le détachement du photosensibilisateur après réaction et qui éloigne ainsi la production d'oxygène singulet de la surface de la nanoparticule. Pour cette raison, le dérivé du Rose Bengal synthétisé a ainsi été incorporé directement dans la structure des ROSNPs en mélangeant le colorant en présence d'APTES pendant la condensation des ROSNPs. Comme

il peut être observé dans les images STEM (**Figure 16.b**), une dégradation totale des nanoparticules a pu être démontrée pendant le même temps d'incubation ce qui prouve l'efficacité du photosensibilisateur lorsqu'il est incorporé dans la structure de la silice.

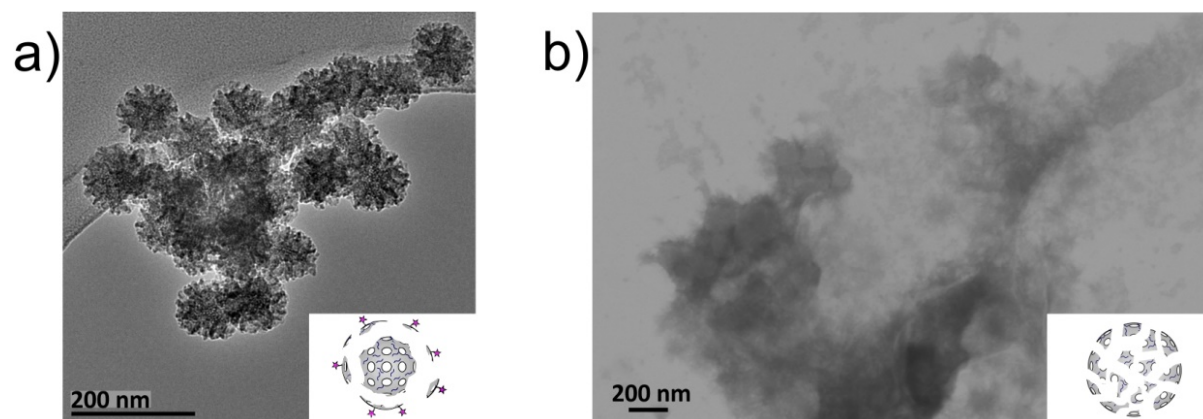


Figure 16: Test de cassure fait sur les ROSNPs préalablement modifiées avec du Rose Bengal dans une solution de PBS à $0.1 \text{ mg}\cdot\text{mL}^{-1}$ pendant 4 h d'irradiation avec une lampe au Hg. a) Image MET après post-fonctionnalisation du colorant sur la surface. b) Image STEM de particules fonctionnalisées in situ. Echelle = 200 nm.

Des études préliminaires *in vitro* ont été conduites dans des lignées cellulaires différentes (Hdfa, Glioma, HeLa et Huh-7) afin d'étudier l'internalisation des ROSNPs. De plus la production de ROS dépend de la lignée cellulaire et peut varier entre les différentes lignées tumorales. Un test d'activité métabolique n'a montré aucune cytotoxicité du matériau après 4 h d'incubation dans les différentes lignées cellulaires jusqu'à une concentration de $100 \mu\text{g}\cdot\text{mL}^{-1}$ (**Figure 17**). Les ROSNPs ont ensuite été fonctionnalisés avec de la fluorescéine, permettant un suivi au microscope confocal, et ont démontré une internalisation après quelques heures d'incubation.

Le design spécifique de nanoparticules de silice mésoporeuse cassables a été démontré dans le but d'atteindre des objectifs précis dans le domaine biomédical et a également démontré leurs potentiels pour l'industrie agroalimentaire. Le **chapitre 2** présente des nanoparticules de silice aux larges pores incorporant des ponts disulfures qui ont ensuite été employées pour le relargage d'un siRNA PLK1 à l'intérieur de carcinome hépatocellulaire Huh-7. Le matériau a démontré des résultats très prometteurs *in vitro* et *in vivo*, permettant une réduction de la prolifération des cellules tumorales dans des modèles de souris xénotransplante. Le **chapitre 3** démontre l'application potentielle de ces nanoparticules pour l'agroalimentaire en piégeant un peptide Hv1a, connu pour être un pesticide très prometteur. Le **chapitre 4** se concentre sur la synthèse de nanoparticules de silice cassable de 50 nm pour

la livraison de Doxorubicine dans les cellules de glioblastome humaines U87. Le matériau présente une amélioration et une accélération du relargage de Doxorubicine par rapport à sa forme liposomale Caelyx[®] durant les premières heures d'incubation. Le chapitre 5 étudie un nouveau type de nanoparticules de silice mésoporeuses cassables, capables de se briser en présence de dérivés réactifs de l'oxygène. Le nanoconteneur présente une cassabilité très rapide qui peut être améliorée en incorporant un photosensibilisateur dans la structure de la nanoparticule. Les études préliminaires in vitro ont démontré une bonne biocompatibilité ainsi qu'une internalisation conséquente dans plusieurs lignées cellulaires.

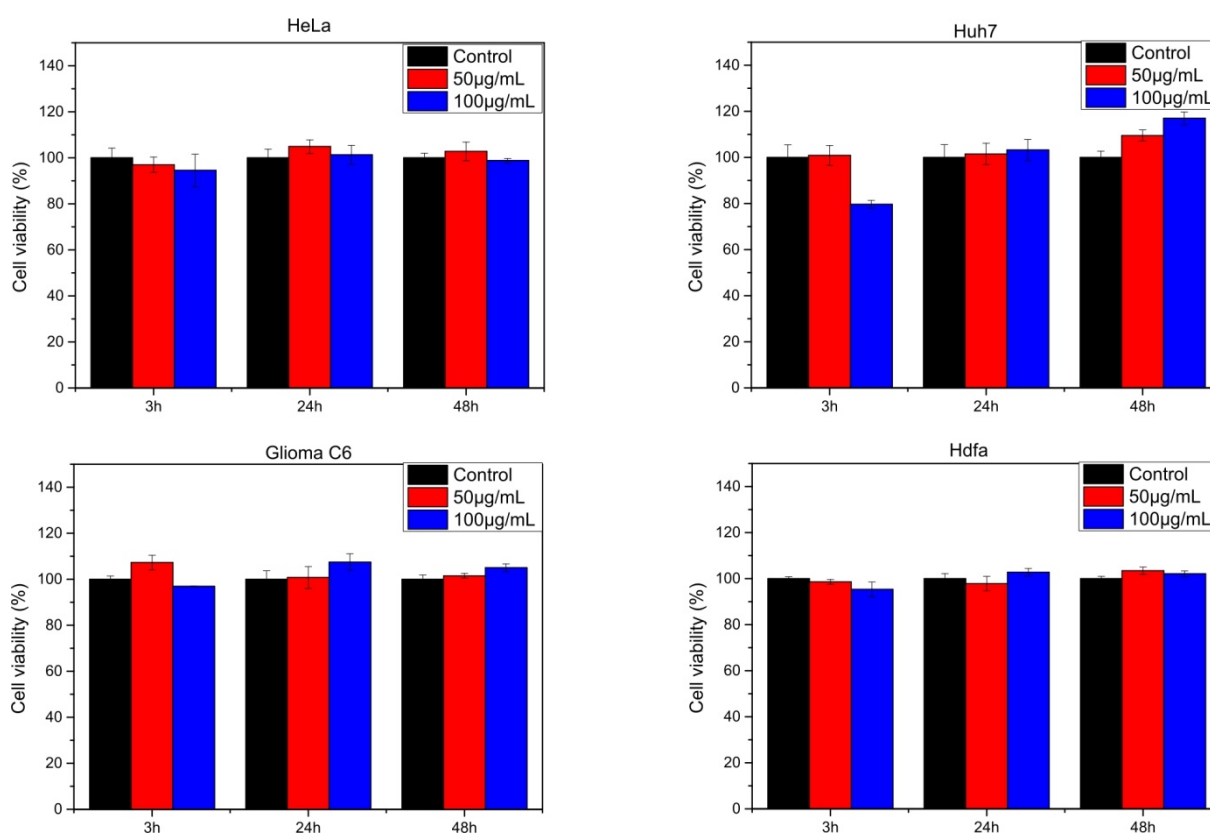


Figure 17: Activité métabolique déterminée par un test à l'Alamar Blue dans différentes lignées cellulaires (HeLa, Huh-7, Glioma C6 and Hdfa) après 3, 24, et 48 h d'incubation avec différentes concentrations de ROSNPs (50 and 100 µg·mL⁻¹).

Références

- [1] J. Li, C. Papadopoulos, J. Xu, *Nature* **1999**, *402*, 253–254.
- [2] W. J. Stark, P. R. Stoessel, W. Wohlleben, A. Hafner, *Chemical Society Reviews* **2015**, *44*, 5793–5805.
- [3] O. Salata, *Journal of Nanobiotechnology* **2004**, *2*, 3.
- [4] C. A. Mirkin, *Small* **2005**, *1*, 14–16.
- [5] Z. Li, J. C. Barnes, A. Bosoy, J. Fraser Stoddart, J. I. Zink, *Chemical Society Reviews* **2012**, *41*, 2590–2605.
- [6] D. A. Richards, A. Maruani, V. Chudasama, *Chemical Science* **2017**, *8*, 63–77.
- [7] S. Nie, *Nanomedicine* **2010**, *5*, 523–528.
- [8] J. D. Lewis, G. Destito, A. Zijlstra, M. J. Gonzalez, J. P. Quigley, M. Manchester, H. Stuhlmann, *Nature Medicine* **2006**, *12*, 354–360.
- [9] T. M. Allen, P. R. Cullis, *Advanced Drug Delivery Reviews* **2013**, *65*, 36–48.
- [10] A. Kumari, S. K. Yadav, S. C. Yadav, *Colloids and Surfaces B: Biointerfaces* **2010**, *75*, 1–18.
- [11] L. Liu, K. Xu, H. Wang, P. K. J. Tan, W. Fan, S. S. Venkatraman, L. Li, Y.-Y. Yang, *Nature Nanotechnology* **2009**, *4*, 457–463.
- [12] S. Goel, F. Chen, W. Cai, *Small* **2014**, *10*, 631–645.
- [13] C. Argyo, V. Weiss, C. Bräuchle, T. Bein, *Chemistry of Materials* **2013**, *26*, 435–451.
- [14] J.-H. Park, L. Gu, G. von Maltzahn, E. Ruoslahti, S. N. Bhatia, M. J. Sailor, *Nature Materials* **2009**, *8*, 331–336.
- [15] A. Bianco, K. Kostarelos, M. Prato, *Current Opinion in Chemical Biology* **2005**, *9*, 674–679.
- [16] A. B. D. Nandiyanto, S.-G. Kim, F. Iskandar, K. Okuyama, *Microporous and Mesoporous Materials* **2009**, *120*, 447–453.
- [17] W. Stöber, A. Fink, E. Bohn, *Journal of Colloid and Interface Science* **1968**, *26*, 62–69.
- [18] A. Monnier, F. Schüth, Q. Huo, D. Kumar, D. Margolese, R. S. Maxwell, G. D. Stucky, M. Krishnamurty, P. Petroff, A. Firouzi, *et al.*, *Science* **1993**, *261*, 1299–1303.
- [19] M. Mizutani, Y. Yamada, T. Nakamura, K. Yano, *Chemistry of Materials* **2008**, *20*, 4777–4782.
- [20] L. Prezzi, L. Mascia, *Advances in Polymer Technology* **2005**, *24*, 91–102.
- [21] M. Vallet-Regi, A. Rámila, R. P. del Real, J. Pérez-Pariante, *Chemistry of Materials* **2001**, *13*, 308–311.
- [22] K. Möller, K. Müller, H. Engelke, C. Bräuchle, E. Wagner, T. Bein, *Nanoscale* **2016**, *8*, 4007–4019.
- [23] A. M. Chen, M. Zhang, D. Wei, D. Stueber, O. Taratula, T. Minko, H. He, *Small* **2009**, *5*, 2673–2677.
- [24] H. Meng, W. X. Mai, H. Zhang, M. Xue, T. Xia, S. Lin, X. Wang, Y. Zhao, Z. Ji, J. I. Zink, *et al.*, *ACS Nano* **2013**, *7*, 994–1005.
- [25] J. Kim, H. S. Kim, N. Lee, T. Kim, H. Kim, T. Yu, I. C. Song, W. K. Moon, T. Hyeon, *Angewandte Chemie* **2008**, *120*, 8566–8569.
- [26] X.-D. Zhang, D. Wu, X. Shen, P.-X. Liu, F.-Y. Fan, S.-J. Fan, *Biomaterials* **2012**, *33*, 4628–4638.
- [27] H. S. Choi, W. Liu, P. Misra, E. Tanaka, J. P. Zimmer, B. I. Ipe, M. G. Bawendi, J. V. Frangioni, *Nature Biotechnology* **2007**, *25*, 1165–1170.
- [28] Y. Lu, H. Fan, A. Stump, T. L. Ward, T. Rieker, C. J. Brinker, *Nature* **1999**, *398*, 223–226.
- [29] K. C.-F. Leung, T. D. Nguyen, J. F. Stoddart, J. I. Zink, *Chemistry of Materials* **2006**, *18*, 5919–5928.

- [30] J. Zhang, M. Niemelä, J. Westermarck, J. M. Rosenholm, *Dalton Transactions* **2014**, 43, 4115–4126.
- [31] S. Mura, J. Nicolas, P. Couvreur, *Nature Materials* **2013**, 12, 991–1003.
- [32] L. Zhao, D. A. Loy, K. J. Shea, *Journal of the American Chemical Society*. **2006**, 128, 14250–14251.
- [33] S. Quignard, S. Masse, G. Laurent, T. Coradin, *Chemical Communications***2013**, 49, 3410–3412.
- [34] J. Croissant, X. Cattoën, M. W. C. Man, A. Gallud, L. Raehm, P. Trens, M. Maynadier, J.-O. Durand, *Advanced Materials* **2014**, 26, 6174–6180.
- [35] J.G. Croissant, Y. Fatieiev, K. Julfakyan, J. Lu, A-H. Emwas, D.H. Anjum, H. Omar, F. Tamanoi, J.I. Zink, N.M. Khashab, *Chemistry – A European Journal* **2016**, 22, 14806–14811.
- [36] J.G. Croissant, Y. Fatieiev, N.M. Khashab, *Advanced Materials* **2017**, 29, 1604634.
- [37] L. Maggini, I. Cabrera, A. Ruiz-Carretero, E. A. Prasetyanto, E. Robinet, L. D. Cola, *Nanoscale* **2016**, 8, 7240–7247.
- [38] L. Maggini, L. Travaglini, I. Cabrera, P. Castro-Hartmann, L. De Cola, *Chemistry – A European Journal* **2016**, 22, 3697–3703.
- [39] E. A. Prasetyanto, A. Bertucci, D. Septiadi, R. Corradini, P. Castro-Hartmann, L. De Cola, *Angewandte Chemie International Edition* **2016**, 55, 3323–3327.
- [40] F. Q. Schafer, G. R. Buettner, *Free Radical Biology and Medicine* **2001**, 30, 1191–1212.
- [41] K. Strebhardt, A. Ullrich, *Nature Reviews Cancer* **2006**, 6, 321–330.
- [42] U. Holtrich, G. Wolf, A. Bräuninger, T. Karn, B. Böhme, H. Rübsamen-Waigmann, K. Strebhardt, *Proceedings of the National Academy of Sciences of the United States of America* **1994**, 91, 1736–1740.
- [43] X.-Z. Yang, S. Dou, T.-M. Sun, C.-Q. Mao, H.-X. Wang, J. Wang, *Journal of Controlled Release* **2011**, 156, 203–211.
- [44] J. Popp, K. Pető, J. Nagy, *Agronomy for Sustainable Development* **2013**, 33, 243–255.
- [45] E. Grishin, *European Journal of Biochemistry* **1999**, 264, 276–280.
- [46] C. Saraiva, C. Praça, R. Ferreira, T. Santos, L. Ferreira, L. Bernardino, *Journal of Controlled Release* **2016**, 235, 34–47.
- [47] K. Möller, J. Kobler, T. Bein, *Advanced Functional Materials* **2007**, 17, 605–612.
- [48] D. S. Wilson, G. Dalmaso, L. Wang, S. V. Sitaraman, D. Merlin, N. Murthy, *Nature Materials* **2010**, 9, 923–928.
- [49] J. S. Kim, S. D. Jo, G. L. Seah, I. Kim, Y. S. Nam, *Journal of Industrial and Engineering Chemistry* **2015**, 21, 1137–1142.
- [50] G. Saravanakumar, J. Kim, W. J. Kim, *Advanced Science* **2017**, 4, 1600124.
- [51] T. P. Szatrowski, C. F. Nathan, *Cancer Research* **1991**, 51, 794–798.
- [52] D. E. J. G. J. Dolmans, D. Fukumura, R. K. Jain, *Nature Reviews Cancer* **2003**, 3, 380–387.
- [53] P. Agostinis, K. Berg, K. A. Cengel, T. H. Foster, A. W. Girotti, S. O. Gollnick, S. M. Hahn, M. R. Hamblin, A. Juzeniene, D. Kessel, *et al.*, *CA: A Cancer Journal for Clinicians* **2011**, 61, 250–281.
- [54] R. R. Allison, C. H. Sibata, *Photodiagnosis and Photodynamic Therapy* **2010**, 7, 61–75.
- [55] E. Gandin, Y. Lion, A. V. de Vorst, *Photochemistry and Photobiology* **1983**, 37, 271–278.

Summary of the thesis

For several decades, nanomaterials have assisted our daily life as they have been widely exploited for cosmetics, oil cracking, electronics *etc.*^[1,2] With their interesting properties, which could lead to the next industrial revolution,^[3,4] nanoparticles have also established an interesting niche in the medical area, constantly exploring new technologies for the development of safe and effective tools.^[5] Thanks to their capability to overcome biological barriers, they have found applications in drug and gene delivery, imaging, biosensing and diagnosis. Such nanocontainers can be divided in three main categories (organic, inorganic and hybrid) and possess high degree of versatility allowing long half-life times, specific biodistribution and release on-demand of guest molecules.

Several nanomaterials already did a breakthrough in the nanomedicine world,^[6,7] namely viral,^[8] liposomes,^[9] polymeric,^[10] peptidic,^[11] metallic (gold, silver and quantum dots),^[12-14] silica,^[15] silicon,^[16] and carbon-based nanoparticles.^[17] Their shapes, sizes, surface charges, and functionalizations are critical parameters to consider for specific delivery of cargoes within specific tissues^[18] and development of precise nanocarriers requires years of investigation between the synthesis and their potential breakthrough on the market.^[19]

Among all the materials reported, mesoporous silica nanoparticles have shown great potential thanks to their easy tailoring^[20-23] and surface/pore functionalization,^[24] high loading capacities,^[25] biocompatibility (**Figure 1**). Thus, they offer a robust inorganic scaffold for the delivery of guest molecules, protecting them from early degradation and allowing their internalization within cells.^[26,27] Furthermore, specific functionalization of the pores or the surface of the material creates specific interactions with guest molecules,^[28] hence increasing their loading and/or the implementation of targeting ligands interacting with a cell type of interest.^[29] Despite their numerous advantages, their clinical translation is still prevented due to early leakage of the cargo combined with bioaccumulation issues, problematic for cancer therapy where frequent injections of chemotherapeutics are required.^[30-32] Functionalizing the pore entrance with complex systems able to, once the desired drug filled, clog the pore cavities has been widely studied to prevent early leakage of guest molecules. Those systems, so-called nanogates, play often with the specific cellular environment and are able to release their payloads only upon a desired stimulus such as pH, redox, light, *etc.*^[33-35]

With the pioneer work of Inagaki, Ozin and Stein^[36–38] on the development of periodic mesoporous organosilica nanoparticles, researchers tackled the bioaccumulation of silica nanoparticles by inserting stimuli-responsive units directly within the framework of silica nanoparticles. Those moieties can be cloven in presence of specific stimuli, leading to a degradation of the particles in small pieces, hence insuring an efficient renal excretion.^[39–42] So far, few examples have been published by our group and others, based on redox or enzyme responsive linkers and demonstrated promising results.^[40,41,43–45]

This thesis called “**Breakable silica nanoparticles for the *in vitro* and *in vivo* delivery of biomolecules**” is based on the tailoring of disulfide-doped breakable mesoporous silica nanoparticles for drug, gene and peptide delivery. It also presents the development of new stimulus-responsive mesoporous silica nanoparticles able to break down in the presence of Reactive Oxygen Species (ROS) that can be further functionalized with photosensitizers for improved breakability properties.

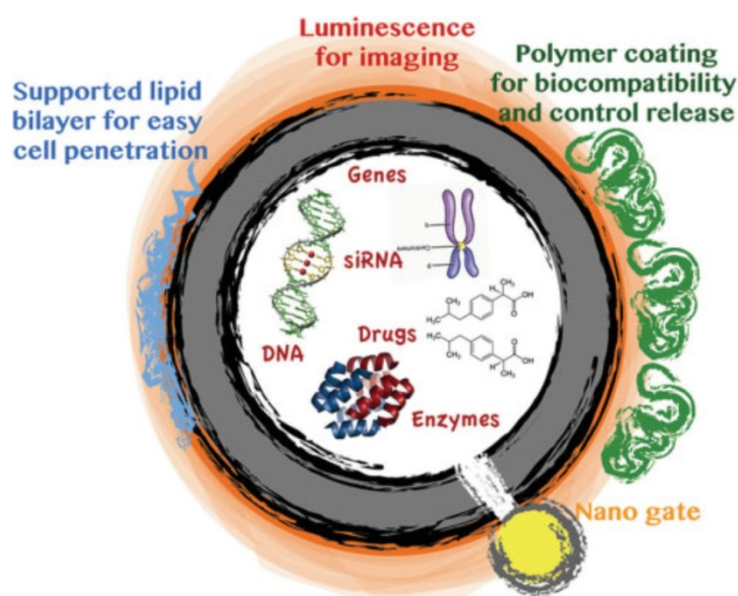


Figure 1: Schematic representation of silica nanoparticles for biomedical applications. It presents the hosting of guest molecules as well as the possible functionalization to obtain stealth and targeting materials. Reprinted with the permission from Lülfi H., Devaux A., Prasetyanto E.A., De Cola L., Porous nanomaterials for biomedical applications, in *Organic Nanomaterials: Synthesis, Characterization, and Device Applications*, Wiley, Ch22 (2013). Copyright 2013, WILEY-VCH Verlag GmbH & Co. KGaA, Weinheim.

Due to its different concentrations between the intra (2-10 mM) and extracellular (2-5 μ M) environment of a cell, glutathione (GSH), a thiol-containing tripeptide able to reduce disulfide bonds, have attracted a lot of attention for the development of redox stimuli-responsive nanomaterials.^[46] In our laboratory, we developed disulfide-doped mesoporous

silica nanoparticles, which upon reaction with the tripeptide, break down in small pieces to release chemotherapeutics within the cytoplasm of the cell but also to promote safe excretion of the material out of the body.^[43,45]

The material was synthesized using a modified Stöber process in presence of cetyltrimethylammonium bromide (CTAB) as a pore template. The particles were formed in presence of tetraethyl orthosilicate (TEOS) and bis(triethoxysilyl-propyl)disulfide (BTSPD) as silane sources in a molar ratio of 70:30 and NaOH as a base catalyst. The resulting disulfide-doped mesoporous silica nanoparticles (ssNPs) presented a size of around 100 nm and a pore size around 2 nm. For the delivery of oligonucleotides such as DNA or siRNA, larger pore sizes are required. In this regard, a post synthetic treatment in presence of the swelling agent trimethylbenzene (TMB) was performed^[23] increasing the final pore size to a broad pore size distribution centered around 12 nm (LP-ssNPs). A schematic representation of the nanoparticles synthesis is represented in **Figure 2**.

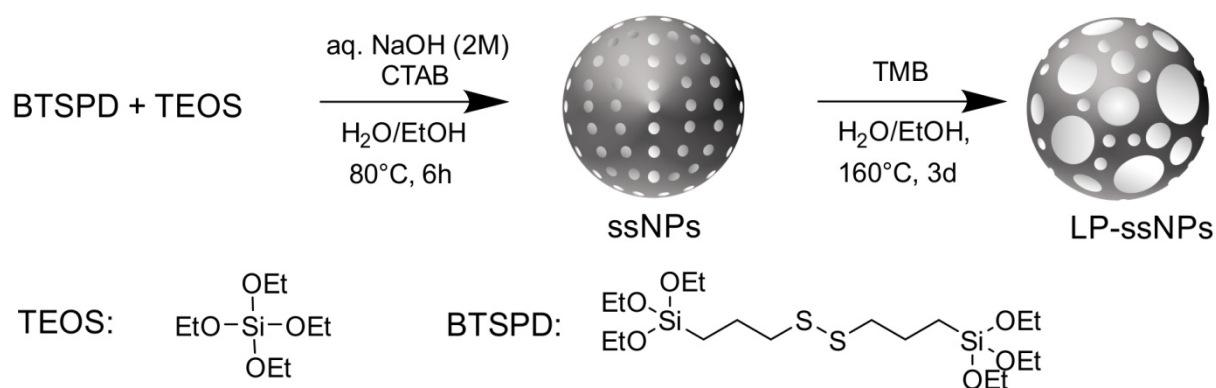


Figure 2: Schematic representation of the nanoparticles synthesis and the post-synthetic treatment for LP-ssNPs.

The negatively charged LP-ssNPs were further functionalized with 3-(aminopropyl) triethoxysilane (APTES) to provide a positively charged material (NH₂-LP-ssNPs), hence allowing electrostatic interactions with a negatively charged oligonucleotide. A breakability test was then performed, mimicking the intracellular concentration of GSH. The nanoparticles were dispersed in a solution of GSH (10 mM) in PBS 7.4 at 37°C and stirred for 7 days. As observed in **Figure 3**, Transmission Electron Microscopy (TEM) micrographs showed an advanced break down of the particles only after 3 days of incubation and presence of very small fragments after 7 days, while control with breakable nanoparticles without GSH did not show any advanced degradability.

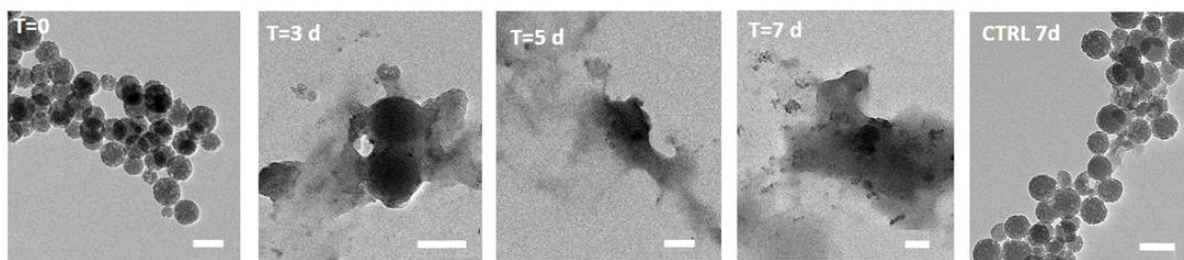


Figure 3: TEM analysis of a suspension of NH₂-LP-ssNPs at 0.1 mg/mL, PBS, 37 °C undergoing GSH (10 mM) reduction (0-7 d). On the right side of the figure CTRL nanoparticles stirred in PBS for 7 days without GSH. Scale bar = 100 nm.

Loading of a double strand polo-like kinase 1 (PLK1) siRNA was then performed. This siRNA was chosen because of its ability to silence the gene expressing the PLK1 protein, overexpressed by cancer cells.^[47] PLK proteins are a family of serine/threonine kinases, able to phosphorylate different proteins, hence regulating cell cycle progression. Such properties, combined with the knowledge that cancer cells proliferates very fast, led to the discovery of the high expression of PLK1 in primary tumor tissues compared to healthy tissues.^[48] In particular, Sun W. *et al.* demonstrated the high expression of PLK1 in hepatocellular carcinomas (HCC). Moreover, they demonstrated that the PLK1 expression was associated with the HCC development.^[49]

To knockdown PLK1 expression, specific sequences of double-stranded siRNA should be delivered within the cells and due to the difficulties of such highly negative and fragile biomolecules to penetrate cells, nanoparticles can be used as carriers.^[50] Therefore loading on NH₂-LP-ssNPs was then performed with both PLK1 and a negative control siRNA reaching a final loading of 182 µg of siRNA per mg of nanoparticles (PLK1@NH₂-LP-ssNPs and control@NH₂-LP-ssNPs)

The nanocarriers were then further coated with a linear polyethylenimine (jetPEI[®]) ensuring protection of the cargo against nucleases, a better internalization within the cells due to its positive charge and promoting endosomal escape (jp-PLK1@NH₂-LP-ssNPs and jp-control@NH₂-LP-ssNPs). A schematic representation of the layer-by-layer assembly is presented in **Figure 4**.

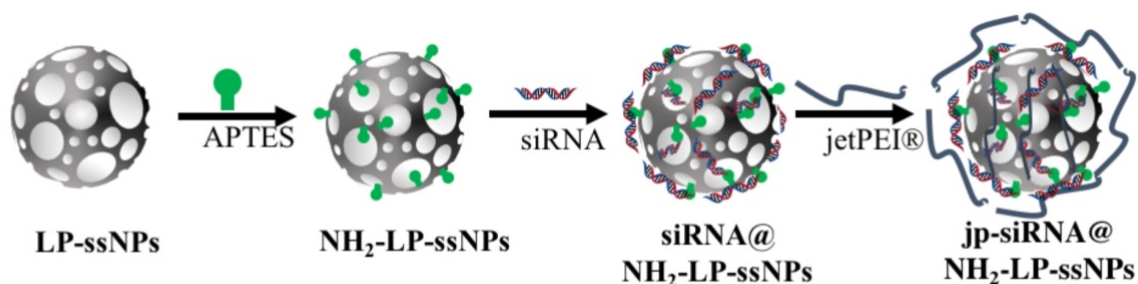


Figure 4: Schematic representation of the different coating steps leading to the final material.

In vitro experiments were carried in hepatocellular carcinoma Huh-7 cells. The LP-ssNPs did not demonstrate any cytotoxicity for the concentrations tested after 48 h of incubation. Confocal laser scanning microscopy (CLSM) and fluorescence activated cell sorting showed a detectable uptake of nanoparticles within 3 h of incubation increasing after 48 h. The particles and the PLK1 siRNA were labelled with Rhodamine and Cyanine 5 respectively to assess the efficient release of the oligonucleotide. The material was then incubated within the Huh-7 cells. As it can be observed on **Figure 5**, after 3 h of incubation, the particles were already internalized within the cells and release of siRNA started to occur, as indicated by the observation of diffusion of the Cyanine 5 signals within the cytoplasm.

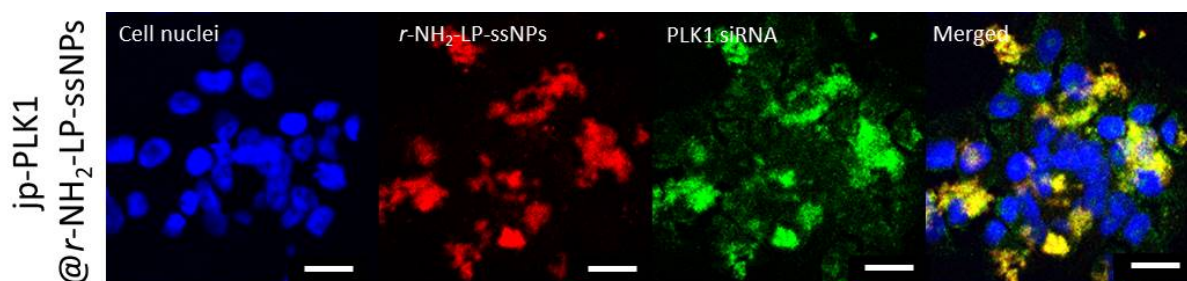


Figure 5: Cellular uptake of jp-PLK1@r-NH₂-LP-ssNPs. Confocal images were taken after 3 h of incubation with the particles. Cell nuclei were stained with Hoechst 33342 (blue) and the particles were doped with Rhodamine B (red). PLK1 siRNA were coupled to a Cyanine 5 dye (green) with a Cy5Label IT[®] siRNA Tracker Intracellular Localization Kit (Mirus) and grafted on the particles. The right images correspond to the merge signal. Excitation wavelengths are 355, 488 and 633 nm. Scale bar = 20 μm.

The potential antitumoral effect was then assessed *in vivo* by intratumoral injections of the system within Huh-7 mice xenograft models (**Figure 6**). Injections of both jp-PLK1@NH₂-LP-ssNPs and jp-control@NH₂-LP-ssNPs were performed every 2 days for 2 weeks. As shown on **Figure 6.b**, injections of PBS 7.4 and control siRNA presented a fast

growing of the tumor volume while jp-PLK1@NH₂-LP-ssNPs demonstrated a slower tumor proliferation for the dosage tested.

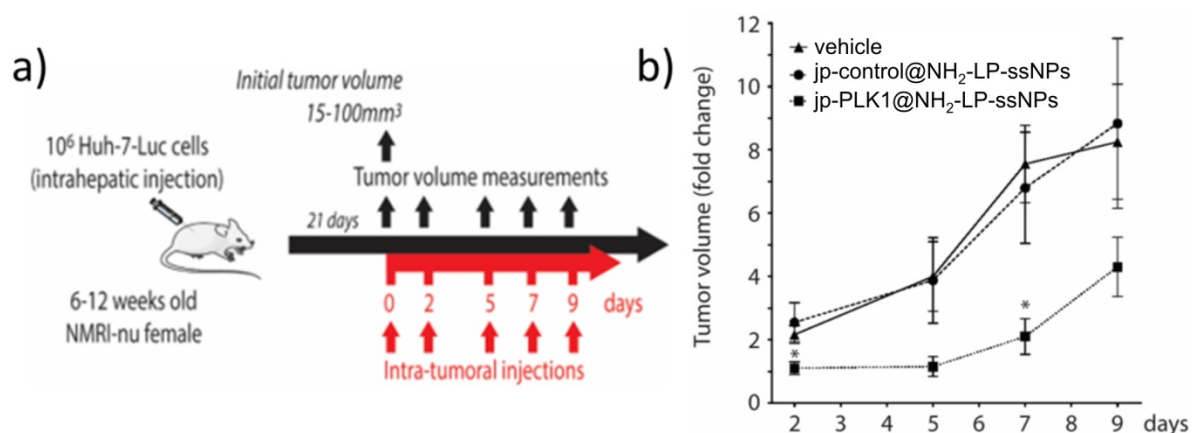


Figure 6: Intratumoral injections of jp-PLK1@NH₂-LP-ssNPs significantly reduce tumor growth in a cell-based xenograft mouse model. a) Scheme showing the experimental workflow. b) jp-siRNA@NH₂-LP-ssNPs reduced and delayed the onset of tumor growth. Huh-7-Luc cells were orthotopically injected into the liver of NMRI-nu mice and tumor growth was monitored by bioluminescence imaging. Once the tumor volume reached 15-100mm³, vehicle (n=5), jp-control@NH₂-LP-ssNPs (n=4), or jp-PLK1@NH₂-LP-ssNPs (n=4) were intra-tumorally injected and the tumor size was measured at days 0, 2, 5, 7, and 9. Results (mean ± s.e.m.) are reported as the tumor volume relative to the initial size. *p<0.05 Fisher's t-test.

The LP-ssNPs were then further employed to entrap a peptide known to kill specifically insects. Such peptides can therefore be used for the crop industry. As the world population keeps increasing by 70 million people every year and should reach a total population of 9.2 billion humans by 2050,^[51] it implies agriculture to face the rising demand in food, feed, fibers, *etc.* and the availability of new lands is limited. Among the possible strategies, the use of effective pesticides could prevent 35 % of annual harvest lost due to infestations. Research has been focus on peptides that could kill pests. Among them, spider venoms have demonstrated high efficiency to kill or paralyze pests.^[52] A peptide, extracted from the venom of Australian funnel-web spiders, has proven high lethality among all the insects tested so far.

The peptide was first labelled with Cyanine 5 for tracking before to be entrapped within the cavities of the LP-ssNPs. Thermogravimetric analysis on LP-ssNPs presented a weight loss of 23 wt%, attributed to the disulfide linker present in the framework of the material. On the other side, the loaded nanoparticles (PepCy5@LP-ssNPs) demonstrated a weight loss of 41 wt%, thus 18 wt% attributed to the peptide. (**Figure 7**).

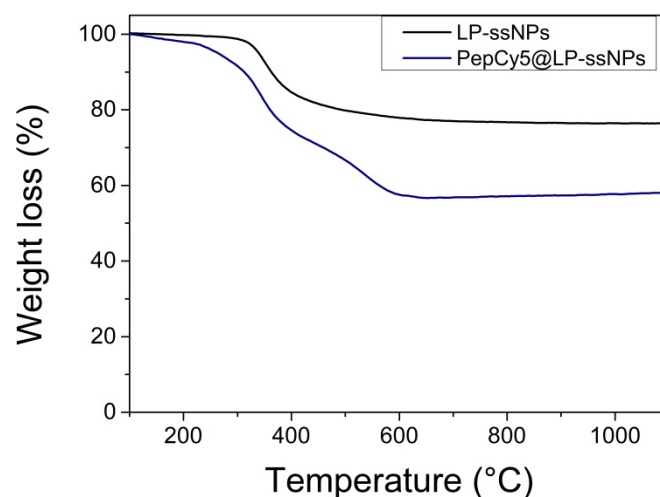


Figure 7: Loading of the PepCy5 on the LP-ssNPs.

As explained previously, the tailoring of silica nanoparticles is very straightforward and allows their use for several biomedical applications. For instance, the treatment of glioblastoma requires usually particles smaller than 50 nm to pass the blood brain barrier (BBB) through different types of mechanism. Receptor-mediated transcytosis of nanocarriers through the endothelial cells is probably the most common type but the passage through loosened tight junctions has also been observed.^[53]

We synthesized 50 nm disulfide-doped mesoporous silica nanoparticles (ssNPs50) with triethanolamine (TEA) as a base catalyst controlling nucleation growth due to its chelating properties and hence influencing silica condensation.^[54] The obtained nanoparticles were characterized by mean of Scanning Electron Microscopy (SEM) and demonstrated spherical nanoparticles about 49 ± 5 nm (**Figure 8**).

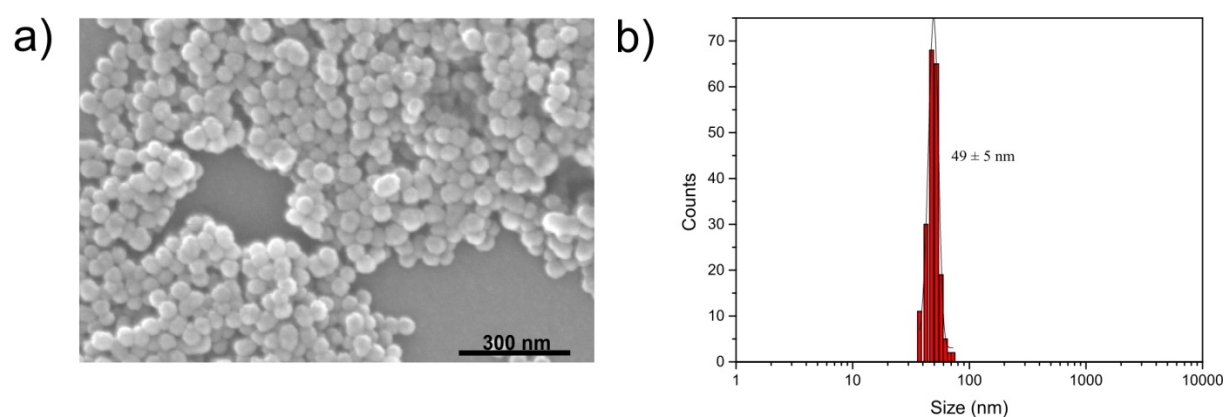


Figure 8: SEM micrograph of ssNPs50. Scale bar = 300 nm. b) Size distribution based on the count of 200 nanoparticles.

The material was further loaded with Doxorubicin, an anticancer drug able to intercalate within the DNA strands and which is easy to track thanks to its luminescent properties. A loading of 50 mg of Doxorubicin per g of ssNPs50 was determined by measuring the supernatant after incubation by UV-Vis spectroscopy.

In vitro studies were then performed in U87 glioblastoma cells at the Institute of Health in Luxembourg by the Dr. Valérie Palissot. The signal of Doxorubicin and squalenoyl-based Doxorubicin (Caelyx[®]) was determined by Raman microspectroscopy. As demonstrated in **Figure 9.a**, 2 characteristic peaks at 1210 and 1241 cm⁻¹ were distinguished. The signals were then observed *in vitro* (**Figure 9.b and c**) in both the cytoplasm and the nucleus giving the possibility to localize the drug once internalized.

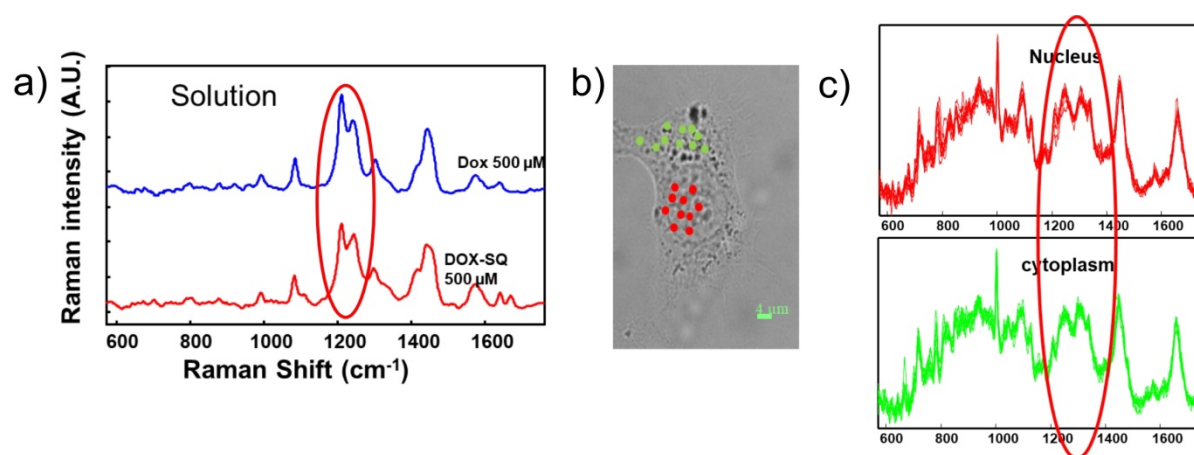


Figure 9: a) Determination of the characteristic peaks of Doxorubicin and squalenoyl-based Doxorubicin by Raman spectroscopy. b) Raman microspectroscopy on single cell. The dots represent the Raman IR scan within the cytoplasm (green) and within the nucleus (red). Scale bar = 4 μm. c) Raman scan performed in the nucleus and in the cytoplasm where the characteristic peaks of Doxorubicin could be observed.

Kinetic of release of Doxorubicin out of the ssNPs50 were then investigated and compared with the commercially available Caelyx[®]. After 3 h of incubation, the liposomal form Caelyx[®] was instead not observed in the perinuclear region, but was mostly still entrapped within vesicles such as endosomes. The same phenomenon was noticed with the DOX@ssNPs50 even though part of the fluorescence was also detected in the nuclear region, suggesting a release of the drug out of the particles. Positive control was also performed with Adriblastina[®], the free drug, and demonstrated a high accumulation of the chemotherapeutic within the nucleus. Kinetic experiments were also studied by Raman microspectroscopy at a concentration of 10 μM of the drug within 4 h of incubation (**Figure 10.a**). As observed in **Figure 10.b**, the concentration of Doxorubicin within the nucleus increases over time until

reaching a value of 250 μM for DOX@ssNPs50 while Caelyx[®] showed a slower release after the same time of incubation (100 μM).

Exploring new possibilities to deliver chemotherapeutics in a controlled manner has been one of the biggest challenges of the last decade. Stimuli-responsive materials, which interact with the characteristic cell environment, have been widely studied as they ensure efficient release of chemotherapeutics within the targeted area. Among the stimuli-responsive moieties, Reactive Oxygen Species (ROS) have also attracted a lot of attention.^[55-57] Compare to GSH, ROS offers a better tumor specificity since hypoxia significantly increase ROS production in cancer cells (up to 100 μM) compare to normal tissue (2 nM).^[58]

In this regard ROS-responsive mesoporous silica nanoparticles (ROSNPs) were developed by inserting within the silica framework, thioketal moieties that are oxidized in presence of singlet oxygen (**Figure 11**). Furthermore, increasing the concentration of singlet

oxygen on the nanoparticle surface can be achieved by the addition of photosensitizer on the surface of the material. Upon irradiation, the photosensitizer produces singlet oxygen and thus destroys the particles, allowing a spatiotemporal control of the system for photodynamic therapy.

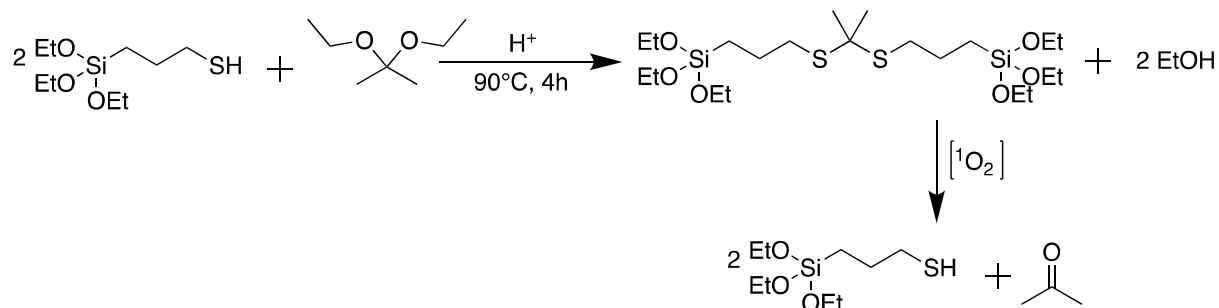


Figure 21: Schematic representation of the synthesis of the ROS-responsive linker. In presence of singlet oxygen, the molecule is oxidized forming then 2 molecules of 3-(mercaptopropyl) triethoxysilane and one molecule of acetone.

Light, especially wavelengths in the range of 600 – 1200 nm (optical window for tissue), penetrates deeply and locally the skin and is therefore often employed for diagnosis and therapies.^[59] Among them, photodynamic therapy (PDT) was the first drug-device approved by the US Food and Drug Administration and is often used in clinics.^[60] It is based on a laser which irradiates a tissue until reaching the tumor, where a photosensitizer that has been injected accumulates and reacts with the surrounding environment to form singlet oxygen. Photosensitizers present usually an absorbance peak between 600 and 800 nm to provide enough energy to promote oxygen to its singlet state and form enough reactive oxygen species.^[60,61]

The linker was synthesized quantitatively in a single step reaction and was directly involved in a modified Stöber process with TEOS to form the ROSNPs. A schematic representation of the design of the material is represented in **Figure 12**.

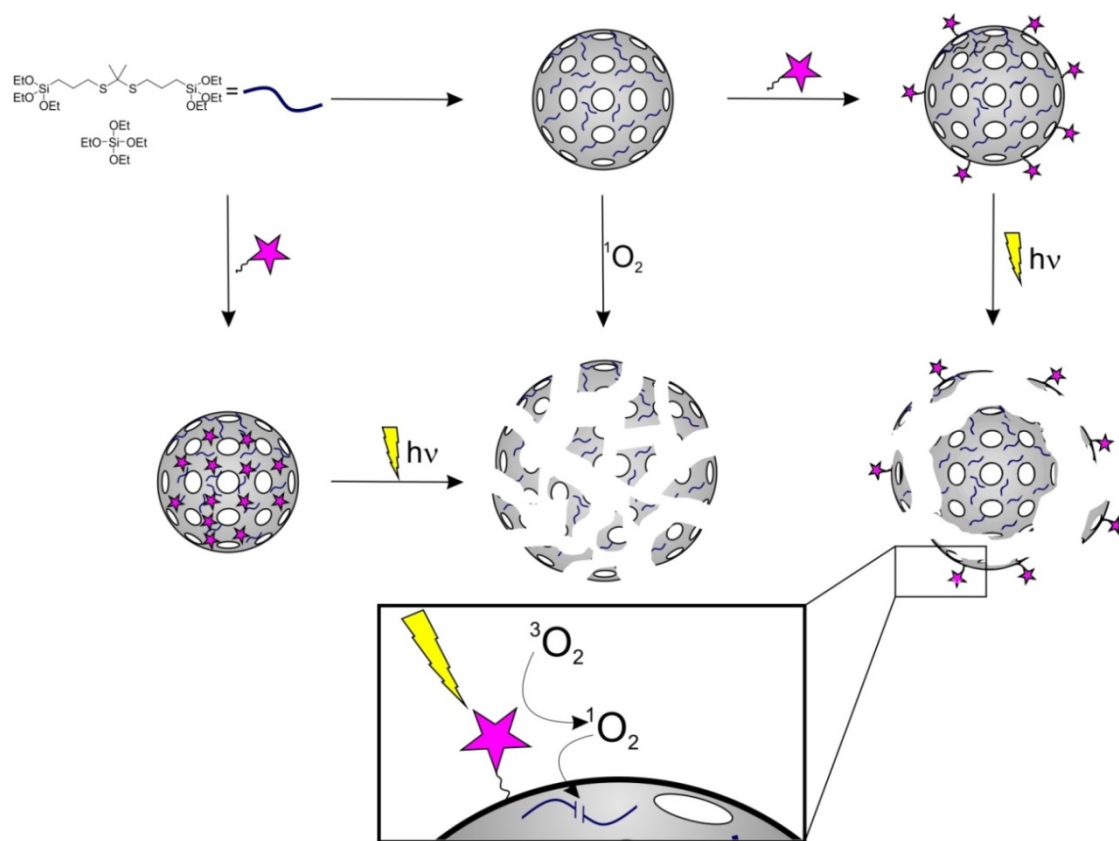


Figure 12: Schematic representation of a ROSNPs synthesis and its breaking process.

The ROSNPs presented a spherical morphology as shown on the SEM (**Figure 13.a**) and TEM (**Figure 13.b**) micrographs and a size of 105 ± 12 nm determined by the counting of 200 nanoparticles. Those data were further confirmed by Dynamic Light Scattering (DLS), presenting a value of 131 ± 28 nm.

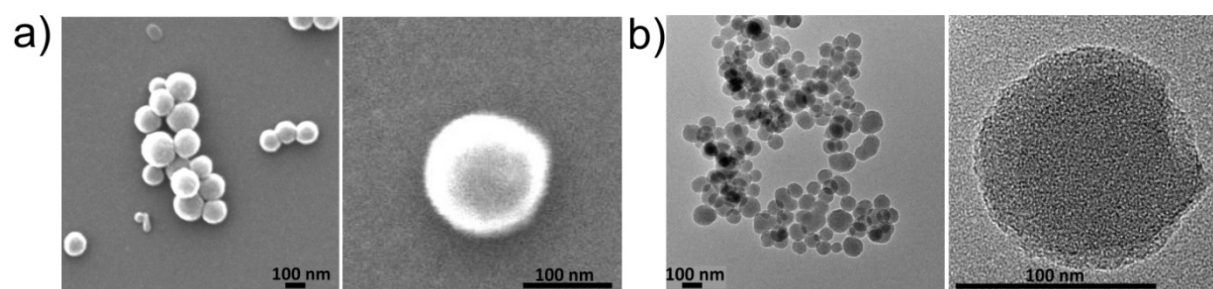


Figure 13: a) SEM and b) TEM images of ROSNPs. On the left side, images of several nanoparticles on the right side, zoomed image of a single nanoparticle. Scale bar = 100 nm.

Breakability of the nanomaterial was further assessed by incubating the ROSNPs particles ($0.1 \text{ mg}\cdot\text{mL}^{-1}$) in an aqueous solution of potassium superoxide (KO_2 , 10 mM). After 3 h of incubation, STEM micrographs presented already an advanced breakability of the particles while after 48 h, only small pieces were detected (**Figure 14.a.**). Negative control experiments, without potassium superoxide, did not show any degradability of the material after 2 d, demonstrating the stability of the system in aqueous medium (**Figure 14.b.**).

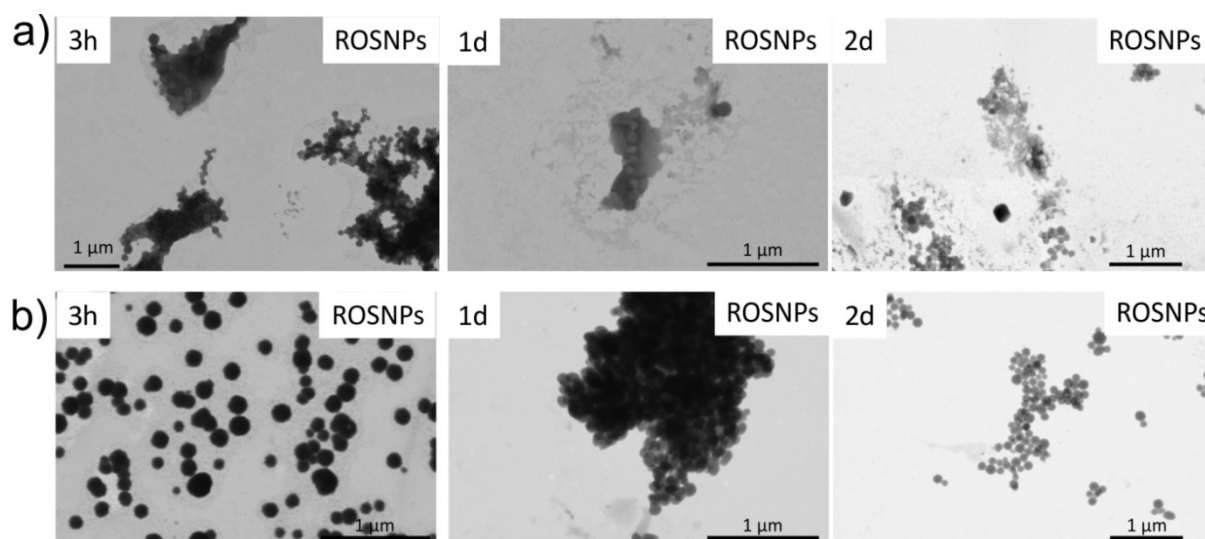


Figure 14: Breakability test on a dispersion of particles ($0.1 \text{ mg}\cdot\text{mL}^{-1}$). a) ROSNPs incubated for 3 h, 1 d and 2 d in a solution of KO_2 (10 mM). b) ROSNPs incubated for 3 h, 1 d and 2 d in milliQ water (control). Scale bar = $1 \mu\text{m}$.

Rose Bengal, a fluorescein analog containing Cl and I possesses a $^1\text{O}_2$ quantum yield of 0.75 and is under clinical trial for the treatment of melanoma and breast cancer under the name of PV-10.^[62] As a good $^1\text{O}_2$ producer, Rose Bengal was therefore used to test the breakability of the particles. **Figure 15** presents the STEM micrographs taken after exposure of ROSNPs incubated with different concentrations of Rose Bengal under light irradiation for 4 h. As predicted, the different concentrations had an impact on the degradability behavior of the material. Incubation at 10^{-2} M presented a really advanced breakability of the particles after only 4 h of incubation. When the concentration is decreased to 10^{-3} M , efficient degradation still occurs. At 10^{-4} M , very light breaking has been observed compared to 10^{-5} M which did not show any destruction of the material.

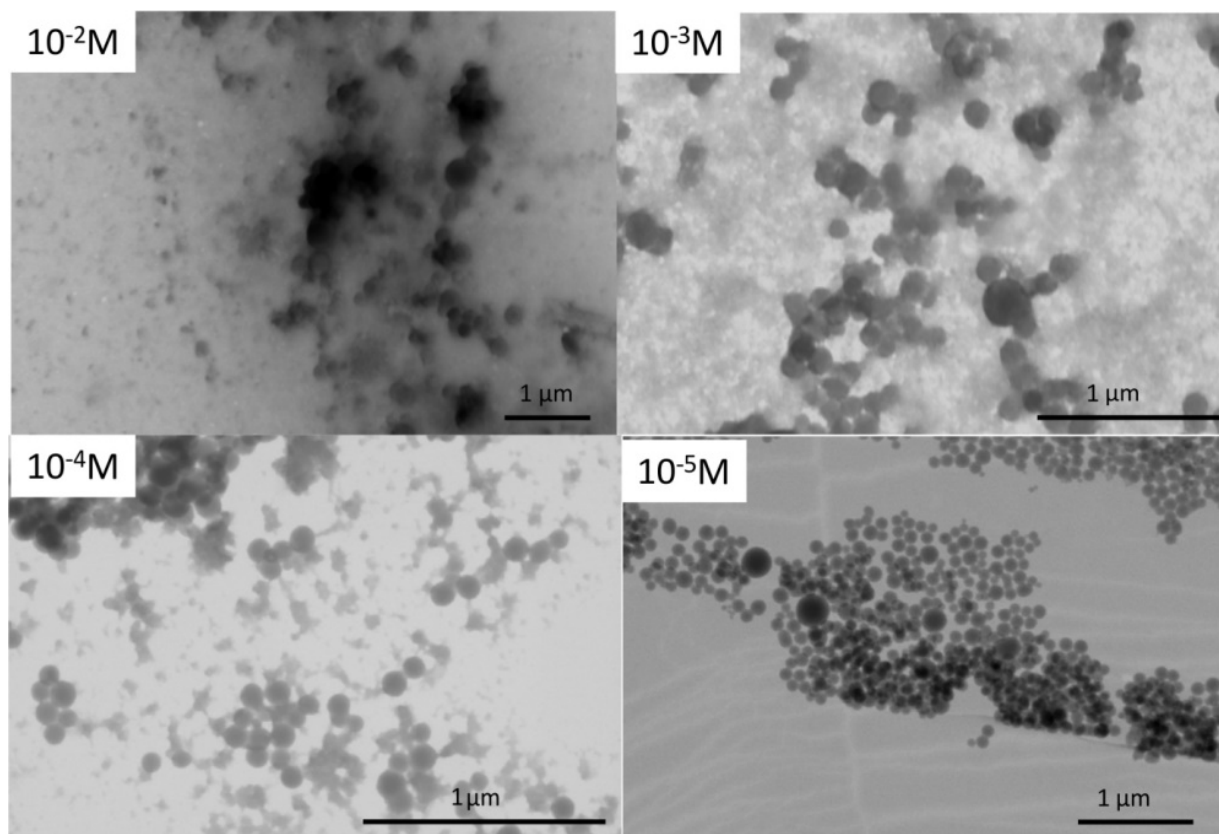


Figure 15: STEM analysis of a suspension of ROSNPs at $0.1 \text{ mg}\cdot\text{mL}^{-1}$, in presence of different concentrations of Rose Bengal in water (from 10^{-2} M to 10^{-5} M). All the samples were irradiated for 4 h with an Hg lamp. Scale bar = $1 \mu\text{m}$.

Covalent grafting of the photosensitizer was further performed to create a localized singlet oxygen production close to the breakable material, ensuring a faster breakability of the material towards light exposure. In this regard, a carboxylic terminated aliphatic chain was attached to Rose Bengal and coupled to the APTES-functionalized ROSNPs by peptidic coupling (ROSNPs-RB). TEM images after 4 h light irradiation of a solution of the ROSNPs-RB presented degradation only on the particle surface and the pore channels (**Figure 16.a**). Thus could be explained by the removal of the photosensitizer after breaking, bringing them far away from the ROSNPs. The modified Rose Bengal was thus incorporated within the framework of the ROSNPs by mixing the organic molecule in presence of APTES during the synthesis of the ROSNPs. As it can be observed by the STEM images (**Figure 16.b**), a complete degradation of the nanoparticles occurs for the same time of incubation due to the presence of the photosensitizer within the material.

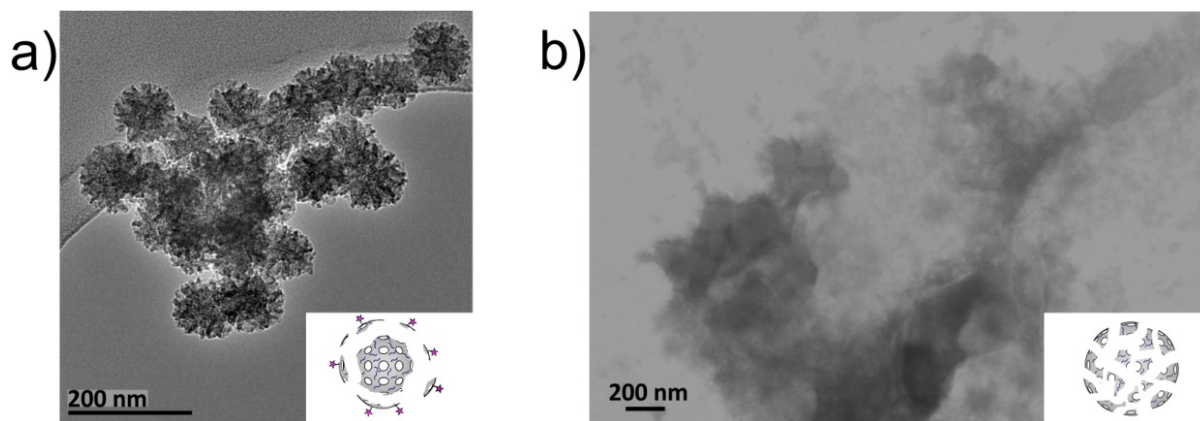


Figure 16: Breakability test performed on ROSNPs modified with Rose Bengal in a PBS solution at $0.1 \text{ mg}\cdot\text{mL}^{-1}$ upon 4 h irradiation with a Hg lamp. a) TEM micrograph of post grafted Rose Bengal on the surface of the material. b) STEM micrographs of Rose Bengal grafted during the synthesis of the ROSNPs. Scale bar = 200 nm.

Preliminary *in vitro* experiments were then performed in different cell lines (Hdfa, HeLa, Glioma and Huh-7) to attest the efficient internalization of the ROSNPs. ROS production is cell line dependent and can vary between tumor lines. Metabolic activity experiments demonstrated no cytotoxicity of the material after 48 h of incubation in the different cell lines up to a concentration of $100 \text{ }\mu\text{g}\cdot\text{mL}^{-1}$ (**Figure 17**). The particles were further functionalized with fluorescein, allowing their tracking by confocal microscopy and presented efficient internalization of the ROSNPs after a few hours of incubation.

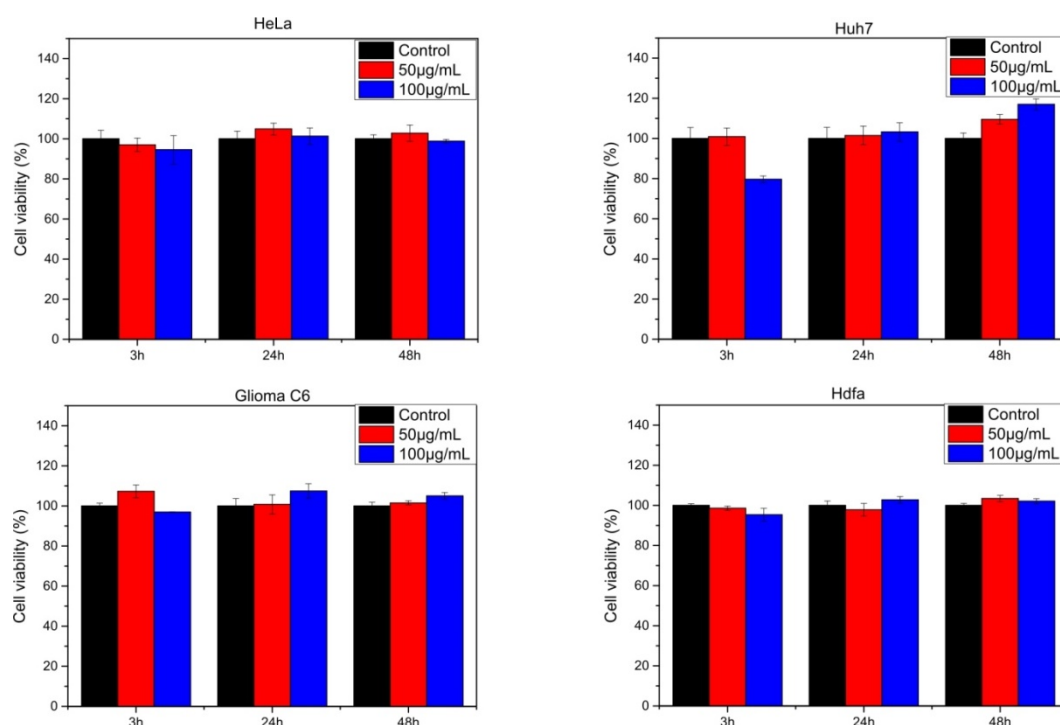


Figure 17: Metabolic activity performed with an Alamar Blue assay on four different cell lines (HeLa, Huh-7, Glioma C6 and Hdfa) after 3, 24 and 48 h with different concentrations of ROSNPs (50 and $100 \text{ }\mu\text{g}\cdot\text{mL}^{-1}$).

The design of efficient breakable mesoporous silica nanocarriers has been demonstrated to achieve specific goals for biomedical applications and demonstrated also potential for the crop industry. **Chapter 2** presents large pore disulfide doped silica nanoparticles for the efficient delivery and release of a PLK1 siRNA within Huh-7 hepatocellular carcinoma cells. The material presented interesting results both *in vitro* and *in vivo*, decreasing tumor growth in cell-based xenograft models. **Chapter 3** demonstrated the potential application of these particles for the crop industry with the loading of a peptide, which should act as an efficient pesticide. **Chapter 4** focused on the synthesis of 50 nm breakable silica nanoparticles and their delivery within U87 glioblastoma cells. The material presented an improved and faster release of Doxorubicin compared to its liposomal form Caelyx™ within the first hours of incubation. **Chapter 5** studies a novel breakable mesoporous silica nanoparticle able to respond in presence of Reactive Oxygen Species. The nanocontainer presented fast degradability kinetics that can be further improved with the grafting of a photosensitizer within the framework of the material. Preliminary *in vitro* results demonstrated a good biocompatibility and efficient internalization in several cell lines.

References

- [1] J. Li, C. Papadopoulos, J. Xu, *Nature* **1999**, *402*, 253–254.
- [2] W. J. Stark, P. R. Stoessel, W. Wohlleben, A. Hafner, *Chemical Society Reviews* **2015**, *44*, 5793–5805.
- [3] O. Salata, *Journal of Nanobiotechnology* **2004**, *2*, 3.
- [4] C. A. Mirkin, *Small* **2005**, *1*, 14–16.
- [5] Z. Li, J. C. Barnes, A. Bosoy, J. Fraser Stoddart, J. I. Zink, *Chemical Society Reviews* **2012**, *41*, 2590–2605.
- [6] D. A. Richards, A. Maruani, V. Chudasama, *Chemical Science* **2017**, *8*, 63–77.
- [7] S. Nie, *Nanomedicine* **2010**, *5*, 523–528.
- [8] J. D. Lewis, G. Destito, A. Zijlstra, M. J. Gonzalez, J. P. Quigley, M. Manchester, H. Stuhlmann, *Nature Medicine* **2006**, *12*, 354–360.
- [9] T. M. Allen, P. R. Cullis, *Advanced Drug Delivery Reviews* **2013**, *65*, 36–48.
- [10] A. Kumari, S. K. Yadav, S. C. Yadav, *Colloids and Surfaces B: Biointerfaces* **2010**, *75*, 1–18.
- [11] L. Liu, K. Xu, H. Wang, P. K. J. Tan, W. Fan, S. S. Venkatraman, L. Li, Y.-Y. Yang, *Nature Nanotechnology* **2009**, *4*, 457–463.
- [12] S. Goel, F. Chen, W. Cai, *Small* **2014**, *10*, 631–645.
- [13] L. Dykman, N. Khlebtsov, *Chemical Society Reviews* **2012**, *41*, 2256–2282.
- [14] K. Chaloupka, Y. Malam, A. M. Seifalian, *Trends in Biotechnology* **2010**, *28*, 580–588.
- [15] C. Argyo, V. Weiss, C. Bräuchle, T. Bein, *Chemistry of Materials* **2013**, *26*, 435–451.
- [16] J.-H. Park, L. Gu, G. von Maltzahn, E. Ruoslahti, S. N. Bhatia, M. J. Sailor, *Nature Materials* **2009**, *8*, 331–336.
- [17] A. Bianco, K. Kostarelos, M. Prato, *Current Opinion in Chemical Biology* **2005**, *9*, 674–679.

- [18] E. Blanco, H. Shen, M. Ferrari, *Nature Biotechnology* **2015**, *33*, 941–951.
- [19] Y. Min, J. M. Caster, M. J. Eblan, A. Z. Wang, *Chemical Review* **2015**, *115*, 11147–11190.
- [20] A. B. D. Nandiyanto, S.-G. Kim, F. Iskandar, K. Okuyama, *Microporous and Mesoporous Materials* **2009**, *120*, 447–453.
- [21] W. Stöber, A. Fink, E. Bohn, *Journal of Colloid and Interface Science* **1968**, *26*, 62–69.
- [22] A. Monnier, F. Schüth, Q. Huo, D. Kumar, D. Margolese, R. S. Maxwell, G. D. Stucky, M. Krishnamurty, P. Petroff, A. Firouzi, *et al.*, *Science* **1993**, *261*, 1299–1303.
- [23] M. Mizutani, Y. Yamada, T. Nakamura, K. Yano, *Chemistry of Materials* **2008**, *20*, 4777–4782.
- [24] L. Prezzi, L. Mascia, *Advances in Polymer Technology* **2005**, *24*, 91–102.
- [25] M. Vallet-Regi, A. Rámila, R. P. del Real, J. Pérez-Pariente, *Chemistry of Materials* **2001**, *13*, 308–311.
- [26] K. Möller, K. Müller, H. Engelke, C. Bräuchle, E. Wagner, T. Bein, *Nanoscale* **2016**, *8*, 4007–4019.
- [27] A. M. Chen, M. Zhang, D. Wei, D. Stueber, O. Taratula, T. Minko, H. He, *Small* **2009**, *5*, 2673–2677.
- [28] H. Meng, W. X. Mai, H. Zhang, M. Xue, T. Xia, S. Lin, X. Wang, Y. Zhao, Z. Ji, J. I. Zink, *et al.*, *ACS Nano* **2013**, *7*, 994–1005.
- [29] J. Kim, H. S. Kim, N. Lee, T. Kim, H. Kim, T. Yu, I. C. Song, W. K. Moon, T. Hyeon, *Angewandte Chemie* **2008**, *120*, 8566–8569.
- [30] X.-D. Zhang, D. Wu, X. Shen, P.-X. Liu, F.-Y. Fan, S.-J. Fan, *Biomaterials* **2012**, *33*, 4628–4638.
- [31] H. S. Choi, W. Liu, P. Misra, E. Tanaka, J. P. Zimmer, B. I. Ipe, M. G. Bawendi, J. V. Frangioni, *Nature Biotechnology* **2007**, *25*, 1165–1170.
- [32] Y. Lu, H. Fan, A. Stump, T. L. Ward, T. Rieker, C. J. Brinker, *Nature* **1999**, *398*, 223–226.
- [33] K. C.-F. Leung, T. D. Nguyen, J. F. Stoddart, J. I. Zink, *Chemistry of Materials* **2006**, *18*, 5919–5928.
- [34] J. Zhang, M. Niemelä, J. Westermarck, J. M. Rosenholm, *Dalton Transactions* **2014**, *43*, 4115–4126.
- [35] S. Mura, J. Nicolas, P. Couvreur, *Nature Materials* **2013**, *12*, 991–1003.
- [36] S. Inagaki, S. Guan, Y. Fukushima, T. Ohsuna, O. Terasaki, *Journal of the American Chemical Society* **1999**, *121*, 9611–9614.
- [37] T. Asefa, M. J. MacLachlan, N. Coombs, G. A. Ozin, *Nature* **1999**, *402*, 867–871.
- [38] B. J. Melde, B. T. Holland, C. F. Blanford, A. Stein, *Chemistry of Materials* **1999**, *11*, 3302–3308.
- [39] S. Quignard, S. Masse, G. Laurent, T. Coradin, *Chemical Communications* **2013**, *49*, 3410–3412.
- [40] J. Croissant, X. Cattoën, M. W. C. Man, A. Gallud, L. Raehm, P. Trens, M. Maynadier, J.-O. Durand, *Advanced Materials* **2014**, *26*, 6174–6180.
- [41] J.G. Croissant, Y. Fatieiev, K. Julfakyan, J. Lu, A-H. Emwas, D.H. Anjum, H. Omar, F. Tamanoi, J.I. Zink, N.M. Khashab, *Chemistry – A European Journal* **2016**, *22*, 14806–14811.
- [42] J.G. Croissant, Y. Fatieiev, N.M. Khashab, *Advanced Materials* **2017**, *29*, 1604634.
- [43] L. Maggini, I. Cabrera, A. Ruiz-Carretero, E. A. Prasetyanto, E. Robinet, L. D. Cola, *Nanoscale* **2016**, *8*, 7240–7247.
- [44] L. Maggini, L. Travaglini, I. Cabrera, P. Castro-Hartmann, L. De Cola, *Chemistry – A European Journal* **2016**, *22*, 3697–3703.

- [45] E. A. Prasetyanto, A. Bertucci, D. Septiadi, R. Corradini, P. Castro-Hartmann, L. De Cola, *Angewandte Chemie International Edition* **2016**, *55*, 3323–3327.
- [46] F. Q. Schafer, G. R. Buettner, *Free Radical Biology and Medicine* **2001**, *30*, 1191–1212.
- [47] K. Strebhardt, A. Ullrich, *Nature Reviews Cancer* **2006**, *6*, 321–330.
- [48] U. Holtrich, G. Wolf, A. Bräuninger, T. Karn, B. Böhme, H. Rübsamen-Waigmann, K. Strebhardt, *Proceedings of the National Academy of Sciences of the United States of America* **1994**, *91*, 1736–1740.
- [49] W. Sun, Q. Su, X. Cao, B. Shang, A. Chen, H. Yin, B. Liu, “High Expression of Polo-Like Kinase 1 Is Associated with Early Development of Hepatocellular Carcinoma,” DOI 10.1155/2014/312130 can be found under <https://www.hindawi.com/journals/ijg/2014/312130/>, **2014**.
- [50] X.-Z. Yang, S. Dou, T.-M. Sun, C.-Q. Mao, H.-X. Wang, J. Wang, *Journal of Controlled Release* **2011**, *156*, 203–211.
- [51] J. Popp, K. Pető, J. Nagy, *Agronomy for Sustainable Development* **2013**, *33*, 243–255.
- [52] E. Grishin, *European Journal of Biochemistry* **1999**, *264*, 276–280.
- [53] C. Saraiva, C. Praça, R. Ferreira, T. Santos, L. Ferreira, L. Bernardino, *Journal of Controlled Release* **2016**, *235*, 34–47.
- [54] K. Möller, J. Kobler, T. Bein, *Advanced Functional Materials* **2007**, *17*, 605–612.
- [55] D. S. Wilson, G. Dalmaso, L. Wang, S. V. Sitaraman, D. Merlin, N. Murthy, *Nature Materials* **2010**, *9*, 923–928.
- [56] J. S. Kim, S. D. Jo, G. L. Seah, I. Kim, Y. S. Nam, *Journal of Industrial and Engineering Chemistry* **2015**, *21*, 1137–1142.
- [57] G. Saravanakumar, J. Kim, W. J. Kim, *Advanced Science* **2017**, *4*, 1600124.
- [58] T. P. Szatrowski, C. F. Nathan, *Cancer Research* **1991**, *51*, 794–798.
- [59] D. E. J. G. J. Dolmans, D. Fukumura, R. K. Jain, *Nature Reviews Cancer* **2003**, *3*, 380–387.
- [60] P. Agostinis, K. Berg, K. A. Cengel, T. H. Foster, A. W. Girotti, S. O. Gollnick, S. M. Hahn, M. R. Hamblin, A. Juzeniene, D. Kessel, *et al.*, *CA: A Cancer Journal for Clinicians* **2011**, *61*, 250–281.
- [61] R. R. Allison, C. H. Sibata, *Photodiagnosis and Photodynamic Therapy* **2010**, *7*, 61–75.
- [62] E. Gandin, Y. Lion, A. V. de Vorst, *Photochemistry and Photobiology* **1983**, *37*, 271–278.

Chapter 1

General Introduction

Abstract

This chapter introduces a general background and the state of art required for the understanding of the work presented in this thesis. The first part is a general definition of nanoparticles and their applications in the biomedical field. The different aspects and requirements for the development of efficient and safe nanovectors are presented. As an important part of the thesis focuses on drug and gene delivery, a short description of those molecules and their interactions within the cells is given in the second part. The third part deals with the utilization of silica nanoparticles, their versatility, their wide applications range and specifically their uses in the medical field. Moreover, their limitations for the translation as performant nanomedical tools are presented. The development of stimuli-responsive materials for the delivery of active molecules is described in a fourth part.

1.1 Nanoparticles for biomedical applications

Nanoparticles have been used for centuries by several civilizations such as the Mayans or the Romans.^[1,2] One of the most famous examples is the Lycurgus cup, dating from the 4th century AD, which contains silver and gold nanoparticles that provide interesting properties upon light exposure.^[3] However, it was only in the late 50's that the term of “nanoscience” was presented by the Nobel Laureate Richard Feynman.^[4] Since then, the interest on functional nanomaterials keeps rising in various fields for their interesting electronical,^[5] optical,^[6] magnetic,^[7] or biological properties and are claimed to be the next industrial revolution.^[8,9]

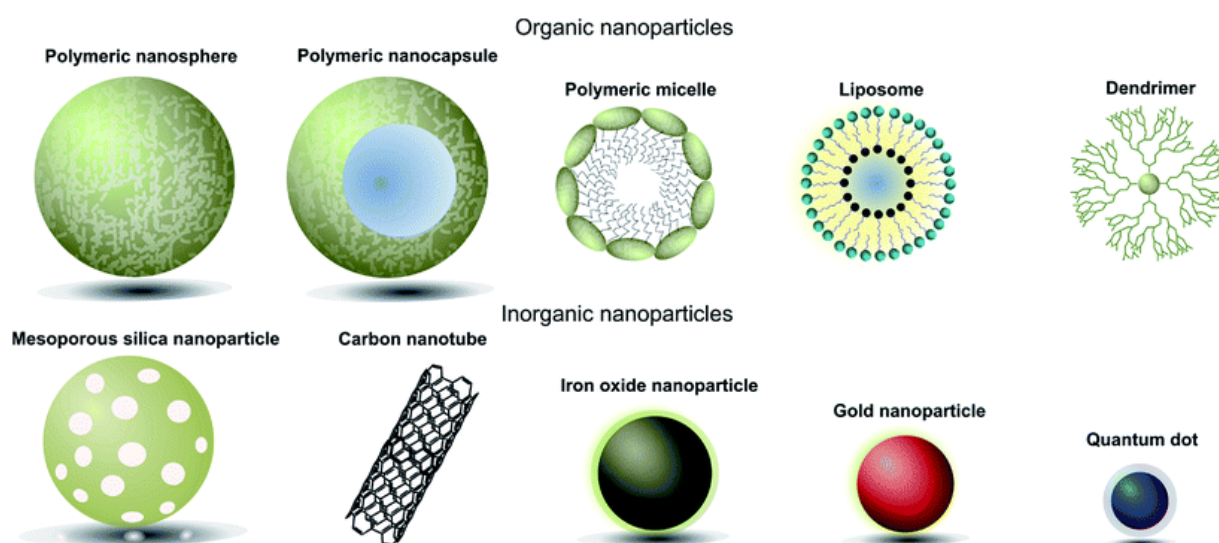


Figure 1.1: Schematic representation of several types of nanoparticles for biomedical applications divided in two categories (organic and inorganic). However, it is worth to mention that a third category based on hybrid (both organic and inorganic) systems exist. Reproduced from A. Richards, D., Maruani, A. & Chudasama, V. Antibody fragments as nanoparticle targeting ligands: a step in the right direction. *Chemical Science* 8, 63–77 (2017). Copyright 2017, Royal Society of Chemistry.

Nanoparticles have been defined as materials displaying a specific size ranging from 1 to 100 nm.^[10] However, the term of nanoparticles is often misused and presents materials of several hundreds of nanometers.^[11] Thanks to their versatility, nanomaterials, which can be divided in three main categories (organic, inorganic or hybrid), offer a broad range of applications in various domains such as cosmetics, environment, electronics *etc.*^[12,13] Especially, their interesting features render nanoparticles very attractive for the biomedical field, constantly exploring new technologies for the development of safe and efficient tools^[14]

and already found applications in drug or gene delivery, imaging,^[15] biosensing,^[16] and diagnosis.^[17]

Several materials already did a breakthrough in the nanomedicine world,^[18,19] namely viral,^[20] liposomes,^[21] polymeric,^[22] peptidic,^[23] metallic (gold, silver and quantum dots),^[24–26] silica,^[27] silicon,^[28] and carbon-based nanoparticles.^[29] A schematic representation of different nanoparticles used for biomedical applications are depicted in **Figure 1.1**. Development of materials for *in vivo* delivery requires years between the optimization of systems and the understanding of their interactions with the biological environment. The tailoring and tuning of nanomaterials play crucial roles for the development of efficient systems as their high surface area to mass ratio increases their loading capacities and optimizes their surface functionalization, reducing the biological response.^[30] The process starts with the synthesis and characterization of nanostructures since nanomaterials that present different physicochemical properties (size, shape or surface charge), exhibit completely different *in vitro* and *in vivo* behaviors and therefore could be then employed for diverse applications.^[31] Blanco *et al.* described the importance of such factors in the biodistribution and crossing ability of the different biological barriers (**Figure 1.2**).^[32]

Intravenous injections of nanomaterials require a proper targeting towards an organ of interest. Among the different parameters that have to be taken into account, the size is

probably the first criterion that provides passive targeting properties. *In vivo* intravenous injections of gold nanoparticles ranging from 15 to 200 nm displayed a different biodistribution after 24 h. Even though most of the particles were located within the liver, the spleen and the kidneys, small nanoparticles of 15 and 50 nm were also located in the lungs and in the brain, proving their ability to cross the blood-brain barrier.^[33]

The still controversial discovery of the enhanced permeability and retention (EPR) effect by Maeda in 1986^[34] confirmed the potential of nanomaterials for the specific delivery of therapeutics within several pathologies ranging from infection^[35] to heart failure.^[36] Such discovery is also of a great importance for the passive targeting of anti-cancer drugs towards solid tumors since the excessive requirement of nutrients generates a fast angiogenesis around the tumor area, therefore creating large gaps between the endothelial cells and leading to a defective architecture of the blood vessels.^[37] **Figure 1.3** depicts the passage of small nanomaterials through the leaky blood vessels surrounding the tumor area representing the EPR effect.^[38]

All those features regarding the size of nanomaterials help to design cargoes able to reach the tumor site environment. Different size-dependent internalization mechanisms have been discovered for the entrance of the particles within the cell. In many cases for large particles (> 5 nm) a general mechanism, called generally endocytosis, involve multiple steps and start with the engulfment of the cargo by the cell membrane, forming small vesicles known as endosomes. Then, the material is transferred within specific vesicles determined by the size of the exogenous particle, before enabling the delivery towards different compartments of the cell. All those mechanism are represented in **Figure 1.4**.^[39]

By playing with the shape of nanomaterials *i.e.* rod-shape, spherical, cubic, *etc.* researchers noticed that such modifications could significantly influence both *in vitro* and *in vivo* behaviors. *In vitro* studies performed in HeLa cells demonstrated that rod-shaped nanoparticles, especially when their long axis is perpendicular to the cell membrane, internalized faster compared to spheres and cubes.^[40] Even though they presented a faster uptake, they also promote phagocytosis and therefore, a response from the immune system, entrapping the nanoparticles in the reticulo-endothelial system.^[41] *In vivo* fate is also affected by the shape of nanoparticles. While asymmetrical nanoparticles would tumble in the blood flow favoring interactions with vessels, spherical carriers would tend to remain in the center of the flow influencing then their residence time in the body.^[42]

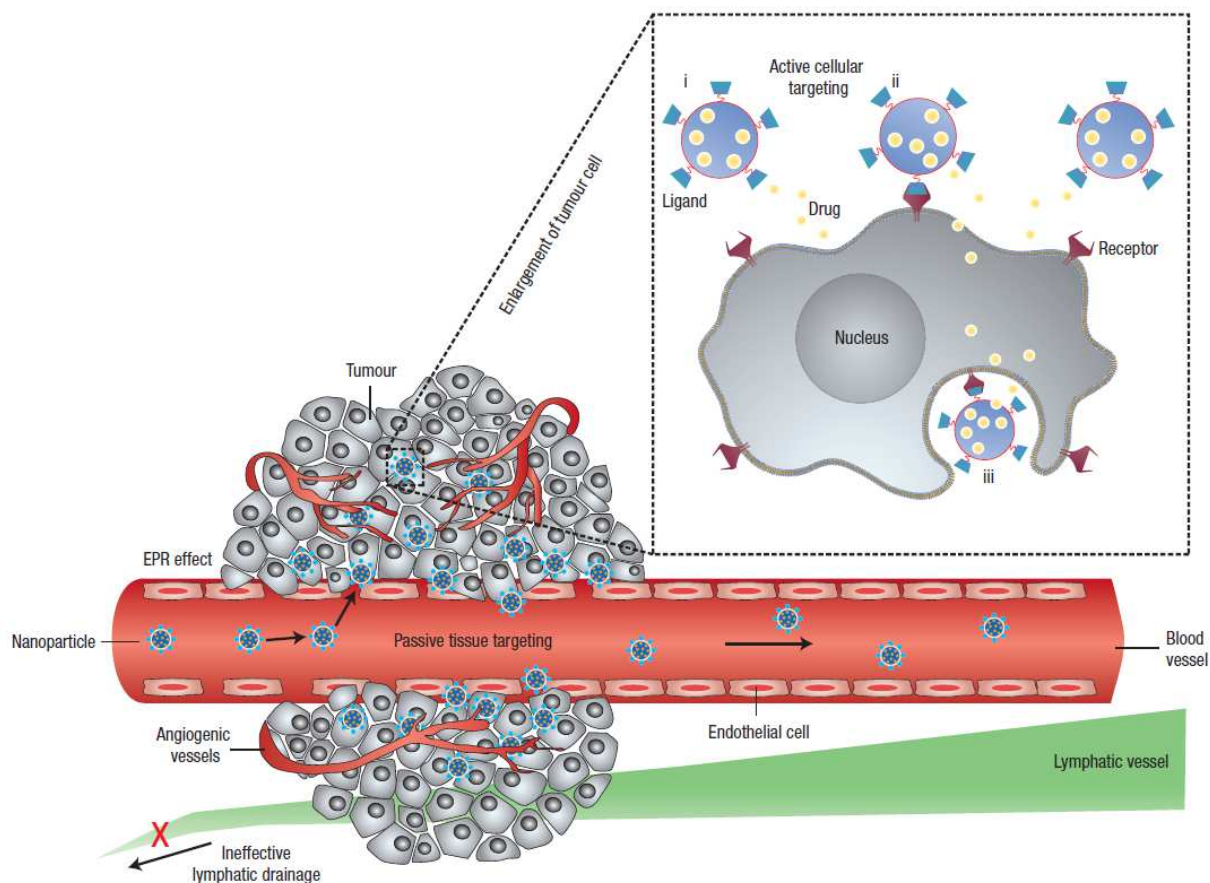


Figure 1.3: Accumulation of nanoparticles to tumor cells through the EPR effect and active targeting by surface functionalized materials with specific ligands (*i.e.* folic acid, antibodies...). Reprinted with permission from Peer D., Karp J.M., Hong S., Farokhzad O.C., Margalit R. and Langer R., Nanocarriers as an emerging platform for cancer therapy, *Nature Nanotechnology*, 2, 751-760 (2007). Copyright 2007, Nature Publishing group.

As a last important parameter, surface charge of nanomaterials interferes strongly in the internalization process. As most of the cell membranes display a negative charge, positively charged particles would hence present a more efficient internalization compared to neutral or negatively charged materials of the same kind.^[43] Positively charged nanocarriers are also often employed for the delivery of negatively charged biomolecules, as DNA or siRNA, forming electrostatic interactions protecting oligonucleotides from endonucleases and allowing their passage through the cell membrane.^[44,45] Unfortunately, highly positively charged materials as polycations exhibit certain cytotoxicity and activate the innate immune system while polyanions can cause anticoagulant activity and enhance cytokine release.^[46,47] Moreover, in a living organism, or in presence of biological media, an external protein shell is formed that affect circulation time, cellular uptake and trigger an immune response.^[48,49] This

shell, called protein corona, modifies the size and shape of nanoparticles while the composition and the surface charge will strongly affect its formation. For positively charged nanoparticles, the layer will mostly be composed of albumin and proteins having an isoelectric point <5.5. On the other side, anionic nanocarriers will tend to attract on their surfaces, proteins having an isoelectric point >5.5, such as immunoglobulin G.^[50]

Specific cellular uptake by tumor cells can also be achieved by functionalizing the nanocarriers with specific targeting ligands.^[51] Antibodies,^[52] short penetrating peptides,^[53] transferrin,^[54,55] or folic acid^[56,57] have shown improvement on the selectivity of nanomaterials towards cancer cells. Their receptors are often aimed to bind substrates linked to the fast proliferation of tumor cells and are often overexpressed on their membrane.^[58] For instance, the folate receptor internalizes nanoparticles after ligand binding and is known to be overexpressed on several cancer types (breast, ovary, kidney, brain, *etc.*). Antibodies have also demonstrated their specificity towards cancer cells thanks to their 3D structure and multiple interactions with specific antigens located on the cell surface. As their large size could influence the properties of the nanoparticles, researchers focused on nanobodies that constitute the smallest functional fragment of antibodies and present an intrinsic stability, as

well as an ease to manufacture.^[59] For small nanoparticles designed for brain delivery, conjugation with carbohydrate or transferrin moieties helps their crossing through the blood brain barrier (BBB).^[60,61] PEGylation of nanoparticles offers multiple benefits *in vivo* by preventing the aggregation and formation of protein corona, granting stealth and reducing therefore cytotoxicity of materials.^[62] Surface PEGylation can also act as a spacer between a nanoparticles and a targeting ligand, offering more flexibility and a better binding affinity towards a specific receptor.^[63]

The ability of nanomaterials to deliver high payloads of chemotherapeutics directly to cancer cells constitutes a huge improvement compare to previous systems that presented a lack of selectivity and/or stability. Nowadays, several nano-formulated drugs made a breakthrough and are already commercially available for the “therapy” of various cancers. On the other side, researchers have also found an interest in nanomaterials for the “diagnosis” of cancer. Thanks to their versatility and the possibility to possess a surface with a great number of molecules, they easily found applications in many imaging based techniques such as positron emission tomography (PET),^[64] computed tomography (CT),^[65] magnetic resonance imaging (MRI)^[66] and optical imaging.^[67] Even more interesting, nanomaterials have also been used during surgery, helping the surgeon to localize easily and with precision, the presence of small tumors.^[68] As depicted in **Figure 1.5**, combining different multimodal imaging is also possible by the grafting of two different dyes on the same nanoparticle (optical and radioisotope for example) or an optical dye grafted on a magnetic nanoparticle.^[69,70] These two different applications of nanomaterials achieving both an accumulation at the cancer sites, led to the development of systems able to combine both dyes for the “diagnostic” and drugs for the “therapy”, evolving the use of materials to a new area of medicine, so called “theranostics”.^[71–73]

All those materials led to an improvement in medicine thanks to their high payload delivery, tracking possibilities, selective targeting towards cancer tissues and long circulation life time. Each type of nanoparticles possesses advantages and limitations and the perfect balance to obtain an ideal nanomaterial is still unknown to the best of my knowledge. It is also worth to mention, that the administration routes of nanocarriers can be diverse (intravenous, orally, cutaneous, or mucosal) and can avoid invasive and painful surgeries. However, those nanomaterials have shown great potential to deliver different types of

therapeutics such as drugs, genes and proteins and several approaches as well as their progression towards the market will be discussed in the following part.

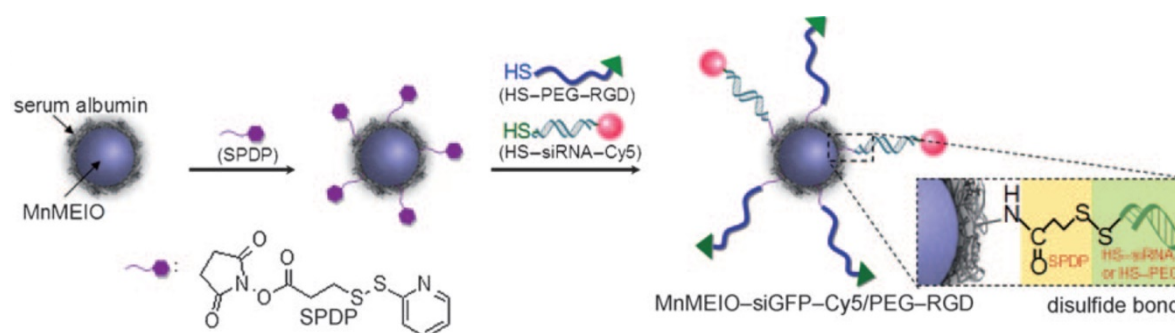


Figure 1.5: Multimodal platform for optical and MRI imaging, and targeted delivery of siRNA. Reprinted with the permission from Lee J.-H., Lee K., Moon S.H., Lee Y., Park T.G., Cheon J., All-in-One Target-Cell-Specific Magnetic Nanoparticles for Simultaneous Molecular Imaging and siRNA Delivery, *Angewandte Chemie International Edition*, 48, 4174-4179 (2009). Copyright© 2009 WILEY-VCH Verlag GmbH & Co. KGaA, Weinheim.

1.2 Drug, gene, and protein delivery

Paul Ehrlich, considered by many as the father of chemotherapy, proposed the development of chemicals to treat specific diseases and the use of animal models to test them at the beginning of the 20th century.^[74] Unfortunately, at his time, the huge library of chemicals to test and the lack of models limited the development of efficient agents. It is only a few decades later, with the arrival of efficient screening systems that chemicals started to make a breakthrough as potential cancer therapeutics.

Among the numerous available anti-cancer agents available on the market, Doxorubicin, paclitaxel, temozolomide and platinum-based complexes are probably the most known and the most studied.^[75-78] All of them present different mechanisms of action and are used for several types of cancer.^[79-81] Despite their great potential for cancer therapy, as small molecules, they do not target specifically cancer cells and are therefore also efficient towards healthy cells leading to various side effects as cardiotoxicity, hepatotoxicity, *etc.*^[82,83]

To overcome these side effects and to offer specific targeting of the drug, nano-conjugated systems were developed in the late 70's by the encapsulation of Doxorubicin within a 100 nm PEGylated liposomes structure. Doxil[®] (or Caelyx[®] on the European market) became in 1995 the first FDA approved nanodrug, constituting a huge step forward for the nanoworld.^[84] Doxorubicin loading into liposomes brought considerable advantages

compared to the bare drug. The major improvement of Doxil[®], remains in its ability to benefit from the EPR effect and therefore achieving an accumulation of the drug at the tumor site, and hence a prolonged drug circulation time.^[85]

Recently, as a result of the big improvement brought by drug delivery systems, new therapies have found their way for the treatment of several diseases. Those biotechnologies, combining materials and genes, permit the protection by endonucleases and efficient transfection of foreign sequences of oligonucleotides within cells. Plasmid DNA (pDNA) transfection have been widely studied for DNA repair over the last 15 years.^[86]

Managing cell behavior by regulating gene expression offers the possibility to interfere with the translation to a target protein and therefore modify the cellular activity. Fire and Mellow demonstrated in 1998, the possibility to affect protein expression by the transfection of exogenous RNA.^[87] Those short sequences of oligonucleotides, acting at the post-transcriptional stage, can be divided in three main categories; microRNAs (miRNA), short hairpin RNAs (shRNA) or small interfering RNA (siRNA). Long of 20-25 pairs of nucleotides, the siRNA enters within a complex of protein named RNA Induced Silencing Complex (RISC) and successive steps promotes the removal of the passenger strand, the recognition and the pairing to the messenger RNA (mRNA) before slicing, thus causing the depletion of a targeted protein (**Figure 1.6**).^[88]

Compare to miRNA and shRNA, siRNA possesses several advantages as it has to be transfected only in the cytoplasm and do not require an uptake within the nucleus. Moreover, even though miRNA are able to silence an entire class of proteins, siRNAs are highly specific and generally silence a single target. Unfortunately, synthetic siRNAs are seen as exogenous materials and therefore require several doses before showing their full capacities. Thanks to their astonishing properties, siRNA have shown huge potential for various diseases such as hypercholesterolaemia,^[89] hepatitis B^{[90],[91]} and C^[92] viruses, neurodegenerative disease^[93] and human papillomavirus.^[94]

Nevertheless, it is worth to mention that the efficiency of exogenous oligonucleotides faces many issues due to their physico-chemical properties.^[95] Their overall negative charge does not allow them to cross the cell membrane and their chemical instability ease their degradation by endogenous enzymes present in the bloodstream.^[95-98] Most of these issues can be solved by nanocarriers, allowing efficient protection and cell penetration of the bare molecule.^[99-103] Among all the siRNA delivery systems under clinical trial, liposome-based

materials are the most represented and generated concrete improvements compared to pristine siRNA.^[104]

In August 2018, the US Food and Drug Administration (FDA) and the European Commission have approved for the first time, a siRNA-liposome complex for the treatment of advanced polyneuropathy of hereditary transthyretin-mediated amyloidosis.^[105] 20 years after the discovery of RNA interference, FDA approval of a gene silencing drug launches the era of RNAi drugs and open doors for new siRNA-based systems to finally accomplish better quality treatments and reaching a vast and exploitable market.

Among the different host that can be loaded within nanoparticles, proteins and peptides also found interest for the understanding of metabolic pathways, vaccination, and cancer therapy.^[106–108] Those macromolecules can therefore be transported through the cell membrane without being denaturated, hence permitting them to perform multiple tasks.^[109,110] However, due to their different isoelectric point (pI), specific tailoring of the nanomaterial is required depending on the protein of interest. Tu *et al.* studied the loading of proteins with various pI on large pore mesoporous silica nanoparticles. Completely different loading can be achieved depending if whether or not the material is functionalized with amino groups. Moreover, it has also been shown that efficient release of the cargo was highly dependent on the ionic strength of the buffer.^[111]

The engineering of efficient cargo promoting the uptake of specific guest molecules within the cells are crucial for the development of new delivery based systems. Among the potential candidates, silica nanoparticles have shown a rising interest for the delivery of drugs and oligonucleotides. The following part will present the synthesis of mesoporous silica nanoparticles as well as their different advantages and drawbacks for the biomedical field.

1.3 Mesoporous Silica Nanoparticles

Even though the metallic and organic nanoparticles have shown interesting properties, they cannot really act as efficient carriers due to the difficulties to load and release drugs from their surfaces. An interesting strategy to achieve high loading and to protect fragile molecules from the interactions with the environment is represented by porous particles. Among them, silica based nanomaterials have been widely studied since they offer high porosity as well as tunable shape. In this regard, cubic,^[112] rod-like^[113] silica nanoparticles have been reported but the spherical one remains the most common one.^[114–116] The synthesis of monodispersed silica spheres was first reported in 1968. The so-called Stöber process, is a base-catalyzed sol-gel reaction which involves, in presence of a mixture of H₂O:EtOH, the hydrolysis of organosilanes precursors (tetraethyl- or tetramethyl orthosilicate, *etc.*) before condensation of the monomers forming the silica spheres (**Figure 1.7**).^[117]

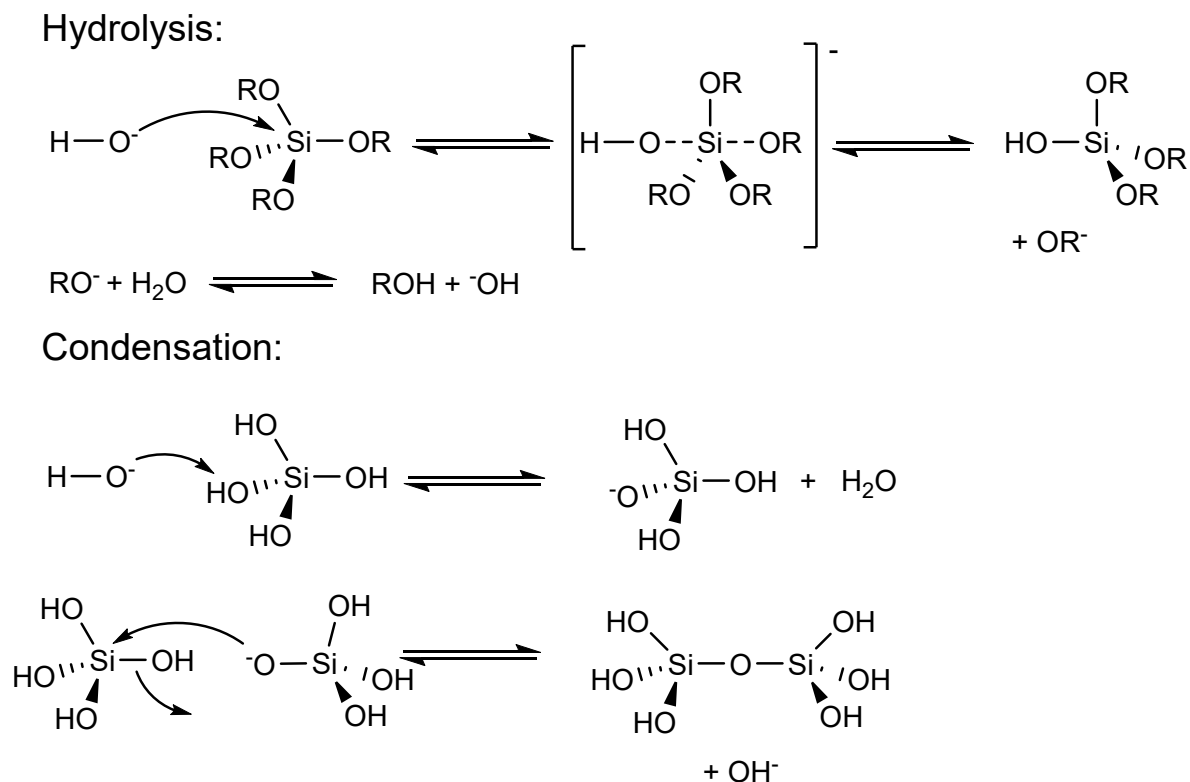


Figure 1.7: Formation of a silica network in basic conditions. The reaction starts with the hydrolysis of the alkoxy-silanes into silanols which further allows the condensation between two precursors.

Size modification of the silica nanoparticles usually relies on the hydrolysis and condensation rates. Factors as pH, co-solvents or the use of additive influence the reaction kinetics and therefore the growth of the nanomaterial.^[118–120]

Recently, the first silica-based material has been approved for clinical trials. The so-called Cornell dots (C dots), developed by the Wiesner group, are small silica based core-shell nanoparticles for multimodal imaging. Aimed to help surgeon to visualize malignant tumors through endoscopic tools, the nanoparticles can be used for PET and optical imaging. The system is based on a core shell nanocarrier encapsulating the fluorescent Cy5 dye for optical imaging. The surface is further decorated with a PEG chain for improved stability in the blood vessels and a ¹²⁴I modified cRGD-peptide for both PET imaging and targeting. The particles, around 6 nm, can then be filtered by the kidneys and be excreted out of the body.^[121–124] A schematic representation is presented in **Figure 1.8**.

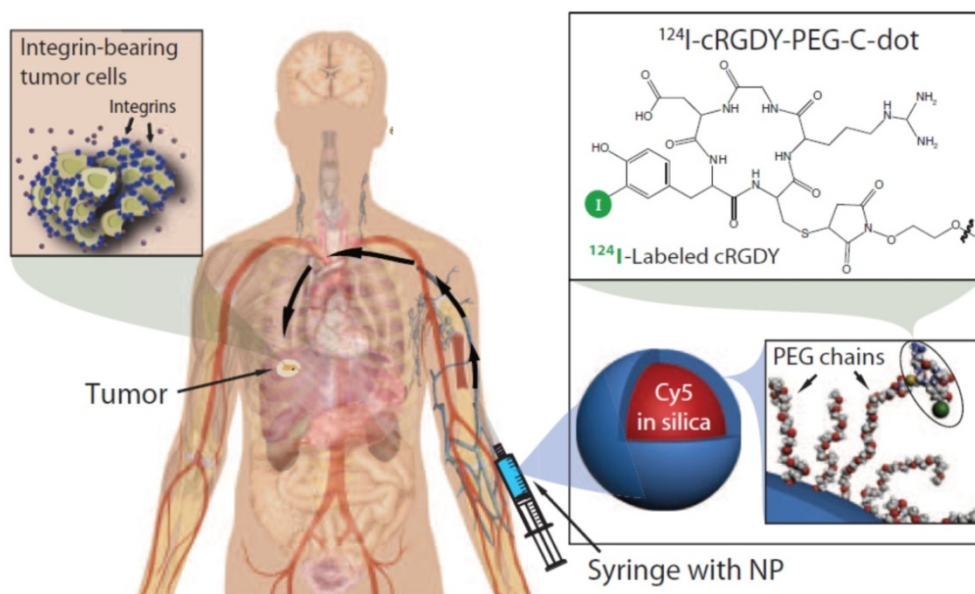


Figure 1.8: Schematic representation of the C dots combining multimodal imaging and targeting units. Reprinted with the permission from Phillips E., Penate-Medina O., Zanzonico P.B., Carvajal R.D., Mohan P., Ye Y, Humm J., Gönen M., Kalaigian H., Schöder H., Strauss H.W., Larson S.M., Wiesner U., Bradbury M.S., Clinical translation of an ultras-small inorganic optical-PET imaging nanoparticle probe, *Science Translational Medicine* 6, 260ra149-260ra149 (2014). Copyright 2014, Science.

The first synthesis of mesoporous silica with pore sizes between 2-10 nm and ordered pore arrays was reported by the Mobil Oil Company in 1992.^[125–127] MCM-41 (Mobile Crystalline Material) are probably the most known family of mesoporous silica materials and their potential as replacement of zeolites has rapidly been noticed and led to their applications in various fields including catalysis, ion exchange, separation, molecular sieving and adsorption.^[128–132] Both pore arrangement and size can be modified by changing surfactant or the amount of silica source and surfactants that further influence the micelle structure and the packing capacity of the mesophase.^[133,134] The general scheme to synthesize porous silica is shown in **Figure 1.9**. Studies have shown that two different mechanisms are involved in the formation of porous silica structures: the first one occurs when there is a high concentration of the surfactant under specific conditions (temperature, pH), which leads to the formation of a lyotropic liquid-crystalline phase without the insertion of the silane precursors. The second mechanism takes place at lower concentrations of the surfactant. In this case, a cooperative self-assembly between the template and the added inorganic species is formed, creating a liquid-crystal phase with specific laminar arrangement.^[118]

Generally, the synthesis of porous silica nanomaterials occurs in basic conditions. However, acid-catalyzed silica nanoparticles have also been developed with the use of triblock copolymer templates. Nevertheless, a supramolecular attractive interaction between the template and the inorganic precursors are fundamental and have been classified by Huo *et al.*^[135,136] A representation of the different interactions is depicted in **Figure 1.10**, where S corresponds to the surfactant and I the inorganic species. Under basic conditions, in which silica species are present as anions, the use of cationic quaternary ammonium surfactants would lead to interaction S^+I^- (**Figure 1.10.a**). On the other side, with a $\text{pH} < 2$, silica precursors are positively charged and a mediator anion (X: usually a halide) is required to favor interactions between the silane and the surfactant ($S^+X^-I^+$; **Figure 1.10.b**). Cationic mediators are also necessary with negative surfactant in basic media to ensure efficient interaction ($S^-M^+I^-$; **Figure 1.10.c**). Thus, in acidic media, the use of a mediator is not required leading to a S^+I^- interaction (**Figure 1.10.d**). Non-ionic surfactants can also be employed and attractive interactions are then mediated through hydrogen bonds with uncharged silica precursors (S^0I^0 ; **Figure 1.10.e**) or in presence of counter ions ($S^0(XI)^0$; **Figure 1.10.f**).

MCM-41 exploits cetyltrimethylammonium bromide (CTAB) as a surfactant and usually presents a characteristic pore size of 2.5 nm and a hexagonal arrangement. However, using surfactants with various hydrophobic chain lengths may give different pore sizes. The last parameter can also be tuned by the pH, which >12 lead to the fast condensation and lamellar arrangement while moderate pH (10-12) allow the formation of hexagonal structures.^[118] Post-synthetic treatments offer other alternatives to obtain wide pores by the insertion of swelling agents. This alternative, more convenient, will not induce a change in the size of the pre-synthesized material. Molecules, such as trimethylbenzene (TMB) or 1,3,5-

triisopropylbenzene are good candidates for efficient pore expansion post-treatment.^[137] The different type of mesoporous silica nanoparticles are presented in **Figure 1.11**.

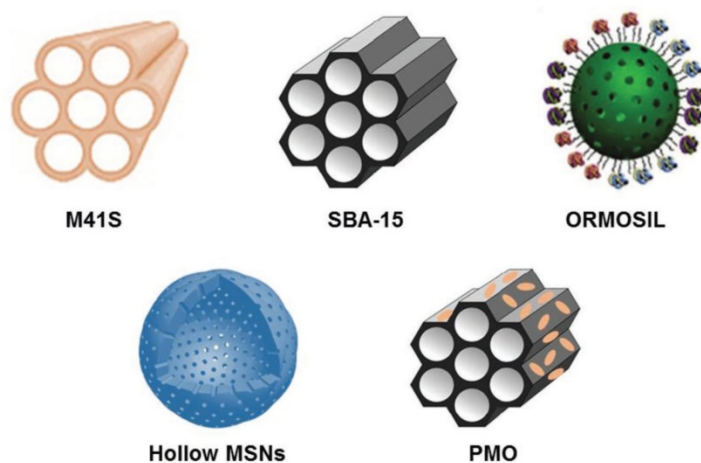


Figure 1.11: Schematic representation of various types of mesoporous silica nanoparticles. Reprinted with permission from Rahikkala A., Pereira S.A.P., Figueiredo P., Passos M.L.C., Araujo A.R.T.S., Saraiva M.L.F.S., Santos H.A., Mesoporous Silica Nanoparticles for Targeted and Stimuli-Responsive Delivery of Chemotherapeutics: A Review, *Adv. Biosys.*, 2, 1800020 (2018). Copyright 2018 WILEY-VCH Verlag GmbH & Co. KGaA, Weinheim.

Material functionalization with organo-substituted moieties can be achieved by different ways (**Figure 1.12**).

The first strategy relies on the “grafting” of organic moieties on the surface after the silica material synthesis. The free silanol groups on the surface allows the reaction with trialkoxy-organosilanes ($(R'O)_3SiR$), chlorosilanes ($ClSiR_3$) or even silazanes ($HN(SiR_3)_3$). Replacing the R residue allows various modifications of the silica surfaces without altering the mesostructure. In this regard, silica materials have been already functionalized with amino groups, diamino, triamino, ethylenediamine, thiol, carboxy, imidazole, saccharides, dithiocarbamate, *etc.*^[138–146] Moreover, the post grafting method also permits selective functionalization of the inner or the outer surface of the mesoporous material. As an example, outer modification can be easily achieved by anchoring organosilanes before the removal of the pore template. After the surfactant extraction, the inner surface can be further modified with the desired functionality.^[147,148]

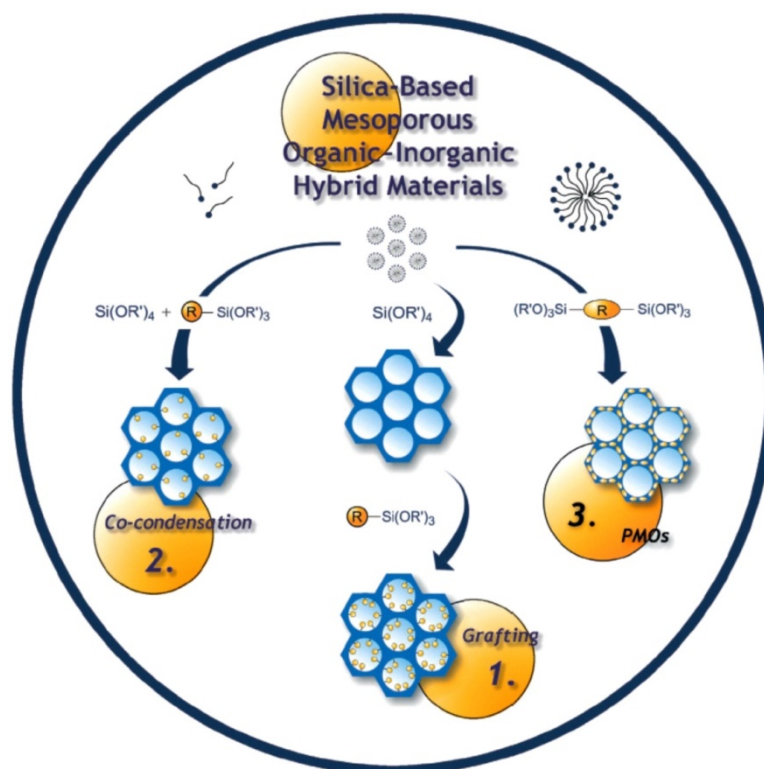


Figure 1.12: Schematic representation of the synthesis of organo-hybrid mesoporous silica nanoparticles. 1. Post synthetic grafting of organic moieties on the surface and within the pore channels. 2. Co-condensation of organo-silanes during the synthesis. 3. Synthesis of Periodic Mesoporous Organo-silica by the insertion of silsequioxanes units within the silica framework. Reprinted with permission from Hoffman F., Cornelius M., Morell J. and Fröba M., *Silica-based mesoporous organic-inorganic hybrid materials*, *Angewandte Chemie International Edition*, 45, 3216-3251 (2006). Copyright 2006, Wiley-VCH Verlag GmbH & Co. KGaA, Weinheim.

A second strategy can be exploited by mixing in “one pot” the tetraalkoxysilanes ((RO)₄Si) and trialkoxyorganosilanes ((RO)₃SiR’) in presence of a surfactant. Such method, called “co-condensations” leads to a homogenous distribution of the organic moieties and prevent pore blocking. In this regard, several organic moieties have been grafted within the pore wall of the mesoporous materials, namely alkyl, thiol, amino, alkoxy, aromatic groups, *etc.*^[142,149–159] More complex molecules, such as dye, azobenzene or cyclodextrin units, can also be anchored in the pore channel.^[160–162] Wirnsberger *et al.* covalently attached fluorescein isothiocyanate (FITC) within the pore channel by pre-reacting the dye with 3-(aminopropyl)triethoxysilane before condensation.^[162] Unfortunately, the direct anchoring of organic moieties within the pore wall leads to a loss of the ordered pore array. Moreover, stability of the organic moiety after surfactant extraction should be taken in consideration.

As a last strategy, the direct synthesis of organic-inorganic hybrid materials involving condensation of bridged organosilica moieties $((R'O)_3Si-R-Si(OR')_3)$ in presence of a surfactant. Examples of organosilica precursors are depicted in **Figure 1.13**. The result composites so-called periodic mesoporous organosilica (PMOs) have been developed for the first time in 1999 simultaneously by several groups. Inagaki *et al.* synthesized 1,2-bis(trimethoxysilyl)ethane-based particles in presence of octadecyltrimethylammonium bromide as a pore template. Stability of the resulted material was demonstrated and decomposition was recorded only above 400°C.^[163] Ozin *et al* developed unsaturated PMOs by inserting 1,2-bis(triethoxysilyl)ethane as an organic precursor.^[164] On the other side, Stein and co-workers reported ethane-bridged PMOs presenting an incredibly high surface area of 1200 m²·g⁻¹.^[165] Later in that year, Yoshina-Ishii *et al* introduced hetero-aromatic groups, overcoming the over-flexibility of traditional PMOs and bringing an improved order of the mesopores.^[166] In the recent years, PMOs demonstrated interesting features for biomedical applications with improved biodegradability compare to standard mesoporous silica nanoparticles. Moreover, the nature of the organic moiety permits a fine tuning of the hydrophobicity for improved loading capacities.^[167]

All those features, together with the biocompatibility of the silica prepared by sol-gel synthesis, triggered the interest of mesoporous silica nanoparticles in the field of nanomedicine. Taking advantage of the porosity of the material, and therefore their capacity to load relevant quantity of specific payloads, the group of M. Vallet-Regi published for the first time in 2001 the use of MCM-41 as drug delivery systems. Particles exhibiting pore sizes of 1.8 and 2.5 nm were tested for the delivery of Ibuprofen, resulting to a loading capacity of 30 wt% for both materials.^[168]

Since then, the number of publications regarding mesoporous silica nanoparticles as drug delivery systems has exploded, exploring all their tuning possibilities especially for cancer treatments, where the lack of effective systems can still be perceived.

The hosting of guest molecules within the pores of mesoporous silica nanoparticles has then been studied ranging from small molecules to macromolecules like proteins.^[169-171] Loading of therapeutics within the pores channels by diffusion techniques can protect them from enzymatic degradation, prolong their circulation lifetime and avoid any unwanted interactions with the surrounding environment. Moreover, compare to injections of free therapeutics, porous nanocontainers offers a control release of the guest molecules, improving

then pharmacokinetics.^[172] For instance, the loading of the chemotherapeutic camptothecin within mesoporous silica nanoparticles demonstrated important tumor growth inhibition in xenograft mice compared to the free drug. The material, benefiting from the EPR effect, where further functionalized with folic acid, improving targeting effect and showed a slight improvement *in vivo* compared to the non-targeted carriers.^[173] Doxorubicin-loaded mesoporous silica nanoparticles improved the bioaccumulation and the EPR within the tumor of xenograft mice after intravenous injections and proved a better shrinkage of the tumor (up to 85 % of inhibition) compare to the bare molecule.^[174] Liu *et al.* developed liposome-coated mesoporous silica nanoparticles for the loading and delivery of Irinotecan within Kras-Derived Orthotopic PDAC models. The system demonstrated a lower drug leakage implying a higher drug concentration at the tumor site compared to standard liposomes. Such improvement reduced drastically the side effect of Irinotecan.^[175]

Delivery of proteins was also demonstrated with the use of mesoporous systems presenting larger pores. In 2007, Slowing *et al.* published the delivery of the impermeable Cytochrome C *in vitro* by using silica nanoparticles presenting 5.4 nm wide pores as a carrier. Interestingly, the nanocontainer did not influence the activity of the enzyme after release (**Figure 1.14**).^[171] Phosphonate-raspberry large pore mesoporous silica nanoparticles were synthesized and presented high affinity for the absorption of bovine serum albumin and reaching a loading of 266 mg.g⁻¹.^[176]

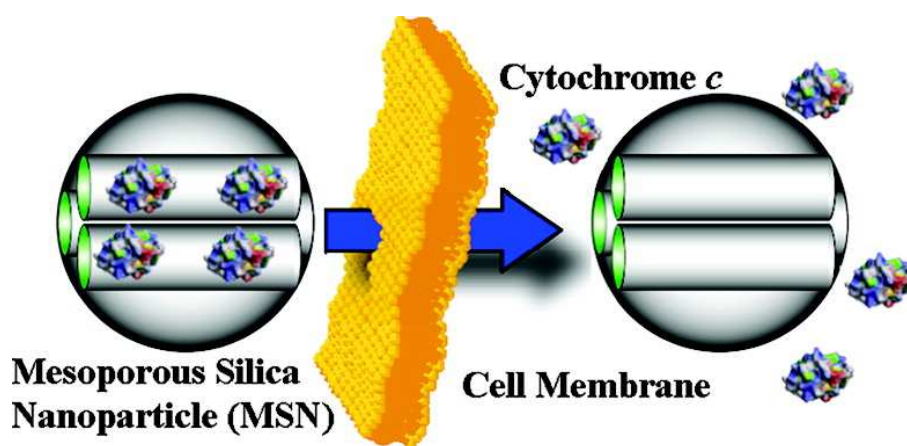


Figure 1.14: First proof of concept of protein delivery through the help of mesoporous silica nanoparticles. Reprinted with the permission from Slowing I.I., Trewyn B.G. and Lin V.S.-Y., *J. Am. Chem. Soc.*, 129 8845–8849 (2007). Copyright 2007 American Chemical Society.

The loading can be further improved in the case of highly charged molecules thanks to surface functionalization of the material. The grafting of amino-functionalized silanes endows the material with positive charges, more suitable for the loading of oligonucleotides or proteins with low isoelectric points compared to simple diffusion within the pores.^[111,177,178] Kros *et al.* developed elongated cuboidal mesoporous silica nanoparticles with disk shaped cavities for the loading of seven model proteins characterized by different isoelectric points. The material presented high loading capacities as well as tunable release profiles.^[111]

Mesoporous silica nanoparticles have also demonstrated great promises for the safe delivery of oligonucleotides, protecting the guest molecules from external endonucleases. As an example 20 nm wide pore amino-functionalized mesoporous silica nanoparticles were able to bind electrostatically DNA protecting the cargo until its release.^[116] The first report about siRNA delivery with mesoporous silica nanoparticles was published in 2010 by Zink and co-workers. The particles were modified with phosphonate groups allowing electrostatic binding

with polyethylenimine (PEI) before loading the siRNA. The system demonstrated improved stability of the oligonucleotides as well as efficient release *in vitro* due to the proton sponge effect brought by the polymer coating.^[179] Na *et al.* functionalized ultralarge mesoporous silica nanoparticles with amino-groups for siRNA loading. The nucleotide resisted to RNase degradation and was able to induce GFP knockdown in xenograft tumors.^[170] Möller *et al.*, designed core-shell silica nanocarriers with various pore sizes and morphologies, surface properties and pH of adsorption. Perfect tuning reached loading capacities of 380 $\mu\text{g}\cdot\text{mg}^{-1}$ of siRNA, which remains so far the highest loading reported in the literature. The particles were further capped with a block copolymer and endosomal release reagent through oleic acid function hence inducing membrane permeability. *In vitro* studies further demonstrated a high luciferase silencing (80-90 %) with very low concentrations of the material.^[180]

New systems also rely on specific dual delivery, combining drug and gene delivery. Those materials are often based on a drug molecule able to induce apoptosis in cancer cells with siRNA silencing overexpression of drug efflux transporters proteins responsible of multi-drug resistance. For example, Chen *et al.* published the first report about co-delivery of Doxorubicin and Bcl-2 siRNA with mesoporous silica nanoparticles in multidrug-resistant cancer cells. The siRNA silences the translation of the Bcl-2 protein, overcoming the drug resistance induced by the anti-apoptotic protein. The Doxorubicin is then free to intercalate the DNA promoting cell apoptosis and decrease by 64-fold the IC₅₀ (Concentration where 50% of the cells die) compared to the pristine Doxorubicin (**Figure 1.15**).^[181]

Several other examples are reported in the literature. As an example, the group of Jeffrey Zink filled their phosphonate-modified mesoporous silica nanoparticles with Doxorubicin and further coated the material with PEI and siRNA. Release of siRNA was triggered at pH 5 and demonstrated an improved killing effect *in vitro* of 2.5 fold compared to the bare drug.^[45] *In vivo* experiments with several multi-resistant siRNAs showed strong synergic effect in MCF-7/MDR xenograft models.^[182] Meng *et al.* published later on the use of lipid-coated mesoporous silica nanoparticles for the dual delivery of Gemcitabine and Paclitaxel. *In vivo* experiments in pancreatic ductal adenocarcinoma xenograft models demonstrated a tumor shrinkage 12 fold better compared to the commercially available Abraxane (Albumin-bound paclitaxel) after intravenous injections.^[183]

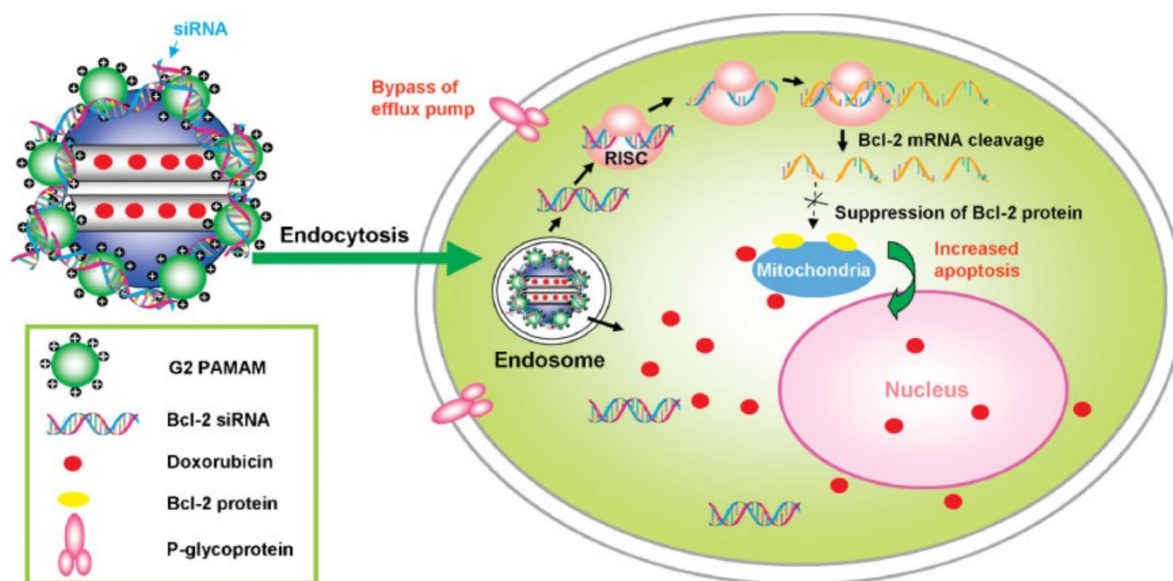


Figure 1.15: Co-delivery system based on MSNs to deliver Dox and Bcl-2-targeted siRNA simultaneously to A2780/AD human ovarian cancer cells. Reprinted with the permission from Chen A.M., Zhang M., Dongguang W., Stueber D., Taratula O., Minko T. and He H., Co-delivery of Doxorubicin and Bcl-2 siRNA by Mesoporous Silica Nanoparticles enhances the efficacy of chemotherapy in multi-drug-resistant cancer cells, *Small*, 23, 2673-2677 (2009). Copyright 2009, WILEY-VCH Verlag GmbH & Co. KGaA, Weinheim.

Surface functionalization of the material is also beneficial for the grafting of specific targeting ligands and/or dyes as already mentioned earlier. Tuning the functionalization parameters gives the opportunity to create multimodal platforms able to both track the nanoparticles for the diagnosis with different type of techniques at the same time and moreover, able to deliver an anticancer drug.^[184] **Figure 1.16** represents the multiple possibilities for the efficient tailoring of silica nanoparticles, from the nanoparticle structure to the surface functionalization.

1.4 Hybrid stimuli-responsive mesoporous silica nanoparticles for specific drug delivery and bioapplications

By designing multiple efficient nanocarriers, researchers have shown the high potential of silica nanoparticles for the medical field. Added to their easy surface functionalization, stealth and targeted materials have been achieved, controlling therefore their pharmacokinetics and their biodistribution. However, some materials have shown some limits due to a leakage of the cargo before reaching the desired target. The development of thermosensitive liposomes in the late 70's introduced the concept of stimuli-responsive

systems by the local release of drugs through hypothermia.^[185] The synthesis of systems able to recognize precisely a specific environment and interact with it specifically allows an on-demand delivery of molecules at a specific location. Those on/off switches permit then a spatiotemporal and controlled drug release.^[186]

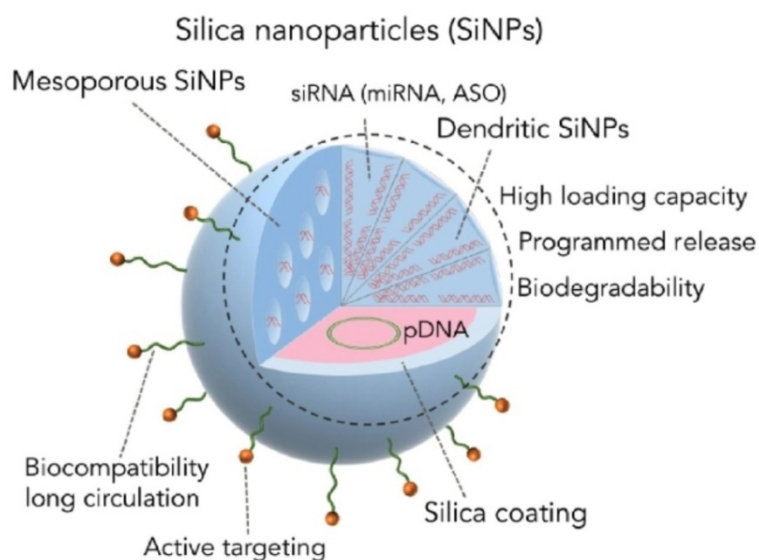


Figure 1.16: Schematic representation of the versatility of mesoporous silica nanoparticles, their loading capacities, advantages, and ease of functionalization. Reprinted with the permission from Kamegawa R., Naito M. Miyata K., Functionalization of silica nanoparticles for nucleic acid delivery, *Nano research*, 1-12 (2017). Copyright 2017, Springer Nature.

Stimuli-responsive systems can be divided in 2 main classes depending if the stimulus can be applied exogenously (temperature changes, magnetic fields, ultrasounds, light, or electric fields) or endogenously (pH, enzymes, redox potentials, or singlet oxygen production). A schematic representation of the different stimuli that can be applied is depicted in **Figure 1.17**.

Functionalization of mesoporous silica nanoparticles with stimuli-responsive moieties as gatekeepers prevents early leakage of the payload and therefore offers a better control of the delivery.^[187] Both exogenous and endogenous stimuli-responsive silica nanocarriers have been developed and presented interesting release properties. Ruiz-Hernández *et al.* combined 100 nm mesoporous silica nanoparticles and 8 nm small iron oxide nanoparticles. Both nanoparticles were functionalized with complementary short sequences of DNA, hence clogging the pores of the mesoporous silica nanoparticles. Upon a magnetic field, the

surrounding environment were heated up until reaching hyperthermia temperature, separating the DNA assembly and allowing the release of the cargo.^[188]

Light triggered drug delivery systems have also attracted a lot of interest due to their non-invasiveness.^[189–191] In response to specific wavelength irradiation, photo-responsive molecules offer a spatiotemporal control on the drug release. Due to its poor penetration depth at short wavelength, molecules presenting high wavelength absorbance or able to exploit two-photon excitation are usually preferred, providing deeper and precise tissue penetration and minimal harm to tissues.^[192] The capping of mesoporous silica nanoparticles responding to light irradiation has also been developed in 2009, by replacing the magnetic capping with gold nanoparticles. Linked to the mesoporous silica nanoparticles with an *o*-nitrobenzyl linker, the gold-silica nanocomplex does not present any escape of the loaded paclitaxel. Upon light irradiation, the spacer is cleaved, and releases the guest molecule within the cell.^[193]

Other approaches have been developed without the necessity of using specific external equipment. Those systems aim to respond only in presence of a particular stimulus that differentiates the target compare to other tissues. pH-sensitive systems have been widely exploited for oral drug delivery to protect the cargo from the harsh conditions of the digestive

system until their absorption in the intestine.^[194,195] The group of Jeffrey Zink has developed numerous gatekeepers for silica nanoparticles responding to specific stimuli. Among them, a supramolecular interaction between aromatic amines and β -cyclodextrin were used as nanovalves able to respond to acidic pH to clog MCM-41 pores for specific cellular compartment delivery.^[196]

Redox stimuli-responsive systems have also found their applications for controlled drug delivery. Especially, disulfide bonds based nanomaterials have been deeply investigated for the specific delivery of payloads within cells. This strategy takes advantage of the difference in concentration of glutathione (GSH) between the extracellular (2-10 μ M) and the intracellular (2-10 mM) environment of the cells.^[197-199] As an example, the delivery of short nucleotides has been performed with mesoporous silica nanoparticles functionalized with a linker bearing an amino group end and a disulfide spacer. Upon reaction with 10 mM GSH, the disulfide bond was cloven improving the release of the loaded oligonucleotide.^[200]

Despite the great improvements brought to mesoporous silica nanoparticles in the last two decades, a major issue still remains as a hurdle for their clinical translation as effective biomedical tool. Due to their robust structure and therefore their chemical stability, mesoporous silica nanoparticles demonstrated very different behaviors regarding their biodegradability, thus problematic for several therapies where frequent injections of therapeutics are required.^[201,202] Physicochemical properties, such as size, porosity, morphology, surface functionalization as well as the chemical environment strongly affect the dissolution of amorphous silica nanoparticles in silicic acid, allowing a clearance through the urine.^[203-210] **Figure 1.18** summarizes all the factors influencing silica dissolution.

Moreover, despite the important size of mesoporous silica nanoparticles which are usually used in the biomedical field (between 100 to 200 nm) and the renal clearance threshold of 5.5 nm, several groups have discovered the presence of intact silica nanoparticles within the mice urines. This discovery raises then about the integrity of the kidneys after injection of silica nanoparticles.^[173,211-213]

To tackle these drawbacks, the possible degradation of silica nanoparticles *in vivo* is a great challenge for researchers. In the last years, many approaches have been studied to break the nanoparticles in pieces small enough to be filtered safely by the kidneys. Following the pioneer work of Iganaki,^[163] Ozin,^[164] and Stein^[165] on the development of periodic mesoporous organosilica and by considering all the knowledge that have led to the

development of stimuli-responsive materials, some groups pushed the idea further and inserted as organic moieties, responsive linkers able to be cloven under the presence of the right stimulus. The rupture in the linkers implies hence a further fragmentation of the particles in pieces small enough to be excreted easily from the cell and by the kidneys.

As presented earlier, redox-stimuli responsive materials have shown a great interest thanks to the difference in concentration of GSH between the extracellular and the intracellular environment. Thus, a lot of devotion has been dedicated on the synthesis of disulfide doped silica nanoparticles, which the breaking is triggered by the high concentration of GSH within the cell.^[214,215] Quignard *et al.* developed non porous 50 nm organosilica nanoparticles based on tetraethyl orthosilicate (TEOS) and bis(triethoxysilylpropyl)disulfide (BTSPD). By increasing the ratio of the disulfide linker up to 40 wt%, faster degradation kinetics were observed.^[216] Unfortunately, due to the lack of porosity, no drug loading could be achieved. In this regard, our group synthesized CTAB-templated disulfide-doped silica nanoparticles, offering porosity to the material and therefore the possibility of hosting molecules within the cavities. As an example, temozolomide was loaded and the carrier was further functionalized with a RGD targeting peptide presenting a killing effect of 50 % in

Glioma C6 cells after 48 h of incubation.^[217] Further improvements have been brought by our laboratory for the delivery of proteins with the synthesis of breakable nanocapsules able to encapsulate and protect several kinds of proteins until their delivery within the cell. The efficient loading and release of cytochrome C was followed by UV-Visible while protein integrity experiments were performed *in vitro* in Glioma C6 cells with the release of green fluorescent protein (GFP) within the cytoplasm and the killing effect of APO TRAIL and onconase proteins dropping the cell viability to 40 % after 24 h of incubation. TEM of nanoparticles within the cells demonstrated a complete breakability of the system after 48 h compare to the control experiment with non-breakable nanocapsules.^[218] A schematic representation of the particles is represented in **Figure 1.19**. The synthesis of fully based breakable mesoporous silsesquioxane nanoparticles was also reported by Croissant *et al.*. Variation in the ratio between bis(triethoxysilyl)ethylene (E) and BTSPD allows the formation of nanomaterials with different shapes. The nanoparticles exhibited high surface areas and degradability occurred in both extracellular and intracellular mimicking conditions with a faster breakability with high concentration of GSH.^[219]

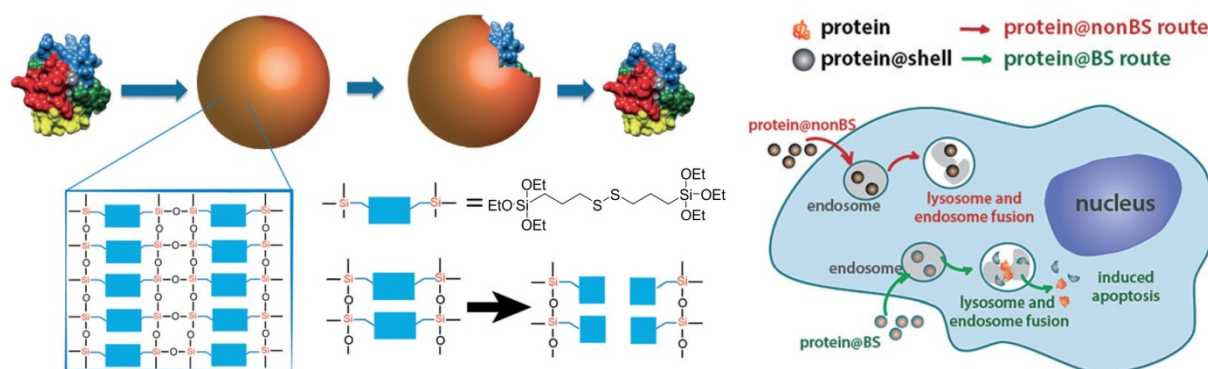


Figure 1.19: Encapsulation of proteins in breakable silica nanoparticles and the schematic representation of their release within cells. Reprinted with the permission from Prasetyanto E.A., Bertucci A., Septiadi D., Corradini R., Castro-Hartmann P., De Cola L., Breakable Hybrid Organosilica Nanocapsules for Protein Delivery, *Angew. Chem. Int. Ed.* 55, 3323 –3327 (2016). Copyright 2016 Wiley-VCH Verlag GmbH & Co. KGaA, Weinheim.

Diselenide bridges have also been studied, thanks to their lower bond energy compare to disulfide linkers ($172 \text{ kJ}\cdot\text{mol}^{-1}$ and $240 \text{ kJ}\cdot\text{mol}^{-1}$). Such strategy benefits of dual-responsive delivery thanks to their reduction in selenol or their oxidation in selenic acid.^[220]

Other approaches have been widely explored, such as enzyme cleavable systems playing with the presence of protease in the body. A tetraalkoxysilylated lysine precursor has

been synthesized by our group for the formation of enzyme-responsive silica nanodons. This strategy relies on proteases present in cells, such as trypsin, that generally cleaves protein at the C side of Lysine. Increased concentrations of trypsin resulted in a faster breakability of the nanosystem.^[221] Porous phenylene-oxamide-based system have also shown breakability in presence of trypsin as presented by Croissant *et al.*, hence resulting to extremely high loading capacities of both hydrophobic and hydrophilic drugs (from 65 to 84 wt%).^[222]

Furthermore, various other stimuli-responsive systems have been developed for controlled drug delivery and destruction of different cargoes. For instance, reactive oxygen species (ROS) have attracted a lot of attention for their specificity towards tumors which produce ROS in higher extent (up to 100 μM) compare to normal tissue (2 nM).^[223] Among the different linkers developed so far, diselenide, arylboronic esters or thioketals moieties are among the most common ones.^[224-229] Moreover, the possibility to attach photosensitizers increases their potential. By light irradiation, such systems produce large quantity of singlet oxygen, which can be hence scavenged by the ROS-responsive nanomaterial favoring its degradability.^[230,231]

pH-sensitive systems have also found interested applications to promote endosomal escape of drugs and increased release within the cytoplasm. As an example of pH-sensitive systems are polyethylenimine polymers, which upon acidic conditions, act as a proton sponge hence inducing vesicles disruption.^[232] We also very recently published imine-doped mesoporous silica nanoparticles showing fast degradation in both acidic and neutral media.^[233]

All those different features, combined with all the efforts to create the perfect silica nanomaterial, designate silica nanoparticles as a powerful tool for biomedical applications.

1.5 Objective of the thesis

The aim of this thesis is to develop and exploit stimuli-responsive nanomaterials for specific delivery of drugs or biomolecules. Organo-hybrid breakable silica nanoparticles were tailored offering multiple possibilities for cancer therapies. Those novel silica nanocarriers are able to break down in small pieces after being triggered by the correct stimulus, improving their drug release capacities and permit safe excretion of the material out of the human body.

Chapter 1 introduces the notions of nanomaterials and their applications in the biomedical field. Especially the delivery of drugs and genes thanks to tailored nanocarriers is described. Mesoporous silica nanoparticles and the insertion of stimuli-responsive moieties are then presented, aimed to prevent early drug leakage and overcome bioaccumulation in tissues.

Chapter 2 studies large pore disulfide doped breakable silica nanoparticles for the delivery of specific siRNA delivery within hepatocellular carcinoma cells. It presents the material synthesis, the complete characterization, surface modification, siRNA loading as well as *in vitro* and *in vivo* studies.

Chapter 3 investigates the potential application of the large pore disulfide doped breakable silica nanoparticles for the crop industry. The material was loaded with a short peptide to improve its uptake within larvae and promotes its cytotoxicity.

Chapter 4 presents the synthesis of 50 nm disulfide doped mesoporous silica nanoparticles and their loading with Doxorubicin. *In vitro* investigations in U87 glioblastoma cells by Confocal microscopy and Raman microspectroscopy demonstrated a faster accumulation of Doxorubicin within the nucleus compared to a liposomal form of the chemotherapeutic (Caelyx[®]).

Chapter 5 explores a novel breakable mesoporous silica nanoparticles based on a ROS-responsive linker. The synthesis of the new linker is described, as well as the particles synthesis and complete characterization of the material. Furthermore, the grafting of a photosensitizer to enhance the breakability is also investigated. Finally preliminary *in vitro* results in different cell lines are shown.

Chapter 6 resumes all principle and the theory behind the instrumental techniques used for this thesis.

This thesis is based on a strong interdisciplinary basis involving material sciences, organic chemistry, photophysics, biology and medicine. All this work was carried out with the help of colleagues, collaborators and expert in different fields, everyone bringing their knowledge and help. It has been mainly supported by the Fondation ARC through the project “Thera-HCC” (grant N° IHU201301187).

1.6 References

- [1] A. Doménech, M. T. Doménech-Carbó, M. S. del Río, M. L. V. de A. Pascual, E. Lima, *New Journal of Chemistry* **2009**, *33*, 2371–2379.
- [2] D. Schaming, H. Remita, *Foundations of Chemistry* **2015**, *17*, 187–205.
- [3] I. Freestone, N. Meeks, M. Sax, C. Higgitt, *Gold Bulletin* **2007**, *40*, 270–277.
- [4] R. P. Feynman, *Engineering and Science* **1960**, *23*, 22–36.
- [5] D. Jariwala, V. K. Sangwan, L. J. Lauhon, T. J. Marks, M. C. Hersam, *Chemical Society Reviews* **2013**, *42*, 2824–2860.
- [6] X. Huang, M. A. El-Sayed, *Journal of Advanced Research* **2010**, *1*, 13–28.
- [7] A.-H. Lu, E. L. Salabas, F. Schüth, *Angewandte Chemie International Edition* **n.d.**, *46*, 1222–1244.
- [8] O. Salata, *Journal of Nanobiotechnology* **2004**, *2*, 3.
- [9] C. A. Mirkin, *Small* **2005**, *1*, 14–16.
- [10] G. M. Whitesides, *Small* **2005**, *1*, 172–179.
- [11] W. H. De Jong, P. J. Borm, *International Journal of Nanomedicine* **2008**, *3*, 133–149.
- [12] J. Li, C. Papadopoulos, J. Xu, *Nature* **1999**, *402*, 253–254.
- [13] W. J. Stark, P. R. Stoessel, W. Wohlleben, A. Hafner, *Chemical Society Reviews* **2015**, *44*, 5793–5805.
- [14] Z. Li, J. C. Barnes, A. Bosoy, J. Fraser Stoddart, J. I. Zink, *Chemical Society Reviews* **2012**, *41*, 2590–2605.
- [15] P. Sharma, S. Brown, G. Walter, S. Santra, B. Moudgil, *Advances in Colloid and Interface Science* **2006**, *123–126*, 471–485.
- [16] S. Jiang, K. Y. Win, S. Liu, C. P. Teng, Y. Zheng, M.-Y. Han, *Nanoscale* **2013**, *5*, 3127–3148.
- [17] A. Laromaine, L. Koh, M. Murugesan, R. V. Ulijn, M. M. Stevens, *Journal of the American Chemical Society* **2007**, *129*, 4156–4157.
- [18] D. A. Richards, A. Maruani, V. Chudasama, *Chemical Science* **2017**, *8*, 63–77.
- [19] S. Nie, *Nanomedicine* **2010**, *5*, 523–528.
- [20] J. D. Lewis, G. Destito, A. Zijlstra, M. J. Gonzalez, J. P. Quigley, M. Manchester, H. Stuhlmann, *Nature Medicine* **2006**, *12*, 354–360.
- [21] T. M. Allen, P. R. Cullis, *Advanced Drug Delivery Reviews* **2013**, *65*, 36–48.
- [22] A. Kumari, S. K. Yadav, S. C. Yadav, *Colloids and Surfaces B: Biointerfaces* **2010**, *75*, 1–18.
- [23] L. Liu, K. Xu, H. Wang, P. K. J. Tan, W. Fan, S. S. Venkatraman, L. Li, Y.-Y. Yang, *Nature Nanotechnology* **2009**, *4*, 457–463.
- [24] S. Goel, F. Chen, W. Cai, *Small* **2014**, *10*, 631–645.
- [25] L. Dykman, N. Khlebtsov, *Chemical Society Reviews* **2012**, *41*, 2256–2282.
- [26] K. Chaloupka, Y. Malam, A. M. Seifalian, *Trends in Biotechnology* **2010**, *28*, 580–588.
- [27] C. Argyo, V. Weiss, C. Bräuchle, T. Bein, *Chemistry of Materials* **2013**, *26*, 435–451.
- [28] J.-H. Park, L. Gu, G. von Maltzahn, E. Ruoslahti, S. N. Bhatia, M. J. Sailor, *Nature Materials* **2009**, *8*, 331–336.
- [29] A. Bianco, K. Kostarelos, M. Prato, *Current Opinion in Chemical Biology* **2005**, *9*, 674–679.
- [30] H. Otsuka, Y. Nagasaki, K. Kataoka, *Advanced Drug Delivery Reviews* **2012**, *64*, 246–255.

- [31] V. Mamaeva, C. Sahlgren, M. Lindén, *Advanced Drug Delivery Reviews* **2013**, *65*, 689–702.
- [32] E. Blanco, H. Shen, M. Ferrari, *Nature Biotechnology* **2015**, *33*, 941–951.
- [33] G. Sonavane, K. Tomoda, K. Makino, *Colloids and Surfaces B: Biointerfaces* **2008**, *66*, 274–280.
- [34] Y. Matsumura, H. Maeda, *Cancer Research* **1986**, *46*, 6387–6392.
- [35] E. A. Azzopardi, E. L. Ferguson, D. W. Thomas, *Journal of Antimicrobial Chemotherapeutics* **2013**, *68*, 257–274.
- [36] C. N. Marti, M. Gheorghide, A. P. Kalogeropoulos, V. V. Georgiopoulou, A. A. Quyyumi, J. Butler, *Journal of the American College of Cardiology* **2012**, *60*, 1455–1469.
- [37] J. Fang, H. Nakamura, H. Maeda, *Advanced Drug Delivery Reviews* **2011**, *63*, 136–151.
- [38] D. Peer, J. M. Karp, S. Hong, O. C. Farokhzad, R. Margalit, R. Langer, *Nature Nanotechnology* **2007**, *2*, 751–760.
- [39] G. Sahay, D. Y. Alakhova, A. V. Kabanov, *Journal of Controlled Release* **2010**, *145*, 182–195.
- [40] S. E. A. Gratton, P. A. Ropp, P. D. Pohlhaus, J. C. Luft, V. J. Madden, M. E. Napier, J. M. DeSimone, *Proceedings of the National Academy of Sciences of the United States of America* **2008**, *105*, 11613–11618.
- [41] A. E. Gregory, D. Williamson, R. Titball, *Frontiers of Cellular Infections Microbiology* **2013**, *3*, DOI 10.3389/fcimb.2013.00013.
- [42] S.-Y. Lee, M. Ferrari, P. Decuzzi, *Nanotechnology* **2009**, *20*, 495101.
- [43] E. Fröhlich, *International Journal of Nanomedicine* **2012**, *7*, 5577–5591.
- [44] Y. Wang, S. Gao, W.-H. Ye, H. S. Yoon, Y.-Y. Yang, *Nature Materials* **2006**, *5*, 791–796.
- [45] H. Meng, M. Liong, T. Xia, Z. Li, Z. Ji, J. I. Zink, A. E. Nel, *ACS Nano* **2010**, *4*, 4539–4550.
- [46] S. Ortega, M. Malumbres, M. Barbacid, *Biochimica et Biophysica Acta (BBA) - Reviews on Cancer* **2002**, *1602*, 73–87.
- [47] K. Sorimachi, K. Akimoto, Y. Hattori, T. Ieiri, A. Niwa, *Cytokine* **1999**, *11*, 571–578.
- [48] A. Lesniak, F. Fenaroli, M. P. Monopoli, C. Åberg, K. A. Dawson, A. Salvati, *ACS Nano* **2012**, *6*, 5845–5857.
- [49] A. E. Nel, L. Mädler, D. Velegol, T. Xia, E. M. V. Hoek, P. Somasundaran, F. Klaessig, V. Castranova, M. Thompson, *Nature Materials* **2009**, *8*, 543–557.
- [50] C. C. Fleischer, C. K. Payne, *Accounts of Chemical Research* **2014**, *47*, 2651–2659.
- [51] T. M. Allen, *Nature Reviews Cancer* **2002**, *2*, 750–763.
- [52] R. Marega, E. A. Prasetyanto, C. Michiels, L. D. Cola, D. Bonifazi, *Small* **2016**, *12*, 5431–5441.
- [53] X. Yu, Y. Song, Y. Di, H. He, D. Fu, C. Jin, *Scientific Reports* **2016**, *6*, 31539.
- [54] V. P. Torchilin, *Nature Reviews Drug Discovery* **2005**, *4*, 145–160.
- [55] O. Ishida, K. Maruyama, H. Tanahashi, M. Iwatsuru, K. Sasaki, M. Eriguchi, H. Yanagie, *Pharmaceutical Research* **2001**, *18*, 1042–1048.
- [56] B. Stella, S. Arpicco, M. T. Peracchia, D. Desmaële, J. Hoebeke, M. Renoir, J. D'Angelo, L. Cattel, P. Couvreur, *Journal of Pharmaceutical Sciences* **2000**, *89*, 1452–1464.

- [57] J. F. Kukowska-Latallo, K. A. Candido, Z. Cao, S. S. Nigavekar, I. J. Majoros, T. P. Thomas, L. P. Balogh, M. K. Khan, J. R. Baker, *Cancer Research* **2005**, *65*, 5317–5324.
- [58] M. J. Akhtar, M. Ahamed, H. A. Alhadlaq, S. A. Alrokayan, S. Kumar, *Clinica Chimica Acta* **2014**, *436*, 78–92.
- [59] B. Van de Broek, N. Devoogdt, A. D’Hollander, H.-L. Gijs, K. Jans, L. Lagae, S. Muyltermans, G. Maes, G. Borghs, *ACS Nano* **2011**, *5*, 4319–4328.
- [60] J. Frigell, I. García, V. Gómez-Vallejo, J. Llop, S. Penadés, *Journal of the American Chemical Society* **2014**, *136*, 449–457.
- [61] Z. Pang, H. Gao, Y. Yu, J. Chen, L. Guo, J. Ren, Z. Wen, J. Su, X. Jiang, *International Journal of Pharmaceutics* **2011**, *415*, 284–292.
- [62] J. V. Jokerst, T. Lobovkina, R. N. Zare, S. S. Gambhir, *Nanomedicine* **2011**, *6*, 715–728.
- [63] M. O. Oyewumi, R. A. Yokel, M. Jay, T. Coakley, R. J. Mumper, *Journal of Controlled Release* **2004**, *95*, 613–626.
- [64] D. W. Bartlett, H. Su, I. J. Hildebrandt, W. A. Weber, M. E. Davis, *Proceedings of the National Academy of Sciences of the United States of America* **2007**, *104*, 15549–15554.
- [65] S. Miyata, S. Kawabata, R. Hiramatsu, A. Doi, N. Ikeda, T. Yamashita, T. Kuroiwa, S. Kasaoka, K. Maruyama, S.-I. Miyatake, *Neurosurgery* **2011**, *68*, 1380–1387.
- [66] Z. Medarova, W. Pham, C. Farrar, V. Petkova, A. Moore, *Nature Medicine* **2007**, *13*, 372–377.
- [67] S. Kunjachan, R. Pola, F. Gremse, B. Theek, J. Ehling, D. Moeckel, B. Hermanns-Sachweh, M. Pechar, K. Ulbrich, W. E. Hennink, *et al.*, *Nano Letters* **2014**, *14*, 972–981.
- [68] M. McElroy, S. Kaushal, G. A. Luiken, M. A. Talamini, A. R. Moossa, R. M. Hoffman, M. Bouvet, *World Journal of Surgery* **2008**, *32*, 1057–1066.
- [69] J.-H. Lee, K. Lee, S. H. Moon, Y. Lee, T. G. Park, J. Cheon, *Angewandte Chemie International Edition* **2009**, *48*, 4174–4179.
- [70] A. Louie, *Chemical Review* **2010**, *110*, 3146–3195.
- [71] J. Xie, S. Lee, X. Chen, *Advanced Drug Delivery Reviews* **2010**, *62*, 1064–1079.
- [72] T. Lammers, S. Aime, W. E. Hennink, G. Storm, F. Kiessling, *Accounts of Chemical Research* **2011**, *44*, 1029–1038.
- [73] S. M. Janib, A. S. Moses, J. A. MacKay, *Advanced Drug Delivery Reviews* **2010**, *62*, 1052–1063.
- [74] V. T. DeVita, E. Chu, *Cancer Research* **2008**, *68*, 8643–8653.
- [75] H. S. Yoo, K. H. Lee, J. E. Oh, T. G. Park, *Journal of Controlled Release* **2000**, *68*, 419–431.
- [76] D. N. Heo, D. H. Yang, H.-J. Moon, J. B. Lee, M. S. Bae, S. C. Lee, W. J. Lee, I.-C. Sun, I. K. Kwon, *Biomaterials* **2012**, *33*, 856–866.
- [77] X.-H. Tian, X.-N. Lin, F. Wei, W. Feng, Z.-C. Huang, P. Wang, L. Ren, Y. Diao, *International Journal of Nanomedicine* **2011**, *6*, 445–452.
- [78] S. Dasari, P. Bernard Tchounwou, *European Journal of Pharmacology* **2014**, *740*, 364–378.
- [79] Y. Pommier, E. Leo, H. Zhang, C. Marchand, *Chemistry & Biology* **2010**, *17*, 421–433.
- [80] B. A. Weaver, *Molecular Biology of the Cell* **2014**, *25*, 2677–2681.

- [81] J. Zhang, M. F. G. Stevens, T. D. Bradshaw, *Current Molecular Pharmacology* **2012**, 5, 102–114.
- [82] W. I. Ganz, K. S. Sridhar, S. S. Ganz, R. Gonzalez, S. Chakko, A. Serafini, *Oilseeds and fats, Crops and Lipids* **1996**, 53, 461–470.
- [83] P. G. Corrie, *Medicine* **2008**, 36, 24–28.
- [84] Y. (Chezy) Barenholz, *Journal of Controlled Release* **2012**, 160, 117–134.
- [85] A. Gabizon, R. Catane, B. Uziely, B. Kaufman, T. Safra, R. Cohen, F. Martin, A. Huang, Y. Barenholz, *Cancer Research* **1994**, 54, 987–992.
- [86] B. Shi, M. Zheng, W. Tao, R. Chung, D. Jin, D. Ghaffari, O. C. Farokhzad, *Biomacromolecules* **2017**, 18, 2231–2246.
- [87] A. Fire, S. Xu, M. K. Montgomery, S. A. Kostas, S. E. Driver, C. C. Mello, *Nature* **1998**, 391, 806–811.
- [88] G. Hutvagner, P. D. Zamore, *Science* **2002**, 297, 2056–2060.
- [89] M. Frank-Kamenetsky, A. Grefhorst, N. N. Anderson, T. S. Racie, B. Bramlage, A. Akinc, D. Butler, K. Charisse, R. Dorkin, Y. Fan, *et al.*, *Proceedings of the National Academy of Sciences of the United States of America* **2008**, 105, 11915–11920.
- [90] D. V. Morrissey, J. A. Lockridge, L. Shaw, K. Blanchard, K. Jensen, W. Breen, K. Hartsough, L. Machemer, S. Radka, V. Jadhav, *et al.*, *Nature Biotechnology* **2005**, 23, 1002–1007.
- [91] E. Song, S.-K. Lee, J. Wang, N. Ince, N. Ouyang, J. Min, J. Chen, P. Shankar, J. Lieberman, *Nature Medicine* **2003**, 9, 347–351.
- [92] A. P. McCaffrey, L. Meuse, T.-T. T. Pham, D. S. Conklin, G. J. Hannon, M. A. Kay, *Nature* **2002**, 418, 38–39.
- [93] M. DiFiglia, M. Sena-Esteves, K. Chase, E. Sapp, E. Pfister, M. Sass, J. Yoder, P. Reeves, R. K. Pandey, K. G. Rajeev, *et al.*, *Proceedings of the National Academy of Sciences of the United States of America* **2007**, 104, 17204–17209.
- [94] Niu X.-Y., Peng Z.-L., Duan W.-Q., Wang H., Wang P., *International Journal of Gynecological Cancer* **2006**, 16, 743–751.
- [95] K. A. Whitehead, R. Langer, D. G. Anderson, *Nature Review Drug Discovery* **2009**, 8, 129–138.
- [96] C. V. Pecot, G. A. Calin, R. L. Coleman, G. Lopez-Berestein, A. K. Sood, *Nature Reviews Cancer* **2011**, 11, 59–67.
- [97] K. Strebhardt, A. Ullrich, *Nature Reviews Cancer* **2006**, 6, 321–330.
- [98] H. J. Kim, A. Kim, K. Miyata, K. Kataoka, *Advanced Drug Delivery Reviews* **2016**, 104, 61–77.
- [99] R. Kanasty, J. R. Dorkin, A. Vegas, D. Anderson, *Nature Materials* **2013**, 12, 967–977.
- [100] M. E. Davis, J. E. Zuckerman, C. H. J. Choi, D. Seligson, A. Tolcher, C. A. Alabi, Y. Yen, J. D. Heidel, A. Ribas, *Nature* **2010**, 464, 1067–1070.
- [101] B. M. Cooper, D. Putnam, *ACS Biomaterials Science & Engineering* **2016**, 2, 1837–1850.
- [102] R. H. Mo, J. L. Zaro, W.-C. Shen, *Molecular Pharmaceutics* **2012**, 9, 299–309.
- [103] Y. Yao, T. Sun, S. Huang, S. Dou, L. Lin, J. Chen, J. Ruan, C. Mao, F. Yu, M. Zeng, *et al.*, *Science Translational Medicine* **2012**, 4, 130ra48–130ra48.
- [104] J. C. Kaczmarek, P. S. Kowalski, D. G. Anderson, *Genome Medicine* **2017**, 9, 60.
- [105] H. Ledford, “Gene-silencing technology gets first drug approval after 20-year wait,” DOI 10.1038/d41586-018-05867-7 can be found under <http://www.nature.com/articles/d41586-018-05867-7>, **2018**.

- [106] N. W. S. Kam, H. Dai, *Journal of the American Chemical Society* **2005**, *127*, 6021–6026.
- [107] N. W. Shi Kam, T. C. Jessop, P. A. Wender, H. Dai, *Journal of the American Chemical Society* **2004**, *126*, 6850–6851.
- [108] M. Zhao, B. Hu, Z. Gu, K.-I. Joo, P. Wang, Y. Tang, *Nano Today* **2013**, *8*, 11–20.
- [109] H. H. P. Yiu, P. A. Wright, *Journal of Material Chemistry* **2005**, *15*, 3690–3700.
- [110] J. Lei, J. Fan, C. Yu, L. Zhang, S. Jiang, B. Tu, D. Zhao, *Microporous and Mesoporous Materials* **2004**, *73*, 121–128.
- [111] J. Tu, A. L. Boyle, H. Friedrich, P. H. H. Bomans, J. Bussmann, N. A. J. M. Sommerdijk, W. Jiskoot, A. Kros, *ACS Applied Materials & Interfaces* **2016**, *8*, 32211–32219.
- [112] M. J. Kim, R. Ryoo, *Chemistry of Materials* **1999**, *11*, 487–491.
- [113] S. Giri, B. G. Trewyn, M. P. Stellmaker, V. S.-Y. Lin, *Angewandte Chemie International Edition* **2005**, *44*, 5038–5044.
- [114] A. B. D. Nandiyanto, S.-G. Kim, F. Iskandar, K. Okuyama, *Microporous and Mesoporous Materials* **2009**, *120*, 447–453.
- [115] Y. Zhang, Z. Zhi, T. Jiang, J. Zhang, Z. Wang, S. Wang, *Journal of Controlled Release* **2010**, *145*, 257–263.
- [116] F. Gao, P. Botella, A. Corma, J. Blesa, L. Dong, *Journal of Physical Chemistry B* **2009**, *113*, 1796–1804.
- [117] W. Stöber, A. Fink, E. Bohn, *Journal of Colloid and Interface Science* **1968**, *26*, 62–69.
- [118] A. Monnier, F. Schüth, Q. Huo, D. Kumar, D. Margolese, R. S. Maxwell, G. D. Stucky, M. Krishnamurty, P. Petroff, A. Firouzi, *et al.*, *Science* **1993**, *261*, 1299–1303.
- [119] D. Zhao, J. Sun, Q. Li, G. D. Stucky, *Chemistry of Materials* **2000**, *12*, 275–279.
- [120] M. Grün, I. Lauer, K. K. Unger, *Advanced Materials* **1997**, *9*, 254–257.
- [121] H. Ow, D. R. Larson, M. Srivastava, B. A. Baird, W. W. Webb, U. Wiesner, *Nano Letters* **2005**, *5*, 113–117.
- [122] A. Burns, H. Ow, U. Wiesner, *Chemical Society Reviews* **2006**, *35*, 1028–1042.
- [123] M. Benezra, O. Penate-Medina, P. B. Zanzonico, D. Schaer, H. Ow, A. Burns, E. DeStanchina, V. Longo, E. Herz, S. Iyer, *et al.*, *Journal of Clinical Investigations* **2011**, *121*, 2768–2780.
- [124] E. Phillips, O. Penate-Medina, P. B. Zanzonico, R. D. Carvajal, P. Mohan, Y. Ye, J. Humm, M. Gönen, H. Kalaigian, H. Schöder, *et al.*, *Science Translational Medicine* **2014**, *6*, 260ra149-260ra149.
- [125] C. T. Kresge, M. E. Leonowicz, W. J. Roth, J. C. Vartuli, J. S. Beck, *Nature* **1992**, *359*, 710–712.
- [126] J. S. Beck, J. C. Vartuli, W. J. Roth, M. E. Leonowicz, C. T. Kresge, K. D. Schmitt, C. T. W. Chu, D. H. Olson, E. W. Sheppard, S. B. McCullen, *et al.*, *Journal of the American Chemical Society* **1992**, *114*, 10834–10843.
- [127] S. Inagaki, Y. Fukushima, K. Kuroda, *Journal of the Chemical Society, Chemical Communications* **1993**, *0*, 680–682.
- [128] S. H. Joo, J. Y. Park, C.-K. Tsung, Y. Yamada, P. Yang, G. A. Somorjai, *Nature Materials* **2009**, *8*, 126–131.
- [129] F. Jiao, H. Frei, *Angewandte Chemie International Edition* **2009**, *48*, 1841–1844.
- [130] A. Corma, *Chemical Review* **1997**, *97*, 2373–2420.
- [131] I. I. Slowing, J. L. Vivero-Escoto, B. G. Trewyn, V. S.-Y. Lin, *Journal of Material Chemistry* **2010**, *20*, 7924–7937.

- [132] X. Liu, J. Li, L. Zhou, D. Huang, Y. Zhou, *Chemical Physics Letters* **2005**, *415*, 198–201.
- [133] J. C. Vartuli, K. D. Schmitt, C. T. Kresge, W. J. Roth, M. E. Leonowicz, S. B. McCullen, S. D. Hellring, J. S. Beck, J. L. Schlenker, *Chemistry of Materials* **1994**, *6*, 2317–2326.
- [134] Q. Huo, D. I. Margolese, G. D. Stucky, *Chemistry of Materials* **1996**, *8*, 1147–1160.
- [135] Q. Huo, D. I. Margolese, U. Ciesla, P. Feng, T. E. Gier, P. Sieger, R. Leon, P. M. Petroff, F. Schüth, G. D. Stucky, *Nature* **1994**, *368*, 317–321.
- [136] Q. Huo, D. I. Margolese, U. Ciesla, D. G. Demuth, P. Feng, T. E. Gier, P. Sieger, A. Firouzi, B. F. Chmelka, *Chemistry of Materials* **1994**, *6*, 1176–1191.
- [137] M. Mizutani, Y. Yamada, T. Nakamura, K. Yano, *Chemistry of Materials* **2008**, *20*, 4777–4782.
- [138] A. Walcarius, M. Etienne, B. Lebeau, *Chemistry of Materials* **2003**, *15*, 2161–2173.
- [139] K. Y. Ho, G. McKay, K. L. Yeung, *Langmuir* **2003**, *19*, 3019–3024.
- [140] A. M. Liu, K. Hidajat, S. Kawi, D. Y. Zhao, *Chemical Communications* **2000**, *0*, 1145–1146.
- [141] C. Lei, Y. Shin, J. Liu, E. J. Ackerman, *Journal of the American Chemical Society* **2002**, *124*, 11242–11243.
- [142] T. Yokoi, H. Yoshitake, T. Tatsumi, *Journal of Material Chemistry* **2004**, *14*, 951–957.
- [143] F. Zheng, D. N. Tran, B. J. Busche, G. E. Fryxell, R. S. Addleman, T. S. Zemanian, C. L. Aardahl, *Industrial and Engineering Chemical Research* **2005**, *44*, 3099–3105.
- [144] K. Venkatesan, T. Srinivasan, P. Vasudeva Rao, *Journal of Radioanalytical and Nuclear Chemistry* **2003**, *256*, 213–218.
- [145] T. Kang, Y. Park, K. Choi, J. S. Lee, J. Yi, *Journal of Material Chemistry* **2004**, *14*, 1043–1049.
- [146] G. Rodríguez-López, M. D. Marcos, R. Martínez-Mañez, F. Sancenón, J. Soto, L. A. Villaescusa, D. Beltrán, P. Amorós, *Chemical Communications* **2004**, *0*, 2198–2199.
- [147] M. Park, S. Komarneni, *Microporous and Mesoporous Materials* **1998**, *25*, 75–80.
- [148] F. de Juan, E. Ruiz-Hitzky, *Advanced Materials* **2000**, *12*, 430–432.
- [149] S. L. Burkett, S. D. Sims, S. Mann, *Chemical Communications* **1996**, *0*, 1367–1368.
- [150] D. J. Macquarrie, *Chemical Communications* **1996**, *0*, 1961–1962.
- [151] C. E. Fowler, S. L. Burkett, S. Mann, *Chemical Communications* **1997**, *0*, 1769–1770.
- [152] R. Richer, *Chemical Communications* **1998**, *0*, 1775–1777.
- [153] A. Walcarius, C. Delacôte, *Chemistry of Materials* **2003**, *15*, 4181–4192.
- [154] T. Yokoi, H. Yoshitake, T. Tatsumi, *Chemistry of Materials* **2003**, *15*, 4536–4538.
- [155] S. Che, A. E. Garcia-Bennett, T. Yokoi, K. Sakamoto, H. Kunieda, O. Terasaki, T. Tatsumi, *Nature Materials* **2003**, *2*, 801–805.
- [156] N. Liu, R. A. Assink, B. Smarsly, C. J. Brinker, *Chemical Communications* **2003**, *0*, 1146–1147.
- [157] F. Cagnol, D. Grosso, C. Sanchez, *Chemical Communications* **2004**, *0*, 1742–1743.
- [158] C. M. Bamrough, R. C. T. Slade*, R. T. Williams, *Journal of Material Chemistry* **1998**, *8*, 569–571.
- [159] R. C. T. Slade, C. M. Bamrough, R. T. Williams, *Physical Chemistry Chemical Physics* **2002**, *4*, 5394–5399.
- [160] R. Huq, L. Mercier, P. J. Kooyman, *Chemistry of Materials* **2001**, *13*, 4512–4519.
- [161] N. Liu, Z. Chen, D. R. Dunphy, Y.-B. Jiang, R. A. Assink, C. J. Brinker, *Angewandte Chemie International Edition* **2003**, *42*, 1731–1734.

- [162] G. Wirnsberger, B. J. Scott, G. D. Stucky, *Chemical Communications* **2001**, *0*, 119–120.
- [163] S. Inagaki, S. Guan, Y. Fukushima, T. Ohsuna, O. Terasaki, *Journal of the American Chemical Society* **1999**, *121*, 9611–9614.
- [164] T. Asefa, M. J. MacLachlan, N. Coombs, G. A. Ozin, *Nature* **1999**, *402*, 867–871.
- [165] B. J. Melde, B. T. Holland, C. F. Blanford, A. Stein, *Chemistry of Materials* **1999**, *11*, 3302–3308.
- [166] C. Yoshina-Ishii, T. Asefa, N. Coombs, M. J. MacLachlan, G. A. Ozin, *Chemical Communications* **1999**, *0*, 2539–2540.
- [167] J. G. Croissant, X. Cattoën, M. W. C. Man, J.-O. Durand, N. M. Khashab, *Nanoscale* **2015**, *7*, 20318–20334.
- [168] M. Vallet-Regi, A. Rámila, R. P. del Real, J. Pérez-Pariante, *Chemistry of Materials* **2001**, *13*, 308–311.
- [169] Y. Gao, Y. Chen, X. Ji, X. He, Q. Yin, Z. Zhang, J. Shi, Y. Li, *ACS Nano* **2011**, *5*, 9788–9798.
- [170] H.-K. Na, M.-H. Kim, K. Park, S.-R. Ryoo, K. E. Lee, H. Jeon, R. Ryoo, C. Hyeon, D.-H. Min, *Small* **2012**, *8*, 1752–1761.
- [171] I. I. Slowing, B. G. Trewyn, V. S.-Y. Lin, *Journal of the American Chemical Society* **2007**, *129*, 8845–8849.
- [172] X. Li, Q. He, J. Shi, *ACS Nano* **2014**, *8*, 1309–1320.
- [173] J. Lu, M. Liong, Z. Li, J. I. Zink, F. Tamanoi, *Small* **2010**, *6*, 1794–1805.
- [174] H. Meng, M. Xue, T. Xia, Z. Ji, D. Y. Tarn, J. I. Zink, A. E. Nel, *ACS Nano* **2011**, *5*, 4131–4144.
- [175] X. Liu, A. Situ, Y. Kang, K. R. Villabroza, Y. Liao, C. H. Chang, T. Donahue, A. E. Nel, H. Meng, *ACS Nano* **2016**, *10*, 2702–2715.
- [176] S. P. Maddala, D. Velluto, Z. Luklinska, A. C. Sullivan, *Journal of Material Chemistry B* **2014**, *2*, 903–914.
- [177] C. Kneuer, M. Sameti, U. Bakowsky, T. Schiestel, H. Schirra, H. Schmidt, C.-M. Lehr, *Bioconjugate Chemistry* **2000**, *11*, 926–932.
- [178] S. B. Hartono, W. Gu, F. Kleitz, J. Liu, L. He, A. P. J. Middelberg, C. Yu, G. Q. (Max) Lu, S. Z. Qiao, *ACS Nano* **2012**, *6*, 2104–2117.
- [179] C. Hom, J. Lu, M. Liong, H. Luo, Z. Li, J. I. Zink, F. Tamanoi, *Small* **2010**, *6*, 1185–1190.
- [180] K. Möller, K. Müller, H. Engelke, C. Bräuchle, E. Wagner, T. Bein, *Nanoscale* **2016**, *8*, 4007–4019.
- [181] A. M. Chen, M. Zhang, D. Wei, D. Stueber, O. Taratula, T. Minko, H. He, *Small* **2009**, *5*, 2673–2677.
- [182] H. Meng, W. X. Mai, H. Zhang, M. Xue, T. Xia, S. Lin, X. Wang, Y. Zhao, Z. Ji, J. I. Zink, *et al.*, *ACS Nano* **2013**, *7*, 994–1005.
- [183] H. Meng, M. Wang, H. Liu, X. Liu, A. Situ, B. Wu, Z. Ji, C. H. Chang, A. E. Nel, *ACS Nano* **2015**, *9*, 3540–3557.
- [184] J. Kim, H. S. Kim, N. Lee, T. Kim, H. Kim, T. Yu, I. C. Song, W. K. Moon, T. Hyeon, *Angewandte Chemie* **2008**, *120*, 8566–8569.
- [185] M. B. Yatvin, J. N. Weinstein, W. H. Dennis, R. Blumenthal, *Science* **1978**, *202*, 1290–1293.
- [186] S. Mura, J. Nicolas, P. Couvreur, *Nature Materials* **2013**, *12*, 991–1003.

- [187] C. R. Thomas, D. P. Ferris, J.-H. Lee, E. Choi, M. H. Cho, E. S. Kim, J. F. Stoddart, J.-S. Shin, J. Cheon, J. I. Zink, *Journal of the American Chemical Society* **2010**, *132*, 10623–10625.
- [188] E. Ruiz-Hernández, A. Baeza, M. Vallet-Regí, *ACS Nano* **2011**, *5*, 1259–1266.
- [189] X. Ding, C. H. Liow, M. Zhang, R. Huang, C. Li, H. Shen, M. Liu, Y. Zou, N. Gao, Z. Zhang, *et al.*, *Journal of the American Chemical Society* **2014**, *136*, 15684–15693.
- [190] X. Yang, X. Liu, Z. Liu, F. Pu, J. Ren, X. Qu, *Advanced Materials* **2012**, *24*, 2890–2895.
- [191] P. Huang, J. Lin, X. Wang, Z. Wang, C. Zhang, M. He, K. Wang, F. Chen, Z. Li, G. Shen, *et al.*, *Advanced Materials Weinheim* **2012**, *24*, 5104–5110.
- [192] J. Yang, J. Lee, J. Kang, S. J. Oh, H.-J. Ko, J.-H. Son, K. Lee, J.-S. Suh, Y.-M. Huh, S. Haam, *Advanced Materials* **2009**, *21*, 4339–4342.
- [193] J. L. Vivero-Escoto, I. I. Slowing, C.-W. Wu, V. S.-Y. Lin, *Journal of the American Chemical Society* **2009**, *131*, 3462–3463.
- [194] X.-Q. Wang, Q. Zhang, *European Journal of Pharmaceutics and Biopharmaceutics* **2012**, *82*, 219–229.
- [195] M. C. Chen, K. Sonaje, K. J. Chen, H. W. Sung, *Biomaterials* **2011**, *32*, 9826–9838.
- [196] H. Meng, M. Xue, T. Xia, Y.-L. Zhao, F. Tamanoi, J. F. Stoddart, J. I. Zink, A. E. Nel, *Journal of the American Chemical Society* **2010**, *132*, 12690–12697.
- [197] H. J. Forman, H. Zhang, A. Rinna, *Molecular Aspects of Medicine* **2009**, *30*, 1–12.
- [198] G. K. Balendiran, R. Dabur, D. Fraser, *Cell Biochemistry and Function* **2004**, *22*, 343–352.
- [199] F. Q. Schafer, G. R. Buettner, *Free Radical Biology and Medicine* **2001**, *30*, 1191–1212.
- [200] J. Zhang, M. Niemelä, J. Westermarck, J. M. Rosenholm, *Dalton Transactions* **2014**, *43*, 4115–4126.
- [201] Y. Chen, H. Chen, J. Shi, *Advanced Materials* **2013**, *25*, 3144–3176.
- [202] J. G. Croissant, Y. Fatieiev, A. Almalik, N. M. Khashab, *Advanced Healthcare Materials* **2018**, *7*, 1700831.
- [203] J. Croissant, Y. Fatieiev, N.M. Khashab., *Advanced Materials* **2017**, *29*, 1604634.
- [204] B. C. Bunker, *Journal of Non-Crystalline Solids* **1994**, *179*, 300–308.
- [205] K. S. Finnie, D. J. Waller, F. L. Perret, A. M. Krause-Heuer, H. Q. Lin, J. V. Hanna, C. J. Barbé, *Journal of Sol-Gel Science and Technology* **2009**, *49*, 12–18.
- [206] H. Ehrlich, K. D. Demadis, O. S. Pokrovsky, P. G. Koutsoukos, *Chemical Review* **2010**, *110*, 4656–4689.
- [207] H. Yamada, C. Urata, Y. Aoyama, S. Osada, Y. Yamauchi, K. Kuroda, *Chemistry of Materials* **2012**, *24*, 1462–1471.
- [208] L. Li, T. Liu, C. Fu, L. Tan, X. Meng, H. Liu, *Nanomedicine: Nanotechnology, Biology and Medicine* **2015**, *11*, 1915–1924.
- [209] D. Shen, J. Yang, X. Li, L. Zhou, R. Zhang, W. Li, L. Chen, R. Wang, F. Zhang, D. Zhao, *Nano Letters* **2014**, *14*, 923–932.
- [210] V. Cauda, A. Schlossbauer, T. Bein, *Microporous and Mesoporous Materials* **2010**, *132*, 60–71.
- [211] X.-D. Zhang, D. Wu, X. Shen, P.-X. Liu, F.-Y. Fan, S.-J. Fan, *Biomaterials* **2012**, *33*, 4628–4638.
- [212] H. S. Choi, W. Liu, P. Misra, E. Tanaka, J. P. Zimmer, B. I. Ipe, M. G. Bawendi, J. V. Frangioni, *Nature Biotechnology* **2007**, *25*, 1165–1170.

- [213] J. Lu, Z. Li, J. I. Zink, F. Tamanoi, *Nanomedicine: Nanotechnology, Biology and Medicine* **2012**, *8*, 212–220.
- [214] M. Huo, J. Yuan, L. Tao, Y. Wei, *Polymer Chemistry* **2014**, *5*, 1519–1528.
- [215] X. Zhang, L. Han, M. Liu, K. Wang, L. Tao, Q. Wan, Y. Wei, *Material Chemistry Frontiers* **2017**, *1*, 807–822.
- [216] S. Quignard, S. Masse, G. Laurent, T. Coradin, *Chemical Communications* **2013**, *49*, 3410–3412.
- [217] L. Maggini, I. Cabrera, A. Ruiz-Carretero, E. A. Prasetyanto, E. Robinet, L. D. Cola, *Nanoscale* **2016**, *8*, 7240–7247.
- [218] E. A. Prasetyanto, A. Bertucci, D. Septiadi, R. Corradini, P. Castro-Hartmann, L. De Cola, *Angewandte Chemie International Edition* **2016**, *55*, 3323–3327.
- [219] J. Croissant, X. Cattoën, M. W. C. Man, A. Gallud, L. Raehm, P. Trens, M. Maynadier, J.-O. Durand, *Advanced Materials* **2014**, *26*, 6174–6180.
- [220] D. Shao, M. Li, Z. Wang, X. Zheng, Y.-H. Lao, Z. Chang, F. Zhang, M. Lu, J. Yue, H. Hu, *et al.*, *Advanced Materials* **2018**, *30*, 1801198.
- [221] L. Maggini, L. Travaglini, I. Cabrera, P. Castro-Hartmann, L. De Cola, *Chemistry – A European Journal* **2016**, *22*, 3697–3703.
- [222] J.G. Croissant, Y. Fatieiev, K. Julfakyan, J. Lu, A.-H. Emwas, D.H. Anjum, H. Omar, F. Tamanoi, J.I. Zink, N.M. Khashab, *Chemistry – A European Journal* **2016**, *22*, 14806–14811.
- [223] T. P. Szatrowski, C. F. Nathan, *Cancer Research* **1991**, *51*, 794–798.
- [224] G. Saravanakumar, J. Kim, W. J. Kim, *Advanced Science* **2017**, *4*, 1600124.
- [225] X. Xu, P. E. Saw, W. Tao, Y. Li, X. Ji, S. Bhasin, Y. Liu, D. Ayyash, J. Rasmussen, M. Huo, *et al.*, *Advanced Materials* **2017**, *29*, 1700141.
- [226] D. S. Wilson, G. Dalmaso, L. Wang, S. V. Sitaraman, D. Merlin, N. Murthy, *Nature Materials* **2010**, *9*, 923–928.
- [227] N. Ma, Y. Li, H. Xu, Z. Wang, X. Zhang, *Journal of the American Chemical Society* **2010**, *132*, 442–443.
- [228] K. E. Broaders, S. Grandhe, J. M. J. Fréchet, *Journal of the American Chemical Society* **2011**, *133*, 756–758.
- [229] J. S. Kim, S. D. Jo, G. L. Seah, I. Kim, Y. S. Nam, *Journal of Industrial and Engineering Chemistry* **2015**, *21*, 1137–1142.
- [230] C. Qian, P. Feng, J. Yu, Y. Chen, Q. Hu, W. Sun, X. Xiao, X. Hu, A. Bellotti, Q.-D. Shen, *et al.*, *Angewandte Chemie International Edition* **2017**, *56*, 2588–2593.
- [231] P. Han, S. Li, W. Cao, Y. Li, Z. Sun, Z. Wang, H. Xu, *Journal of Material Chemistry B* **2013**, *1*, 740–743.
- [232] J.-P. Behr, *CHIMIA International Journal for Chemistry* **1997**, *51*, 34–36.
- [233] L. Travaglini, P. Picchetti, R. Totovao, E. A. Prasetyanto, L. D. Cola, *Material Chemistry Frontiers* **2018**, DOI 10.1039/C8QM00438B.

Chapter 2

Large pore breakable mesoporous silica nanoparticles for PLK1 siRNA delivery

Abstract

Herein we report the synthesis and seminal biological applications of large pore disulfide-doped mesoporous silica nanoparticles (LP-ssNPs) for efficient siRNA delivery to hepatocellular carcinoma Huh-7 cells. In order to host siRNA and ensure a high loading capacity, the physico-chemical properties of the carrier have been specifically tailored. The LP-ssNPs are characterized by pores of 12 nm, a size able to accommodate the bulky biomolecule, and their surface was grafted with amino groups to ensure favorable electrostatic interactions with the negatively charged siRNA. As a result, a loading of 182 $\mu\text{g}/\text{mg}$ was achieved, which is a satisfactory value if compared with similar materials already reported. Moreover, disulfide groups have been embedded into the silica framework to enable the nanoparticles to break down in the reducing intracellular environment of tumor cells, hence ensuring enhanced release efficiency and clearance from the body. Once the siRNA has been loaded on the LP-ssNPs, the material was coated with linear polyethylenimine (jetPEI[®]) through a layer-by-layer assembly, since the polycationic coating not only protects the siRNA towards enzyme degradation but also enhances the cellular uptake. *In vitro* investigation assessed the cytocompatibility of the carrier and showed high cellular uptake and efficient release of siRNA into tumor cells. Degradation in the intracellular environment was also proven. *In vivo* proofs of concept studies showed an inhibition of tumor growth in an animal model. By enabling patient cancer-specific delivery of siRNA this approach will enable precision medicine for cancer treatment.

2.1 Introduction

Since its discovery in 1998 by Fire and Mellow,^[1] small interfering RNA (siRNA) has attracted increasing attention for its potential in medicine, showing possible applications in the treatment of various diseases such as hypercholesterolaemia,^[2] hepatitis B^[3,4] and C^[5] viruses, neurodegenerative diseases^[6] and human papillomavirus.^[7]

In particular, siRNA holds a great deal of promises in cancer treatment being able to silence the expression of specific genes by binding messenger RNA (mRNA).^[8] Several studies have shown the inhibition in the growth and proliferation of cancer cells when using siRNA-based approach *in vitro* and *in vivo*.^[9] Nevertheless, despite its clinical potential, the effective delivery of siRNA to the tumor site is a major hurdle.^[10] Some of the factors contributing to this drawback are: *i*) the siRNA negative charge, which hinders its ability to cross the cell membrane; *ii*) its easy degradation by endogenous enzymes^[10,11] and *iii*) its instability in the bloodstream due to uptake by phagocytes and aggregation with serum proteins.^[9,12] Delivery systems are therefore highly needed for efficient protection and transfection of the bare biomolecule.

Among the carriers so far reported only a few successfully performed delivery of siRNA,^[13] namely polymers,^[14,15] peptides^[16] and antibodies.^[17] Moreover, several siRNA lipid-based nanoparticles are also under clinical trial for the treatment of various diseases.^[18–20] For these types of nanocarriers it has been also reported that their shape, size and charge offers already a passive targeting towards the organs.^[21,22] Despite all the efforts invested in the development of siRNA nanocarriers, the main issue still remaining is the short half-life due to their capture by the reticulo-endothelial system, thus inducing an inefficient payload delivery.^[12,23]

Among the materials so far reported, polymeric nanoparticles have attracted attention due to their good designability and multifunctional potential.^[24] Several examples have been reported so far for the delivery of specific genes, especially with the use of polyethylenimine (PEI), which is the most studied polymer thanks to its buffering capacities and its ability to bind high loading of oligonucleotides. As branched PEI with high molecular weight represents the most promising transfection agent, it often suffers from toxicity while linear and short PEI usually shows less toxicity but inefficient transfection capacities.^[25]

Recently mesoporous silica nanoparticles (MSNs), offering instead a more chemically robust framework and high loading capacity, have been proven to be good candidates to overcome the issue of short blood circulation and stability. In the last two decades MSNs have been widely studied as carriers for biomedical applications^[27–29] because of their large surface

area,^[30] ease of functionalization, possibility to tailor the mesostructure,^[31,32] non-toxicity^[33,34] and high cellular uptake, which are features that clearly make MSNs ideal tools in designing efficient carriers. Their ability to delivery small drugs has been firmly established^[26] and CTAB-templated MSNs with 2-3 nm pores are commonly used to this purpose.^[35] Nevertheless, the delivery of biomolecules, namely proteins or oligonucleotide sequences, usually requires a more sophisticated design due to the size and complexity of the guest biomolecules.^[36-38] For instance, the pore size is crucial if biomolecules have to be hosted within the pores of the MSNs,^[39] and several methods have been in fact developed to achieve the pore expansion.^[40-42] The most common one exploits the use of swelling agents, such as 1,3,5-trimethylbenzene (TMB) or 1,3,5-triisopropylbenzene, which can be added during the synthesis of MSNs^[43] or in a post-synthetic treatment.^[44] In addition, another aspect to take into account is the particle surface functionalization, since specific interactions with the guest biomolecule can be beneficial to achieve significant loading capacity. For instance, the loading of a negatively charged biomolecule, such as siRNA, into negatively charged MSNs will be favored if on the pore and particle surface charge-matching functionalities are introduced, such as amino functional groups, positively charged in aqueous media.^[36,45]

In spite of all the advances witnessed in the design of efficient MSNs carriers for drug delivery, the biodegradability and clearance of MSNs still remains debated.^[28,46,47] In fact, it has been reported that in aqueous media MSNs slowly degrade being hydrolyzed to silicic acid.^[48,49] On the other hand, some studies showed that in gastric fluids MSNs were stable over seven days.^[50,51] The contradictory results reported so far and the difficulties to investigate the actual fate of non-degraded particles *in vivo*, due both to the complexity of the system and to technological obstacles, still prevent the clinical translation of MSNs for cancer therapy, especially when frequent injections are required during the treatment. Kumar R. *et al* studied the *in vivo* clearance of 20 nm labelled mesoporous silica nanoparticles and demonstrated a presence of particles several days post intravenous injections.^[52]

In order to tackle the issues of MSNs bioaccumulation in living organs and allowing a safe excretion of the carrier from the body,^[53,54] stimuli-responsive organosilica particles have been recently investigated and emerged as promising materials. The doping of the silica framework with organic alkoxy silanes bearing cleavable bonds allows the preparation of particles responsive to intracellular stimuli, whose breakdown into small debris can be therefore triggered inside the cells and enable a complete extraction. In particular, the insertion of redox-responsive disulfide bonds^[55-59] or enzyme-cleavable groups^[60,61] has been reported.

As a potential application for this promising nanocarriers, cancer therapy and more precisely for hepatocellular carcinoma (HCC), which is the most common form of liver cancer and a major cause of cancer death worldwide with more than 600 000 deaths each year.^[62] HCC is often diagnosed when it is not curable. Thus, there are many challenges associated with the treatment of HCC from the beginning to the end including screening, treatment decision, actual treatment option and palliative care. The heterogeneity of HCC is associated to the activation of multiple intracellular signal transduction pathways and thus greatly complicates treatment strategies.^[63] Therefore, efficient treatment will require a patient specific approach.

Herein we present large pore disulfide-doped mesoporous silica nanoparticles (LP-ssNPs) characterized by large pores of ca 12 nm and able to degrade in small pieces upon exposure to reduced glutathione (GSH), which is a natural reducing agent overexpressed in cancer cells. LP-ssNPs have been functionalized with amino groups on the external and internal surface to ensure a more efficient adsorption of siRNA thanks to favorable electrostatic interactions. The responsiveness of the material instead ensures not only a safe clearance of the carrier but also an increased release activity, as we recently reported.^[55]

We loaded the LP-ssNPs with a specific sequence of siRNA able to silence the expression of the polo-like kinase 1 (PLK1), which regulates cell proliferation and is overexpressed in a variety of cancer cells,^[64] such as the hepatocellular carcinoma Huh-7 cells.^[65,66] Once loaded with siRNA, the LP-ssNPs have been coated with jetPEI[®], a linear polyethylenimine (PEI), in order to protect then the siRNA from nuclease degradation and increase the cellular uptake, thanks to its positive charge which ensures strong electrostatic interactions with the negatively charged cell membrane. In addition, PEI has been proven to help MSNs to escape endosomes, thus increasing the delivery into the cytoplasm.^[67,68] Linear PEI, despite their poor efficacy in siRNA delivery, present a lower cytotoxicity compared to high molecular weight branched PEI.^[69-71] By means of *in vitro* and *in vivo* studies, we demonstrated that our system was able not only to release efficiently the biomolecule, but also to breakdown in small debris, ensuring improved delivery and excretion.

2.2 Synthesis of large pore breakable mesoporous silica nanoparticles

2.2.1 Synthesis of small pore breakable mesoporous silica nanoparticles.

The synthesis of the small pore breakable mesoporous silica nanoparticles (ssNPs) has been performed following a procedure that we recently described.^[55] The ssNPs were therefore synthesized through a modified Stöber process,^[72] being one of the most commonly used methods for the synthesis of silica nanoparticles. It involves, in general, the condensation of a molecular building block, *i.e.* tetraethyl orthosilicate, in presence of water in an alcoholic solution. The addition of a catalyst (acid or basic) is generally required to help the hydrolysis of the monomer. By varying several parameters such as the quantity of catalyst and the ratio between the water and the alcoholic solution, particles of different sizes ranging from several nm to a few micrometers could be achieved.^[73] By adding a second building block, namely bis(triethoxysilyl-propyl)disulfide (BTSPD), to the widely used tetraethyl orthosilicate (TEOS) in a 30:70 molar ratio, it is then possible to create silica nanoparticles containing within the framework of the particles, disulfide bonds that are prone to be cleaved in presence of a reducing agent, leading to the breakdown in small pieces of the organo-hybrid silica nanoparticles. Moreover, the insertion of a porous structure can still be achieved by using cetyltrimethylammonium bromide (CTAB) as template, resulting in a final porous material with pore size around 2 nm.

2.2.2 Post synthetic treatment and the formation of large pore mesoporous silica nanoparticles (LP-ssNPs)

The CTAB is probably the most commonly used surfactant for the formation of mesoporous silica nanoparticles. Since 2001, and the first example of CTAB-templated silica nanoparticles as drug delivery systems by the group of Prof. Maria Vallet-Regi,^[26] their use in the nanomedicine world has kept increasing for the delivery of various drugs.^[74-77] However, with the rising field of gene and protein delivery, 2 nm pore size are generally considered as too small to host such guests, and therefore, the development of larger pores nanoparticles are required. For example, the change of surfactant can lead to a slight variation in the pore size but also in a different arrangement. The use of Pluronic block copolymer is often used to reach larger pore sizes.^[77] Another possibility is the insertion of so-called “swelling agents” (decane/trimethylbenzene, 1,3,5-triisopropylbenzene, *etc.*) that penetrate within the apolar domain of micelles increasing then their size before condensation of the silica. However, the complexity of the organo-hybrid ssNPs and especially the presence of the disulfide linker

reduce the amount of options available. For instance, the use of Pluronic block copolymers should be avoided since it has to be removed by calcination after synthesis and therefore might damage the organic linker. On the other side, the insertion of swelling agents during the synthesis has led to the formation of particles without any defined morphology. The use of such molecules has also been demonstrated to be efficient post-synthesis, as an additional step after the condensation of the silica network.^[44] This method, probably more suitable for our material has then been tested using a protocol described by Kim M.H. *et al.* treating the ssNPs at high temperature (160 °C) in the presence of the swelling agent trimethylbenzene (TMB) in a H₂O:EtOH mixture (50/50, v/v).^[78] A complete schematic representation of the synthesis of the large pore ssNPs (LP-ssNPs) is reported in **Figure 2.1**.

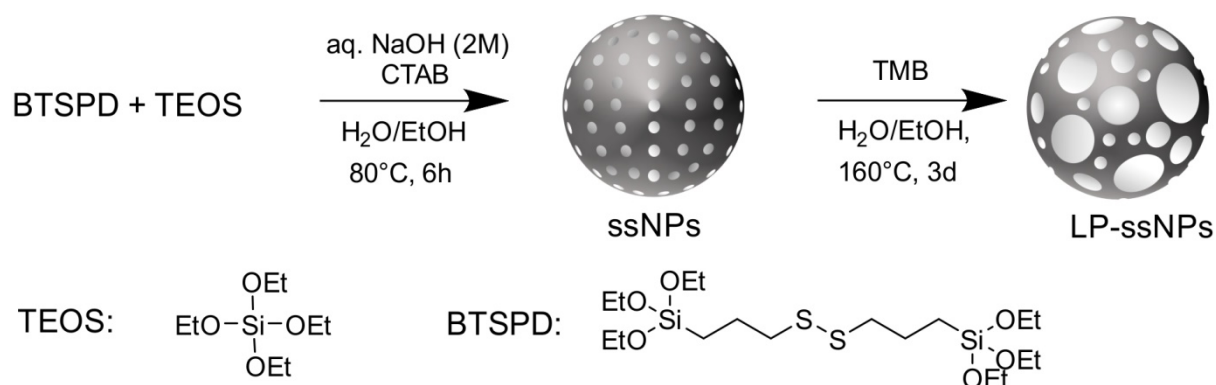


Figure 2.1: Schematic representation of the synthetic process for LP-ssNPs. The synthesis of the material occurs by mixing the 2 silanes precursors in presence of CTAB as a pore-template and NaOH as a base catalyst. The pore expansion was performed in a post-synthetic treatment in presence of 1,3,5-trimethylbenzene as a swelling agent.

2.2.3 Material characterizations.

Morphological characterization by mean of SEM and TEM:

The morphological characterization of the organosilica material was first performed by scanning and transmission electron microscopy (SEM and TEM). The SEM images reported in **Figure 2.2.a** and **2.2.b** displayed homogeneous spherical particles characterized by an average diameter of 99 ± 24 nm. TEM images (**Figure 2.2.c** and **d**) revealed an enlarged mesoporous structure after the post synthetic treatment, as suggested by the variation of the contrast within the particles, and a rougher particle surface. The surface etching process occurred to a certain extent, due to the dissolution of small pieces of silica in the water/ethanol mixture during the solvothermal treatment.^[44] Conversely, the ssNPs showed a higher contrast and a smoother surface, and no evidence of an ordered array of pores.

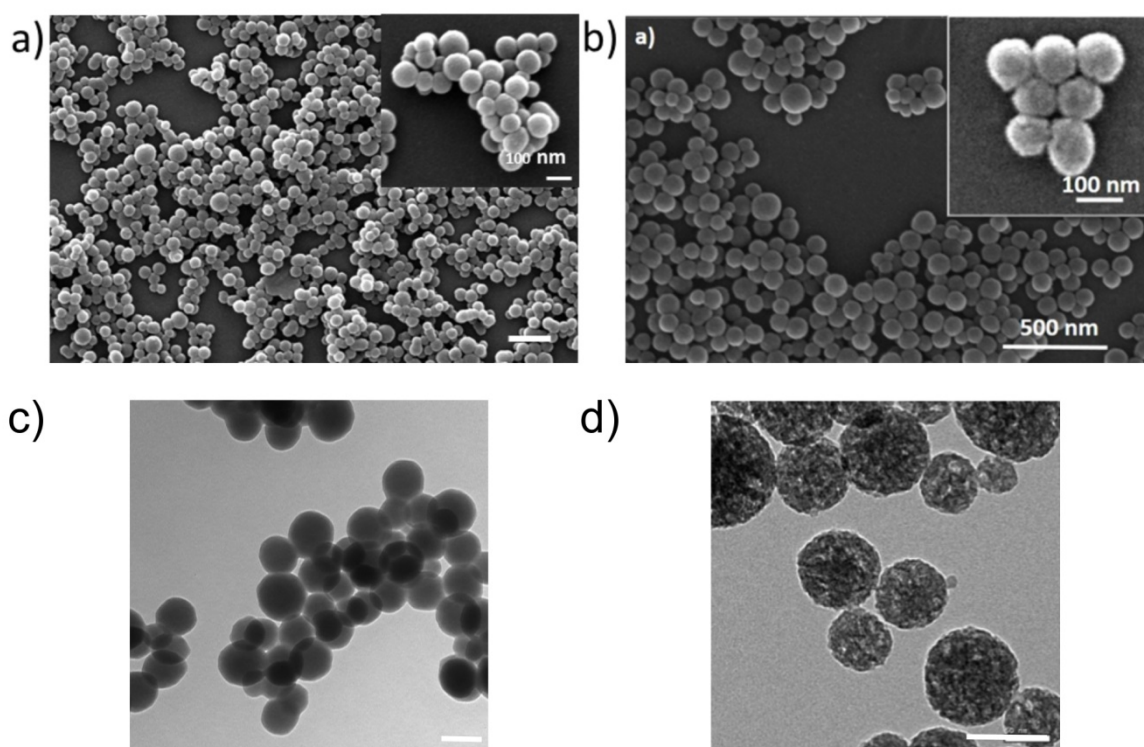


Figure 2.2: Microscopy analyses of the small pore disulfide-doped silica nanoparticles before and after pore expansion. After treatment, the particles demonstrated the presence of larger pores and rougher surface. SEM images of a) ssNPs and b) LP-ssNPs. Scale bar = 500 nm. TEM images of c) ssNPs and d) LP-ssNPs. Scale bar = 100 nm.

Pore size distribution, pore volume and surface area:

The porosity was assessed by nitrogen adsorption measurements performed on both the particles before and after the enlargement process and that clearly showed a 6-fold pore enlargement (**Figure 2.3.a**). In fact, the analysis of the adsorption/desorption isotherms allowed to calculate for ssNPs a BET surface area of $684 \text{ m}^2 \cdot \text{g}^{-1}$, total pore volume of $0.67 \text{ cm}^3 \cdot \text{g}^{-1}$ and an average pore size of 2.2 nm (**Figure 2.3.b**). The LP-ssNPs showed instead a smaller BET surface area of $430 \text{ m}^2 \cdot \text{g}^{-1}$ as a result of the presence of larger pores and related decreased wall thickness, the total pore volume at $p/p_0=0.99$ resulted to $1.07 \text{ cm}^3 \cdot \text{g}^{-1}$ and the increase can be explained by the increase of interstitial voids due the presence of non-smooth particles surfaces. The data analysis gave a broader pore width distribution centered at 12 nm (**Figure 2.3.a**) with the presence, to a lesser extent though, of micropores (1.7 nm) and smaller mesopores (2.7 nm).

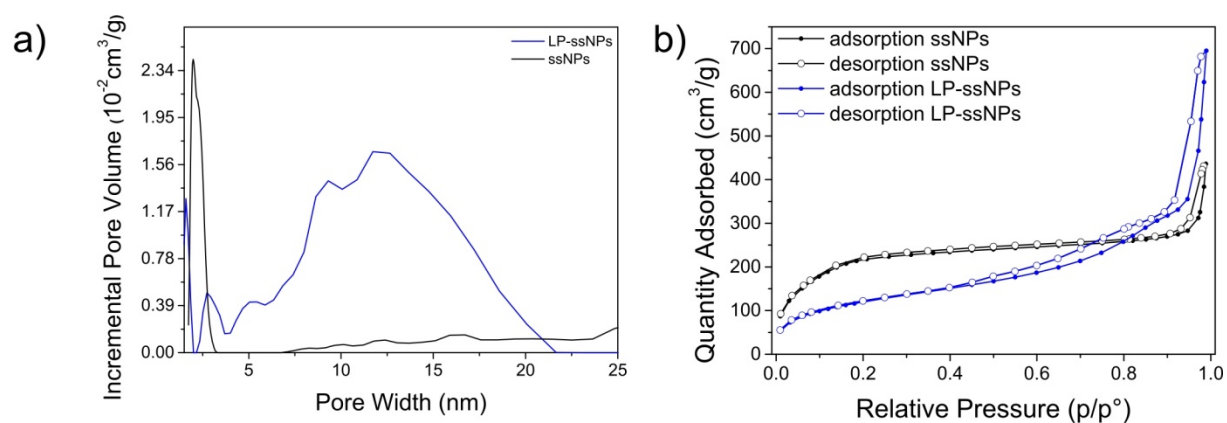


Figure 2.3: a) Pore width distribution before (black) and after pore expansion treatment (blue). b) N_2 adsorption/desorption isotherms recorded on the ssNPs and LP-ssNPs.

Ordered porosity:

MCM-41 silica nanoparticles show usually a highly ordered hexagonal porosity structure. This characteristic can be verified using small angle X-ray scattering (SAXS). **Figure 2.4** presents spectrum recorded on non breakable mesoporous silica NPs, ssNPs, and LP-ssNPs. The typical (100) Bragg peak of MCM-41 can be observed on the ssNPs, demonstrating a certain pore arrangement. The additional (110) and (200) peaks were not present, usually demonstrating the hexagonal arrangement of the pores.^[79] Such characteristics hypothesized a disordered pore arrangement, which could be explained by the presence of the disulfide linker. After the pore expansion treatment, the pattern of the LP-ssNPs did not show the Bragg peak, revealing the loss of an ordered array of the mesopores that has also been verified with the TEM images as shown in **Figure 2.2.c and d**.

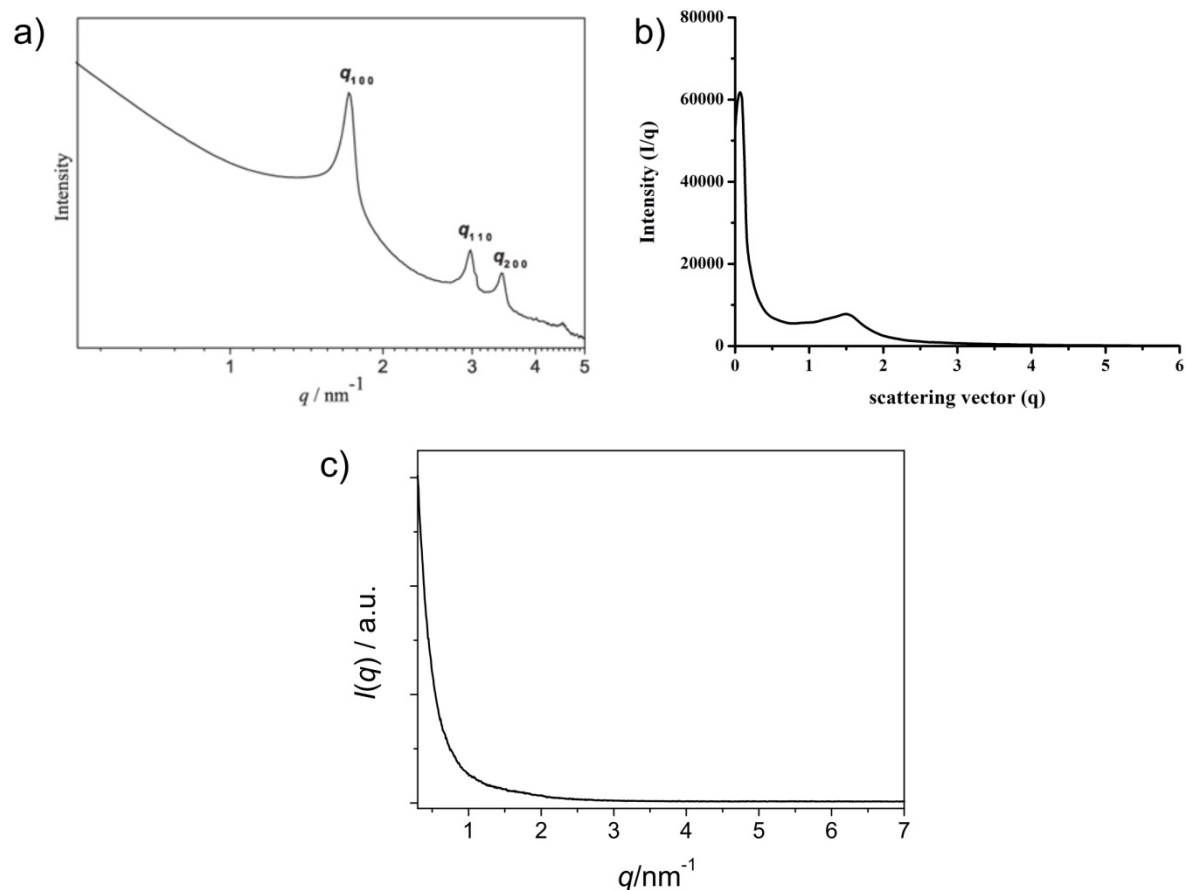


Figure 2.4: Small Angle X-Ray Scattering (SAXS) pattern of a) Mesoporous silica nanoparticles. Image taken from J.A.S. Costa, A. C. F.S. Garcia, D.O. Santos, V.H.V. Sarmiento, A.L.M. Porto, M.E. de Mesquita and L.P.C. Romão, A New Functionalized MCM-41 Mesoporous Material for Use in Environmental Applications, *J. Braz. Chem. Soc.*, Vol. 25, No. 2, 197-207 (2014). Copyright 2014, SciELO. b) ssNPs and c) LP-ssNPs representing the loss in pore organization with the introduction of the cleavable linker and the pore expansion treatment.

Elemental composition:

The presence of the cleavable linker within the particles was confirmed by elemental analysis of the material conducted by X-ray Photoelectron Spectroscopy (XPS; **Table 2-1** and **Figure 2.5**). The presence of the silica framework was demonstrated by the high atomic percentage of O(1s) and Si(2p) whereas the doping of the organic linker was proven by the detection of C(1s) and S(2p) signals.

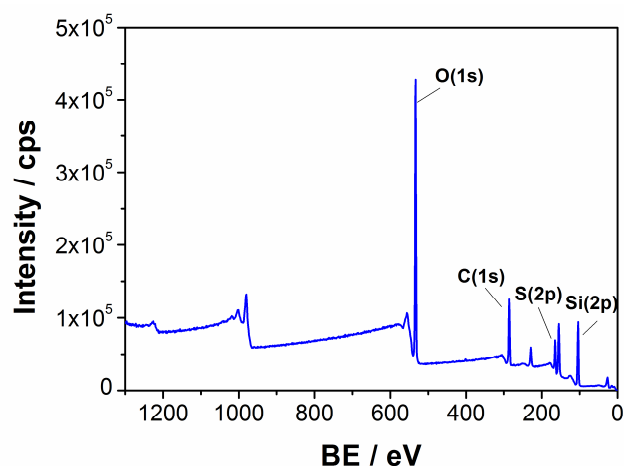


Figure 2.5: X-Ray Photoelectron Spectroscopy (XPS) survey of the LP-ssNPs. The scan showed the presence of O and Si corresponding to the silica framework but also C and S related to the organic linker.

Table 2.1: Elemental composition of the LP-ssNPs determined by XPS analysis:

Name	Peak BE	Atomic %
O1s	535.25	42.86
Si2p	106.74	23.77
C1s	288.03	27.69
S2p	167.16	5.68

Percentage of organic doping:

The ratio between organic/inorganic moieties was then characterized by thermogravimetric analysis (TGA; **Figure 2.6**). A significant weight loss of 23 % has been observed corresponding exclusively to the organic linker present in the framework of the particle.

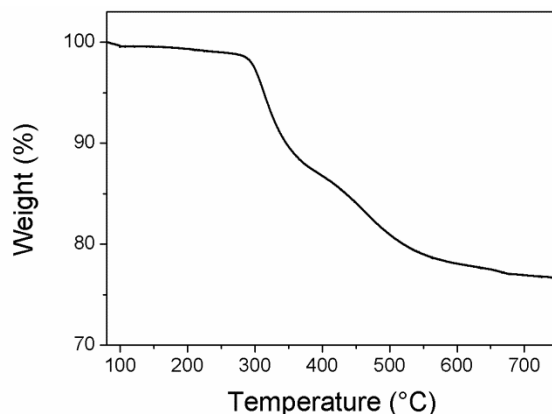


Figure 2.6: Thermogravimetric analysis (TGA) plot of LP-ssNPs presenting a weight loss a 23% corresponding to the organic linker.

Surface charge analysis:

ζ potential analysis was performed in order to verify the surface charge of the LP-ssNPs. As the charge of a molecule/particle varies depending on the pH, measurements have been done in a 2-(*N*-morpholino)ethanesulfonic acid (MES) buffer at pH 5.0. The choice of such buffer will be explained later in the discussion (part. 2.2.6.). The ζ potential value of the LP-ssNPs in MES buffer at pH 5.0 was found to be -22.4 ± 1.3 mV (**Figure 2.8.a**).

2.2.4 Breakability test of LP-ssNPs towards the presence of glutathione (GSH)

Once the particles were fully characterized, their response to reduced glutathione (GSH) was investigated in order to verify their breakability upon exposure to reducing agents, allowing for a selective disintegration of the particles within cancerous cells. GSH is in fact a thiol-containing tripeptide able to reduce disulfide bonds, present in the cytosol of cells at a concentration (2–10 mM), which is significantly higher than the one in the plasma (1–2 μ M).^[80]

A dispersion of LP-ssNPs, in PBS ($0.1 \text{ mg}\cdot\text{mL}^{-1}$, pH 7.4) was therefore stirred at 37 °C in the presence of GSH (10 mM) and aliquots of the suspension taken at several time points (up to 7 days) and analyzed by TEM. The images reported in **Figure 2.7** clearly show that the exposure to the reducing agent leads to the degradation of the nanoparticles upon exposure to GSH. Already after 3 days it was possible to observe a significant structural breakdown leading to a loss of the spherical morphology and the presence of small fragments after 7 days. As a control experiment, the same analysis was performed in the absence of GSH and after 7 days the particles mostly retained their morphology and only a few particles seemed to start degrading suggesting silica hydrolysis, known to occur in PBS (to a rate that generally depends on many and diverse parameters), starts to take place.^[53,81]

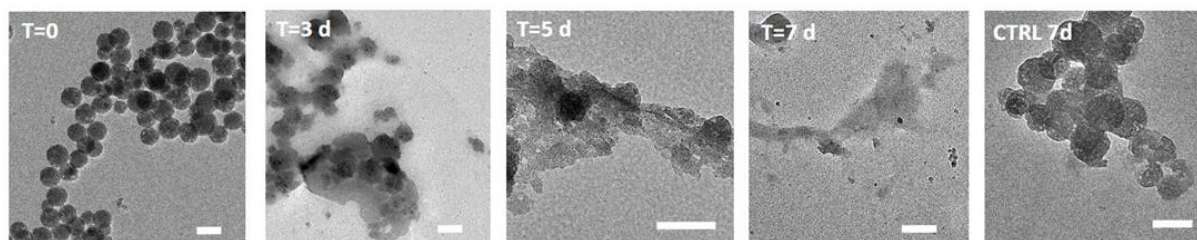


Figure 2.7: TEM analysis of a suspension of a) LP-ssNPs at $0.1 \text{ mg}\cdot\text{mL}^{-1}$, PBS, 37 °C undergoing GSH (10 mM) reduction (0-7 d). On the right side of the figure CTRL nanoparticles stirred in PBS for 7 days without GSH. Scale bar = 100 nm.

2.2.5 Surface functionalization of LP-ssNPs with 3-aminopropyltriethoxysilane (APTES)

As mentioned above, in order to achieve an efficient loading, the surface charge is critical. siRNA and oligonucleotides usually displays a highly negative charge, preventing then their electrostatic binding to the LP-ssNPs. For this reason, surface modification of the silica nanoparticles is required. As already said, the tuning of silica materials is relatively easy to achieve. To favor electrostatic interactions between the LP-ssNPs and the siRNA, primary amine groups were introduced on the interior and exterior of LP-ssNPs by using 3-aminopropyltriethoxysilane (APTES) through a post-synthetic grafting (NH₂-LP-ssNPs). Nevertheless, APTES creates a supplementary silica layer on the surface of the LP-ssNPs that might affect the breakability properties of the material. In this regard, the amount of such silanes is critical and demand further investigations. Thus, grafting with different amounts of APTES on LP-ssNPs was performed for comparison. 20 mg of LP-ssNPs were grafted with 5 μ L (NH₂-LP-ssNPs) and 10 μ L (NH₂-LP-ssNPs(10)) of APTES respectively. ζ potential measurements in PBS 7.4 resulted in values of -25, -1.7 and +8 mV for LP-ssNPs, NH₂-LP-ssNPs and NH₂-LP-ssNPs(10) respectively (**Figure 2.8.a**).

Scanning transmission electron microscopy (STEM) investigations showed that functionalization with 5 μ L of APTES appeared to be the best compromise for an efficient grafting of the oligonucleotide without preventing the breakability properties of the material. In fact, it is possible to observe that for particles grafted using higher quantities of APTES, the breakdown upon exposure to GSH occurred to be slower (**Figure 2.8.b**). TEM was then performed to have a better visualization of the destruction of the particles (**Figure 2.9**).

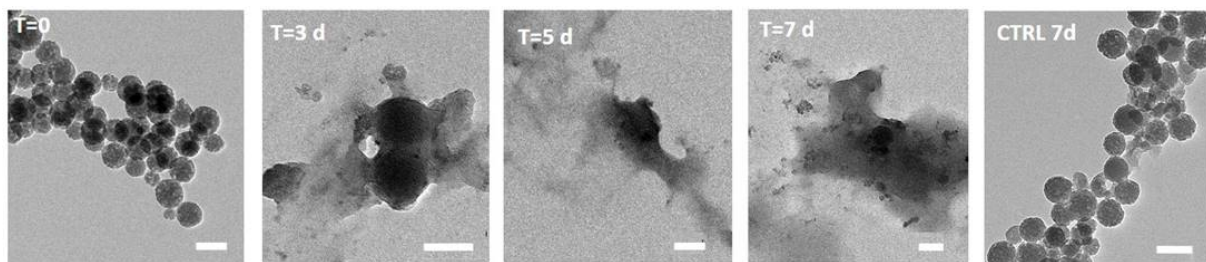


Figure 2.9: TEM analysis of a suspension of $\text{NH}_2\text{-LP-ssNPs}$ at $0.1 \text{ mg}\cdot\text{mL}^{-1}$, PBS, $37 \text{ }^\circ\text{C}$ undergoing GSH (10 mM) reduction (0-7 d). On the right side of the figure CTRL nanoparticles stirred in PBS for 7 days without GSH. Scale bar = 100 nm.

For further experiments, the introduction of the amino groups on $\text{NH}_2\text{-LP-ssNPs}$ was confirmed by ζ -potential measurements in MES buffer at pH 5.0 with a shift to a positive value of $26.6 \pm 3.2 \text{ mV}$ (**Figure 2.12.c**).

Quantification of primary amino groups on the surface was performed by Kaiser test, a colorimetric assay widely used for proteins^[82] but also applicable for nanoparticles in some cases.^[83,84] Upon reaction with a primary amine, ninhydrin converts into an adduct (2-[(3-hydroxy-1-oxo-1H-inden-2-yl)imino]-1H-indene-1,3(2H)) characterized by an absorption band centered at 570 nm.^[82,85] The formation of this adduct was obtained dispersing the particles in a solution of ninhydrin heating up to $80 \text{ }^\circ\text{C}$. Once the product was cooled down and centrifuged, the supernatant was collected and the absorption was recorded. In this way, we were able to estimate the amount of amino groups on the particles as $26 \text{ } \mu\text{mol}/\text{mg}$.

2.2.6 siRNA loading and jetPEI covering of LP-ssNPs

The LP-ssNPs were then loaded with a double stranded polo-like kinase 1 (PLK1) specific siRNA (PLK1@ $\text{NH}_2\text{-LP-ssNPs}$). As mentioned above, the choice of this particular siRNA was dictated by its ability to silence the gene expressing the PLK1 protein, which is an interesting target for cancer therapy.^[9]

PLK proteins are a family of serine/threonine kinase, able to phosphorylate different proteins or different sites of the same protein. The phosphorylation, as well as proteolysis, regulates the cell cycle progression. More precisely, the PLK1 phosphorylates the mitotic kinesin-like protein 1 regulating cytoplasmic separation and membrane formation during the telophase.^[86] These important properties, combined with the knowledge that cancer cells proliferates very fast, led to the discovery of the high expression of PLK1 in primary tumor tissues compare to healthy tissues.^[87] Sun W. *et al.* demonstrated the high expression of PLK1 in hepatocellular carcinomas. Moreover, they demonstrated that the PLK1 expression was

associated with the HCC development. Further studies showed also that the tumor suppressor protein p53 is phosphorylated by PLK1, and therefore can inhibit its proapoptotic function. PLK1 knockdown induces then a slower cell proliferation but also promote p53 expression, contributing then to the cell cycle arrest and finally cell apoptosis (**Figure 2.10**).^[66,88]

To knockdown PLK1 expression, specific sequences of double-stranded siRNA can be delivered within the cells thanks to delivery systems such as nanoparticles.^[89] Therefore, in order to clearly assess both the efficacy of the anti-PLK1 siRNA and the beneficial effect of using large pore particles, we decided to perform for our biological investigations control experiments using also NH₂-LP-ssNPs loaded with a non-specific double stranded siRNA (Control) and showing no silencing activity on genes present in hepatocellular carcinoma cells (Control@NH₂-LP-ssNPs) and small pore ssNPs loaded with PLK1 siRNA (PLK1@NH₂-ssNPs). The different sequences employed can be found in **Table 2.2**.

Table 2.2: siRNA sequences

siRNA name	Sequence (5' → 3')
PLK1-fwd	AGA-UCA-CCC-UCC-UUA-AAU-AUU
PLK1-rev	UAU-UUA-AGG-AGG-GUG-AUC-UUU
CtrlNeg-fwd	AUG-UCU-ACU-GGC-AGU-CCU-G99
CtrlNeg-rev	CAG-GAC-UGC-CAG-UAG-ACA-U99

The loading experiments were performed shaking a dispersion of nanoparticles ($c = 0.1 \text{ mg}\cdot\text{mL}^{-1}$) in MES buffer (pH = 5.0) overnight in the presence of siRNA (concentration range from 10 to 200 $\mu\text{g}\cdot\text{mL}^{-1}$). MES buffer at pH 5.0 was chosen in order to ensure the protonation of the primary amino groups and therefore a favored adsorption of siRNA to the carrier.

The nanoparticles were then recovered by centrifugation and the supernatant analyzed by means of UV-Vis absorption spectroscopy to quantify the non-physioadsorbed siRNA and, subsequently, the oligonucleotide loading. A calibration curve was made using the absorbance at 260 nm, in correspondence of the maximum intensity of the siRNA (**Figure 2.11.a and b**) and the collected supernatants was finally measured (**Figure 2.11.c**). The loaded siRNA was calculated to reach a maximum of 182 $\mu\text{g}\cdot\text{mg}^{-1}$ for NH₂-LP-ssNPs and only 25 μg of siRNA per mg for small pore NH₂-ssNPs (**Figure 2.11.c and d**).

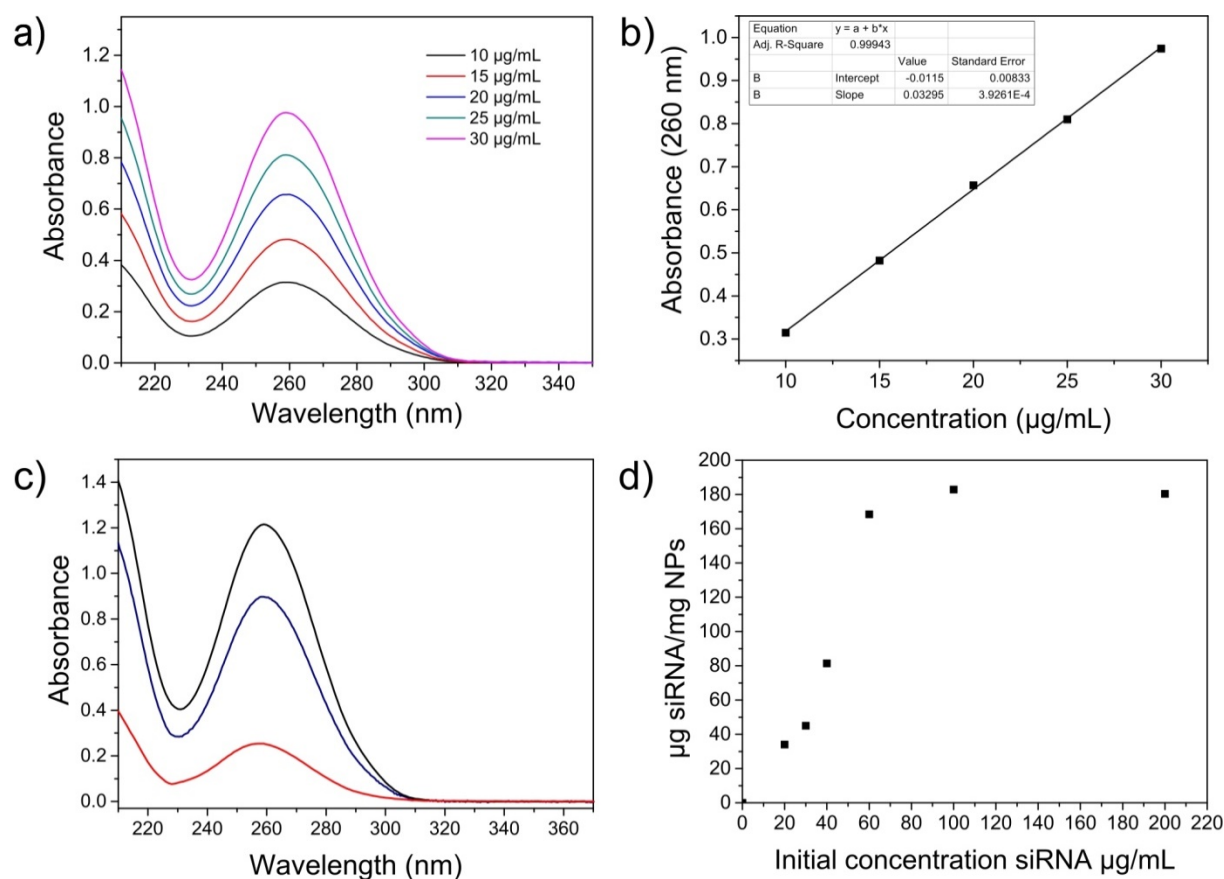


Figure 2.11: Loading of PLK1 siRNA on the surface of NH₂-LP-ssNPs. a) UV-Vis spectra of different concentrations of the PLK1 siRNA in MES buffer (pH 5), b) Calibration curve plot for the PLK1 siRNA in MES buffer pH 5.0 ($R^2 = 0.99943$). c) Adsorption spectra of the supernatants collected after centrifuging particles incubated with the PLK1 siRNA in the following conditions: 0.5 mg·mL⁻¹ of particles incubated with 200 μg·mL⁻¹ of siRNA incubated overnight at r.t. Reference of PLK1 siRNA at a concentration of 40 μg·mL⁻¹ (black curve), supernatant of jp-PLK1@NH₂-ssNPs (blue) and supernatant of jp-PLK1@NH₂-LP-ssNPs (red). d) Loading achieved after incubation of different concentration of siRNA with NH₂-LP-ssNPs. The initial concentration of particles was 0.1 mg·mL⁻¹.

The efficient adsorption of siRNA, was also proven by dynamic light scattering (DLS) measurements on the loaded particles showing an increase of NH₂-LP-ssNPs hydrodynamic diameter (D_h) of 10 nm (Figure 2.12.b), consistent with the loading of siRNA that possess a large molecule structure of 2 x 8 nm.^[36] Further confirmation was provided by the drop of surface charge down to -24.0 ± 3.9 mV determined by ζ -potential in MES buffer at pH 5.0 after the incubation (Figure 2.12.c).

The last step in the preparation of our carrier was the coating with jetPEI[®] in order to prevent degradation of the oligonucleotide by nucleases. The presence of the positive charge also enhances the cellular uptake of the cargo into the cells. In addition, it has been reported that, once internalized into the endosomes, the polycation is able to induce a series of cellular events that leads to the opening of the polymeric network and release the siRNA. In fact, once

in the endosomes, the jetPEI[®] acts as a proton sponge, altering the osmolarity of the vesicles and inhibiting the lysosomal nucleases.^[90] The accumulation of protons within the endosomes induces an influx of chloride anions, resulting in an osmotic swelling of the vesicles,^[91] and to the protonation of the jetPEI[®], creating an internal charge repulsion, opening the polymeric network. These combined effects reduce the endosomal life and allow for the release of the siRNA into the cytoplasm. However, recent studies performed by Vermeulen *et al.* showed that this phenomenon depends highly on the cell type. By using the jetPEI[®] as a transfection reagent, they demonstrated that the endosomal escape depends on the size of the endosomes produced by the cells.^[92] For instance, a cell line that would present a high transfection efficiency would not necessary show a high endosomal escape and vice versa.

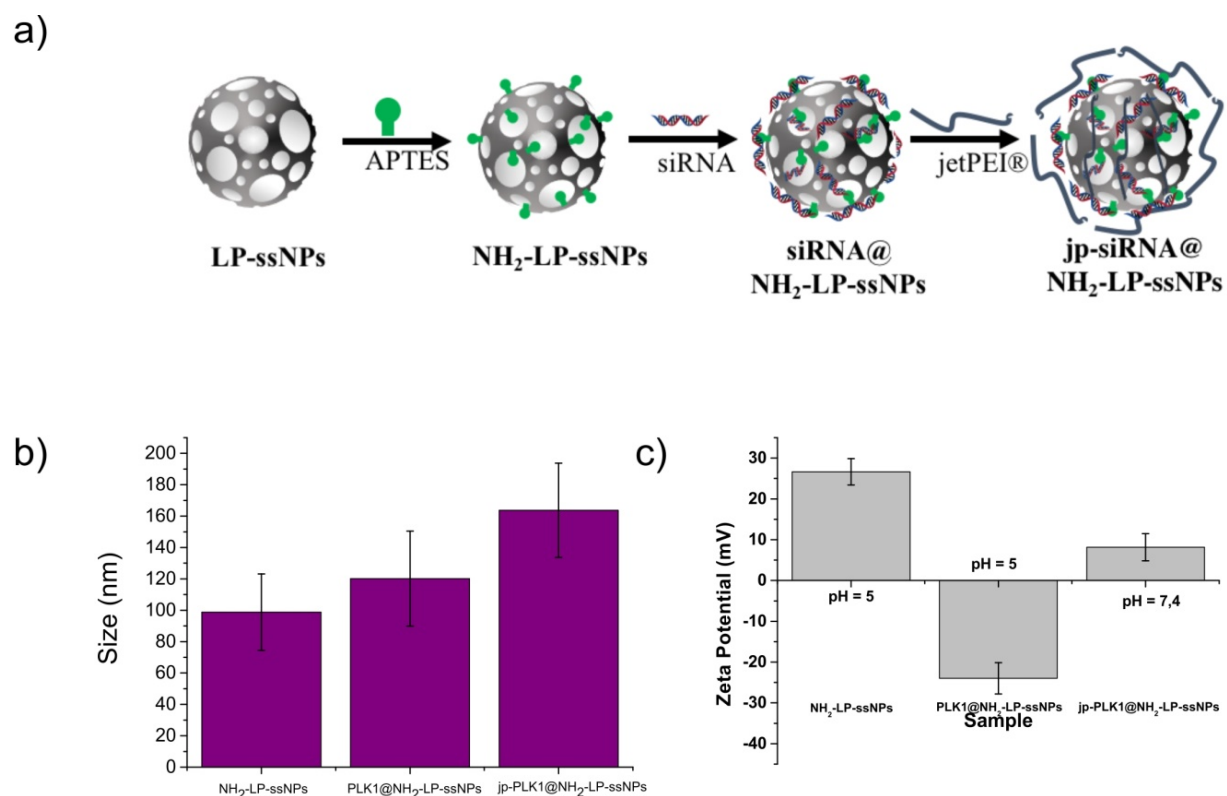


Figure 2.12: a) Schematic representation of the different coating steps leading to the final material. b) Dynamic light scattering and c) Zeta Potential measurements proving the grafting of the different layer on the surface of the LP-ssNPs.

In our case, after incubation with the siRNA and centrifugation, the particles were dispersed in 890 μL of MES buffer pH 5 before the addition of 110 μL of a jetPEI[®] solution ($0.2 \text{ mg}\cdot\text{mL}^{-1}$). After 1h incubation, the jp-siRNA@NH₂-LP-ssNPs were centrifuged and re-suspended in PBS pH 7.4. The presence of jetPEI[®] around the loaded nanoparticles was proven both by the increase of D_h of ca. 40 nm for the coated nanoparticles ($163 \pm 30 \text{ nm}$,

Figure 2.12.b) revealed by DLS and by the positive surface charge corresponding to 8.15 ± 3.32 mV as determined by ζ -potential measurements (**Figure 2.12.c**). A schematic representation of the final material is depicted in **Figure 2.12.a**.

2.3 *In vitro* behavior of LP-ssNPs

2.3.1 Cytotoxicity

The cytotoxicity of the materials is usually one of the first studies to perform to prove its biocompatibility and its ability to deliver safely a molecule of interest. Even though the biocompatibility of silica nanoparticles in general has been proved by many groups,^[27,53] slight modification in the synthesis, such as the insertion within the framework of new moieties, raises new questions about their cytotoxicity. In this regard, the hepatocellular carcinoma Huh-7 cells were incubated with LP-ssNPs, NH₂-LP-ssNPs and jp-PLK1@NH₂-LP-ssNPs at 3 different concentrations (50, 100 and 150 $\mu\text{g}\cdot\text{mL}^{-1}$) and the cell activity was evaluated by an Alamar blue assay, an assay often used in biology to determine the metabolic activity. After 72 h, no cytotoxicity was observed in the entire range of concentrations tested for the LP-ssNPs and NH₂-LP-ssNPs as shown in **Figure 2.13**. Cytotoxicity of jp-PLK1@NH₂-LP-ssNPs was also carried on to prove the efficient release and toxicity of the PLK1 siRNA. In this case, the metabolic activity of the cells has been reduced to 70 %, due to the cytotoxic siRNA, demonstrating the efficient release of the biomolecule.

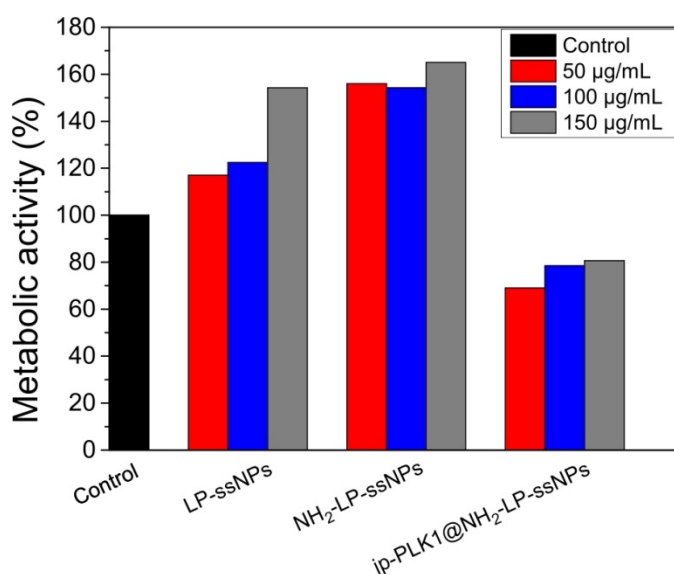


Figure 2.13: Metabolic activity of Huh-7 cells after incubation for 72 h with different concentrations of LP-ssNPs.

2.3.2 Rhodamine B grafting on LP-ssNPs for cellular uptake studies

The capacity of nanoparticles to penetrate efficiently the cell membrane is crucial. Their efficient transfection can be followed by confocal laser scanning microscopy (CLSM) or fluorescence-activated cell sorting (FACS) analysis based on dyes attached to the nanoparticles. The use of Rhodamine B isothiocyanate for this purpose has been chosen because of the quick reaction between the amino group on the NH_2 -LP-ssNPs and the isothiocyanate group present on the dye. Moreover, this fluorescent molecule will not overlap with the emission spectrum of the dyes used to stain the cells afterwards. The NH_2 -LP-ssNPs were stirred for 3 h at r.t. in the dark in presence of Rhodamine B isothiocyanate. Once the reaction was over, the particles were centrifuged and thoroughly rinsed to remove the unreacted dye giving pink nanoparticles (*r*-LP-ssNPs). The efficient functionalization was then proved by recording the fluorescence spectrum before and after loading with the siRNA (*r*-LP-ssNPs and jp-PLK1@*r*-LP-ssNPs). As observed on **Figure 2.14**, both excitation and emission properties did not change after the grafting of the dye on the surface of the nanoparticles and after the loading with the siRNA.

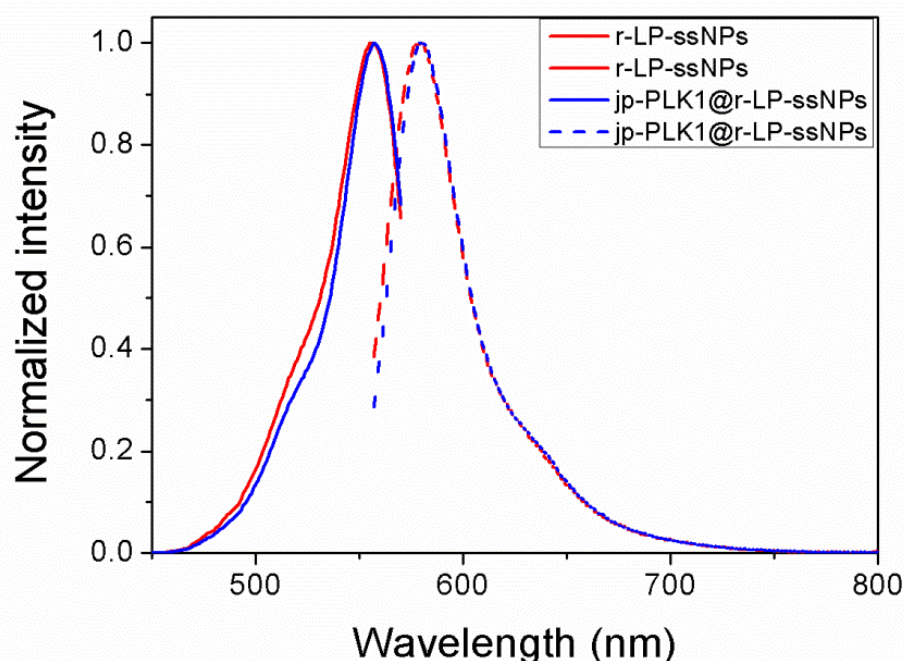


Figure 2.14: Excitation (solid lines) and emission spectra (dashed lines) of *r*-LP-ssNPs (red) and jp-PLK1@*r*-LP-ssNPs (blue). $\lambda_{\text{exc}} = 547 \text{ nm}$ $\lambda_{\text{em}} = 580 \text{ nm}$.

2.3.3 FACS analysis

The cellular association of the NH₂-LP-ssNPs was quantified by fluorescence-activated cell sorting (FACS) analysis. The Huh-7 cells were then incubated with 50 μg and 100 μg·mL⁻¹ suspensions of *r*-LP-ssNPs and jp-PLK1@NH₂-LP-ssNPs in a Dulbecco complete culture medium for 3, 24 and 48 h. FACS analysis showed an efficient cellular uptake after 3 h increasing overtime. As shown in **Figure 2.15.a**, the mean fluorescence intensity (MFI) of the Rhodamine B grafted on the particles increased significantly with the increasing incubation time (3 to 48 h) and concentration (50 μg and 100 μg·mL⁻¹) proving a continuous uptake of the *r*-LP-ssNPs within the Huh-7 cells with almost 100 % positive cells after 3 h incubation (**Figure 2.15.b**). For jp-PLK1@NH₂-LP-ssNPs, FACS analysis shows a similar MFI after 3 h incubation demonstrating a same kinetic of internalization of the particles. However, after 24 and 48 h, the intensity decreased drastically, probably due to the efficient uptake of the particles within the cells and an efficient delivery of the siRNA leading to apoptosis of the cancer cells. The washing and fixation steps would have therefore removed all the dead cells and debris and might have not been analyzed by the FACS. This result encourages the efficient delivery and the cytotoxic effect of the PLK1 siRNA within the cells (**Figure 2.15.a**). However, such technique gives only information if weather or not there is the presence of the nanoparticles on the cells, thanks to the Rhodamine B signal, but is however unable to determine if the particles is just deposited on the cell surfaces or if it really penetrated the cell membrane. A better understanding of the cellular uptake can therefore be done using confocal microscopy.

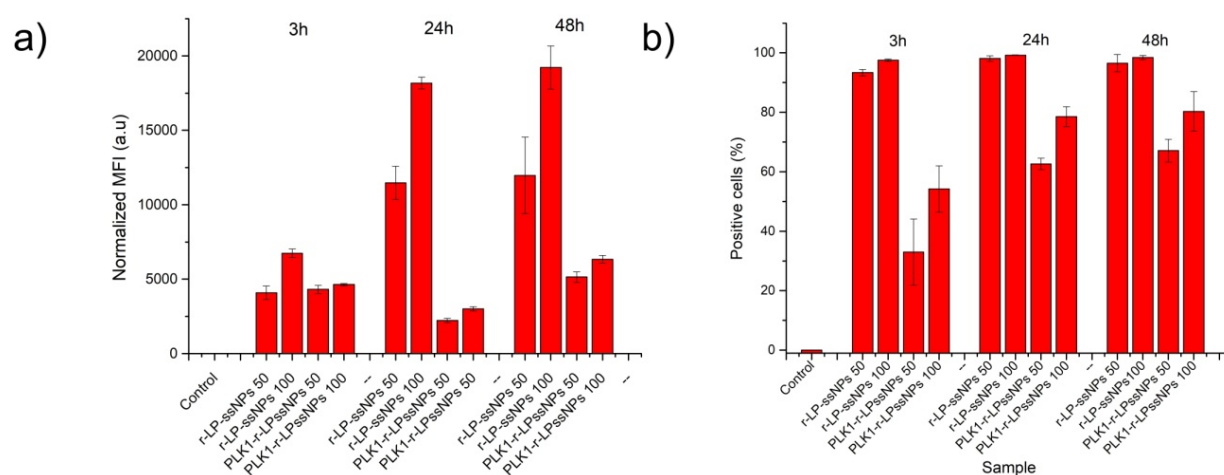


Figure 2.15: FACS analysis after 3, 24 and 48 h incubation with *r*-LP-ssNPs at 50 and 100 μg·mL⁻¹ with a) the mean fluorescence intensity and b) the percentage of positive cells.

2.3.4 Cellular uptake followed by confocal microscopy

Confocal laser scanning microscopy (CLSM) analysis was performed on the cancerous cells incubated with *r*-NH₂-LP-ssNPs (50 μg·mL⁻¹) to prove the occurred internalization (**Figure 2.16.a**). In agreement with FACS data, a good uptake is shown already after the first 3 h of incubation, clearly increasing over time as it can be observed by the increasing red signal. However, here again, a 2D image does not allow to determine if the nanoparticles are on the surface or within the cell. Confocal microscopy gives also the opportunity to perform 3D images by taking 2D pictures at different Z positions (called Z-stacking). The Z-stacking analysis on cells incubated for 24 h (**Figure 2.16.b**) and recorded after staining the f-actin with Alexa Fluor[®] 647 Phalloidin demonstrated that the nanoparticles are internalized inside the cells as it can be observed by the diffusion of the red signal on the y-z and x-z axes.

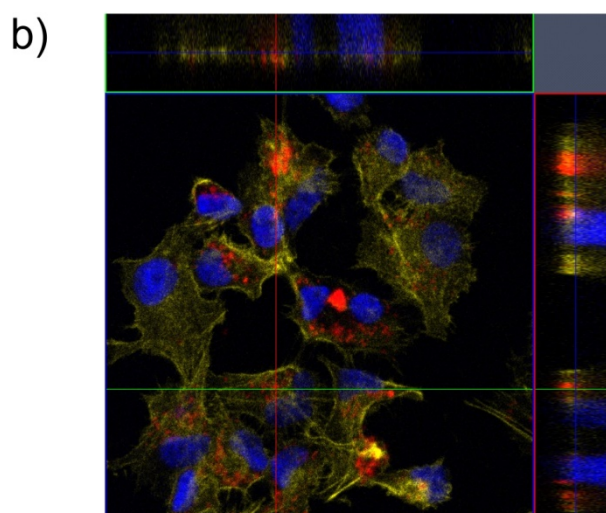
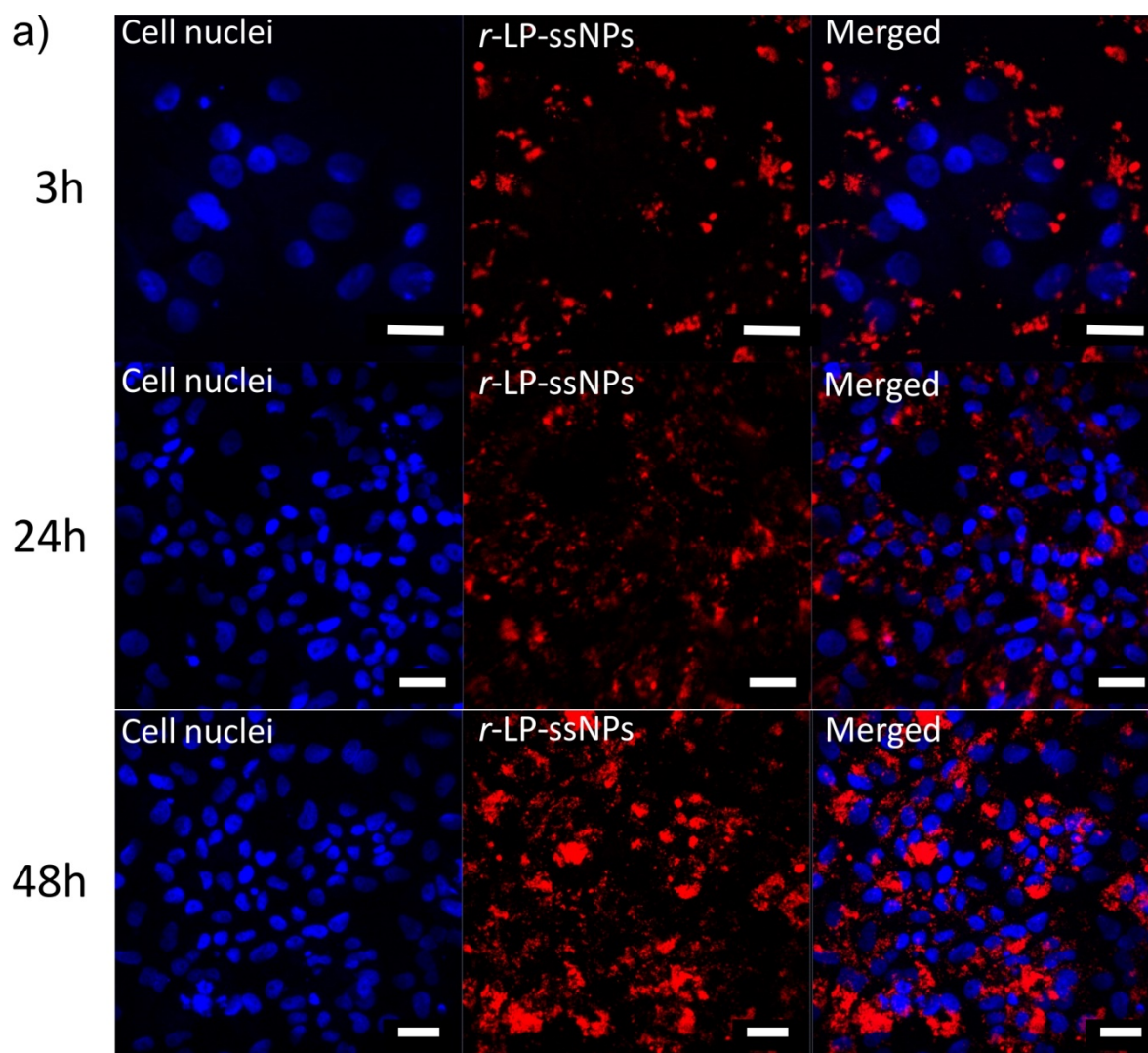


Figure 2.16: a) Confocal images taken after 3, 24 and 48 h of incubation with the *r*-LP-ssNPs ($50 \mu\text{g}\cdot\text{mL}^{-1}$). Cell nuclei were stained with Hoechst 33342 (blue signal). The images on the right correspond to the merged signal. b) Z-stacking image of cells incubated for 24 h with *r*-LP-ssNPs ($50 \mu\text{g}\cdot\text{mL}^{-1}$). The cell nuclei were stained with Hoechst 33342 (blue channel), f-actin was stained with Alexa Fluor[®] Phalloidin 647 (yellow channel). Excitation wavelengths are 355, 488 and 633 nm for Hoechst 33342, Rhodamine B, and Alexa Fluor[®] 647 Phalloidin, respectively. Scale bars = 20 μm .

2.3.5 Lysosomes co-localization

Several mechanisms for the uptake of materials have been discovered. Each of these pathways involves the formation of different vesicles leading to the final lysosomes. Colocalization of the nanoparticles with lysosomes would also prove an efficient uptake and therefore, the possibility to release within the cell, the cargo. In this regard, co-localization studies using the lysosome-specific fluorescent marker Lysotracker[®] Blue DND-22 were also carried out to gain insight on the localization of the internalized particles within the cells. As shown in **Figure 2.17**, after 24 h of incubation the *r*-NH₂-LP-ssNPs were mostly localized into lysosomes, indicating that the internalization of the nanoparticles occurs through a classical endocytosis process (overlapping coefficient of 0.62).^[93] The release of the material within the cytoplasm could be therefore improved by using specific agents improving endosomal escape. The use of polymers, such as for instance, PEI, present interesting endosomal disruption properties. On the other side, the use of specific protein as Sticholysin II could also be a way to obtain an improved endosomal escape (2.2.6).^[94]

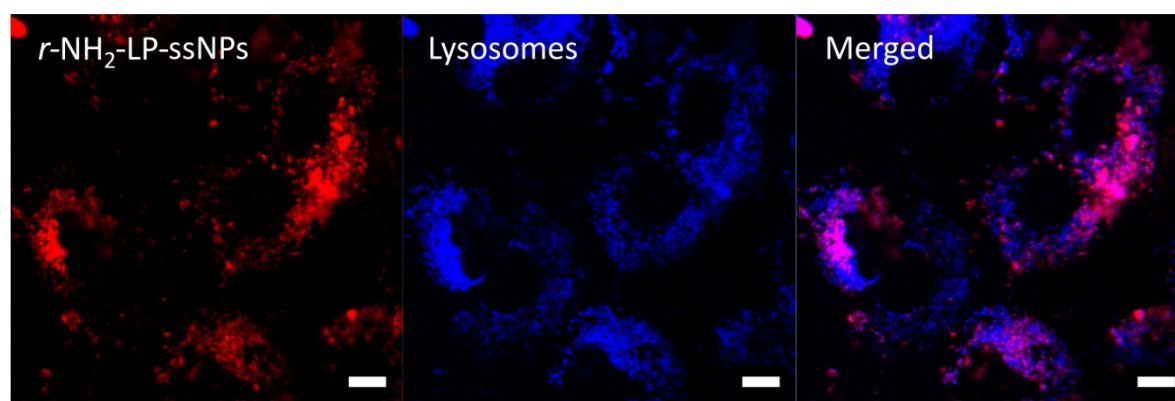


Figure 2.17: Confocal images taken on Huh-7 cells after 24 h of incubation with *r*-NH₂-LP-ssNPs (50 $\mu\text{g}\cdot\text{mL}^{-1}$). Colocalization experiments with Lysotracker[®] Blue DND-22 revealed the sub-localization of particles in lysosomes area (overlap coefficient 0.62). Red channel: Rhodamine B; blue channel: Lysotracker[®]. $\lambda_{\text{exc}} = 405$ and 488 nm for Lysotracker[®] Blue DND-22 and Rhodamine B, respectively. Scale bars = 20 μm .

2.3.6 Uptake and degradability determined by means of TEM

To confirm and to investigate the fate and degradation of the nanoparticles within the tumor cells, TEM analysis was conducted on cells incubated with the nanoparticles (**Figure 2.18**). After 3 h incubation, the particles were mainly localized into early endosomes, first step of clathrin-dependent endocytosis.^[93,95] Whereas after 24 h, the nanoparticles were mostly present within lysosomes and their partial degradation already occurred, most

probably triggered by the high intracellular concentration of GSH as we recently demonstrated for ssNPs.^[55] The decrease of contrast in the imaged nanoparticles and the loss of spherical morphology for those in a more advanced degradation phase clearly demonstrated the occurring dissolution. After 48 h incubation, a more extensive degradation could be imaged, indicating that already an efficient release of the PLK1 siRNA may be achieved.

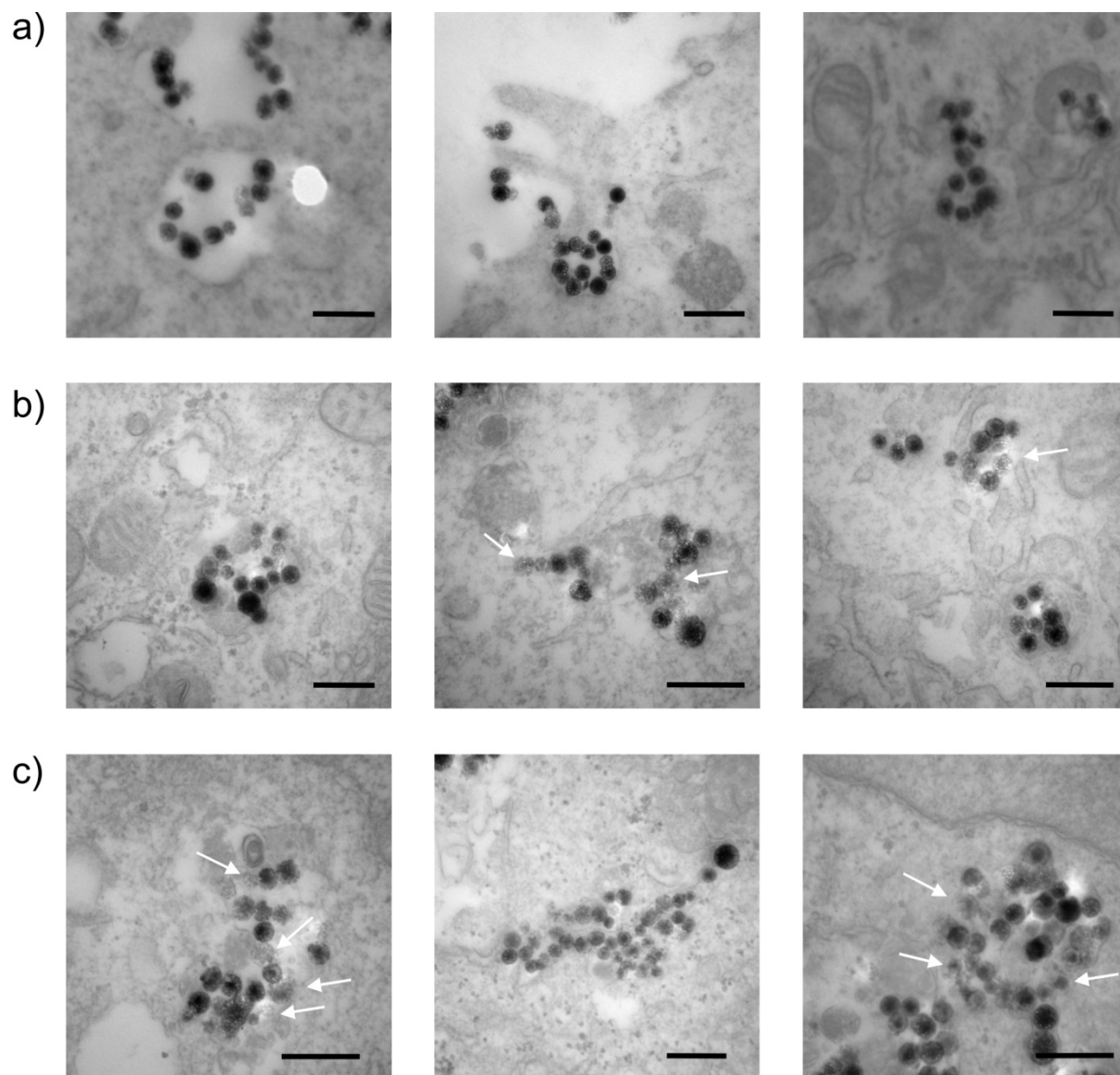


Figure 2.18: TEM analysis of Huh-7 cells incubated with LP-ssNPs at a concentration of $50 \mu\text{g}\cdot\text{mL}^{-1}$ for a) 3h, b) 24h and c) 48h. Scale bar = 500 nm.

2.3.7 Delivery and release of siRNA

The delivery and release of PLK1 siRNA were investigated by CLSM analysis. Cyanine-5 labelled PLK1 siRNA was used in order to track the oligonucleotide within the

cell. The labelling was performed by using Cy5Label IT[®] siRNA Tracker Intracellular Localization Kit. The cells were then incubated with the *r*-LP-ssNPs loaded with Cy5-labelled PLK1 siRNA and coated with jetPEI[®] for 3 h and then washed with PBS. After cell nuclei staining with Hoechst 33342, the confocal analysis on the cells (**Figure 2.19**) showed an intense red signal coming from the *r*-LP-ssNPs within the cells proving their efficient internalization. Moreover, the green signal, corresponding to the labelled PLK1 siRNA on the surface of the particles, show also a high intensity mostly co-localized with the red signal of the particles. However, the picture shows also a diffusion of the green signal within the cells, proving the efficient release of the siRNA within the cancer cells.

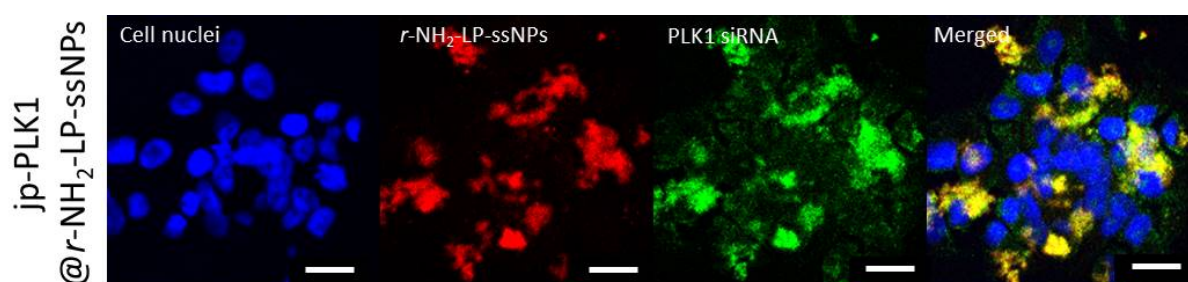


Figure 2.19: Cellular uptake of jp-PLK1@*r*-NH₂-LP-ssNPs. Confocal images were taken after 3 h of incubation with the particles. Cell nuclei were stained with Hoechst 33342 (blue) and the particles were doped with Rhodamine B (red). PLK1 siRNA were coupled to a Cyanine 5 dye (green) with a Cy5Label IT[®] siRNA Tracker Intracellular Localization Kit (Mirus) and grafted on the particles. The right images correspond to the merge signal. Excitation wavelengths are 355, 488 and 633 nm. Scale bar = 20 μm.

2.4 *In vivo* efficacy of jp-PLK1@NH₂-LP-ssNPs.

2.4.1 1st experiment

In a first series of experiments, the efficacy of jp-PLK1@NH₂-LP-ssNPs nanoparticles was evaluated in NMRI-Nude mice bearing subcutaneous Huh-7-Luc tumors. Six intratumoral injections of jp-PLK1@NH₂-LP-ssNPs were performed at day 0 (d₀) and after 1, 3, 6, 8 and 10 days and the tumor growth was monitored by bioluminescence imaging. The median tumor size showed a 2.4-fold increase in the vehicle-injected control group. A non-specific decrease of the median tumor size (32% of decrease, as compared with the initial median size) was observed in jp-control@NH₂-LP-ssNPs-treated group while > 95% decrease of median tumor size was observed in the jp-PLK1@NH₂-LP-ssNPs-treated group (**Figure 2.20**), indicating jp-PLK1@NH₂-LP-ssNPs were able to efficiently provide a potent anti-tumor effect.

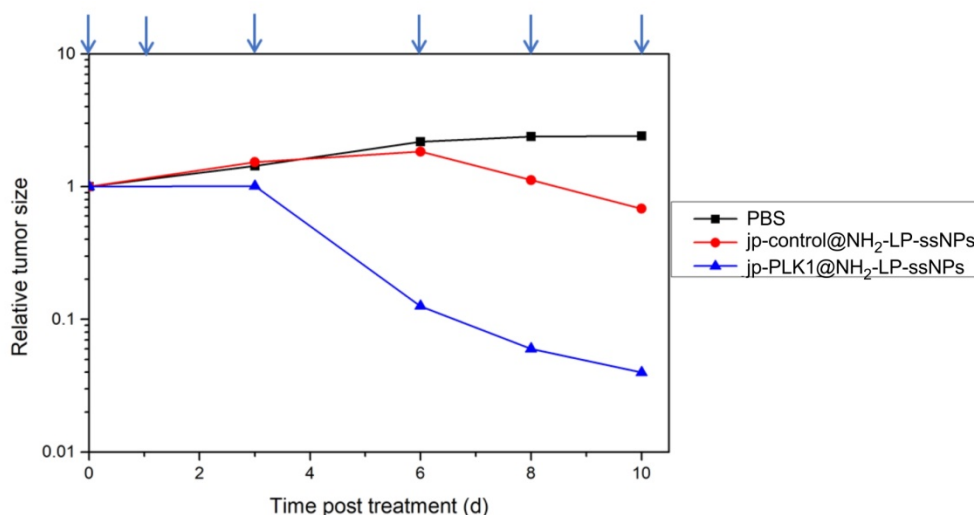


Figure 2.20: Anti-tumor activity jp-PLK1@NH₂-LP-ssNPs in subcutaneous Huh-7 tumors. NMRI-Nude mice bearing subcutaneous luciferase-expressing Huh-7 tumors were injected at the indicated time points (arrows) with vehicle (PBS), jp-control@NH₂-LP-ssNPs or jp-PLK1@NH₂-LP-ssNPs. Tumor sizes, monitored by *in vivo* bioluminescence, are normalized at each time point to the initial value at day 0.

2.4.2 2nd experiment

To analyze the *in vivo* tumor suppression efficacy of our LP-ssNPs-based siPLK1-delivery system, we performed intra-tumoral injections^[96,97] (twice per week, 10 μg of siRNA per mouse) of jp-siRNA@NH₂-LP-ssNPs in orthotopic tumors of Huh7-derived xenograft mouse model as described in the method section. Treatments with jp-PLK1@NH₂-LP-ssNPs were initiated when the average tumor volume reached 15-100 mm³ and the tumor growth was monitored at day 2, 5, 7, and 9 post treatments. As expected, we found that jp-control@NH₂-LP-ssNPs did not affect tumor growth while jp-PLK1@NH₂-LP-ssNPs significantly reduced the tumor volume compared to the controls (**Figure 2.21**) confirming that PLK1 siRNA was efficiently released from the particles targeting Huh 7 cells.

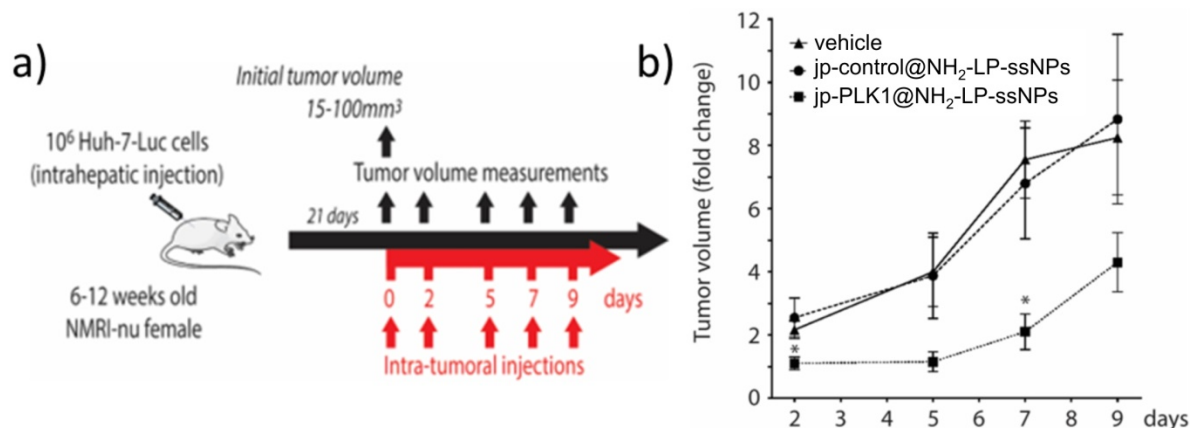


Figure 2.21: Intratumoral injection of jp-PLK1@NH₂-LP-ssNPs significantly reduces tumor growth in a cell-based xenograft mouse model. a) Scheme showing the experimental workflow. b) jp-siRNA@NH₂-LP-ssNPs reduced and delayed the onset of tumor growth. Huh-7-Luc cells were orthotopically injected into the liver of NMRI-nu mice and tumor growth was monitored by bioluminescence imaging. Once the tumor volume reached $15-100\text{mm}^3$, vehicle (n=5), jp-control@NH₂-LP-ssNPs (n=4), or jp-PLK1@NH₂-LP-ssNPs (n=4) were intra-tumorally injected and the tumor size was measured at days 0, 2, 5, 7, and 9. Results (mean \pm s.e.m.) are reported as the tumor volume relative to the initial size. * $p < 0.05$ Fisher's t-test.

2.4.3 Blood analyses

Some hepatic markers as Albumin, Bilirubin, Alanine aminotransferase (ALAT) and Aspartate aminotransferase (ASAT) are suitable markers to diagnose liver abnormality. Therefore, blood samples were taken before and after the treatment to compare whether or not the injections of materials induce a hepatic response. **Figure 2.22 and 2.23** represent the different analyses and their respective increased after treatment. Albumin is the most abundant protein produced by the liver and thus a low concentration corresponds usually to a deficiency induced by chronic diseases.^[98] As shown in **Figure 2.22.a**, the concentration in albumin slightly increased from 25 g/L to 26 g/L after treatment for each group. Bilirubin, molecule resulting from the degradation of hemoglobin, is insoluble in water and is usually conjugated with glucuronic acid in the liver before excretion by the urines. High level of bilirubin could correspond to a liver malfunction since degradation and solubilization within the urines does not occur. The concentration of bilirubin before and after treatment is represented in **Figure 2.22.b**. This time, an increase has been observed for each group, ranging from 20 (for jp-PLK1@NH₂-LP-ssNPs) to 40 % (Vehicle) depending on the group, suggesting an efficient treatment with the PLK1 siRNA. ASAT and ALAT are enzymes associated to liver cells. High ASAT levels are generally related to health issue, but the origin cannot be determined since ASAT enzymes are present in the liver, the heart, the muscles... ALAT, on the opposite, is a specific marker since it is produced and located only in the liver.

As observed in **Figure 2.22.c and d**, both ALAT and ASAT concentrations increased after the treatment with the nanoparticles. The concentration of ASAT increased of around 2.5 fold compared to the ALAT (1.4 fold).

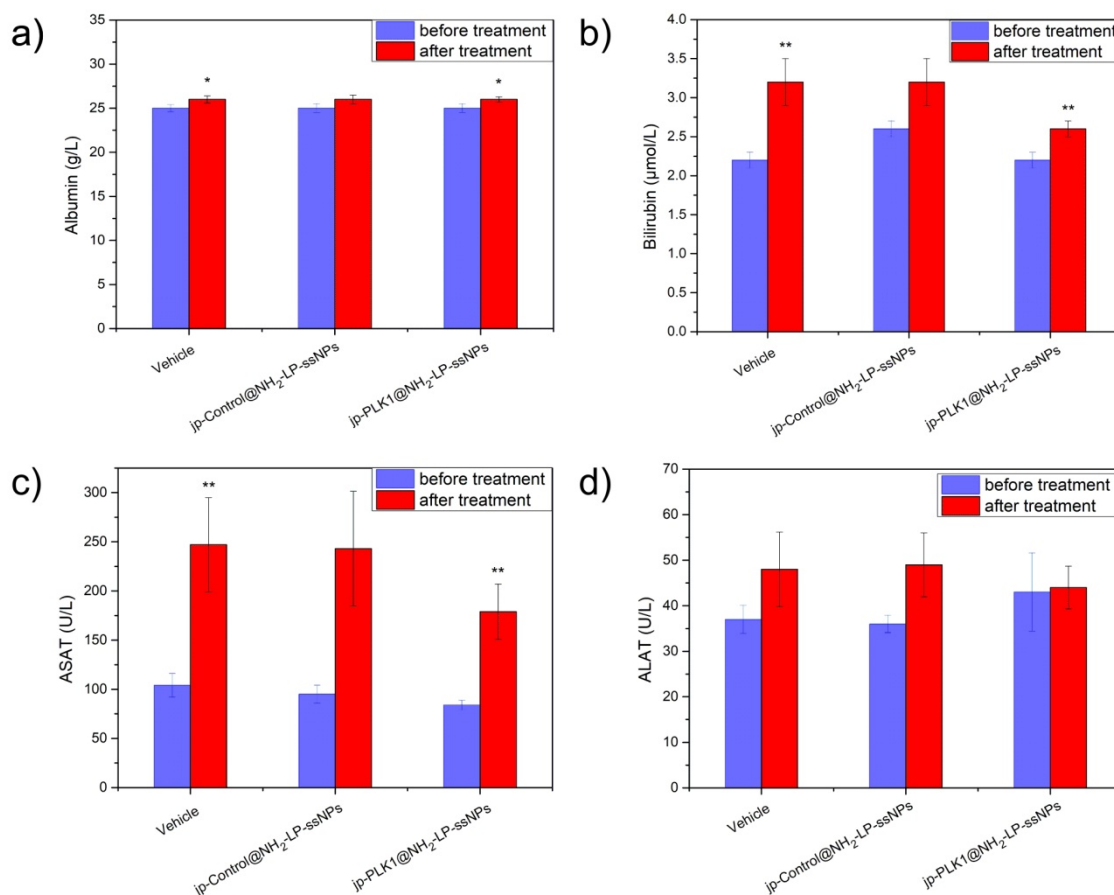


Figure 2.22: Concentrations of the different hepatic markers before and after treatment with PBS (vehicle), jp-control@NH₂-LP-ssNPs and jp-PLK1@NH₂-LP-ssNPs. a) Albumin (g/L), b) Bilirubin (μmol/L), c) ASAT (U/L) and d) ALAT (U/L).

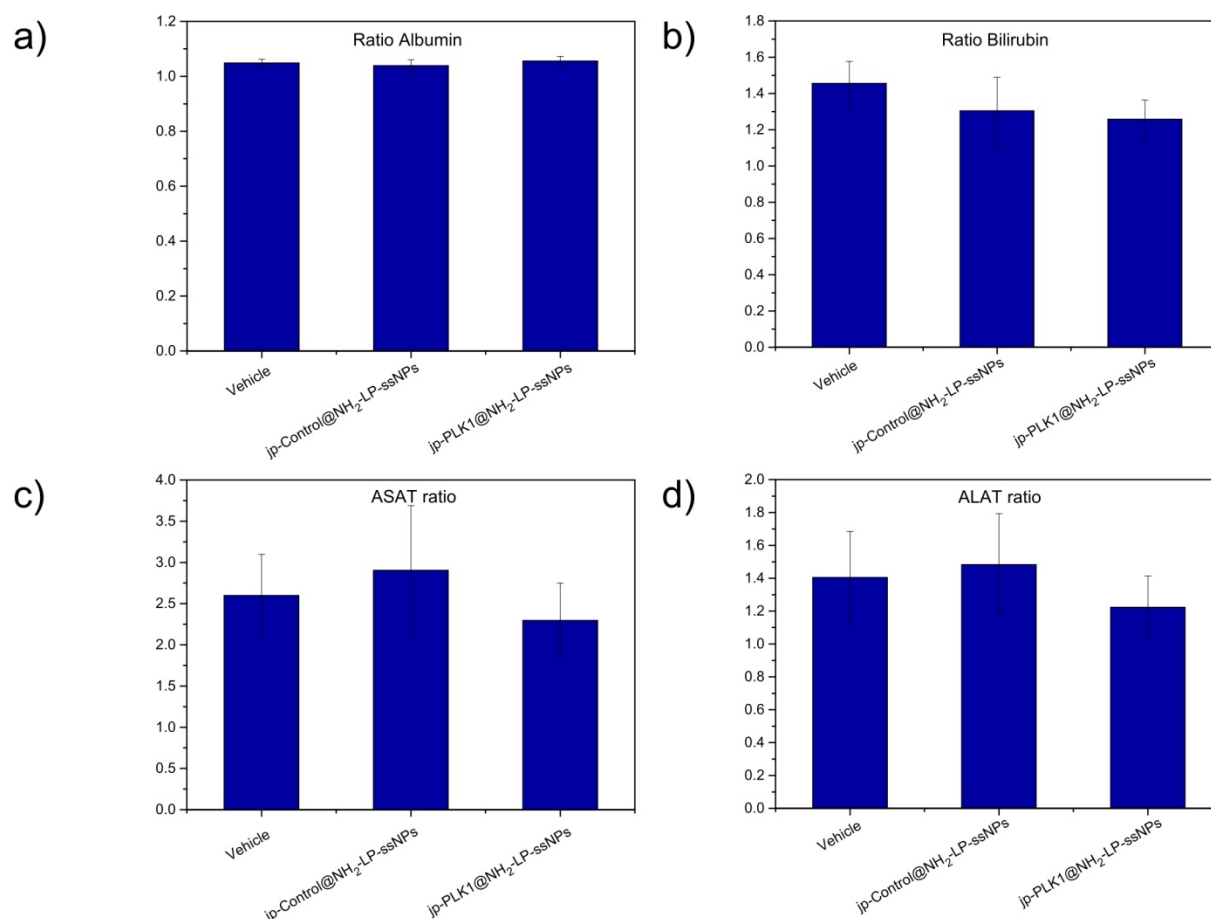


Figure 2.23: Ratio calculated from the concentrations obtained before and after the treatment with PBS, jp-control@NH₂-LP-ssNPs and jp-PLK1@NH₂-LP-ssNPs. a) Albumin (g/L), b) Bilirubin ($\mu\text{mol/L}$), c) ASAT (U/L) and d) ALAT (U/L).

However, the ratio between ASAT and ALAT, so called the De Ritis ratio, is the one determining if whether or not there are hepatic issues.^[99] This ratio is typically between 0.5 and 0.7 and increases in case of issues. As shown in **Figure 2.24**, with orthotopic tumors of Huh-7-derived xenograft mouse model, the De Ritis ratio increases to 2.81, 2.63 and 1.95 before the injection of PBS, jp-control@NH₂-LP-ssNPs and jp-PLK1@NH₂-LP-ssNPs respectively. After the treatment, and with the growth of the tumor, those ratios increase to 5.14, 4.95 and 4.06 respectively, probably due to the growing of the tumor over time.

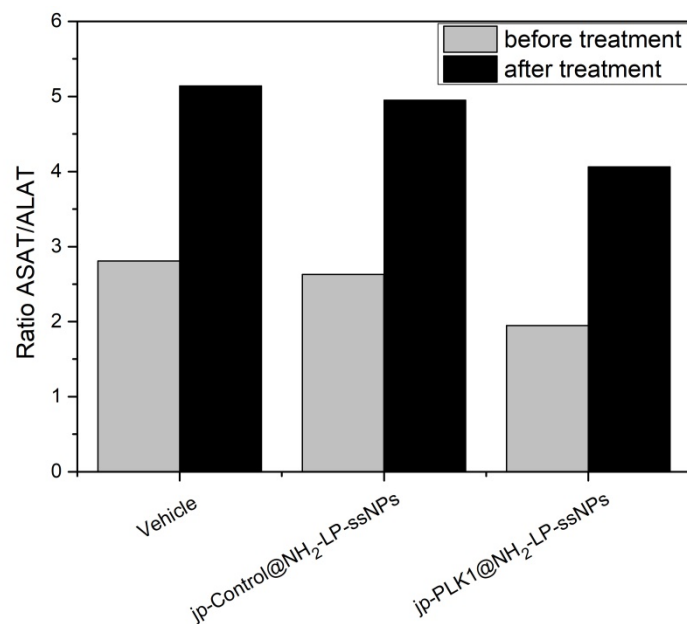


Figure 2.24: ASAT/ALAT ratio from the concentrations obtained before and after the treatment with PBS, jp-control@NH₂-LP-ssNPs and jp-PLK1@NH₂-LP-ssNPs.

2.5 Loading optimization

Able to deliver efficiently drugs, oligonucleotides and proteins to cancer cells are very challenging. More than the possibility to release specific molecules within the cells, the loading capacity of a cargo is also a crucial parameter to take into account. Liposomes and silica nanoparticles are usually drug delivery systems presenting very high loading capacities and a lot of studies are ongoing trying to push further the limits. For instance, Möller *et al.*, presented in 2017 the highest siRNA loading achieved with silica nanoparticles. The particles were able to host 382 µg of siRNA per mg of particles.^[36] Here again, several parameters in the building of the nanoparticles have to be taken into account such as the pore size (and pore volume), the quantification of the group able to interact with the oligonucleotides (often amino groups) and so on...

As already mentioned earlier in this chapter, the amount of amino groups grafted on the surface plays also an important role since it might prevent the breakability of the nanoparticles. Thus, the utilization of molecules able to bind electrostatically the siRNA on several points and anchor the particles on only one point has been decided.

The strategy adopted was the use of a commercially available silane composed of 1 primary amino group and 2 secondary amino groups. The use of the N¹-(3-trimethoxysilylpropyl)diethylenetriamine has been chosen thanks to its 3 amino groups present on the same silane. This molecule has already been studied for siRNA loading and

presented a slight increase of electrostatically attached nucleotides compare to APTES functionalized nanoparticles.^[100]

In this regard, the particles has been grafted with N¹-(3-trimethoxysilylpropyl)diethylenetriamine using exactly the same conditions as for the APTES grafting (polyNH₂-LP-ssNPs). The molecular structure of the silane is represented in **Figure 2.25.a**. The efficient grafting of the polyamine was proven by a shift in the ξ -Potential from -22.4 ± 1.3 mV to $+53 \pm 1.7$ mV in a MES buffer at pH 5. The grafted nanoparticles were then incubated with the PLK1 siRNA in a MES buffer at pH 5 following the same procedure as for the APTES with a siRNA concentration ranging from 20 to 200 $\mu\text{g}\cdot\text{mL}^{-1}$. As depicted in **Figure 2.25.b**, a loading of 278 $\mu\text{g}\cdot\text{mg}^{-1}$ has been observed by UV-Visible measurement of the supernatant, thus increasing the loading of +52% compared to NH₂-LP-ssNPs.

Such improvement renders it interesting for further experiments since the new loading increases therefore the siRNA/LP-ssNPs ratio. However, since the properties of the material changed again, all the bio experiments would need to be repeated. Moreover, increasing the number of silanes moieties would possibly allow to reach a loading close (or even higher) than the one of 380 $\mu\text{g}\cdot\text{mg}^{-1}$ reported by Möller K. *et al.*^[36]

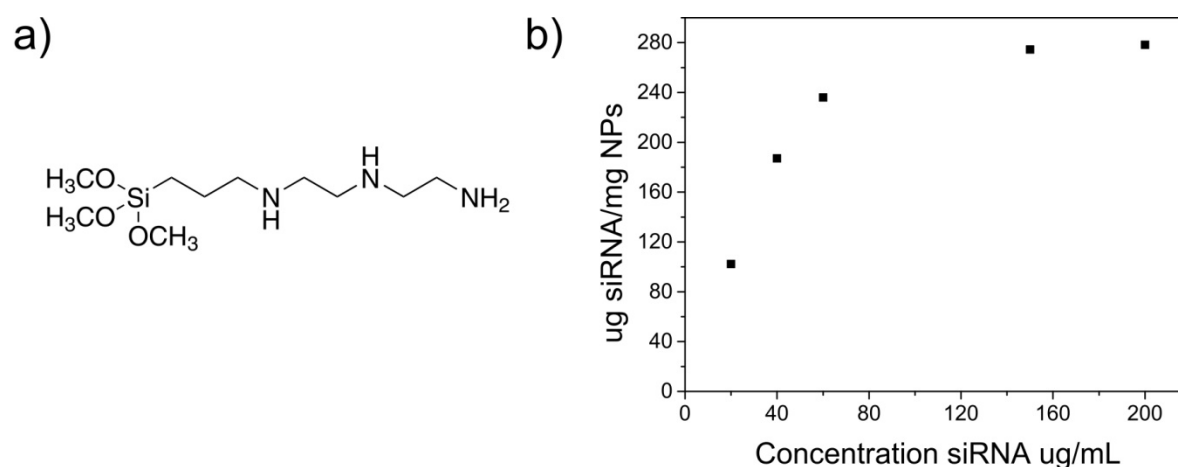


Figure 2.25: a) Chemical structure of N¹-(3-trimethoxysilylpropyl)diethylenetriamine. b) Loading achieved after incubation of different concentration of siRNA with polyNH₂-LP-ssNPs. The initial concentration of particles was 0.1 $\text{mg}\cdot\text{mL}^{-1}$.

2.6 Conclusion

Herein, we developed breakable large pore mesoporous silica nanoparticles for the efficient delivery and release of a double stranded PLK1-siRNA. The amino functionalized material present a broad pore distribution centered around 12 nm able to bind electrostatically to the oligonucleotide. The particles were then coated with jetPEI[®], a linear polyethylenimine, and their internalization were then tested in hepatocellular carcinoma Huh-7 cells. Finally, in

in vivo experiments were performed using orthotopic tumors of Huh7-derived xenograft mouse and showed a significant decrease in the cancer cell proliferation.

Chemotherapeutic approach using MSNs to deliver toxic anticancer drugs requires a well-controlled transport and release of the molecules avoiding their premature release that could have detrimental impact on non-tumorous cells. We show here an absence of cytotoxicity and a good cellular uptake of our LP-ssNPs, associated with a tumor cells specific release of the cargo highlighting those LP-ssNPs as an optimal delivery system for cancer treatments. Furthermore, we could envision to enhance the therapeutic efficacy and intracellular concentration of our anticancer drugs by generating antibody fragment-armed LP-ssNPs against glypican-3, a highly expressed cell surface protein on tumor cells. Altogether, our data support the concept of using our newly designed mesoporous silica nanoparticles to deliver anticancer molecules targeting specifically tumor cells. By enabling to design siRNAs for patient-specific cancer drivers this approach will enable precision medicine for cancer.

2.7 Acknowledgments

I would like to thank Dr. Laura Maggini and Dr. Valentina Giglio for their help on the synthesis of the material, Dr. Simone Silvestrini for XPS and Dr. Leana Travaglini for nitrogen absorption analysis, Sarah Durand for the cytotoxicity experiment, Dr. Cathy Royer and Dr. Valérie Demais of the Plateforme d'Imagerie *in vitro* of the Faculty of Neurochimie, University of Strasbourg, for the preparation of TEM samples of the cells and in the interpretation of the results. Dr Catherine Trautmann for the FACS analysis, All the people for the *in vivo* experiments, Dr. Eric Robinet, Dr. François Duong, Antonio Savano, Prof. Tania Sorg-Guss, Dr. Ghina Bouabout and Emilie Thiebaut.

2.8 Materials and Methods

2.8.1 Chemicals

All commercial solvents and reagents were used as received without further purification. Tetraethyl orthosilicate (TEOS), (3-aminopropyl)triethoxysilane (APTES), glutathione (GSH), rhodamine B isothiocyanate (RITC, mixed isomers), triethylamine (TEA), paraformaldehyde (PFA), glutaraldehyde 25 wt.%, Triton X-100, Bovine Serum Albumine (BSA), Fluoromont aqueous mounting medium, diethyl pyrocarbonate (DEPC),

trimethylbenzene (TMB), 2-(4-morpholino)ethanesulfonic acid hydrate (MES), Kaiser test kit, and all solvents were purchased from Sigma Aldrich and used as such. Bis(triethoxysilylpropyl)disulfide (BTSPD, 95%) was purchased from Fluorochem and Cetyltrimethylammonium bromide (CTAB) was purchased from Acros Organics. The jetPEI[®] was kindly provided by Polyplus-transfection SA. Control and PLK1 siRNAs were purchased from Eurogentec. Alamar Blue was purchased from Thermo Fisher. Dulbecco's Modified Eagle's Medium (DMEM), Phosphate Buffered Saline 7.4 (PBS), Fetal Bovine Serum (FBS), penicillin, streptomycin and L-glutamine 200 mM were purchased from Gibco (Life Technologies). Hoechst 33342, LysoTracker Blue-DND 22 and Alexa Fluor[®] 647 Phalloidin were purchased from Invitrogen. Huh-7 cells were obtained from ATCC/LGC Standards GmbH (Wesel, Germany) and cultivated according to the provider's protocol.

2.8.2 *Synthesis of breakable disulfide mesoporous silica nanoparticles (ssNPs):*

The breakable disulfide mesoporous silica nanoparticles have been synthesized as previously described in our group.^[55] Basically, 250 mg CTAB (0.685 mmol) were dissolved in a mixture of 110 mL of distilled H₂O, 875 μ L of NaOH (2 M, 1.75 mmol) and 10 mL of EtOH. The mixture was then heat up to 80 °C at 800 rpm. In another flask, 875 μ L of TEOS (3.91 mmol) and 390 μ L of BTSPD (0.84 mmol) were dissolved in 5 mL EtOH. Once the temperature was stabilized at 80 °C, the silane solution was added to the aqueous solution and the mixture was stirred at 800 rpm for 6 h. The resulted nanoparticles were then cooled down at r.t. and centrifuged (30 krcf for 20 min) before drying under vacuum.

2.8.3 *Post synthetic pore expansion treatment (LP-ssNPs):*

100 mg of ssNPs previously synthesized were dispersed in 10 mL of EtOH by sonication for 30 min, followed by the addition of 20 mL of a 1:1 mixture (v/v) of H₂O and TMB. The mixture was placed in the oven and kept at 160 °C for 3 days without stirring. The resulting white powder was washed with ethanol and water four times each. Finally, the organic surfactant was removed by means of extraction in a mixture HCl/EtOH (5% v/v) under reflux overnight. LP-ssNPs were then centrifuged, washed thoroughly with ethanol several times and finally dried under vacuum. The material was characterized by means of: SEM, TEM, XPS, TGA, SAXS, DLS and ζ -potential.

2.8.4 Grafting of 3-(aminopropyl)triethoxysilane (NH₂-LP-ssNPs):

20 mg of LP-ssNPs were dispersed in toluene by sonication for 10 min, then 5 μ L of APTES and 3 μ L of TEA were added and the mixture was stirred overnight at rt. NH₂-LP-ssNPs were then collected by centrifuging for 20 min at 14.5 krpm. The precipitate was finally re-dispersed by sonication in ethanol and centrifuged five times to remove unreacted silane. The material was recovered and dried under vacuum before being characterized by means of ζ -potential. Quantification of functional primary amino groups was performed with a Kaiser test kit following the providers protocol.

2.8.5 Breakability of LP-ssNPs and NH₂-LP-ssNPs:

A solution of LP-ssNPs and NH₂-LP-ssNPs in PBS (0.1 mg·mL⁻¹) were prepared. Glutathione was then added at a final concentration of 10 mM and the sample was heated up to 37 °C. Aliquots were taken each days (up to 7 days) and dropcasted on a TEM grid before analysis under TEM.

2.8.6 Grafting of Rhodamine B isothiocyanate for confocal imaging (r-LP-ssNPs):

10 mg of NH₂-LP-ssNPs were dispersed in 2 mL of EtOH and sonicated for 30 min. Then, 0.1 mg of RITC were then added and stirred for 3 h. The particles were then washed several times by sequences of sonication/centrifugation cycles until a clear supernatant was obtained. The RITC-grafted nanoparticles r-LP-ssNPs were then dried under vacuum.

2.8.7 siRNA loading and jetPEI® coating (jp-siRNA@LP-ssNPs):

1 mg of amino-functionalized LP-ssNPs were dispersed in 1 mL of a MES buffer at pH 5 (5 mM) in an Eppendorf tube. In another Eppendorf tube, the two strands of siRNA were mixed together in the same MES buffer pH 5 (1 mL in total) at the desired concentration. The siRNA solution was shaken for 5 min before to add the dispersion of particles (total volume 2 mL). The particles were swirled overnight at r.t. with a rotatory mixer before centrifugation for 1 h at 14.5 krpm. The supernatant was removed and stored for further measurements. The particles were then redispersed in 1.89 mL of MES buffer before to add 110 μ L of a jetPEI® solution (0,2 mg/mL). After 1 h, the material was centrifuged for 1 h at 14.5 krpm, the supernatant removed and the particles were redispersed in 1 mL of a PBS (pH 7.4) solution. The loading of the siRNA was determined by UV-Vis spectroscopy measuring the absorbance

at 260 nm in the supernatant solution collected after centrifugation, determining the concentration of siRNA in the supernatant and calculating by the difference, the amount of siRNA loaded.

2.8.8 *Grafting of N^l-(3-trimethoxysilylpropyl)diethylenetriamine (polyNH₂-LP-ssNPs)*

20 mg of LP-ssNPs were dispersed in toluene by sonication for 10 min, then 5 μ L of APTES and 3 μ L of TEA were added and the mixture was stirred overnight at rt. NH₂-LP-ssNPs were then collected by centrifuging for 20 min at 14.5 krpm. The precipitate was finally re-dispersed by sonication in ethanol and centrifuged five times to remove unreacted silane. The material was recovered and dried under vacuum before being characterized by means of ζ -potential. Quantification of functional primary amino groups was performed with a Kaiser test kit following the providers protocol.

2.8.9 *Cell culture experiments*

Huh-7 cells were cultured in culture medium (CM) containing 88% Dulbecco's Modified Eagle Medium (DMEM), 10% Fetal Bovine Serum (FBS), 1% Penicillin-Streptomycin and 1% L-Glutamine 200 mM at 37°C under 5% of CO₂ atmosphere and let grown until reaching 80 to 90 % confluency. Then, cells were washed twice with Phosphate Buffer Solution (PBS) and treated with trypsin to detach them from the flask surface. Cells were split every 2-3 days.

2.8.10 *Cell viability*

1.5x10⁴ Huh-7 cells were seeded in 24 well plates and allowed to grow for 24 h. The cells were then incubated with LP-ssNPs, NH₂-LP-ssNPs and jp-PLK1@ NH₂-LP-ssNPs in CM (50, 100 and 150 μ g/mL). After 72 h, 100 μ L of Alamar Blue were added in each well plate and let incubate for 2 to 4 h. Then the culture media were transferred to a 96 well plates and the absorbance of each well plates was measured at 570 nm and 600 nm with a microplate reader. Each samples were triplicate.

2.8.11 *Flow cytometry*

For FACS analysis, Huh-7 cells were seeded in a 24 well plate (30000 per well) and allowed to adhere and grow for 24 h. The cells were then incubated with *r*-LP-ssNPs and jp-PLK1@*r*-LP-ssNPs in CM (50 and 100 μ g/mL). After 3, 24 and 48 h, the cells were washed 5 times

with PBS, trypsinated and centrifuged for 3 min at 1 krpm. The pellets were resuspended in 500 μ l of PBS and centrifuged again for 3 min before to be resuspended in 500 μ l of PFA (2 % in PBS) for FACS measurements.

2.8.12 Confocal microscopy

30 000 Huh-7 cells were seeded onto glass cover slips in a 24 well plate and allowed to adhere and grow for 24 h. The cells were then incubated with *r*-LP-ssNPs in CM (40 μ g/mL). After 3 h, 24 h and 48 h, the cells were washed 5 times with PBS and fixed with 4 % PFA for 15 min. The cells were then washed again 3 times with PBS. In order to visualize the nuclear region, the samples were then stained with Hoechst 33342 and washed 3 times with PBS. The glass cover slips were mounted and fixed on a glass microscope slide with Fluoromont aqueous mounting medium for confocal microscope analysis. For Z-stacking experiments, cells (Huh-7) were prepared as previously explained for the cellular uptake and incubated with *r*-LP-ssNPs under the same conditions. After 24 h of incubation, cells were washed 5 times with PBS and fixed with 4 wt. % PFA for 15 min. Cells were then washed with PBS and kept in Triton X-100 (0.1 % in PBS) for 10 min and afterwards in 1% bovine serum albumin (BSA) in PBS for 20 min. The cell layer on glass cover slip was stained with Phalloidin Alexa Fluor[®] 647 for F-actin/membrane staining, for 20 min in the dark at room temperature, and washed twice with PBS. The nuclear region was stained with Hoechst 33342 for 5 min and washed 3 times with PBS. The cover slips were mounted onto glass slides for confocal microscopy measurements. The excitation wavelength for Hoechst 33342 and RITC (grafted on the particles surface) were 355 and 488 nm respectively, while with Alexa Fluor[®] 647 Phalloidin was excited at 650 nm. For co-localization experiments, Huh-7 cells (30000 cells) were seeded onto glass bottom dishes (MatTek) and allowed to grow for 24 h. After this time, the culture media was removed and fresh media containing *r*-LP-ssNPs at a concentration of 50 μ g/mL was added to the cells and incubated for 24 h. Cells were then washed 5 times with PBS and incubated for 2 h with a solution of 75 nM of LysoTracker[®] Blue DND-22 in culture media. The cells were washed three times with PBS and fresh culture media was added before live cell imaging with the confocal microscope. The excitation wavelength for LysoTracker[®] Blue DND-22 was 405 nm.

2.8.13 siRNA labelling and cellular uptake

40 µg of PLK1 siRNA were labelled using a Cy5Label IT[®] siRNA Tracker Intracellular Localization Kit (Mirus). The siRNA was incubated for 1 h at 37 °C with the labelling kit (total volume 100 µL). Then, 10 µL of 4 M NaCl and 250 µL of ice cold 100% ethanol were added. The solution was then placed at -20 °C for 1h before centrifuging at full speed (14 krpm) in a refrigerated microcentrifuge for 30 min. The pellets were then washed with 500 µL room temperature 70% ethanol and centrifuged for 30 min at 4 °C. Finally, the siRNA was resuspended in 20 µL of siRNA buffer solution. In another Eppendorf, 200 µg of *r*-LP-ssNPs were dispersed in 200 µL of MES buffer pH 5 before adding the siRNA solution. The suspension was shaken overnight at room temperature. The siRNA labelled particles were centrifuged (1 h, 14.5 krpm) and resuspended in 200 µL of MES buffer pH 5 + 5 µL of jetPEI (2 mg/mL) and incubated 1 h at room temperature. Finally, the particles were centrifuged (1 h, 14.5 krpm) and suspended in 200 µL of PBS (7.4). The particles were then incubated with 30 000 cells at a concentration of 50 µg/mL for 3 h. Then, the samples were washed 5 times with PBS (7.4), fixed with PFA (4%) for 15 min and washed again 3 times. Finally, the cells were stained with Hoechst 33342 for 10 min and washed again 3 times before mounting on microscope glass slides for confocal imaging. Excitation wavelengths were 355, 488 and 633 nm for Hoechst 33342, *r*-LP-ssNPs and PLK1 siRNA respectively.

2.8.14 In vitro breakability test by means of TEM

For the preparation of biological TEM samples 1.10⁶ Huh-7 cells were seeded on glass cover slips and allowed to grow for 24 h. After this time the media was removed and fresh media containing LP-ssNPs in CM (50 µg/mL) was added to the cells and incubated for 3 h, 24 h and 48 h at 37°C in a humidified atmosphere with 5% CO₂. Subsequently, cells were washed with PBS five times fixed with glutaraldehyde (2.5 wt. %). The cells were post fixed with 0.5% osmium tetroxyde (EMS) in H₂O and dehydrated through immersion in different solutions, where the content of EtOH in the mixture H₂O/EtOH was varied from 50 to 100 %, before being embedded in epoxy resin, Embed 812 (EMS). The resin was cut with an ultramicrotome, Leica EM UC6 (Leica) and the ultrathin sections were counterstained with uranyl acetate before TEM analysis.

2.8.15 *Animal experimentation*

Animal experimentations were performed in accordance with European recommendations (Directive 2010/63/UE, September 22nd, 2010) and French regulations (Edict 2013-118, February 1st, 2013) and received the approval of the local ethical committee (Comité Régional d’Ethique en Matière d’Expérimentation Animale de Strasbourg, approval n° 03111). Six to twelve weeks-old NMRI-nu (Rj:NMRI-Foxn1nu/Foxn1nu) female mice purchased from Janvier Labs (Le Genest Saint Isle, France) were used for experimentation.

2.8.16 *Cell-Derived Xenograft tumor model*

10.6 luciferase-expressing Huh-7 (Huh-7-Luc) human hepatoma cells were either orthotopically transplanted by echo-guided intrahepatic injection and monitored by ultrasound imaging (USI) or were subcutaneously injected and monitored by bioluminescence imaging (BLI) as previously described.^[96] All surgical procedures were performed under 1 to 3% isoflurane anesthesia (Axience Laboratories, Pantin, France) with 2 to 3 L/min air flow rate, with or without 0.2 L/min O₂ flow rate. Analgesia was performed at initiation of the procedures by administration, directly in the abdominal cavity, of buprenorphine (Buprecare[®], Axience Laboratories) at a dose of 0.1 mg/kg. Intraperitoneal injections of buprenorphine at the same dose were performed eight hours later and, if required, the following days. Paracetamol (Doliprane, Sanofi-Aventis, Paris) was given at a dose of 1 mg/ml in the drinking water until the end of the experimentation.

2.8.17 *Experimental protocol*

Ultrasound imaging was performed as previously described^[97] and was used for the percutaneous intrahepatic injection of Huh-7 cells, the intratumoral injection of nanovectors and the monitoring of tumor growth. B-Mode, or brightness mode, imaging was used to acquire two dimensional images of an area of interest and for identification of anatomical structures using Vevo 2100 high-resolution imaging system (Visualsonics, Toronto, Ontario, Canada). Three weeks after Huh-7-Luc transplantation, i.e. at day 0 of treatment, mice were analyzed for tumor surface and randomly allocated to the experimental groups. The median tumor surface of each experimental group was then calculated and the randomization was considered as valid when the coefficient of variation of the median values was below 5%. Six US-guided intratumoral injections of nanovectors (10 ug of siRNA per injection) were performed at D0, D2, D4, D7, D9 and D11. At each time points after treatment, data were

expressed as the relative tumor growth, calculated for each tumor as the its surface at the indicated time point, normalized to the tumor surface at D0 of treatment.^[96,97]

2.8.18 Blood analysis

Blood was collected by retro orbital puncture under isoflurane anesthesia on non-fasted mice. Blood chemistry was performed on an OLYMPUS AU-480 automated laboratory work station (Beckmann Coulter, US) with kits and controls supplied by Beckmann Coulter. The following parameters were measured: ALAT, ASAT, total bilirubin, and albumin. Internal quality control materials (Olympus) were analyzed on a daily basis to monitor our precision throughout the experiment.

2.8.19 Instruments

SEM images were recorded with a FEI Quanta FEG 250 instrument (FEI corporate, Hillsboro, Oregon, USA) with an acceleration voltage of 20 kV. The sample is prepared by drop-casting a dispersion of particles in EtOH onto a glass cover slip, subsequently sputter coated with Au (Emitech K575X peltier cooled) for 60 s at 60 mA prior to fixation on an Al support. TEM samples of particles were analyzed on a FEI Philips CM120 instrument at an acceleration voltage of 120 kV. Ethanolic suspensions of the materials (0.1 mg/mL) were drop-casted onto Formvar coated Cu grids (400 mesh) and dried overnight prior to visualization. TEM samples of cells were observed on a Hitachi 7500 transmission electron microscope (Hitachi High Technologies Corporation) equipped with an AMT Hamamatsu digital camera (Hamamatsu Photonics). XPS analysis was performed using a K-AlphaTM+ X-ray Photoelectron Spectrometer (XPS) System (Thermo Scientific). Monochromatic Al K alpha X-rays were used (15 keV, 72 W, 200 mm spot diameter). Spectra were measured using a pass energy of 200 eV for survey spectra and 50 eV for core level spectra. The analyzed samples were prepared by drop-casting an ethanolic dispersion (0.1 mg/mL) of the particles onto a glass coverslip precoated with Au (Emitech K575X peltier cooled) for 3 min at 60 mA. TGA analyses were conducted on a Perkin Elmer TGA4000 Instrument machine under nitrogen atmosphere. The samples (0.1-2mg) were kept at 100°C for 30 min for stabilization, then heated from 100 to 750°C at a speed of 10°C/min, before being held at this temperature for further 30 min before cooling. The analyses were performed under a gas flow of N₂ at 60 mL/min. DLS and ZP measurements were conducted on a Delsa Nano C Particle Analyzer (Beckman Coulter, Brea, CA, USA; operative wavelength 655 nm). All DLS measurements

of the nanoparticles were conducted in water (0.1 mg/mL), and the Contin algorithm was used to supply the hydrodynamic diameters as intensity and volume distributions. ZP analyses were performed in PBS (pH 7.4) or MES buffer (pH 5). Porosimetry analyses of the samples were performed using a Micrometrics porosimeter (model ASAP-2020). The samples were degassed at 80 °C for 6 h and N₂ adsorption/desorption measurement was performed at -196 °C. The surface areas and pore volume were calculated by BET method and the pore size distribution was calculated by DFT methods. The surface area was calculated by Brunauer-Emmett-Teller (BET) method in the relative pressure range p/p_0 0.06-0.3.^[101] The pore size distribution and pore volume were calculated by density functional theory (DFT) method on the adsorption branch using a slit-based model. The total pore volume was estimated at p/p_0 0.989. The small-angle X-ray scattering set-up comprised the SAXSess mc² instrument from Anton Paar GmbH (Graz, Austria), containing a slit collimation system, and the PW3830 laboratory X-ray generator (40 kV, 50 mA) with a long-fine focus sealed X-ray tube (CuK α wavelength of $\lambda = 0.1542$ nm) from PANalytical. Detection was performed with the 2D imaging-plate reader Cyclone[®] by Perkin Elmer. Measurements were performed on powder sample for 5 min and the data collected up to a scattering vector q value of 7 nm^{-1} , where $q = (4 \pi/\lambda) \sin(\theta/2)$ and 2θ the scattering angle. The 2D data were converted to 1D data and background-corrected by using SAXSQuant software (Anton Paar GmbH). Absorbance spectra were measured on a Shimadzu UV-3600 spectrophotometer double-beam UV-VIS-NIR spectrometer and baseline corrected. Steady-state emission spectra were recorded on a Horiba Jobin–Yvon IBH FL-322 Fluorolog 3 spectrometer equipped with a 450 W xenon arc lamp, double-grating excitation, and emission monochromators (2.1 nm mm^{-1} of dispersion; $1200 \text{ grooves mm}^{-1}$) and a TBX-04 single photon-counting detector. Emission spectra were corrected for source intensity (lamp and grating) and emission spectral response (detector and grating) by standard correction curves. Confocal imaging was performed with a Zeiss LSM 710 confocal microscope system equipped with a 63x magnification, numerical aperture 1.3 of Zeiss LCI Plan-NEOFLUAR water immersion objective lens (Zeiss GmbH, Germany). The excitation wavelength for Hoechst 33342 and RITC were 355 and 488 nm respectively, while with Phalloidin Alexa Fluor[®] 647 was excited at 650 nm. LysoTracker blue-DND 22 and Cyanine 5 were excited at 405 nm and 633 nm respectively. Flow cytometry samples were acquired on a LSRII cytometer (Becton Dickinson Biosciences, San Diego, CA, USA). Quality control was performed regularly using Cytometer Setup and Tracking beads (BD Biosciences) to ensure consistency of fluorescence intensity measurements throughout all experiments. Cell debris and dead cells were excluded using Forward Scatter Area and Side

Scatter Area and cell aggregates were excluded using Side Scatter Width and Side Scatter Area. Rhodamine fluorescence of 10,000 living single cells was analyzed after monoparametric acquisition using the FL 2 Area parameter (excitation with a 488 nm Blue Laser, 575/26 nm emission filter). FACSDiva™ software version 6.1.2. (BD Biosciences) was used for data analysis and graphical output. Data are expressed as the percentage of positive cells, normalized by the relative emission intensities of the particles. 96 well plates samples were analyzed using a Victor-X5 2030 Multilabel from Perkin Elmer. Absorbance was measured in 96 well plates using a filter at $\lambda = 570$ nm.

2.9 References

- [1] A. Fire, S. Xu, M. K. Montgomery, S. A. Kostas, S. E. Driver, C. C. Mello, *Nature* **1998**, *391*, 806–811.
- [2] M. Frank-Kamenetsky, A. Grefhorst, N. N. Anderson, T. S. Racie, B. Bramlage, A. Akinc, D. Butler, K. Charisse, R. Dorkin, Y. Fan, *et al.*, *Proceedings of the National Academy of Sciences of the United States of America* **2008**, *105*, 11915–11920.
- [3] D. V. Morrissey, J. A. Lockridge, L. Shaw, K. Blanchard, K. Jensen, W. Breen, K. Hartsough, L. Machemer, S. Radka, V. Jadhav, *et al.*, *Nature Biotechnology* **2005**, *23*, 1002–1007.
- [4] E. Song, S.-K. Lee, J. Wang, N. Ince, N. Ouyang, J. Min, J. Chen, P. Shankar, J. Lieberman, *Nature Medicine* **2003**, *9*, 347–351.
- [5] A. P. McCaffrey, L. Meuse, T.-T. T. Pham, D. S. Conklin, G. J. Hannon, M. A. Kay, *Nature* **2002**, *418*, 38–39.
- [6] M. DiFiglia, M. Sena-Esteves, K. Chase, E. Sapp, E. Pfister, M. Sass, J. Yoder, P. Reeves, R. K. Pandey, K. G. Rajeev, *et al.*, *Proceedings of the National Academy of Sciences of the United States of America* **2007**, *104*, 17204–17209.
- [7] Niu X.-Y., Peng Z.-L., Duan W.-Q., Wang H., Wang P., *International Journal of Gynecological Cancer* **2006**, *16*, 743–751.
- [8] M. Jinek, J. A. Doudna, *Nature* **2009**, *457*, 405–412.
- [9] K. Strebhardt, A. Ullrich, *Nature Reviews Cancer* **2006**, *6*, 321–330.
- [10] K. A. Whitehead, R. Langer, D. G. Anderson, *Nature Review Drug Discovery* **2009**, *8*, 129–138.
- [11] C. V. Pecot, G. A. Calin, R. L. Coleman, G. Lopez-Berestein, A. K. Sood, *Nature Reviews Cancer* **2011**, *11*, 59–67.
- [12] H. J. Kim, A. Kim, K. Miyata, K. Kataoka, *Advanced Drug Delivery Reviews* **2016**, *104*, 61–77.
- [13] R. Kanasty, J. R. Dorkin, A. Vegas, D. Anderson, *Nature Materials* **2013**, *12*, 967–977.
- [14] M. E. Davis, J. E. Zuckerman, C. H. J. Choi, D. Seligson, A. Tolcher, C. A. Alabi, Y. Yen, J. D. Heidel, A. Ribas, *Nature* **2010**, *464*, 1067–1070.
- [15] B. M. Cooper, D. Putnam, *ACS Biomaterials Science & Engineering* **2016**, *2*, 1837–1850.
- [16] R. H. Mo, J. L. Zaro, W.-C. Shen, *Molecular Pharmaceutics* **2012**, *9*, 299–309.
- [17] Y. Yao, T. Sun, S. Huang, S. Dou, L. Lin, J. Chen, J. Ruan, C. Mao, F. Yu, M. Zeng, *et al.*, *Science Translational Medicine* **2012**, *4*, 130ra48-130ra48.

- [18] D. Strumberg, B. Schultheis, U. Traugott, C. Vank, A. Santel, O. Keil, K. Giese, J. Kaufmann, J. Drevs, *Int. Journal of Clinical Pharmacology and Therapeutics* **2012**, *50*, 76–78.
- [19] B. Schultheis, D. Strumberg, A. Santel, C. Vank, F. Gebhardt, O. Keil, C. Lange, K. Giese, J. Kaufmann, M. Khan, *et al.*, *Journal of Clinical Oncology* **2014**, *32*, 4141–4148.
- [20] J. E. Zuckerman, M. E. Davis, *Nature Reviews Drug Discovery* **2015**, *14*, 843–856.
- [21] E. Blanco, H. Shen, M. Ferrari, *Nature Biotechnology* **2015**, *33*, 941–951.
- [22] X. Huang, L. Li, T. Liu, N. Hao, H. Liu, D. Chen, F. Tang, *ACS Nano* **2011**, *5*, 5390–5399.
- [23] R. Duncan, *Nature Review Drug Discovery* **2003**, *2*, 347–360.
- [24] X. Zhang, L. Han, M. Liu, K. Wang, L. Tao, Q. Wan, Y. Wei, *Material Chemistry Frontiers* **2017**, *1*, 807–822.
- [25] G. Lin, H. Zhang, L. Huang, *Molecular Pharmaceutics* **2015**, *12*, 314–321.
- [26] M. Vallet-Regi, A. Rámila, R. P. del Real, J. Pérez-Pariente, *Chemistry of Materials* **2001**, *13*, 308–311.
- [27] C. Argyo, V. Weiss, C. Bräuchle, T. Bein, *Chemistry of Materials* **2013**, *26*, 435–451.
- [28] Lu Jie, Liong Monty, Li Zongxi, Zink Jeffrey I., Tamanoi Fuyuhiko, *Small* **2010**, *6*, 1794–1805.
- [29] F. Tang, L. Li, D. Chen, *Advanced Materials* **2012**, *24*, 1504–1534.
- [30] L. Tang, T. M. Fan, L. B. Borst, J. Cheng, *ACS Nano* **2012**, *6*, 3954–3966.
- [31] K.-C. Kao, C.-Y. Mou, *Microporous and Mesoporous Materials* **2013**, *169*, 7–15.
- [32] A. B. Fuertes, P. Valle-Vigón, M. Sevilla, *Journal of Colloid and Interface Science* **2010**, *349*, 173–180.
- [33] W. Lin, Y. Huang, X.-D. Zhou, Y. Ma, *Toxicology and Applied Pharmacology* **2006**, *217*, 252–259.
- [34] R. Wottrich, S. Diabaté, H. F. Krug, *International Journal of Hygiene and Environmental Health* **2004**, *207*, 353–361.
- [35] I. I. Slowing, J. L. Vivero-Escoto, C.-W. Wu, V. S.-Y. Lin, *Advanced Drug Delivery Reviews* **2008**, *60*, 1278–1288.
- [36] K. Möller, K. Müller, H. Engelke, C. Bräuchle, E. Wagner, T. Bein, *Nanoscale* **2016**, *8*, 4007–4019.
- [37] Y. Yang, J. Wan, Y. Niu, Z. Gu, J. Zhang, M. Yu, C. Yu, *Chemistry of Materials* **2016**, *28*, 9008–9016.
- [38] W. Meiyong, M. Qingshuo, C. Yu, Z. Lingxia, L. Mengli, C. Xiaojun, L. Yaping, Y. Pengcheng, Z. Linlin, S. Jianlin, *Advanced Materials* **2016**, *28*, 1963–1969.
- [39] N. Ž. Knežević, J.-O. Durand, *Nanoscale* **2015**, *7*, 2199–2209.
- [40] I. I. Slowing, J. L. Vivero-Escoto, B. G. Trewyn, V. S.-Y. Lin, *Journal of Material Chemistry* **2010**, *20*, 7924–7937.
- [41] J. Sun, H. Zhang, R. Tian, D. Ma, X. Bao, D. S. Su, H. Zou, *Chemical Communications* **2006**, *0*, 1322–1324.
- [42] J. Gu, K. Huang, X. Zhu, Y. Li, J. Wei, W. Zhao, C. Liu, J. Shi, *Journal of Colloid and Interface Science* **2013**, *407*, 236–242.
- [43] B. Lefèvre, A. Galarneau, J. Iapichella, C. Petitto, F. Di Renzo, F. Fajula, Z. Bayram-Hahn, R. Skudas, K. Unger, *Chemistry of Materials* **2005**, *17*, 601–607.
- [44] M. Mizutani, Y. Yamada, T. Nakamura, K. Yano, *Chemistry of Materials* **2008**, *20*, 4777–4782.
- [45] J. Zhang, M. Niemelä, J. Westermarck, J. M. Rosenholm, *Dalton Transactions* **2014**, *43*, 4115–4126.

- [46] K. S. Finnie, D. J. Waller, F. L. Perret, A. M. Krause-Heuer, H. Q. Lin, J. V. Hanna, C. J. Barbé, *Journal of Sol-Gel Science and Technology* **2009**, *49*, 12–18.
- [47] I. Slowing, B. G. Trewyn, V. S.-Y. Lin, *Journal of the American Chemical Society* **2006**, *128*, 14792–14793.
- [48] B. C. Bunker, *Journal of Non-Crystalline Solids* **1994**, *179*, 300–308.
- [49] H. Ehrlich, K. D. Demadis, O. S. Pokrovsky, P. G. Koutsoukos, *Chemical Review* **2010**, *110*, 4656–4689.
- [50] L. Li, T. Liu, C. Fu, L. Tan, X. Meng, H. Liu, *Nanomedicine: Nanotechnology, Biology and Medicine* **2015**, *11*, 1915–1924.
- [51] J. Lu, Z. Li, J. I. Zink, F. Tamanoi, *Nanomedicine: Nanotechnology, Biology and Medicine* **2012**, *8*, 212–220.
- [52] R. Kumar, I. Roy, T. Y. Ohulchanskyy, L. A. Vathy, E. J. Bergey, M. Sajjad, P. N. Prasad, *ACS Nano* **2010**, *4*, 699–708.
- [53] J. Croissant, Y. Fatieiev, N.M. Khashab., *Advanced Materials* **2017**, *29*, 1604634.
- [54] J. Zhu, Y. Niu, Y. Li, Y. Gong, H. Shi, Q. Huo, Y. Liu, Q. Xu, *Journal of Material Chemistry B* **2017**, *5*, 1339–1352.
- [55] L. Maggini, I. Cabrera, A. Ruiz-Carretero, E. A. Prasetyanto, E. Robinet, L. D. Cola, *Nanoscale* **2016**, *8*, 7240–7247.
- [56] J. Croissant, X. Cattoën, M. W. C. Man, A. Gallud, L. Raehm, P. Trens, M. Maynadier, J.-O. Durand, *Advanced Materials* **2014**, *26*, 6174–6180.
- [57] P. Huang, Y. Chen, H. Lin, L. Yu, L. Zhang, L. Wang, Y. Zhu, J. Shi, *Biomaterials* **2017**, *125*, 23–37.
- [58] K. Möller, T. Bein, *Chemistry of Materials* **2017**, *29*, 371–388.
- [59] L. Zhang, L. Wang, H. Yao, F. Xu, Y. Chen, *Journal of Material Chemistry B* **2017**, *5*, 8013–8025.
- [60] L. Maggini, L. Travaglini, I. Cabrera, P. Castro-Hartmann, L. De Cola, *Chemistry – A European Journal* **2016**, *22*, 3697–3703.
- [61] J.G. Croissant, Y. Fatieiev, K. Julfakyan, J. Lu, A.-H. Emwas, D.H. Anjum, H. Omar, F. Tamanoi, J.I. Zink, N.M. Khashab, *Chemistry – A European Journal* **2016**, *22*, 14806–14811.
- [62] Ryerson A. Blythe, Eheman Christie R., Altekruise Sean F., Ward John W., Jemal Ahmedin, Sherman Recinda L., Henley S. Jane, Holtzman Deborah, Lake Andrew, Noone Anne-Michelle, *et al.*, *Cancer* **2016**, *122*, 1312–1337.
- [63] R. Weiskirchen, *Hepatobiliary Surgery and Nutrition* **2016**, *5*, 183–187.
- [64] X. Liu, *Translational Oncology* **2015**, *8*, 185–195.
- [65] W. C. Mok, S. Wasser, T. Tan, S. G. Lim, *World Journal of Gastroenterology* **2012**, *18*, 3527–3536.
- [66] W. Sun, Q. Su, X. Cao, B. Shang, A. Chen, H. Yin, B. Liu, “High Expression of Polo-Like Kinase 1 Is Associated with Early Development of Hepatocellular Carcinoma,” DOI 10.1155/2014/312130 can be found under <https://www.hindawi.com/journals/ijg/2014/312130/>, **2014**.
- [67] T. Xia, M. Kovoichich, M. Liong, H. Meng, S. Kabehie, S. George, J. I. Zink, A. E. Nel, *ACS Nano* **2009**, *3*, 3273–3286.
- [68] H. Duan, S. Nie, *Journal of the American Chemical Society* **2007**, *129*, 3333–3338.
- [69] K. V, O. Y, *Bioimpacts* **2017**, *1*, 23–30.
- [70] Wightman Lionel, Kircheis Ralf, Rössler Vanessa, Carotta Sebastian, Ruzicka Regina, Kursal Malgorzata, Wagner Ernst, *The Journal of Gene Medicine* **2001**, *3*, 362–372.
- [71] R. B. Shmueli, D. G. Anderson, J. J. Green, *Expert Opinion on Drug Delivery* **2010**, *7*, 535–550.

- [72] W. Stöber, A. Fink, E. Bohn, *Journal of Colloid and Interface Science* **1968**, *26*, 62–69.
- [73] C. N. Wu, T. S. Tsai, C. N. Liao, K. J. Chao, *Microporous Materials* **1996**, *7*, 173–185.
- [74] C. Bharti, U. Nagaich, A. K. Pal, N. Gulati, *International Journal of Pharmaceutical Investigation* **2015**, *5*, 124.
- [75] A. Watermann, J. Brieger, *Nanomaterials* **2017**, *7*, 189.
- [76] Y. Wang, Q. Zhao, N. Han, L. Bai, J. Li, J. Liu, E. Che, L. Hu, Q. Zhang, T. Jiang, *et al.*, *Nanomedicine: Nanotechnology, Biology and Medicine* **2015**, *11*, 313–327.
- [77] M. Kruk, *Accounts of Chemical Research* **2012**, *45*, 1678–1687.
- [78] M.-H. Kim, H.-K. Na, Y.-K. Kim, S.-R. Ryoo, H. S. Cho, K. E. Lee, H. Jeon, R. Ryoo, D.-H. Min, *ACS Nano* **2011**, *5*, 3568–3576.
- [79] J. S. Beck, J. C. Vartuli, W. J. Roth, M. E. Leonowicz, C. T. Kresge, K. D. Schmitt, C. T. W. Chu, D. H. Olson, E. W. Sheppard, S. B. McCullen, *et al.*, *Journal of the American Chemical Society* **1992**, *114*, 10834–10843.
- [80] F. Q. Schafer, G. R. Buettner, *Free Radical Biology and Medicine* **2001**, *30*, 1191–1212.
- [81] J. Andersson, J. Rosenholm, S. Areva, M. Lindén, *Chemistry of Materials* **2004**, *16*, 4160–4167.
- [82] E. Kaiser, R. L. Colescott, C. D. Bossinger, P. I. Cook, *Analytical Biochemistry* **1970**, *34*, 595–598.
- [83] H.-T. Lu, *Colloidal Journal* **2013**, *75*, 311–318.
- [84] S. Carrara, F. Arcudi, M. Prato, L. De Cola, *Angewandte Chemie International Edition* **2017**, *56*, 4757–4761.
- [85] E. Soto-Cantu, R. Cueto, J. Koch, P. S. Russo, *Langmuir* **2012**, *28*, 5562–5569.
- [86] S. Schmucker, I. Sumara, *Molecular & Cellular Oncology* **2014**, *1*, e954507.
- [87] U. Holtrich, G. Wolf, A. Bräuninger, T. Karn, B. Böhme, H. Rübsamen-Waigmann, K. Strebhardt, *Proceedings of the National Academy of Sciences of the United States of America* **1994**, *91*, 1736–1740.
- [88] K. Ando, T. Ozaki, H. Yamamoto, K. Furuya, M. Hosoda, S. Hayashi, M. Fukuzawa, A. Nakagawara, *Journal of Biological Chemistry* **2004**, *279*, 25549–25561.
- [89] X.-Z. Yang, S. Dou, T.-M. Sun, C.-Q. Mao, H.-X. Wang, J. Wang, *Journal of Controlled Release* **2011**, *156*, 203–211.
- [90] J.-P. Behr, *CHIMIA International Journal for Chemistry* **1997**, *51*, 34–36.
- [91] N. Nelson, *Trends in Pharmacological Sciences* **1991**, *12*, 71–75.
- [92] L. M. P. Vermeulen, T. Brans, S. K. Samal, P. Dubruel, J. Demeester, S. C. De Smedt, K. Remaut, K. Braeckmans, *ACS Nano* **2018**, *12*, 2332–2345.
- [93] G. Sahay, D. Y. Alakhova, A. V. Kabanov, *Journal of Controlled Release* **2010**, *145*, 182–195.
- [94] V. de los Ríos, J. M. Mancheño, A. Martínez del Pozo, C. Alfonso, G. Rivas, M. Oñaderra, J. G. Gavilanes, *FEBS Letters* **1999**, *455*, 27–30.
- [95] B. Yameen, W. I. Choi, C. Vilos, A. Swami, J. Shi, O. C. Farokhzad, *Journal of Controlled Release* **2014**, *190*, 485–499.
- [96] C. Leboeuf, L. Mailly, T. Wu, G. Bour, S. Durand, N. Brignon, C. Ferrand, C. Borg, P. Tiberghien, R. Thimme, *et al.*, *Molecular Therapy* **2014**, *22*, 634–644.
- [97] T. Wu, E. Heuillard, V. Lindner, G. B. About, M. Ignat, J.-P. Dillenseger, N. Anton, E. Dalimier, F. Gossé, G. Fouré, *et al.*, *Scientific Reports* **2016**, *6*, 35230.
- [98] K. Oettl, R. Birner-Gruenberger, W. Spindelboeck, H. P. Stueger, L. Dorn, V. Stadlbauer, C. Putz-Bankuti, P. Krisper, I. Graziadei, W. Vogel, *et al.*, *Journal of Hepatology* **2013**, *59*, 978–983.

- [99] M. Botros, K. A. Sikaris, *Clinical Biochemist Review* **2013**, *34*, 117–130.
- [100] J. L. Steinbacher, C. C. Landry, *Langmuir* **2014**, *30*, 4396–4405.
- [101] S. Brunauer, P. H. Emmett, E. Teller, *Journal of the American Chemical Society* **1938**, *60*, 309–319.

Chapter 3

Loading of a neutral peptide on breakable silica nanoparticles

Abstract

As the world population keeps increasing, agriculture is facing new challenges for the crop production. However, with the lack of space and pests infestations, the development of new tools to produce efficiently and safely the required needs is critical. In order to reduce pest infestations, researchers focused on a new class of peptides, especially neurotoxins extracted from the venom of spiders. Among them, a specific peptides, extracted from Australian funnel-web spiders showed promising results by blocking specifically the calcium channel of insects, overcoming the resistance of synthetic insecticide targeting usually the sodium channels.

This chapter presents the development of large pore disulfide breakable mesoporous silica nanoparticles (LP-ssNPs) and their loading with the peptide for the crop industry. It is aim to enhance the cellular uptake and therefore show an higher mortality in insects. The particles presented good loading capacities and were spread on cotton leaves to test their efficiency towards larvae.

This chapter is confidential. Therefore no mention of the peptide neither the animal tested will be done.

3.1 Introduction

World population keeps increasing by 70 million people every year and should reach a total population of 9.2 billion humans by 2050.^[1] Those facts imply agriculture to face the rising demand in food, feed, fibers, *etc.* and the availability of new lands is limited. Thus, increasing productivity on existing lands remains the best choice to fulfill the needs of a growing world population. In this regard, different options can be taken by accelerating the development of goods and/or reduce pests infestations.

Biotechnologies as genes, peptides and proteins have attracted a lot of attention from researchers since several decades. Their complexity and wide properties render them interesting for our daily life use and in this regard, found already their place in the market as cosmetics,^[2] therapeutics^[3] and in the crop industry.^[4]

Proteins, divided in three main categories (antibodies, enzymes and structural proteins) are composed of a long sequence of amino acids and possess a specific 3D structure, and achieve usually specific and complex tasks in the cell.^[5] On the opposite, peptides are very short amino acids sequences that can be synthesized easily and play significant roles in signal transduction.^[6] Proteins and peptides have found interest in several fields including catalysis,^[7] sensing^[8] and therapeutics due to their high specificity and interesting properties. Fast growing of fields generally requires genetically modified seeds by the insertion in the genome of genes responsible for the production of specific growth hormone.^[9] However, increasing the production is not sufficient, since about 35 % of pre harvested crop are lost due to pests infestations.^[10] In this regard, research has been focus on peptides that could kill pests. Among them, spider venoms have demonstrated high efficiency to kill or paralyze pests,^[11] and a specific peptide has proven high lethality among all the insects tested so far. Herein, we present the use of large pore breakable silica nanoparticles (LP-ssNPs) for the entrapment of the peptide. This collaboration with a company aimed to enhance the killing effect of the spider venom peptide to induce mortality towards larvae. As it will be shown in this chapter, the peptide was efficiently entrapped within the cavities of the LP-ssNPs and the nanoparticles were further spread on cotton leaves before infestation.

3.2 Syntheses and characterizations

The design of two different carriers was performed to entrap the neutral peptide within the mesoporous silica nanoparticles. The first carrier was the LP-ssNPs, which the synthesis has already been reported in Chapter 2. Therefore in this case, as reported in **Figure 3.1**, the nanomaterial exhibits a larger size of 157 nm confirmed by DLS analysis and a broader pore size distribution ranging from 2.5 to 20 nm.

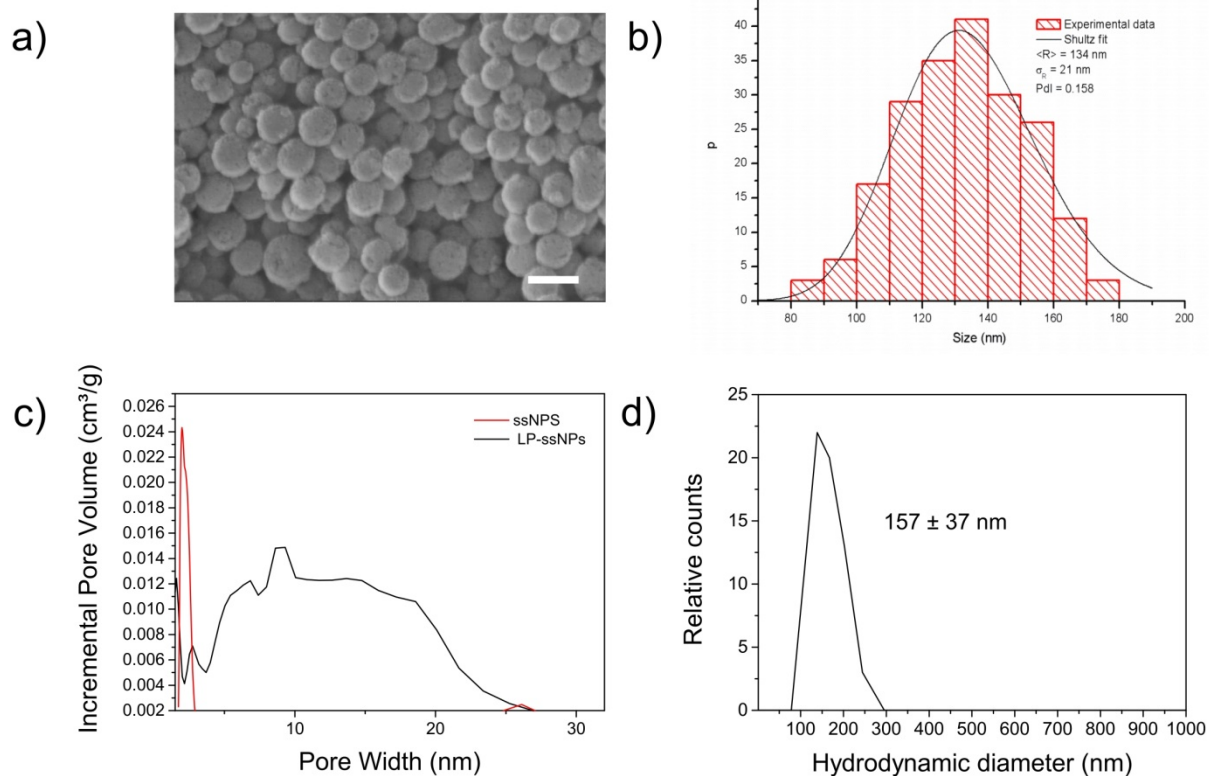


Figure 3.1: a) SEM images of the LP-ssNPs. Scale bar = 200 nm. b) Size distribution performed on the counting of 200 particles taken from the SEM images. c) Dynamic Light Scattering (DLS) analysis performed on the LP-ssNPs. d) Pore width distribution before (red) and after pore expansion treatment (black).

The other carrier was designed by Dr. Leana Travaglini and was synthesized by using CTAB as a surfactant and TEOS as a silane source. The mixture was stirred overnight at room temperature giving mesoporous silica nanoparticles (MSNs) with a size of 241 ± 36 nm determined by the counting of 100 nanoparticles on TEM micrographs (**Figure 3.2.a and b**). Small angle X-rays scattering presented the characteristic (100) Bragg peak, however the (110) and (200) peaks were not present (**Figure 3.2.c**). N_2 adsorption analysis determined a pore size of 3 nm as depicted on **Figure 3.2.d**.

3.3 Peptide labelling with a cyanine 5 dye (PepCy5)

In order to track visually the peptide, it has been covalently grafted with a Cy5 dye. The peptide and the Cy5 were incubated together in DMSO for 12 h at r.t in the dark (**Figure 3.3.a**), precipitated and washed with a Et₂O/Cy mixture (1/1). The peptide can be functionalized at 3 different positions, either the N-terminal or the 2 Lys residues that also present primary amino groups. As it can be observed on the MALDI TOF spectra (**Figure 3.3.b**), the grafted peptide shows three different mass at m/z: 4515, 4980 and 5446 respectively corresponding to the mono, di or tri adduct that could not be separated. Moreover, there is no possibility to determine the activity of the peptide after the functionalization.

The different photophysical properties of the labelled peptide were then measured in a $\text{HCO}_3^-/\text{CO}_3^{2-}$ buffer (pH = 9.5) to mimic the gut environment of the larvae. First a calibration curve on a UV Vis spectrophotometer was performed using different concentrations of the labeled peptide. Thus, giving a linear curve (equation: $A = 156821.9 [\text{PepCy5}] + 0.01366$ and a $R^2 = 0.993$ (**Figure 3.4.a and b**). As shown in **Figure 3.4.c**, excitation and emission spectra were then measured showing a maximum intensity of λ_{em} at 649 nm and λ_{exc} at 666 nm. Finally, the labelled peptide presents a lifetime of 91 ns and a quantum yield of 4% as shown on **Figure 3.4.d**.

3.4 Peptide loading

Loading of peptide are often performed on the surface of materials thanks to electrostatic interactions between either a positively charged peptide and a negatively charged nanoparticles or vice versa. Xie *et al.* developed recently hollow mesoporous silica nanoparticles functionalized with both amino-terminated groups in the inner core and carboxyl-terminated groups within the pores, thus allowing the loading of peptides with different isoelectric points (pI). The amino groups were utilized for the loading of a TRP2 hydrophobic peptide with a pI of 3.75 while the carboxylated groups where electrostatically bounded to a hydrophilic HGP100 peptide presenting a pI of 9.71.^[16]

Regarding the peptide of interest, several charged amino acids at pH 7 composed the sequence. However, all the charged are compensated by an opposite charged amino acid present close by and therefore electrostatic interactions between the peptide and the nanoparticle were not possible.

LP-ssNPs and MSNs (8 mg) were incubated with the peptide (8.4 mg) and incubated together for 4 h in MeOH. The MeOH was then evaporated under vacuum and the particles were washed using two different conditions to remove the non-adsorbed protein. The first one was a simple washing with EtOH while the second trial was performed by washing twice with a mixture of EtOH:Hexane (1:9). The particles were then centrifuged (14.5 krpm for 30 min) and dried. The different samples will be named as following: Pep@LP-ssNPs(EtOH), Pep@LP-ssNPs(EtOH:Hex), Pep@MSN(EtOH) and Pep@MSN(EtOH:Hex) and the loading was determined by TGA analysis (**Figure 3.5 a and b**).

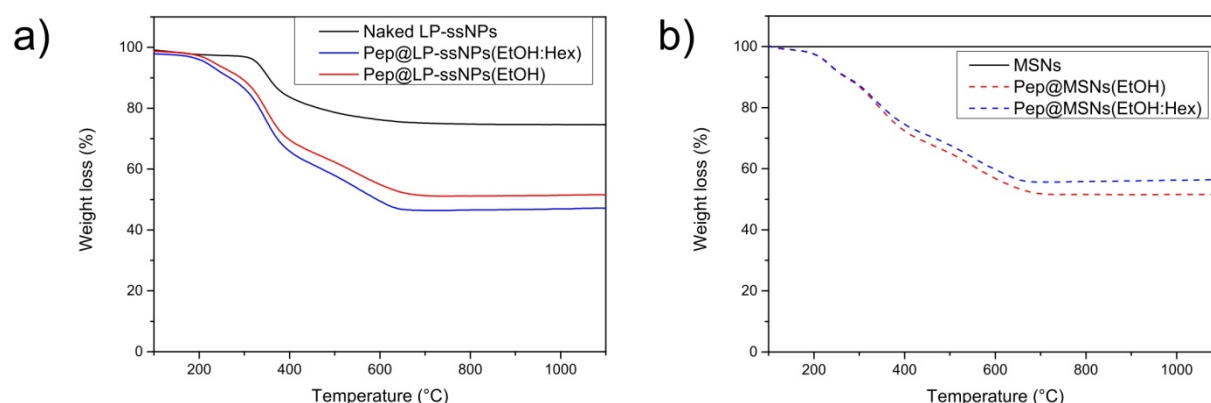


Figure 3.5: Thermogravimetric analysis of a) before loading of the peptide on LP-ssNPs (black), and after loading and washing with EtOH (red) and a mixture EtOH:Hexane (blue) and b) before loading of the peptide on MSN (black) and after loading and washing with EtOH (dashed red) and a mixture EtOH:Hexane (dashed blue).

As it can be observed on **Figure 3.5.a**, the pristine LP-ssNPs present a weight loss of 25% attributed to the presence of the disulfide linker. After incubation with the peptide and washing, Pep@LP-ssNPs(EtOH) and Pep@LP-ssNPs(EtOH:Hex) presented total weight losses of 48 and 52 % respectively. The weight losses attributed then to the peptide were 23 and 28 % for Pep@LP-ssNPs(EtOH), Pep@LP-ssNPs(EtOH:Hex) respectively.

Figure 3.5.b, however, represents the loading on MSNs. As the particles do not contain any organic linker, the pristine particles did not show any weight loss. After incubation with the peptide and washing, weight losses of 48 and 43% for Pep@MSN(EtOH:Hex) and Pep@MSN(EtOH) respectively have been observed.

Both types of particles presented a consequent loading of the peptide. However, in the case of the MSNs and due to their structural properties, especially their pore size of 3 nm, a loading of 48% is almost impossible and would suggest therefore, that the peptide is present mostly on the surface rather than within the pore. On the opposite, the LP-ssNPs, which

contain larger cavities and a stellate like structure, offer a higher probability of containing the peptide within the pores and were then chosen for further experiments.

Once the loading determined, the presence of the peptide within the LP-ssNPs was also characterized by Fourier Transform InfraRed spectroscopy (FTIR). As shown in **Figure 3.6**, pristine particles present a broad peak around 1060 cm^{-1} corresponding to the Si-O bond. The peptide, in green, present a characteristic C=O peak at 1660 cm^{-1} . Pep@LP-ssNPs presents both characteristic peaks, proving the presence of the peptide on the particles.

The efficient loading with the peptide was proven and characterized, the procedure was repeated with the PepCy5. As observed on **Figure 3.7**, a weight loss of 41 % was analyzed by TGA, corresponding then to a final loading of 18 % of the PepCy5.

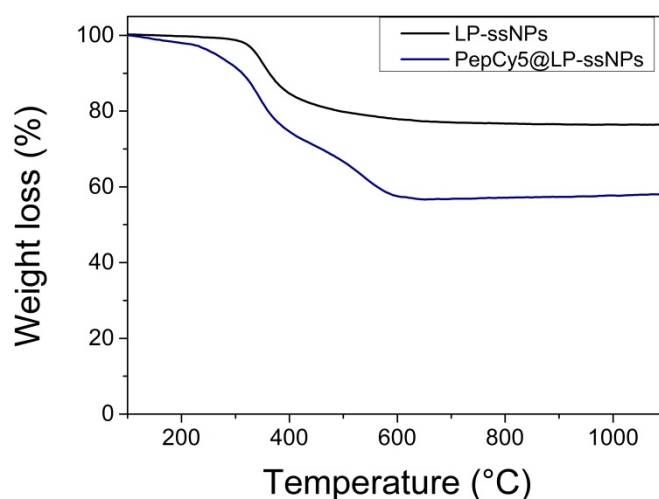


Figure 3.7: Thermogravimetric analysis of: before loading of Pep on LP-ssNPs (black) and after loading and washing with a mixture of EtOH:Hexane (blue) of the peptide

3.5 Killing effect of the Pep@LP-ssNPs on larvae

The materials were then sent to the company to test the efficiency of the loaded nanoparticles for the crop industry and especially their killing effect on larvae. The different treatments used are summarized in **Table 3.1.** and will be then discussed as treatment 1 to 8. Treatment 4 was done in water, due to the high solubility of the peptide. However, due to its too high solubility, the peptide might leak out of the LP-ssNPs before being eaten by the larva and therefore render inefficient and useless the use of the material. Thus, a mixture containing hydrofluorether:acetone:ethanol at ratios 90:5:5 (HFE mix) was used for treatment 1, 2, 3, 5, 7 and 8, preventing then the early leakage of the peptide out of the nanoparticles. In treatments 3, 6 and 7, calcofluor white and DMSO were added to enhance the killing effect by improving the cellular internalization of Pep and transcytosis of the peptide through the Lepidoptera gut. Positive control was also performed using different concentrations of Spinosad, a commercially available insecticide extracted from *Saccharopolyspora spinosa* bacterias.^[17] Spinosad is derived in many commercial products and presents interesting features for the grain protection.^[18] For the treatment, 24 well plates were filled with cotton leaves on which the different treatments were thereafter spread. The leaves were then infested with 5 larvae and the mortality was followed every day for 3 days after infestation. Each experiment was performed in quadruple representing 20 larvae per condition tested.

As shown in **Table 3.1,** cotton leaves treated with Spinosad presented a killing effect of 100 % already after 1 day of treatment for the highest concentrations and about 50 % for the lowest concentration. Negative control presented a larval mortality of 5 % only.

Calcofluor treatment presented also a larval mortality of 5 % (treatment 5). The LP-ssNPs in HFE mix with calcofluor and DMSO (treatment 7) showed a mortality of 5 % while the LP-ssNPs alone in HFE mix presented a larval mortality of 0 % after two days and 25 % after 3 days (treatment 1). Thus, describing an antifeedant effect probably due to the heavy coating of the material on the leaves. Treatments 4, 6 and 8, containing the peptide only in water, in water/calcofluor/DMSO or in HFE mix presented a larval mortality of 10, 15 and 25 % respectively, as well as an antifeedant effect of 13 % for the treatment 8. A killing effect of 15 and 5 % were observed for treatment 2 and 3 respectively, containing the Pep@LP-ssNPs and presented an antifeedant effect of 8 and 5 % respectively.

The antifeedant effect could also be observed thanks to the cotton leaves. **Figure 3.8** presents the cotton leaves before and up to 6 days after infestation. Positive control experiments with Spinosad demonstrated intact leaves for the highest concentrations. On the opposite, the untreated well plates presented completely degraded leaves only after 1 day and almost nothing remained after 6 days. Treatments with Pep, LP-ssNPs and Pep@LP-ssNPs showed a slower degradation of the cotton leaves after 1 day of incubation but no improvement compared to the negative control was observed after 6 days of infestation.

As a general remark, the encapsulated peptide did not show an improved activity compared to the free peptide, probably due to an early leakage of the peptide or the inefficiency of the particles to go through the gut and release the peptide and therefore kill the larvae.

Table 3.1: Description of the different solutions spread on cotton leaves and their killing effect on larvae.

Treatment	Description	Treatment	ppm active ingredient		Co-treatment	1 Day after infestation	2 Days after infestation	3 Days after infestation		
						Larval mortality (%)	Larval mortality (%)	Larval mortality (%)	Larval growth (%)	Larval antifeeding (%)
Treatment 1	LP-ssNPs in HFE mix	LP-ssNPs	10000			0	0	25	0	25
Treatment 2	Pep@LP-ssNPs in HFE mix	Pep@LP-ssNPs	10000			5	15	15	0	8
Treatment 3	Pep@LP-ssNPs + calcofluor in HFE mix + 2%DMSO	Pep@LP-ssNPs	10000	200	calcofluor	0	5	5	0	5
Treatment 4	Pep in water	Pep	10000			0	10	10	0	0
Treatment 5	Pep + calcofluor in HFE mix + 2% DMSO	calcofluor	200			0	5	5	0	0
Treatment 6	Pep + calcofluor in water + 2% DMSO	Pep	10000	200	calcofluor	10	15	15	0	0
Treatment 7	LP-ssNPs + calcofluor in HFE mix + 2% DMSO	LP-ssNPs	10000	200	calcofluor	0	5	5	0	0
Treatment 8	Pep in HFE mix	Pep	10000			5	15	25	0	13
Standard	Spinosad in water + 2% DMSO + 0.075% Lsg. 33	Spinosad	12.5			100	100	100		100
		Spinosad	3			100	100	100		100
		Spinosad	0.8			50	60	60	0	55
		Spinosad	0.2			30	30	50	0	40
Check						3	5	5	0	0

3.6 Synthesis of breakable organo-hybrid nanocapsules (PepCy5@ssBS)

To tackle the early leakage of the peptide out of the nanoparticles, breakable nanocapsules were synthesized following a procedure we published recently.^[19] Basically, the peptide was entrapped in a reverse micelle before condensation of the breakable silica shell catalyzed by ammonia. The SEM picture (**Figure 3.9.a**) shows spherical nanoparticles about 70 nm. The loading of the peptide was further quantified thanks to the photoluminescence properties of the labelled peptide (**Figure 3.9.b**). A calibration curve based on the emission intensity of the peptide was performed in milliQ water resulting to the following equation: $\text{Intensity} = 16676 \cdot [\text{PepCy5}] + 1167$ (**Figure 3.9.c**). The intensity of a solution at $0.1 \text{ mg} \cdot \text{mL}^{-1}$ of the PepCy5@ssBs was measured and a final loading of $37 \text{ } \mu\text{g}$ of peptide per mg of particles was determined (**Figure 3.9.d**). The PepCy5@ssBS was then sent to the company to assess the cytotoxicity effect of the new material.

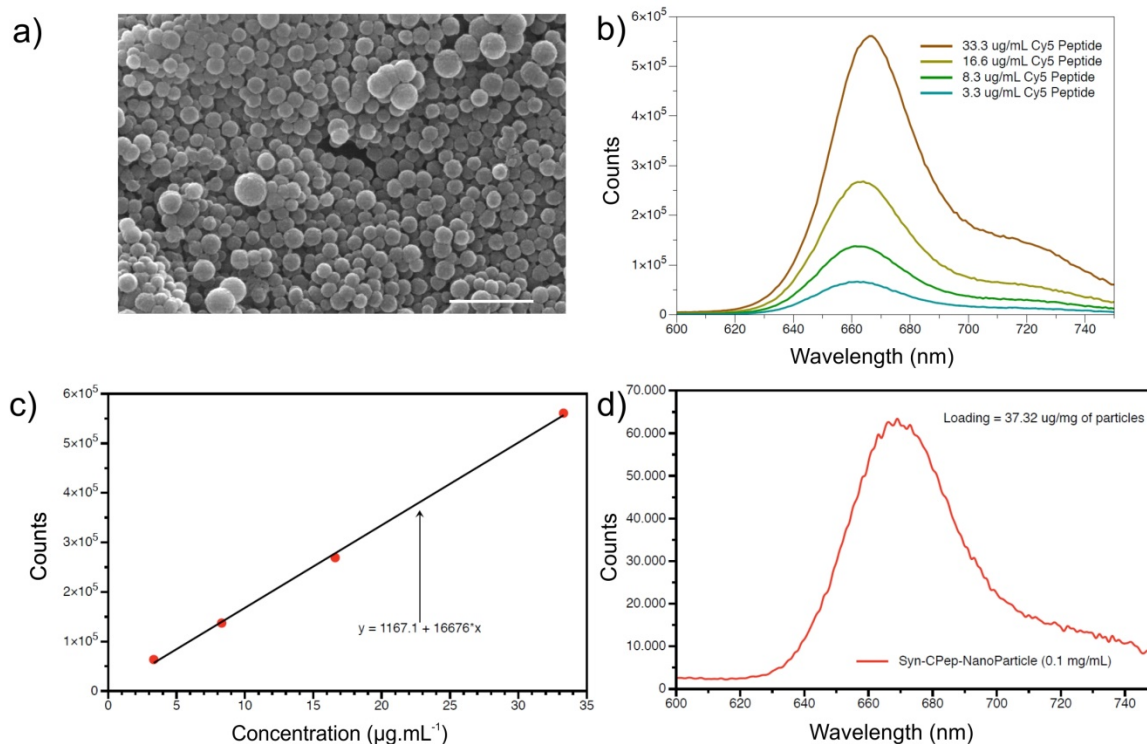


Figure 3.9: Characterization of organo-hybrid breakable nanocapsules. a) SEM of the breakable nanocapsules. Scale bar = 500 nm. b) Calibration curve performed based on the emission spectra of different concentrations of peptide. c) Intensity vs concentration at 666 nm resulting to a equation: Intensity = 16676.[PepCy5] + 1167 d) Emission intensity of a solution at 0.1 mg·mL⁻¹ of the PepCy@ssBS in milliQ water.

3.7 Conclusion

Two different materials have been tested for the entrapment of the peptide, able to kill specifically the larvae and could therefore find application for the crop industry. Both nanoparticles presented good loading capacities, however, large pore breakable silica nanoparticles were preferred thanks to their large cavities and loadings of 23 and 18% was achieved for Pep and PepCy5. The loaded nanoparticles were then sent to the company to test their killing effect by spraying solution of materials on cotton leaves. Unfortunately, no improvement compare to the peptide alone were observed suggesting either a too fast release of the peptide or an inability of penetrating the Lepidoptera gut. A new strategy has been designed by encapsulating the peptide within breakable shells, which are currently under investigation at the company.

3.8 Materials and Methods

3.8.1 Materials

All commercial solvents and reagents were used as received without further purification. Tetraethyl orthosilicate (TEOS), and trimethylbenzene (TMB), Triton X-100 and all solvents were purchased from Sigma Aldrich and used as such. Bis(triethoxysilyl-propyl)disulfide (BTSPD, 95%) was purchased from Fluorochem and Cetyltrimethylammonium bromide (CTAB) were purchased from Acros Organics. The peptide was bought from BACHEM.

3.8.2 Synthesis of the disulfide doped breakable mesoporous silica nanoparticles (ssNPs):

In a flask, CTAB (250 mg) was dissolved in a solution of distilled water (110 mL), EtOH (10 mL) and NaOH (2 M, 0.875 mL) that was heated to 80 °C and stirred vigorously. In another flask, TEOS (0.875 mL) and BTSPD (0.390 mL) were dissolved in 5 mL of EtOH. Once the temperature of the CTAB solution had stabilized, the solution containing the silane sources was added dropwise. After 6 h, the solution was cooled to r.t. and the particles, recovered by centrifugation (20 min at 40 krcf).

3.8.3 Pore expansion treatment (LP-ssNPs):

100 mg of ssNPs previously synthesized as reported were dispersed in EtOH by sonication for 30 min, followed by the addition of 20 mL of a 1:1 mixture (v/v) of H₂O and TMB. The mixture was placed in the oven, and kept at 140 °C for 3 days without stirring. The resulting white powder was washed with ethanol (x4) and water (x4). Finally, the organic surfactant was removed by means of extraction in a mixture HCl/EtOH (5% v/v) under reflux overnight. **LP-ssNPs** were then centrifuged, washed thoroughly with ethanol several times and finally dried under vacuum. The material was characterized by means of: SEM, TGA, SAXS, DLS and ζ -potential.

3.8.4 Synthesis of non breakable mesoporous silica nanoparticles (MSNs) :

100 mg of CTAB was dissolved in 60 mL of water and 30 mL of EtOH. Then 0.71 mL of NH₃ (28%) and 0.250 mL of TEOS were added and the solution was stirred at 1000 rpm overnight at room temperature. The particles were then washed by means of sonication/centrifugation in water (3 times) and EtOH (3 times). Finally the particles were dried and the surfactant was removed by calcination.

3.8.5 Peptide coupling with a Cy5 dye (PepCy5):

To a 0.5 mM solution of peptide in DMSO, triethylamine was added, so that the concentration of triethanolamine = 100 mM. Subsequently the amine reactive dye was added (3:1 molar ratio to the peptide). The reaction mixture was allowed to stir for 12 h at room temperature. The reaction progress was monitored by TLC (silica gel; CHCl₃/MeOH/14% NH₃ = 2/2/0.5). The peptide was precipitated by adding a Et₂O/Cy mixture (1/1, 15 mL) and collected by centrifuge. The precipitate was washed with an Et₂O/Cy mixture (1/1), centrifuged and dried under reduced pressure.

3.8.6 Incubation with the peptide:

4 mg of LP-ssNPs were dispersed in 500 µL of MeOH in Eppendorf tubes. In another falcon tube, 4.2 mg of Pep or PepCy5 were dissolved in 500 µL of MeOH. This solution were then added to each Eppendorf tubes containing the particles and were then swirled for 4 h at r.t.. The MeOH was then evaporated under vacuum overnight and the particles were washed once with 500 µL of EtOH. The samples were then dried and a TGA was performed.

3.8.7 Killing effect of the Pep@LP-ssNPs on larvae

Cotton leaf discs were placed onto agar in 24-well microtiter plates and treated with test solutions by pipetting (10 x 1 µl droplets). Six hours after application, the plates were infested with 5 larvae (L1) per well (4 replicates per treatment). The samples were assessed for mortality 1 and 2 days after application and on mortality, anti-feeding effect, and growth inhibition in comparison to untreated samples 3 days after infestation.

3.8.8 Synthesis of the breakable nanocapsules (PepCy5@ssBS)

Triton X-100 (1.77 mL) and n-hexanol (1.8 mL) were dissolved in cyclohexane (7.5 mL). Separately, 200 µL of a 0.5 mg.mL⁻¹ aqueous solution of the PepCy5 peptide were mixed with 40 µL of TEOS and 60 µL of BTSPD. After shaking, this mixture was added to the previous organic medium. Eventually, 50 µL of 30% ammonia aqueous solution were added in order to precipitate the PepCy5@ssBS particles and the material was stirred overnight at room temperature. The solution was then precipitated by adding acetone and the particles were centrifuged, washed with water 3 times.

3.8.9 Instruments

SEM images were recorded with a FEI Quanta FEG 250 instrument (FEI corporate, Hillsboro, Oregon, USA) with an acceleration voltage of 20 kV. The sample is prepared by drop-casting a dispersion of particles in EtOH onto a glass cover slip, subsequently sputter coated with Au (Emitech K575X peltier cooled) for 60 s at 60 mA prior to fixation on an Al support. TEM samples of particles were analyzed on a FEI Philips CM120 instrument at an acceleration voltage of 120 kV. Ethanolic suspensions of the materials (0.1 mg/mL) were drop-casted onto Formvar coated Cu grids (400 mesh) and dried overnight prior to visualization. TGA analyses were conducted on a Perkin Elmer TGA4000 Instrument machine under nitrogen atmosphere. The samples (0.1-2mg) were kept at 100°C for 30 min for stabilization, then heated from 100 to 750°C at a speed of 10°C/min, before being held at this temperature for further 30 min before cooling. The analyses were performed under a gas flow of N₂ at 60 mL/min. DLS and ZP measurements were conducted on a Delsa Nano C Particle Analyzer (Beckman Coulter, Brea, CA, USA; operative wavelength 655 nm). The small-angle X-ray scattering set-up comprised the SAXSess mc² instrument from Anton Paar GmbH (Graz, Austria), containing a slit collimation system, and the PW3830 laboratory X-ray generator (40 kV, 50 mA) with a long-fine focus sealed X-ray tube (CuK α wavelength of $\lambda = 0.1542$ nm) from PANalytical. Detection was performed with the 2D imaging-plate reader Cyclone[®] by Perkin Elmer. Measurements were performed on powder sample for 5 min and the data collected up to a scattering vector q value of 7 nm⁻¹, where $q = (4 \pi/\lambda) \sin(\theta/2)$ and 2θ the scattering angle. The 2D data were converted to 1D data and background-corrected by using SAXSQuant software (Anton Paar GmbH). Attenuated Total Reflectance (ATR-FTIR) measurements were performed on an ATR IRAffinity-1 instrument (Shimadzu Scientific Instruments). The analyzed samples were prepared by drop-casting particles directly onto the sample plate surface. Absorbance spectra were measured on a Shimadzu UV-3600 spectrophotometer double-beam UV-VIS-NIR spectrometer and baseline corrected. Steady-state emission spectra were recorded on a Horiba Jobin–Yvon IBH FL-322 Fluorolog 3 spectrometer equipped with a 450 W xenon arc lamp, double-grating excitation, and emission monochromators (2.1 nm mm⁻¹ of dispersion; 1200 grooves mm⁻¹) and a TBX-04 single photon-counting detector. Emission spectra were corrected for source intensity (lamp and grating) and emission spectral response (detector and grating) by standard correction curves.

3.9 References

- [1] J. Popp, K. Pető, J. Nagy, *Agronomy for Sustainable Development* **2013**, *33*, 243–255.
- [2] G. Secchi, *Clinics in Dermatology* **2008**, *26*, 321–325.
- [3] K. Fosgerau, T. Hoffmann, *Drug Discovery Today* **2015**, *20*, 122–128.
- [4] Y. L. Yamaguchi, T. Ishida, S. Sawa, *Journal of Experimental Botany* **2016**, *67*, 4813–4826.
- [5] R. de la Rica, H. Matsui, *Chemical Society Reviews* **2010**, *39*, 3499–3509.
- [6] D. R. Nässel, *Invertebrate Neuroscience* **2009**, *9*, 57.
- [7] S. Weber, *Biochimica et Biophysica Acta (BBA) - Bioenergetics* **2005**, *1707*, 1–23.
- [8] J. E. Ghadiali, M. M. Stevens, *Advanced Materials* **2008**, *20*, 4359–4363.
- [9] W. M. Gray, *PLOS Biology* **2004**, *2*, e311.
- [10] E.-C. Oerke, *The Journal of Agricultural Science* **2006**, *144*, 31–43.
- [11] E. Grishin, *European Journal of Biochemistry* **1999**, *264*, 276–280.
- [12] J. R. Bloomquist, *Invertebrate Neuroscience* **2003**, *5*, 45–50.
- [13] J. I. Fletcher, R. Smith, S. I. O'Donoghue, M. Nilges, M. Connor, M. E. H. Howden, M. J. Christie, G. F. King, *Nature Structural & Molecular Biology* **1997**, *4*, 559–566.
- [14] H. W. Tedford, N. Gilles, A. Ménez, C. J. Doering, G. W. Zamponi, G. F. King, *Journal of Biological Chemistry* **2004**, *279*, 44133–44140.
- [15] Y. Chong, J. L. Hayes, B. Sollod, S. Wen, D. T. Wilson, P. G. Hains, W. C. Hodgson, K. W. Broady, G. F. King, G. M. Nicholson, *Biochemical Pharmacology* **2007**, *74*, 623–638.
- [16] J. Xie, C. Yang, Q. Liu, J. Li, R. Liang, C. Shen, Y. Zhang, K. Wang, L. Liu, K. Shezad, *et al.*, *Small* **2017**, *13*, 1701741.
- [17] F. P. MERTZ, R. C. YAO, *International Journal of Systematic and Evolutionary Microbiology* **1990**, *40*, 34–39.
- [18] M. B. Hertlein, G. D. Thompson, B. Subramanyam, C. G. Athanassiou, *Journal of Stored Products Research* **2011**, *47*, 131–146.
- [19] E. A. Prasetyanto, A. Bertucci, D. Septiadi, R. Corradini, P. Castro-Hartmann, L. De Cola, *Angewandte Chemie International Edition* **2016**, *55*, 3323–3327.

Chapter 4

Intracellular pharmacokinetics of chemotherapeutics delivery within 50 nm disulfide doped breakable silica nanoparticles

Abstract

Safe and efficient delivery of chemotherapeutics towards tumor cells has been among the most important challenges of the last decades. The opportunity to benefit from the enhanced and permeability retention effect (EPR) combined with the possibility of functionalization with targeting ligands, render nanomaterials very attractive for the biomedical field. Unfortunately, with the important amount of biological barriers as for instance the blood brain barrier (BBB), several nanomaterials suffer from incomplete release to the target due to early leakage or endosomal entrapment. Therefore, it is necessary to understand the kinetic of release of a chemotherapeutic out of the nanocarrier as well as the efficiency of the drug internalized in the cell compartment of interest.

Herein, the efficient release of doxorubicin entrapped within the pore channels of disulfide doped breakable mesoporous silica nanoparticles of 50 nm is studied. The nanocarrier was compared with the free drug which serves as a positive control and Caelyx[®], a liposomal-based doxorubicin delivery system that is already on the market. Pharmacokinetics of release as well as the accumulation of doxorubicin were studied within the cell nuclei of U87 glioblastoma cells.

4.1 Introduction

Nanomaterials have been used since several decades for the safe and efficient delivery of chemotherapeutics within tumor cells.^[1-3] With the FDA approval of Doxil in 1995,^[4] that consist in a liposomal-based system entrapping Doxorubicin, a chemotherapeutic employed for various cancers, many drug delivery systems made a breakthrough towards the market.^[5,6] Drug delivery systems offer a better protection of the cargo but more importantly allow a better selectivity towards tumors thanks to the EPR effect.^[7,8] However, despite these advantages, the brain remains a huge challenge and expensive market niches for the specific delivery of molecules due to the presence of the blood brain barrier (BBB) preventing the entrance of exogenous molecules.^[9,10] Small nanoparticles of size bellows or equal to 50 nm have shown potential for the crossing of the BBB through different possible mechanisms. Receptor-mediated transcytosis of nanocarriers through the endothelial cells is probably the most common type but the passage through loosened tight junctions has also been observed (Figure 4.1).^[10]

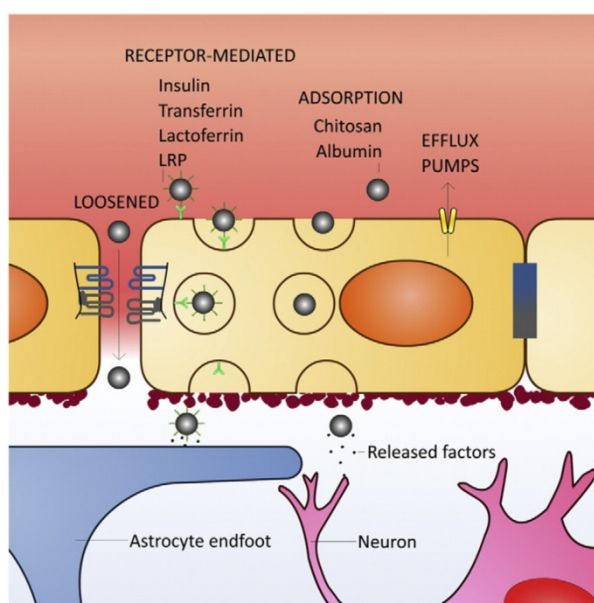


Figure 4.1: Blood–brain barrier (BBB) separating the nervous system from the circulating blood and controlling the passage of ions and molecules. Transport mechanisms for the delivery of nanoparticles within the brain are also presented. Reprinted with the permission from Sairava C., Praça C., Ferreira R., Santos T., Ferreira L and Bernardino L., Nanoparticle-mediated brain drug delivery: Overcoming blood-brain barrier to treat neurodegenerative diseases, *Journal of Controlled Release*, 235, 34-47 (2016). Copyright 2016, Elsevier.

Among all the drug delivery systems, mesoporous silica nanoparticles which, thanks to their versatility, are easy to tune to achieve specific goals.^[11-16] Between all the transformations possible, size variation affects strongly the biodistribution of nanocarriers

within the body allowing passive targeting towards specific organs.^[17,18] Moreover, silica nanoparticles have demonstrated their ability to cross the blood brain barrier for the delivery of specific therapeutics or for imaging purposes.^[19] Unfortunately, strong unwanted effects have been observed, leading to cell apoptosis which are mostly related to the high silica content within specific region of the brain 7 days after the intranasal injection.^[20]

In this regard, to prevent accumulation and improved the drug kinetic release, disulfide doped breakable mesoporous silica nanoparticles of 50 nm have been synthesized and characterized. The freshly prepared nanocarriers were then loaded with Doxorubicin and tested *in vitro* within U87 glioblastoma cells. We compared the accumulation of the therapeutic within cell nuclei by confocal microscopy and by Raman microspectroscopy and the pharmacokinetics of our system was compared with Caelyx[®], a liposomal formed of Doxorubicin, which presented a faster release of the cargo compared to the commercial available chemotherapeutic.

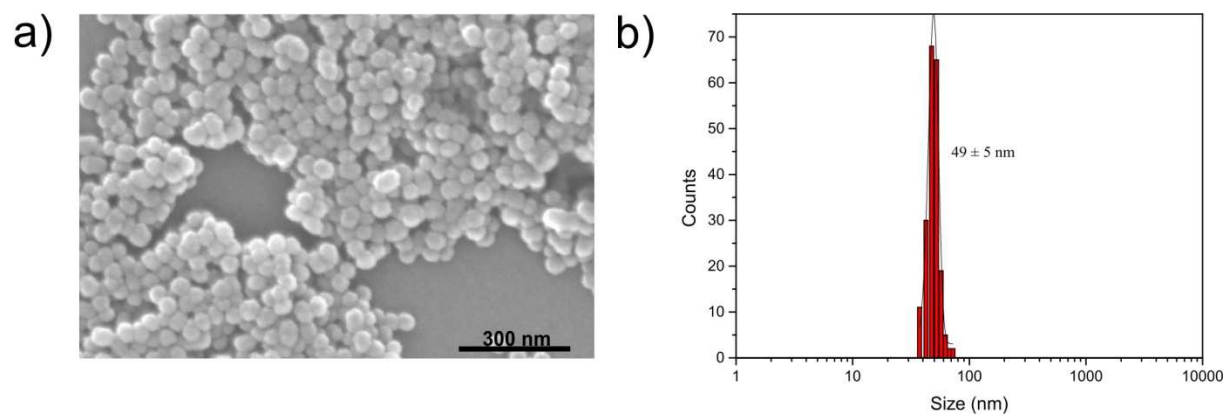
4.2 Synthesis and characterization of 50 nm disulfide-doped breakable silica nanoparticles

4.2.1 Synthesis of the 50 nm disulfide doped silica nanoparticles (ssNPs50)

50 nm breakable silica nanoparticles (ssNPs50) were synthesized by a modified Stöber process.^[21] In this case, triethanolamine (TEA) was used as a base catalyst to control nucleation growth and prevent agglomeration of the formed particles due to its chelating properties thus influencing the condensation of the silica.^[22-24] In order to include the breakability properties, the stimuli-responsive linker, namely bis(triethoxysilylpropyl)disulfide (BTSPD), as well as the usual tetraethyl orthosilicate (TEOS), were employed with the same molar ratio as reported in Chapter 2 (70:30). Cetyltrimethylammonium bromide (CTAB) was used as a template during the silica condensation to form the mesoporous network. Moreover, this method does not include ethanol and therefore the mechanism of the material is slightly modified. As explained by Lv *et al*, the cationic micelles are first formed followed by the formation of oil drops of TEOS where hydrolysis only occurs at the water oil interface thus allowing electrostatic interactions between the micelle and the oil drop surface (**Figure 4.2**). The condensation starts and is controlled by TEA that prevents the particles growth forming the final material.

4.2.2 Material characterizations

Scanning Electron Microscopy (SEM) was performed to assess the spherical morphology of the material as it can be observed in **Figure 4.3.a**. The counting of 200 nanoparticles on SEM pictures with Image J software showed a size distribution of 49 ± 5 nm (**Figure 4.3.b**). The global charge was also measured by ξ -Potential analysis and gave a surface charge value of $-22.74 \pm 1,52$ mV.



Porosity was further confirmed by nitrogen adsorption measurements 3.2 nm (**Figure 4.4.a and b**) and adsorption/desorption isotherms analysis allowed to calculate for ssNPs50 a BET surface area of $765 \text{ m}^2 \cdot \text{g}^{-1}$ and a total pore volume of $1.49 \text{ cm}^3 \cdot \text{g}^{-1}$.

Small angle X-ray scattering SAXS was performed to determine a possible ordered porosity (**Figure 4.4.c**). ssNPs50, as the ssNPs reported in Chapter 2, presented the same characteristic (100) Bragg peak, resulting again to a disordered pore arrangement due to the presence of the organic linker.

The presence of the cleavable moiety within the particles was confirmed by elemental analysis of the material conducted by X-ray photoelectron spectroscopy (XPS; **Table 4-1**) The presence of the silica framework was characterized by the high atomic percentage of O(1s) and Si(2p) whereas the doping of the organic linker was proven by the detection of C(1s) and S(2p) signals.

Table 4-1: Elemental composition of the ssNPs50 determined by XPS analysis

Name	Peak BE	Atomic %
O1s	532.81	40.61
Si2p	103.16	19.42
C1s	285.19	33.64
S2p	163.52	6.33

The ratio between organic/inorganic moieties was then characterized by thermogravimetric analysis (TGA; **Figure 4.4.d**). A weight loss of 12 % has been observed corresponding exclusively to the organic linker present in the framework of the particle.

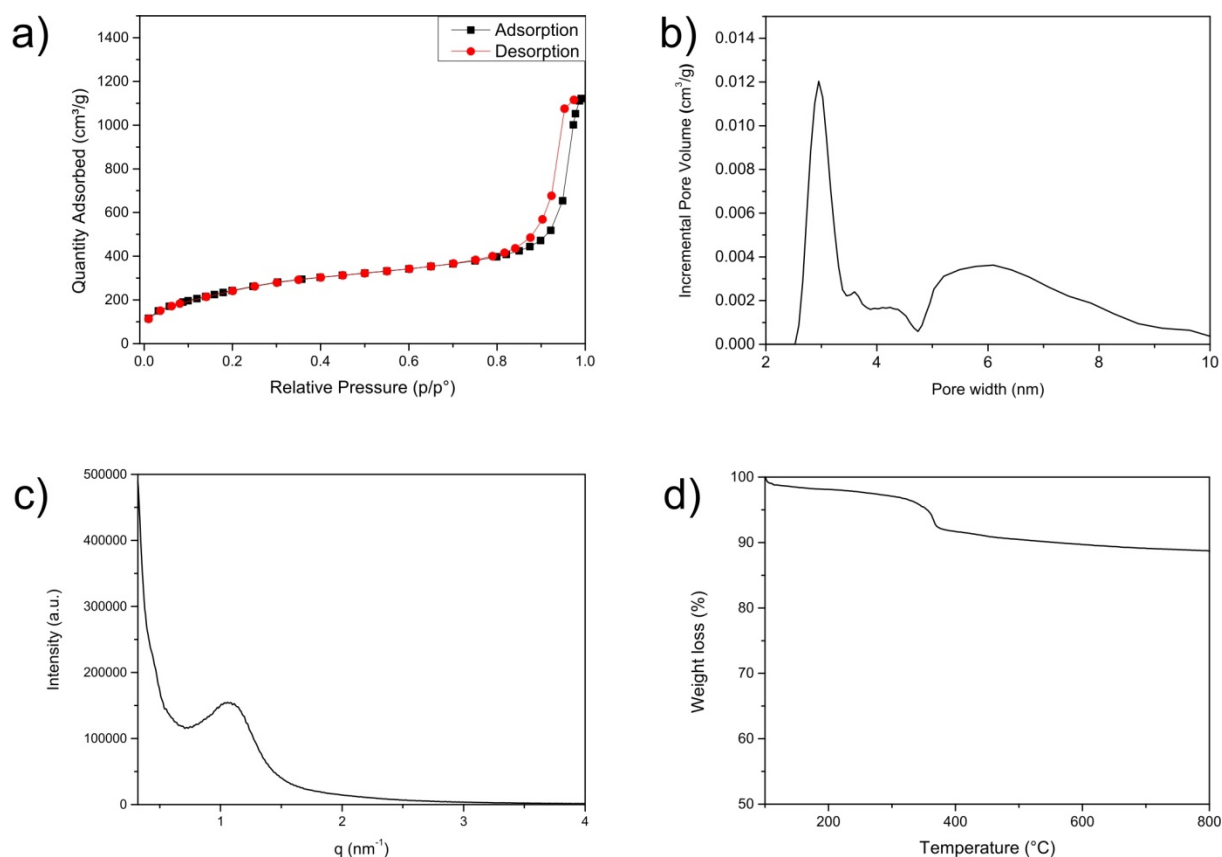


Figure 4.4: Characterization of the ssNPs50. a) N₂ adsorption/desorption isotherms. b) Pore width distribution. c) SAXS pattern. d) XPS survey. e) TGA plot presenting a weight loss a 12 % corresponding to the organic linker.

4.2.3 Breakability of ssNPs50

After characterization of the material, a breakability test was performed following the same procedure as for Chapter 2. Taking advantage of the disulfide linker, a dispersion of ssNPs50, in PBS (0.1 mg·mL⁻¹, pH 7.4) was therefore stirred at 37 °C in the presence of GSH (10 mM) and aliquots of the suspension taken after 7 days and analyzed by STEM. **Figure 4.5** shows the particles before and after incubation with GSH. After 7 days of incubation, the particles were completely destroyed due to the presence of the reducing agent.

4.3 Loading of Doxorubicin within ssNPs50 (DOX@ssNPs50)

Doxorubicin was chosen to fill the pores of the carrier for *in vitro* delivery and release study as it is a good candidate for drug delivery systems thanks to its luminescent properties, allowing tracking of the release of the drug out of the cargo *in vitro* as it will be shown later in this chapter.

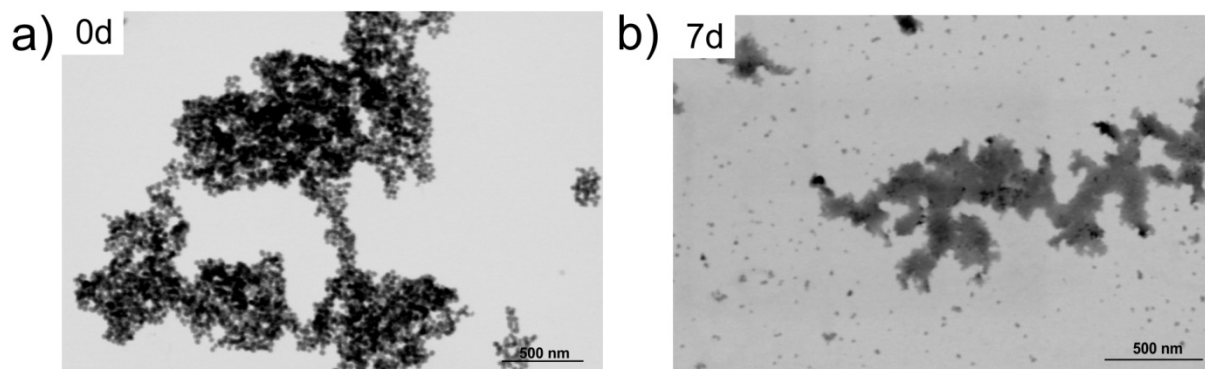


Figure 4.5: STEM analysis of a suspension of ssNPs50 at $0.1 \text{ mg}\cdot\text{mL}^{-1}$, PBS, $37 \text{ }^\circ\text{C}$ undergoing GSH (10 mM) reduction (0-7 d). a) Control experiment without GSH and b) Particles after 7 days incubation with GSH. Scale bar = 500 nm.

Loading of ssNPs50 with Doxorubicin (DOX@ssNPs50) was performed by dispersing the nanoparticles at a concentration of $1 \text{ mg}\cdot\text{mL}^{-1}$ in an aqueous solution of the drug ($1 \text{ mg}\cdot\text{mL}^{-1}$) and were incubated for 24 h at room temperature and afterwards centrifuged and washed with water for DOX@ssNPs50. The nanoparticles were then recovered by centrifugation and the supernatant analyzed by means of UV-Vis absorption spectroscopy to quantify the non-physioadsorbed drugs and, subsequently, the loading. A calibration curve was made using the absorbance at 490 nm for Doxorubicin (**Figure 4.6**). The calculated loadings resulted in values of 50 mg of DOX per gram of particles for DOX@ssNPs50.

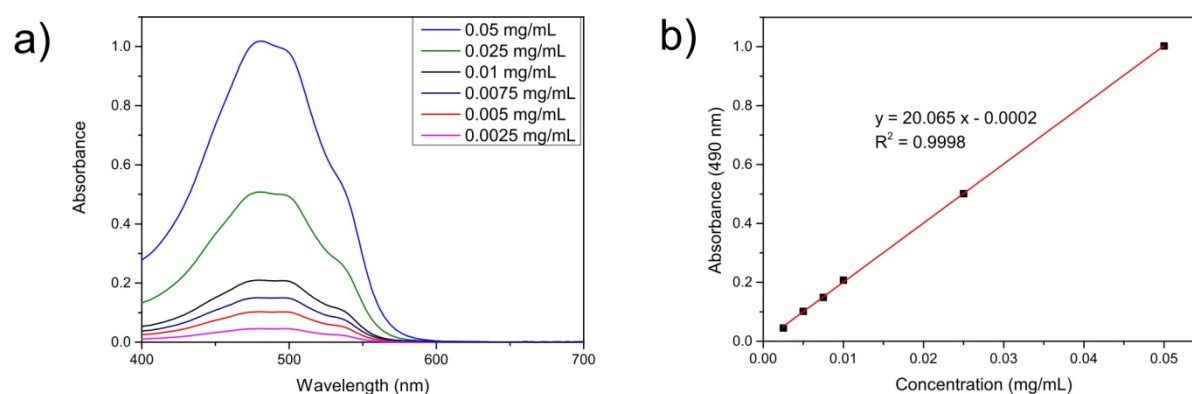


Figure 4.6: Calibration curve spectrum for the determination of the loading of Doxorubicin within ssNPs50. a) Full range spectrum of different concentrations of Doxorubicin. b) Calibration curve at 490 nm for the determination of the loading of Doxorubicin. Equation: $y = 20.065x - 0.0002$ with $R^2 = 0.9998$.

4.4 *In vitro* experiments

In vitro experiments were all conducted in human U87 glioblastoma models. Intracellular pharmacokinetics were performed using Raman microspectroscopy on single cell by comparing three different Doxorubicin based systems: Adriblastina (free doxorubicin in

aqueous solution), Caelyx[®] (liposomal form of Doxorubicin) and the DOX@ssNPs50. The chemical structure of Doxorubicin is depicted in **Figure 4.7.a**. As shown in **Figure 4.7.b**, Raman spectrum of both Adriblastina and Caelyx[®] at a concentration of 500 μM presented two characteristic peaks at 1210 and 1241 cm^{-1} . Those peaks are attributed to the C-O and C-O-H respectively and were then employed to demonstrate the presence of Doxorubicin within the cells by Raman microspectroscopy as it can be observed in **Figure 4.7.c**. Peaks observed at 1445 and 1570 cm^{-1} correspond to the skeletal ring vibrations.^[25] The microscope image presents the different spots where Raman scans were taken. As shown in **Figure 4.7.d**, Doxorubicin signals could be observed in both cytoplasm (green spots and spectra) and nucleus (red spots and spectra) demonstrating the efficient internalization of the free drug within the cell and the possibility to track its presence by Raman microspectroscopy. In the next experiments, Adriblastina, as the free drug, will be used as a positive control.

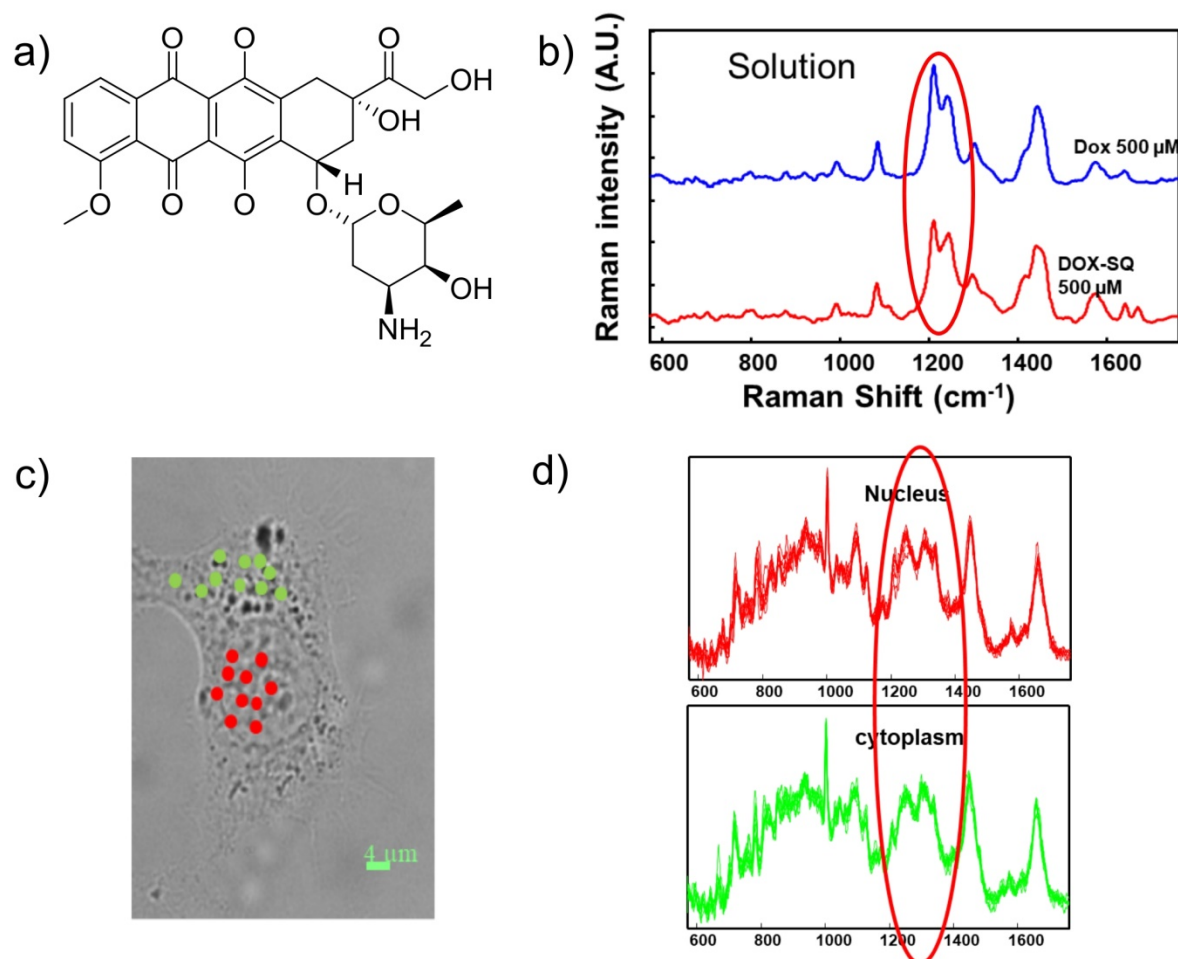


Figure 4.7: a) Chemical structure of Doxorubicin. b) Determination of the characteristic peaks of Doxorubicin and squalenoyl-based Doxorubicin by Raman spectroscopy. c) Raman microspectroscopy on single cell. The dots represent the Raman IR scan within the cytoplasm (green) and within the nucleus (red). Scale bar 4 μm . d) Raman scan performed in the nucleus and in the cytoplasm where the characteristic peaks of Doxorubicin could be observed.

U87 cells were then incubated with different concentrations of Doxorubicin to study the possible quantification of Doxorubicin within the nucleus and the cytoplasm. As shown in **Figure 4.8**, the intensity increased clearly with the increase in concentration of Doxorubicin within the nucleus. At 20 μM a clear peak can be observed and could therefore be used as a standard concentration for the following experiments. However, as it can be seen on the right image, such difference was not observed in the different spectrum, suggesting that it is not possible to have an approximate quantification of the drug within the cytoplasm.

Incubation for 5 h with the drugs of interest was then performed to evaluate their efficient internalization within the glioblastoma cells. As observed in **Figure 4.9**, Adriblastina[®], the free Doxorubicin, presented a clear peak within the nucleus after 5 h of incubation, demonstrating an efficient delivery of the drug within the cell and more precisely in the nucleus where it intercalates the DNA. For the liposomal based chemotherapeutic, Caelyx[®], only a small peak could be observed after the same time of incubation either showing an inefficient uptake by the cells or the entrapment of the drug within endosomes.

Figure 4.10 presents the Raman micrograph regarding the dispersion of DOX@ssNPs50 compared to Adriblastina[®]. As it can be seen on the red scan, the particles alone at a concentration of 1 mg·mL⁻¹ showed an intense and clear peak at 1210 and 1241 cm⁻¹ proving the presence of the Doxorubicin within the particles. Cells were then incubated with the DOX@ssNPs50 for 6 h at 0.1 mg·mL⁻¹ corresponding to a concentration of 94 μM of Doxorubicin. As it can be seen on the black scan, which correspond to the signal of the treated cells (green) compared to the untreated cells (purple), the peak of Doxorubicin is present within the nuclei, demonstrating the efficient release of the anticancer agent out of the particles.

To assess the efficient internalization of the chemotherapeutic with the different materials, colocalization experiments were performed with confocal laser scanning microscopy. Adriblastina[®], Caelyx[®] and DOX@ssNPs50 were incubated for 24 h at a concentration of 10 μ M of Doxorubicin in U87 cells. After that, cells were fixed and nuclei were stained with a Vybrant blue dye. As it can be seen on **Figure 4.11** with the single cells imaging, Adriblastina[®] was completely localized within the nucleus demonstrating an efficient internalization of the free drug and an efficient intercalation between the DNA strands. The liposomal form Caelyx[®] was instead not observed in the perinuclear region, but was mostly still entrapped within vesicles such as endosomes. The same phenomenon was noticed with the DOX@ssNPs50 even though part of the fluorescence was also detected in the nuclear region, suggesting a release of the drug out of the particles.

Nuclear Raman microspectroscopy was performed again to attest the presence of the Doxorubicin in the nuclear region. Adriblastina[®], Caelyx[®] and DOX@ssNPs50 were incubated for 4 h in U87 cells at a concentration of 10 μM of Doxorubicin. In this case, the presence of drug within the nucleus could be observed in the different conditions tested as it can be seen by the presence of the characteristic Doxorubicin peaks after spectrum deconvolution in **Figure 4.12**.

The release kinetic of Doxorubicin for both Caelyx[®] and DOX@ssNPs50 were then compared. On **Figure 4.13.a**, the Raman spectra present the scans within the nuclei of cell incubated with DOX@ssNPs50 at a concentration of 10 μM in Doxorubicin. Control experiment was performed by incubating the cells with ssNPs50 at a concentration of 20 $\mu\text{g}\cdot\text{mL}^{-1}$. **Figure 4.13.b** presents the quantification of the chemotherapeutic in the nuclear region. Adriblastina[®], as already observed by confocal microscope, presented a fast accumulation within the nucleus reaching a value above 400 μM of Doxorubicin after 4 h of incubation. However, since it is the free drug and therefore not selective towards tumors, the effect on healthy tissues would also be observed. Caelyx[®], on the other side, presented a very low accumulation of the drug with a value around 100 μM of Doxorubicin that in correlation with the confocal pictures could assess the possible entrapment of the drug within the endosomes. On the other side, DOX@ssNPs50 presented a faster release with a value around 250 μM of Doxorubicin in the perinuclear region, suggesting a more efficient endosomal escape and therefore a better accumulation within the nucleus. These data

represent an improvement in the release of such chemotherapeutics from the pores of DOX@ssNPs50 compared to the commercially available liposomal-based systems Caelyx[®].

4.5 Conclusion

The synthesis of 50 nm breakable mesoporous silica nanoparticles has been presented for delivery of therapeutics towards U87 glioblastoma cells. Delivery kinetics of Doxorubicin were studied by confocal and Raman microspectroscopy and compared with a commercially available liposome-based Doxorubicin, Caelyx[®]. The breakable nanoparticles presented a higher accumulation of the therapeutic within the nucleus after 4 h of incubation, demonstrating the faster delivery of our system, probably resulting from combined effect of the diffusion and the cleavage of the disulfide bound leading to the breakability of the particles.

4.6 Acknowledgments

We would like to thank Dr. Valérie Palissot from the Luxembourg Institute of Health for all the *in vitro* and the Raman microspectroscopy experiments.

4.7 Materials and Methods

4.7.1 Chemicals

All commercial solvents and reagents were used as received without further purification. Tetraethyl orthosilicate (TEOS), glutathione (GSH), triethanolamine (TEA) and all solvents were purchased from Sigma Aldrich and used as such. Bis(triethoxysilyl-propyl)disulfide (BTSPD, 95%) was purchased from Fluorochem and Cetyltrimethylammonium bromide (CTAB) was purchased from Acros Organics. Doxorubicin (DOX) was obtained from Téra Santé and Caelyx was purchased from Laboratories. Dulbecco's Modified Eagle's Medium (DMEM), Phosphate Buffered Saline 7.4 (PBS), Fetal Bovine Serum (FBS), penicillin, Vybrant blue, streptomycin and L-glutamine 200 mM were purchased from Gibco (Life Technologies). Human glioblastoma cell line (U87) were purchased from ATCC and cultured according to the recommended protocols.

4.7.2 Synthesis of 50 nm disulfide-doped silica nanoparticles (*ssNPs50*)

Hexadecyltrimethylammonium bromide (CTAB) (0.6 g, 1.64 mmol) was dissolved in 20 mL of water. Then, triethanolamine (0.06 g, 0.40 mmol) were added and the solution was heated up to 95 °C for 1 h. In another flask, tetraethylorthosilicate (TEOS) (1.03 mL, 4.5 mmol) and Bis(triethoxysilylpropyl) disulfide (BTSPD) (0.462 mL, 1.00 mmol) were mixed together and stirred at room temperature. Once the CTAB solution stabilized, the silanes sources solution was added dropwise to the CTAB flask. The solution was then stirred at 300 rpm for 1 h. The particles were then cooled down to room temperature and washed thoroughly through the meaning of centrifugation/sonication (15 min at 25 krcf) with ethanol. The particles were then put under reflux (100 mL EtOH, 60 μ L of HCl) overnight. Once again, the particles were centrifuged (25 krcf/15 min) and washed many times with EtOH. The particles were finally dried under vacuum.

4.7.3 Breakability test of ssNPs50

A solution of ssNPs50 in PBS ($0.1 \text{ mg}\cdot\text{mL}^{-1}$) was prepared. Glutathione was then added at a final concentration of 10 mM and the sample was heated up to 37 °C. After 7 days, an aliquot was taken and dropcasted on a TEM grid before analysis under STEM.

4.7.4 Loading of Doxorubicin within ssNPs50 (DOX@ssNPs50)

10 mg of particles were dispersed in 5 mL of water. Then 5 mL of a solution of Doxorubicin hydrochloride (2 mg/mL) was added and stirred for 24 h at room temperature. The particles were then washed many times with water until to have a clear supernatant. The loading of the DOX was determined by UV-Vis spectroscopy measuring the absorbance at 480 nm in the supernatant solutions collected after centrifugation, determining the concentration of DOX in the supernatant and calculating by the difference, the amount of DOX loaded.

4.7.5 Cell culture

Human glioblastoma cell line (U87) were purchased from ATCC and cultured according to the recommended protocols. Cells were grown in Dulbecco's modified Eagle's medium (DMEM) supplemented with fetal bovine serum (10% v/v), penicillin and streptomycin (1% v/v). Cells were grown in 100 mm diameter culture dishes in a cell culture incubator at 37 °C in a humidified atmosphere of 5% CO₂. The number of cells was counted by a hemocytometer to determine the seeding density. All treatments have been done with an equivalent of 10 μM of Doxorubicin

4.7.6 Raman spectroscopy

Adherent cells ($50 \cdot 10^3$ cells/ml /window) were seeded directly on CaF₂ windows (previously sterilized in ethanol 70°) in 6-well plate 24 h before treatment. Cells were incubated with and without DOX (drugs or nanoparticles) at concentration of 10 μM placed into Petri dishes for 24 and 48 h. After incubation time, medium was then removed and the cells were rinsed twice with sterile PBS. Cells were kept in PBS for Raman acquisition. 10 spectra were acquired on 5 individual cell nuclei at different location to account for heterogeneity. Each spectrum was measured with 10 s integration time, in the range from 600 cm⁻¹ to 1800 cm⁻¹. After acquisition, spectra are first calibrated using Raman calibration standards. The spectrum of the halogen lamp is used to correct for the wavelength-dependent signal detection efficiency

of the Raman setup. All spectra were corrected for the PBS solution and CaF_2 background, baseline corrected using a fourth order polynomial and smoothed with fifth points Savitzky-Golay algorithm in order to minimize the influence of noises.

4.7.7 *Microspectrofluorimetry*

The cells were seeded into easygrip 2.5 cm diameter petri dishes ($50 \cdot 10^3$ cells/ml) and incubated overnight before treatment in fresh medium with drugs or nanoparticles.

4.7.8 *Fluorescence imaging*

The cells were seeded 4-well Lab-Teck coverglass borosilicate ($15 \cdot 10^3$ cells/500 μL) and incubated overnight before treatment in fresh medium with drugs or nanoparticles. After treatment, cells were washed three times with PBS, and stained for 30 min at 37 °C using 2 μL of Vybrant blue in fresh medium. Fluorescence images were acquired without washing using a 40 \times objective lens on a fluorescence microscope consisting of wide field fluo + spinning.

4.7.9 *Instruments*

SEM and STEM images were recorded with a FEI Quanta FEG 250 instrument (FEI corporate, Hillsboro, Oregon, USA) with an acceleration voltage of 20 kV. The sample is prepared by drop-casting a dispersion of particles in EtOH onto a glass cover slip, subsequently sputter coated with Au (Emitech K575X peltier cooled) for 60 s at 60 mA prior to fixation on an Al support. For STEM analyses, ethanolic suspensions of the materials (0.1 mg/mL) were drop-casted onto Formvar coated Cu grids (400 mesh) and dried overnight prior to visualization. XPS analysis was performed using a K-AlphaTM+ X-ray Photoelectron Spectrometer (XPS) System (Thermo Scientific). Monochromatic Al K alpha X-rays were used (15 keV, 72 W, 200 mm spot diameter). Spectra were measured using a pass energy of 200 eV for survey spectra and 50 eV for core level spectra. The analyzed samples were prepared by drop-casting an ethanolic dispersion (0.1 mg/mL) of the particles onto a glass coverslip precoated with Au (Emitech K575X peltier cooled) for 3min at 60 mA. TGA analyses were conducted on a Perkin Elmer TGA4000 Instrument machine under nitrogen atmosphere. The samples (0.1-2 mg) were kept at 100°C for 30 min for stabilization, then heated from 100 to 750°C at a speed of 10°C/min, before being held at this temperature for

further 30 min before cooling. The analyses were performed under a gas flow of N₂ at 60 mL/min. DLS and ZP measurements were conducted on a Delsa Nano C Particle Analyzer (Beckman Coulter, Brea, CA, USA; operative wavelength 655 nm). All DLS measurements of the nanoparticles were conducted in water (0.1 mg/mL), and the Contin algorithm was used to supply the hydrodynamic diameters as intensity and volume distributions. ZP analyses were performed in PBS (pH 7.4) or MES buffer (pH 5). Porosimetry analyses of the samples were performed using a Micrometrics porosimeter (model ASAP-2020). The samples were degassed at 80 °C for 6 h and N₂ adsorption/desorption measurement was performed at -196 °C. The surface areas and pore volume were calculated by BET method and the pore size distribution was calculated by DFT methods. The surface area was calculated by Brunauer-Emmett-Teller (BET) method in the relative pressure range p/p_0 0.06-0.3.^[26] The pore size distribution and pore volume were calculated by density functional theory (DFT) method on the adsorption branch using a slit-based model. The total pore volume was estimated at p/p_0 0.989. The small-angle X-ray scattering set-up comprised the SAXSess mc2 instrument from Anton Paar GmbH (Graz, Austria), containing a slit collimation system, and the PW3830 laboratory X-ray generator (40 kV, 50 mA) with a long-fine focus sealed X-ray tube (CuK α wavelength of $\lambda = 0.1542$ nm) from PANalytical. Detection was performed with the 2D imaging-plate reader Cyclone[®] by Perkin Elmer. Measurements were performed on powder sample for 5 min and the data collected up to a scattering vector q value of 7 nm^{-1} , where $q = (4 \pi/\lambda) \sin(\theta/2)$ and 2θ the scattering angle. The 2D data were converted to 1D data and background-corrected by using SAXSQuant software (Anton Paar GmbH). Absorbance spectra were measured on a Shimadzu UV-3600 spectrophotometer double-beam UV-VIS-NIR spectrometer and baseline corrected. Raman spectra were recorded with a near infrared confocal Raman spectrometer (Labram ARAMIS, Horiba Jobin Yvon S.A.S., France). This setup consists of a microscope (Olympus, BX41, France) coupled to the Raman spectrometer equipped with 600 groove/mm diffraction grating. The microscope was equipped with a xy-motorized (Marzhauser, Germany), computer controlled sample stage, which enabled automatic scanning of the sample with a spatial resolution of 1 μm . The excitation source (785 nm) was provided by diode laser (Toptica Photonics, Germany) delivering 60 mW of laser power on the sample. This laser excitation was focused on the single cell with water immersion NIR 100x objective (NA 1, Olympus, France). This backscattered light is collected by the objective and is transmitted to the spectrometer equipped with a Pelletier-cooled charge-coupled device detector.

4.8 References

- [1] P. Sharma, S. Brown, G. Walter, S. Santra, B. Moudgil, *Advances in Colloid and Interface Science* **2006**, 123–126, 471–485.
- [2] N. Jiang, X.-Y. Yang, G.-L. Ying, L. Shen, J. Liu, W. Geng, L.-J. Dai, S.-Y. Liu, J. Cao, G. Tian, *et al.*, *Chemical Science* **2014**, 6, 486–491.
- [3] A. Laromaine, L. Koh, M. Murugesan, R. V. Ulijn, M. M. Stevens, *Journal of the American Chemical Society* **2007**, 129, 4156–4157.
- [4] Y. (Chezy) Barenholz, *Journal of Controlled Release* **2012**, 160, 117–134.
- [5] S. Nie, *Nanomedicine* **2010**, 5, 523–528.
- [6] D. A. Richards, A. Maruani, V. Chudasama, *Chemical Science* **2017**, 8, 63–77.
- [7] Y. Matsumura, H. Maeda, *Cancer Research* **1986**, 46, 6387–6392.
- [8] J. Fang, H. Nakamura, H. Maeda, *Advanced Drug Delivery Reviews* **2011**, 63, 136–151.
- [9] N. J. Abbott, A. A. K. Patabendige, D. E. M. Dolman, S. R. Yusof, D. J. Begley, *Neurobiology, Disease* **2010**, 37, 13–25.
- [10] C. Saraiva, C. Praça, R. Ferreira, T. Santos, L. Ferreira, L. Bernardino, *Journal of Controlled Release* **2016**, 235, 34–47.
- [11] M. J. Kim, R. Ryoo, *Chemistry of Materials* **1999**, 11, 487–491.
- [12] S. Giri, B. G. Trewyn, M. P. Stellmaker, V. S.-Y. Lin, *Angewandte Chemie International Edition* **2005**, 44, 5038–5044.
- [13] A. B. D. Nandiyanto, S.-G. Kim, F. Iskandar, K. Okuyama, *Microporous and Mesoporous Materials* **2009**, 120, 447–453.
- [14] A. Monnier, F. Schüth, Q. Huo, D. Kumar, D. Margolese, R. S. Maxwell, G. D. Stucky, M. Krishnamurty, P. Petroff, A. Firouzi, *et al.*, *Science* **1993**, 261, 1299–1303.
- [15] M. Mizutani, Y. Yamada, T. Nakamura, K. Yano, *Chemistry of Materials* **2008**, 20, 4777–4782.
- [16] L. Prezzi, L. Mascia, *Advances in Polymer Technology* **2005**, 24, 91–102.
- [17] E. Blanco, H. Shen, M. Ferrari, *Nature Biotechnology* **2015**, 33, 941–951.
- [18] G. Sonavane, K. Tomoda, K. Makino, *Colloids and Surfaces B: Biointerfaces* **2008**, 66, 274–280.
- [19] D. Liu, B. Lin, W. Shao, Z. Zhu, T. Ji, C. Yang, *ACS Applied Materials & Interfaces* **2014**, 6, 2131–2136.
- [20] J. Wu, C. Wang, J. Sun, Y. Xue, *ACS Nano* **2011**, 5, 4476–4489.
- [21] W. Stöber, A. Fink, E. Bohn, *Journal of Colloid and Interface Science* **1968**, 26, 62–69.
- [22] C. L. Frye, G. A. Vincent, W. A. Finzel, *Journal of the American Chemical Society* **1971**, 93, 6805–6811.
- [23] X. Lv, L. Zhang, F. Xing, H. Lin, *Microporous and Mesoporous Materials* **2016**, 225, 238–244.
- [24] K. Möller, J. Kobler, T. Bein, *Advanced Functional Materials* **2007**, 17, 605–612.
- [25] Z. Farhane, F. Bonnier, A. Casey, H. J. Byrne, *Analyst* **2015**, 140, 4212–4223.
- [26] S. Brunauer, P. H. Emmett, E. Teller, *Journal of the American Chemical Society* **1938**, 60, 309–319.

Chapter 5

ROS breakable silica nanoparticles

Abstract

The development of safe and efficient drug delivery systems has been a rising field for the last decades and recently, a novel class of stimuli-responsive nanomaterials has emerged for biomedical applications. Based on redox-, pH-, light- or enzyme-responsive moieties, those materials, once stimulated, allow the delivery of a cargo and simultaneously the nanomaterial allows then a safe excretion out of the body. Reactive Oxygen Species (ROS) responsive materials have also attracted a lot of attention for targeted drug delivery systems. Moreover, spatiotemporal control of the system can be achieved with the grafting of photosensitizers, which in presence of light, generate singlet oxygen and therefore create a self-destructible material. Such on/off switches render the material very attractive for photodynamic therapies and sustained drug delivery. In the following chapter, the development of ROS-breakable mesoporous silica nanoparticles will be presented. The synthesis of the ROS-cleavable linker was performed through a single-step reaction which leads to the development of the organo-hybrid mesoporous silica nanoparticles and their complete physico-chemical characterization. The breakability of the system has then been studied using singlet oxygen producers such as potassium superoxide or a photosensitizer with Rose Bengal. Finally, *in vitro* experiments were carried on to determine their efficient cellular uptake and the effect on the ROS level in cell lines such as HeLa, Glioma C6, Huh-7 and Hdfa cells.

5.1 Introduction

The rising field of nanomedicine and the wish to develop controlled drug delivery systems have led to the development of stimuli-responsive nanomaterials able to react on demand and release small molecules, oligonucleotides, or peptides in a precise manner.^[1-4] Stimuli-responsive polymers or liposomes have already been developed, presenting interesting properties and reaching clinical trials.^[5-7] In the case of mesoporous silica nanoparticles, stimuli-responsive moieties were mostly used as gatekeepers, protecting the guest entrapped within the pores from an early release.^[8] As an example, the collaboration between Prof. Zink and the Nobel Laureate Prof. Stoddard led to the development of several stimuli-responsive nanovalves grafted on the surface of mesoporous silica nanoparticles and which are able to open on demand to release their cargo.^[9-11]

However, as mentioned in the previous chapters, silica nanoparticles present interesting features as drug delivery systems although their degradability remains a big debate in the scientific community.^[12,13] In this regard, several organo-hybrid silica nanoparticles, containing stimuli-responsive moieties within their frameworks, have been synthesized. Thus, in presence of different stimuli such as a reducing agent,^[14-17] or an enzyme,^[18,19] the particles are breaking down in small pieces allowing the material to be cleared out from the body.^[20,21]

Recently, researchers have been focused on a novel type of linkers able to respond exclusively in presence of Reactive Oxygen Species (ROS). Such systems are much more tumor specific compared to redox-responsive strategies, thanks to the hypoxia environment of tumor cells which significantly increases the ROS production in cancer cells (up to 100 μM) compared to normal tissue (2 nM).^[22] Redox-responsive strategies, on the other side, rely on the concentration of glutathione in the cytoplasm of both cancer and healthy cells (2-10 mM) compared to the plasma (1-2 μM) and therefore do not offer a real tumor specificity.^[23] Selenium-, Tellurium- or Borane-based moieties, as well as sulfur-based linkers have been developed and react specifically towards oxidation by hydrogen peroxidase or singlet oxygen. In 2010, Wilson D.S *et al.* reported a poly-(1,4-phenyleneacetone dimethylene thioketal) polymer for the oral administration of a tumor necrosis factor α (TNF- α) small interfering RNA (siRNA) stable towards acidic, basic and protease degradation.^[24] Such stability confers to the material, the possibility to travel through different organ environments without being degraded until reaching the intestine inflammation where high levels of ROS are produced.^[25] Moreover, the increase of ROS is generally related to DNA mutation, linking their production to the progression of several cancers.^[26,27] Another interesting example has been recently published by Xu *et al.*, where prodrug nanoparticles were developed by synthesizing a

(NIR)-emitting anticancer drug mitoxantrone prodrug that can self-assemble with a lipid-polyethyleneglycol and a targeting Arginylglycylaspartic acid (RGD) peptide. Upon ROS exposure, the prodrug nanoparticles break and release the encapsulated mitoxantrone.^[28] For mesoporous silica nanoparticles, diselenide-based mesoporous silica nanoparticles have been synthesized very recently. Compare to the S-S moieties which have a bond energy of 240 kJ mol⁻¹, Se-Se presents a lower bond energy (172 kJ mol⁻¹) rendering their more sensitive under mild conditions and additionally can be cloven in both oxidative and reductive conditions.^[29]

Furthermore, increasing the concentration of singlet oxygen within the cells can easily be done by the addition of photosensitizer on the surface of the material. Light, especially wavelengths in the range of 600 – 1200 nm (optical window for tissue), penetrates deeply and locally the skin and is therefore often employed for diagnosis and therapies.^[30] Among them, photodynamic therapy (PDT) was the first drug-device approved by the US Food and Drug Administration and is often used in clinics.^[31] It is based on a laser which irradiates a tissue until reaching the tumor, where a photosensitizer previously injected accumulates and reacts with the surrounding environment to form singlet oxygen. Increasing singlet oxygen concentration within the cell thus leads to cell apoptosis and slow down the tumor growth. Photosensitizers present usually an absorbance peak between 600 and 800 nm to provide enough energy to promote oxygen to its singlet state and form enough reactive oxygen species.^[31,32] **Figure 5.1.a** presents the energy transfer from the triplet state of the photosensitizer to molecular oxygen, forming ¹O₂.

Good candidates are often tetrapyrrole rings based systems but modified organic dyes also present interesting properties. Moreover, replacing atoms by heavier ones increased the probability of reaching a triplet state, leading to a better photosensitizing effect.^[33] For example, fluorescein, a dye commonly used in microscopy present a low ¹O₂ quantum yield ($\Phi_{\Delta} = 0.03$). On the opposite, Rose Bengal, a fluorescein analog containing Cl and I increases the ¹O₂ quantum yield to 0.75 and is under clinical trial for the treatment of melanoma and breast cancer under the name of PV-10 (**Figure 5.1.b**).^[34] Upon irradiation, the photosensitizer produces singlet oxygen and thus destroys the particles, allowing a spatiotemporal control of the system for photodynamic therapy.

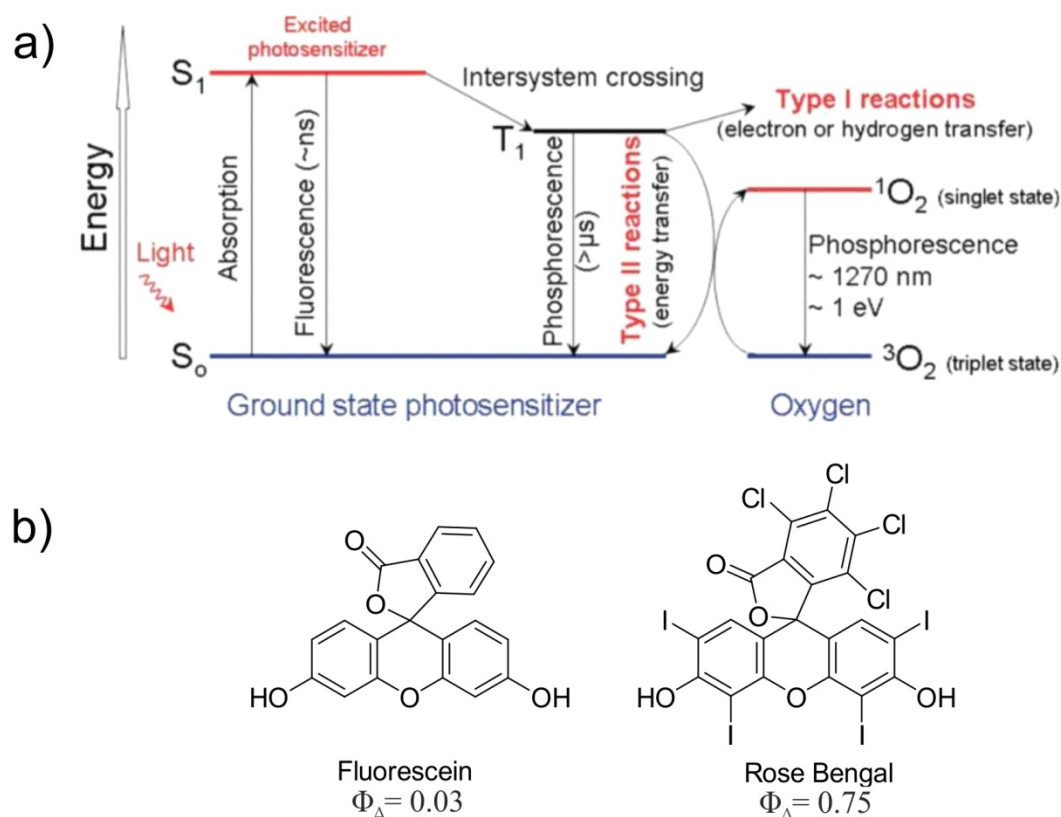


Figure 5.1: a) Modified Jablonski Diagram explaining the photosensitizing effect leading to the production of singlet oxygen and cytotoxic effect. Reprinted with permission from P Agostinis *et al.*, Photodynamic therapy of cancer: An update, *Cancer J. Clin*, 6, 250-281, 2011. Copyright © 2011 WILEY-VCH Verlag GmbH & Co. KGaA, Weinheim. b) Molecular structure of fluorescein (F) and Rose Bengal (RB) and their different $^1\text{O}_2$ quantum yields.

Diverse molecules, as for example porphyrins or indocyanine green have already been used.^[35,36] Qian *et al.* developed nanovesicles composed of a sensitizer (chlorin e6), a 2-nitroimidazole-thioether diblock copolymer, and Tirapazamine, a hypoxia-activated prodrug. Irradiation of the sample at 650 nm ensures a fast ROS production by the chlorin e6 leading to the disruption of the endosomes and the oxidation of the thioether into a sulfoxide. Simultaneously, the localized hypoxic environment generated thanks to the high oxygen consumption reduces the nitro-imidazole in amino-imidazole and rendering it perfectly water soluble. The prodrug is then released and activated in the hypoxic environment leading to cell apoptosis.^[37] These features imply then a safe destruction of the cargo, generally faster compared to the use of redox- or protease-responsive materials.

It has been demonstrated also that the uptake of exogenous materials by the cells increases the production of ROS within the cells.^[38] Lehman *et al.* recently published a study about the formation of ROS directly on the surface of silica nanoparticles within murine macrophage cell line (RAW 264.7).^[39] Factors, such as silanol density, porosity and surface

functionalization affect the quantity of ROS produced and therefore the cell viability. Moreover, oxidative stress is induced after exposition to nanoparticles, leading to glutathione depletion, and thus to cellular damage due to the excess of ROS generated.^[40]

In the following chapter, the development of ROS-breakable mesoporous silica nanoparticles will be presented. The synthesis of the ROS-cleavable linker was performed through a single-step reaction and the ROS-responsive organo-hybrid mesoporous silica nanoparticles were then synthesized, followed by their complete physico-chemical characterization. The breakability tests were then performed with potassium superoxide or Rose Bengal, known to produce large amounts of singlet oxygen (**Figure 5.2**). Finally, cytotoxicity of the nanoparticles, as well as the efficient cellular uptake was tested *in vitro* in different cell lines such as HeLa, Glioma C6, Huh-7 and Hdfa cells.

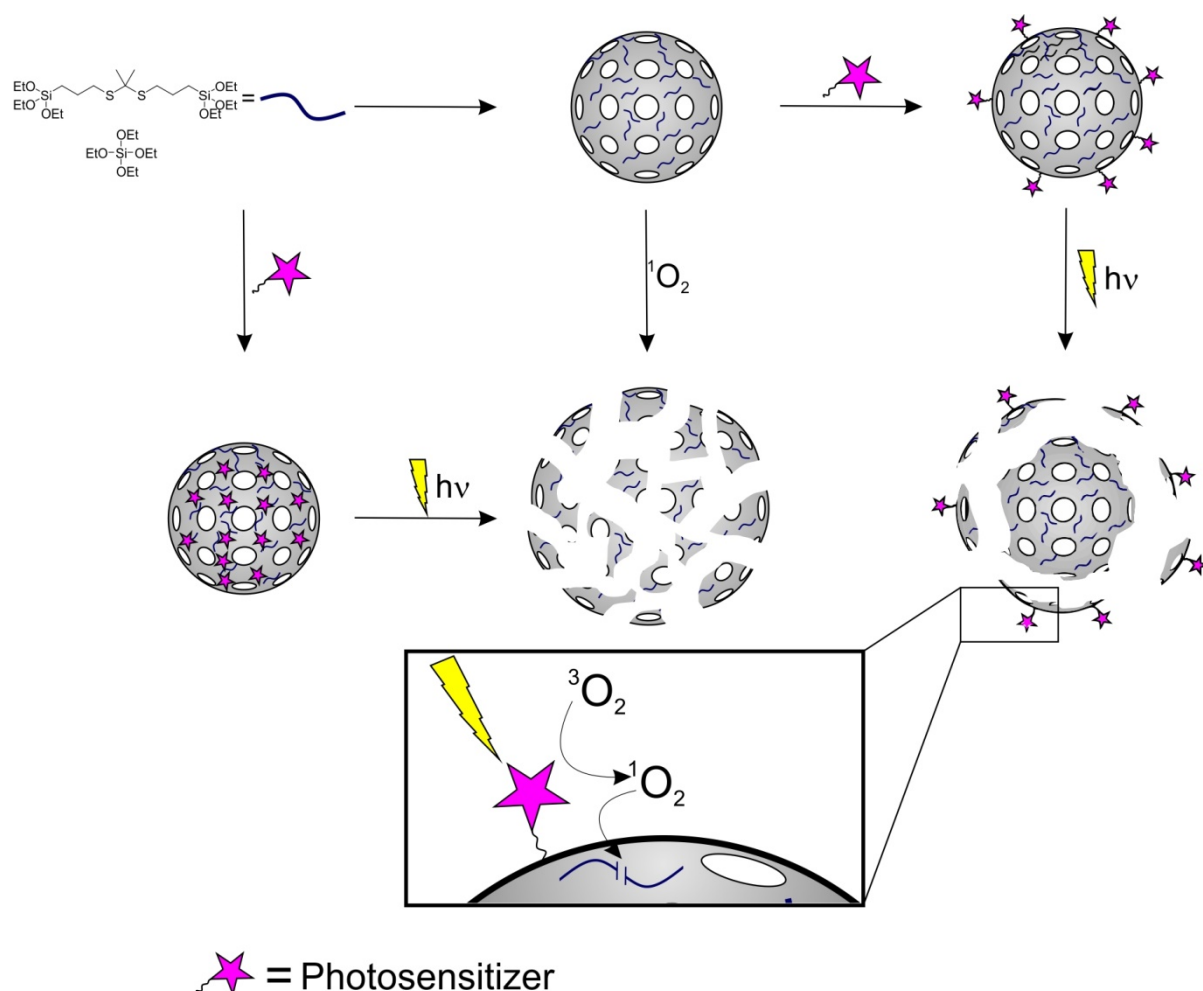


Figure 5.2: Schematic representation of the different ROSNPs synthesized.

5.2 Synthesis of the ROS-responsive linker

The first step for the smart design of a stimuli-responsive material is the choice of a stable linker able to respond only in a presence of a certain stimulus. As seen in previous chapters, several linkers have been developed or used in the laboratory for the synthesis of organo-hybrid stimuli-responsive breakable silica nanoparticles. Moieties able to be cloven in presence of specific reducing agent (glutathione), enzymes, by a change of pH or even simply by irradiation has been already developed and published for a few of them. The synthesis of ROS-breakable silica nanoparticles has then been thought in order to react specifically towards singlet oxygen. Several types of ROS responsive linkers have already been reported to develop stimuli-responsive polymeric nanoparticles and a schematic representation of them can be seen in **Figure 5.3**.^[41] Those linkers have been categorized in three compartments divided by sulfur-containing linkers; Se-, Te- and B- based linkers and finally the one that cannot be classified.

For the large scale development of organo-hybrid nanomaterials, the synthesis of the linkers has to be easy and straightforward leading to the final moiety in a one- or two-steps reaction. After assessing several types of linkers already reported for polymeric nanoparticles, the choice of using a thioketal group was made. Thanks to the commercially available 3-(mercaptopropyl)triethoxysilane (MPTES), the main issue of grafting a silane group on the linker was avoided. As depicted in **Figure 5.4.a**, the MPTES was mixed with a stoichiometric amount of neat 2,2-diethoxypropane at 90 °C for 4 h in presence of methane sulfonic acid as an acidic catalyst. Through the reaction, the formed EtOH was distilled out in order to push the reaction equilibrium towards the formation of the final linker. The product was then solubilized in chloroform and the acid was removed before drying followed by characterization by ^1H NMR (**Figure 5.4.b**). ^1H NMR characterization revealed the presence of the peak at 1.58 ppm (s, 6H) characterizing the thioketal protons. Then, at 1.22 ppm (t, 18H) and 3.81 ppm (q, 12H) represent the ethoxy groups and finally at 0.74 ppm (t, 4H), 1.69 ppm (m, 4H) and 2.62 ppm (t, 4H) are the alkyl chains. ^{13}C NMR revealed instead 7 peaks corresponding to the seven different carbons observable. The 2 peaks at 18.37 ppm and 58.44 ppm correspond to the ethoxy groups. Peaks at 10.58, 23.24 and 33.37 ppm represent the carbons from the aliphatic chain and finally, at 31.26 and 55.61 ppm, the carbons from the thioketal group are represented. A complete attribution of the peaks is represented in **Figure 5.3.c**.

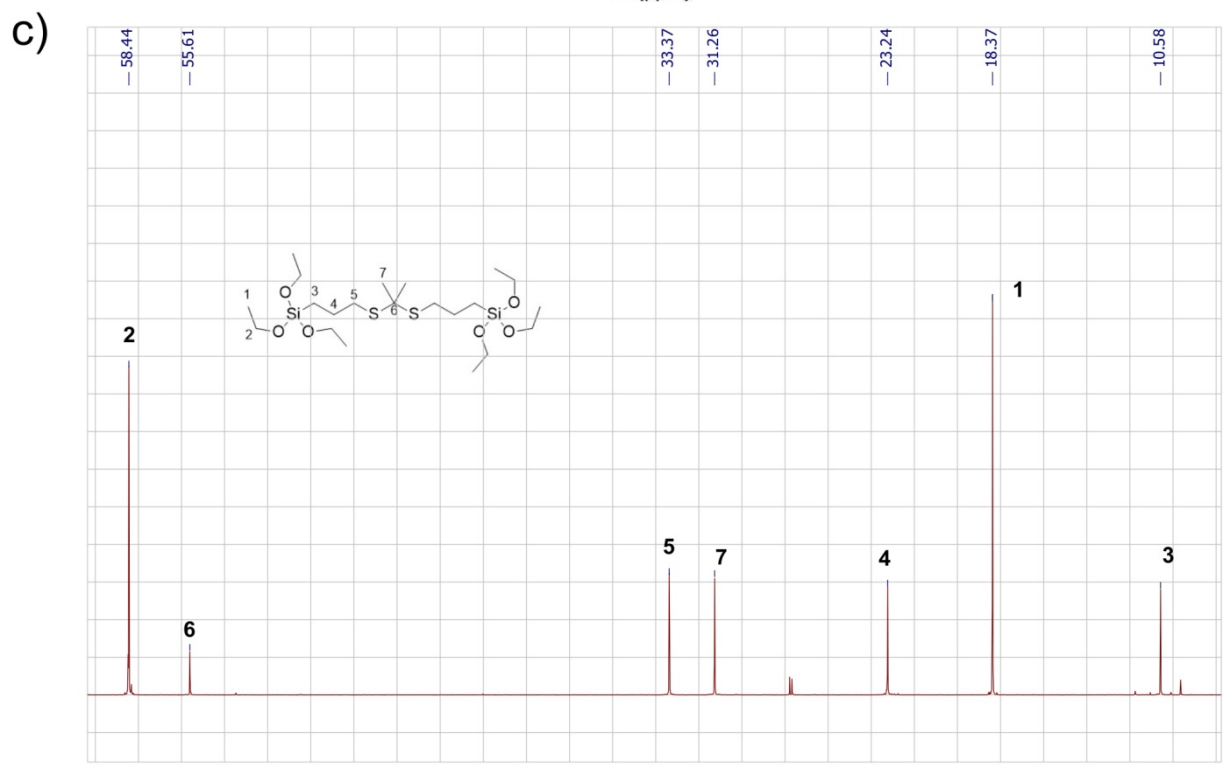
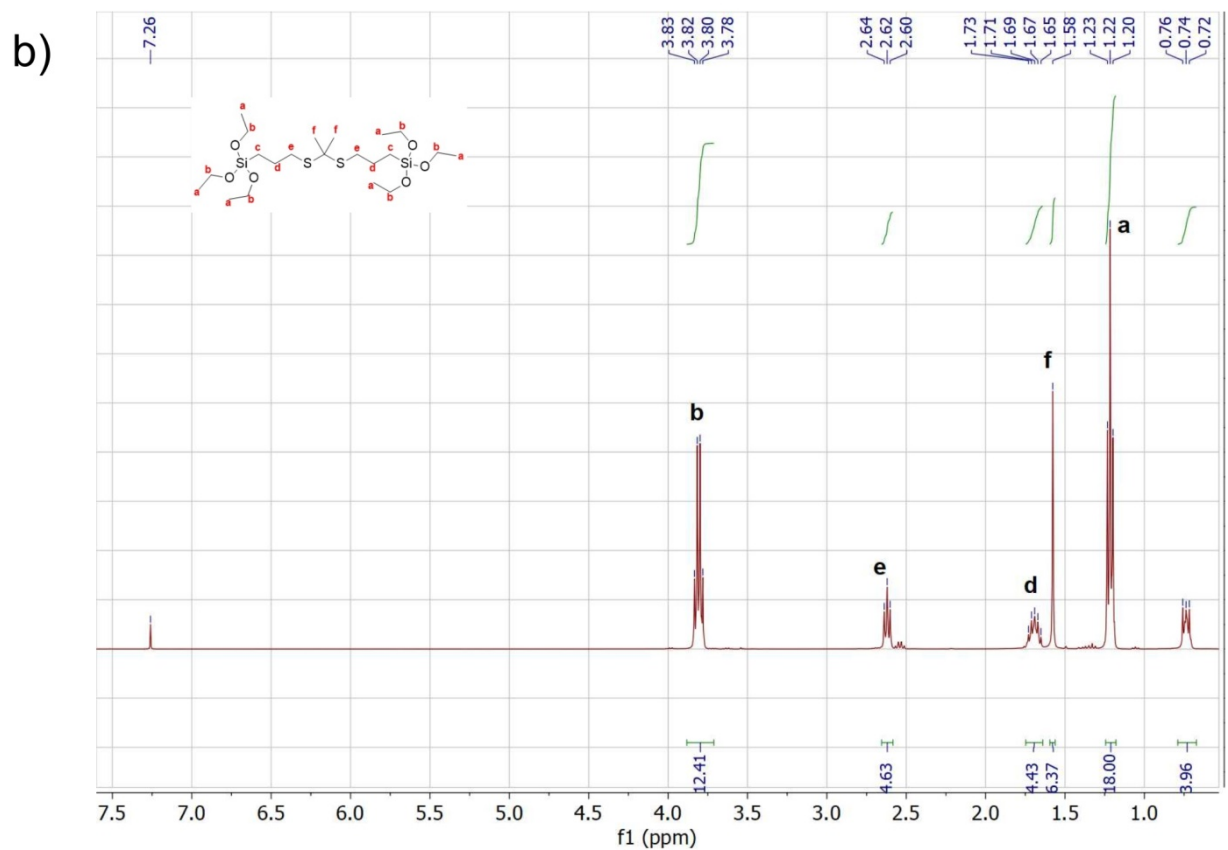
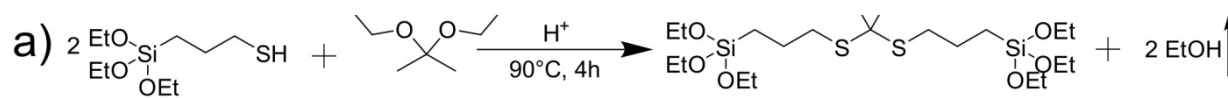


Figure 5.4: a) Synthetic representation for the formation of the ROS-responsive linker and b) the ^1H NMR and c) ^{13}C NMR.

The compound was also characterized by high resolution ESI-TOF MS. As depicted on **Figure 5.5**, a peak can be observed at 539 m/z matching with the molecule of interest ($m/z = 516.24$) plus an atom of sodium ($m/z = 22$).

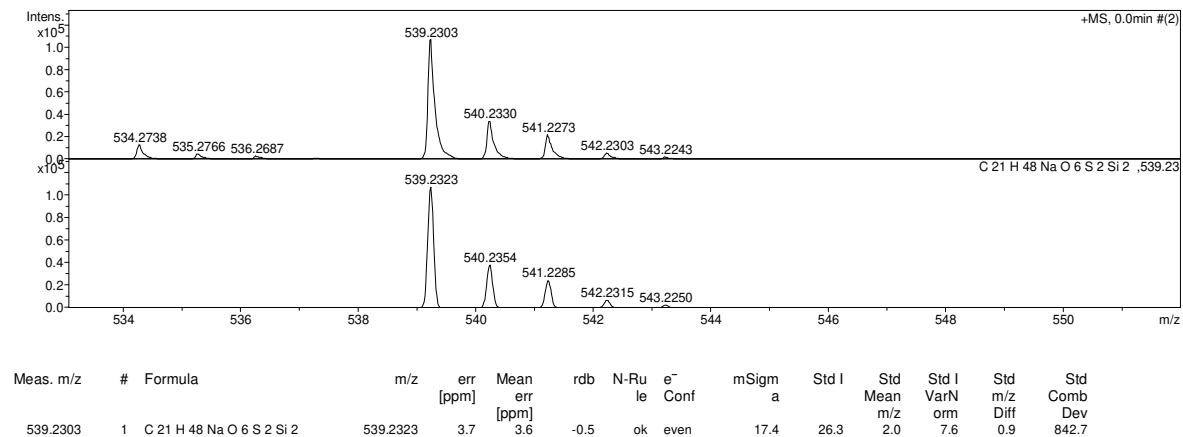


Figure 5.5: ESI-TOF Mass spectroscopy of the ROS linker.

5.3 Synthesis and characterization of ROSNPs

5.3.1 Synthesis of ROSNPs

The particles were synthesized using, as previously reported for the ssNPs (Chapter 2), a modified Stöber process for the preparation of circa 100 nm nanoparticles.^[14,42] In this case, the bis(triethoxysilyl-propyl)disulfide was replaced by the ROS-responsive linker keeping exactly the same molar ratio. Once again, cetyltrimethylammonium bromide (CTAB) was used as a surfactant template and the reaction was heat up at 80 °C for 6 h before washing by means of sonication/centrifugation cycles with EtOH. CTAB removal was then performed by refluxing the particles in acidic EtOH (50 mL, 20 μ L of HCl).

5.3.2 Material characterizations

As already explained in the previous chapters, the first characterization is the morphology of the nanomaterial. For this purpose, SEM (**Figure 5.6.a**) and TEM (**Figure 5.6.b**) analysis were performed and presented homogeneous spherical nanoparticles. Counting of 200 nanoparticles on SEM pictures with Image J software showed a size distribution of 105 ± 12 nm (**Figure 5.6.c**).

The particles, also measured by Dynamic Light Scattering, presented a size of 131 ± 28 nm. Slight increase compare to SEM measurements can be observed, due to the presence of hydrodynamic shell around the particles during the DLS measurement (**Figure 5.6.d**).

The pore size could also be observed by the TEM images where the profile of frame presented a distance between two pores of 2 nm (**Figure 5.6.e**). Porosity was further confirmed by nitrogen adsorption measurements (**Figure 5.7.a**) and adsorption/desorption isotherms analysis allowed to calculate for ROSNPs a BET surface area of $327 \text{ m}^2 \text{ g}^{-1}$, total pore volume of $0.62 \text{ cm}^3 \text{ g}^{-1}$ and an average pore size of 2.0 nm (**Figure 5.7.b**).

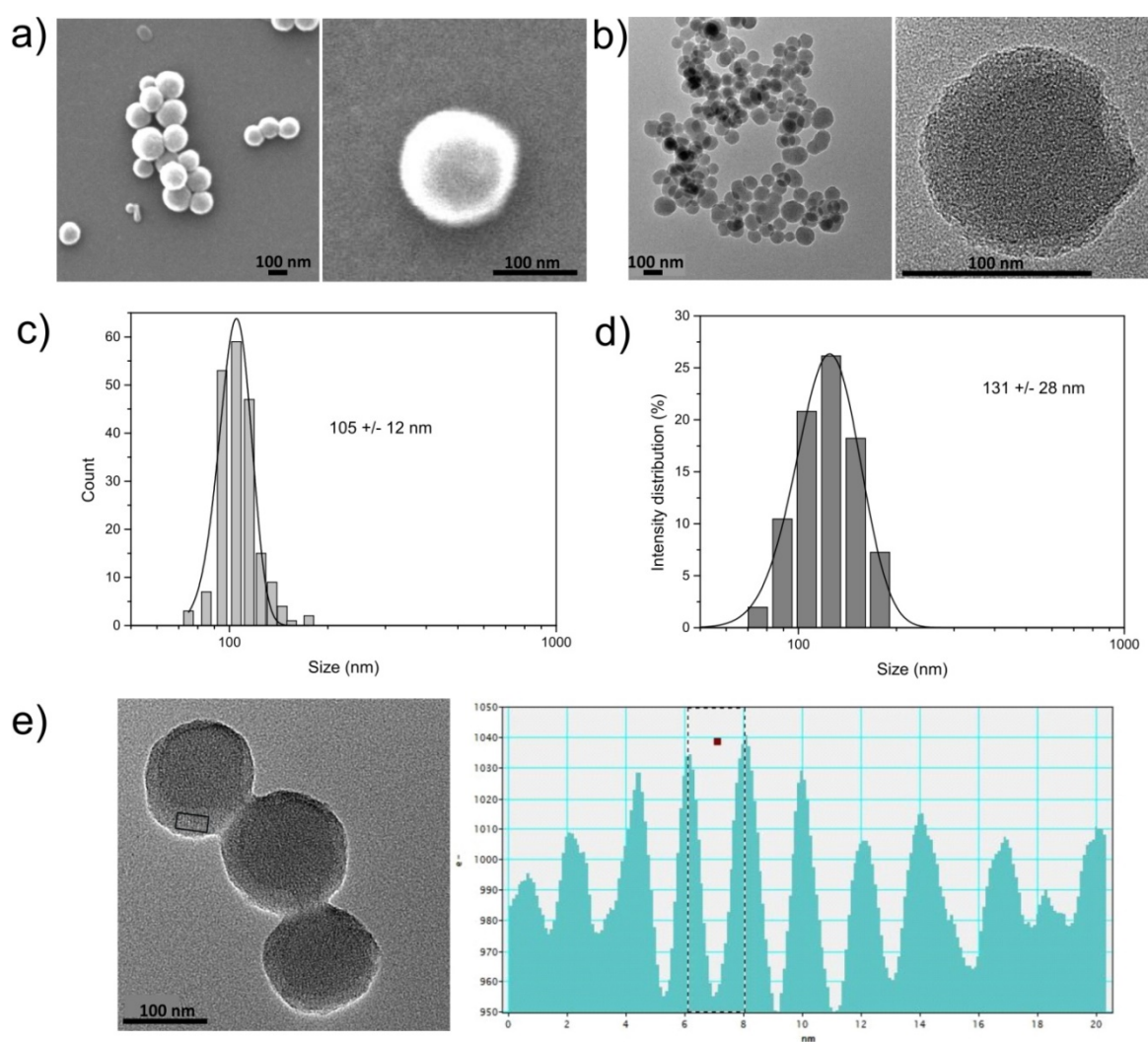


Figure 5.6: a) SEM and b) TEM images of ROSNPs. On the left size, images of several nanoparticles on the right side, zoomed image of a single nanoparticle. Scale bar = 100 nm. Size distribution of ROSNPs determined by c) SEM counting of 200 particles and d) DLS analysis of a suspension at $0.1 \text{ mg} \cdot \text{mL}^{-1}$. e) TEM images (on the left) and profile of frame (on the right) taken from the rectangle. Scale bar = 100 nm.

Small angle X-ray scattering SAXS was performed to determine a possible ordered porosity (**Figure 5.7.c**). ROSNPs presented the same characteristic as the ssNPs presented in Chapter 2. The characteristic (100) Bragg peak could be observed, however once again the (110) and (200) peaks were not present resulting to a disordered pore arrangement due to the presence of the organic linker.

The presence of the cleavable linker within the particles was confirmed by elemental analysis of the material conducted by X-ray photoelectron spectroscopy (XPS; **Table 5-1** and **Figure 5.7.d**). The presence of the silica framework was characterized by the high atomic percentage of O(1s) and Si(2p) whereas the doping of the organic linker was proven by the detection of C(1s) and S(2p) signals.

Table 5-1: XPS analysis of ROSNPs.

Name	Peak BE	Atomic %
O1s	532.81	39.61
Si2p	103.16	20.76
C1s	285.19	35.87
S2p	163.52	3.76

The ratio between organic/inorganic moieties was then characterized by thermogravimetric analysis (TGA; **Figure 5.7.e**). A significant weight loss of 24% was observed corresponding exclusively to the organic linker present in the framework of the particle.

All those results are comparable to the one obtained with the disulfide-doped breakable mesoporous silica nanoparticles. Small changes in the linker did not change the principal characteristics of the organo-hybrid material.

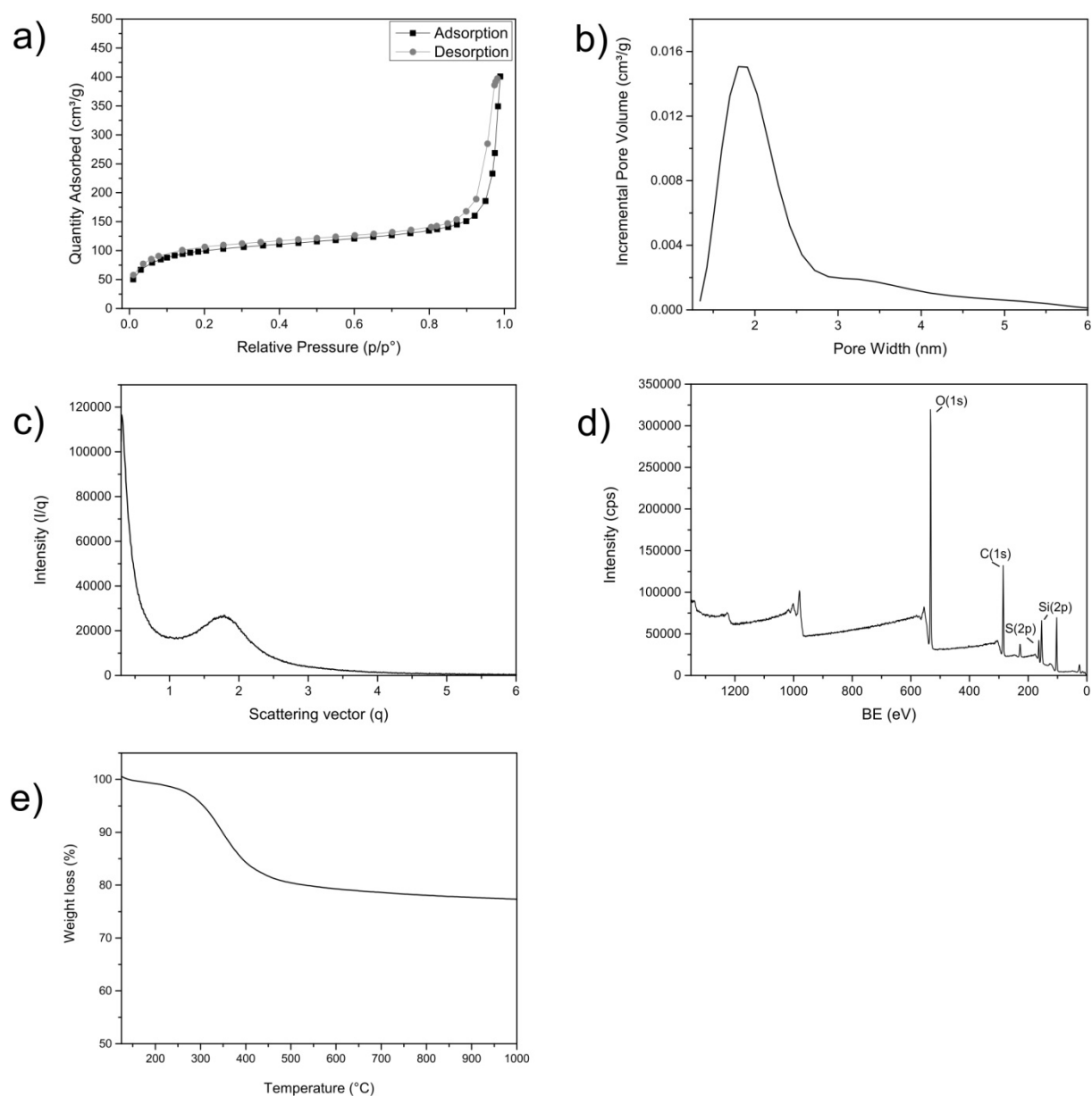


Figure 5.7: Physico-chemical characterization of the ROSNPs. a) N_2 adsorption/desorption isotherms. b) Pore width distribution. c) SAXS pattern. d) XPS survey. e) TGA plot presenting a weight loss a 24 % corresponding to the organic linker.

5.4 Breakability tests

5.4.1 Breakability by Potassium superoxide (KO_2)

Once internalized within the cells, the particles should be able to deliver their cargo and most importantly, to break down in small pieces. In order to follow the degradation process, several chemical compounds able to produce singlet oxygen can be exploited. As an example, potassium superoxide is often employed as it is decomposing in 1O_2 , KOH and H_2O_2 in presence of water. Researchers usually incubated polymeric nanoparticles in presence of

KO₂ for several hours and measure the molecular weight by HPLC.^[24,28] For formed particles, electron microscopy offers directly the possibility to image the breaking of the nanoparticles. In this regard, 0.1 mg·mL⁻¹ dispersion of ROSNPs and MSN were incubated in a 10 mM KO₂ solution in milliQ water for 2 d. After 3 h, 1 d and 2 d, aliquots were taken and dropcasted on TEM grids before observation under STEM. As negative control, dispersion of ROSNPs and MSN were also dispersed in milliQ water and incubated for 3 h, 1 d and 2 d. As observed on **Figure 5.8**, slight deformation of the particles could be observed already after 3 h of incubation whereas MSNs remained intact after the same amount of time. After one day, the degradability was even more pronounced until being almost completely destroyed after 2 days of incubation. On the other side, MSNs remained completely intact for the same amount of time and no degradability was observed in presence of potassium superoxide. Control experiments without KO₂ presented no degradability after 2 days for both MSN and ROSNPs.

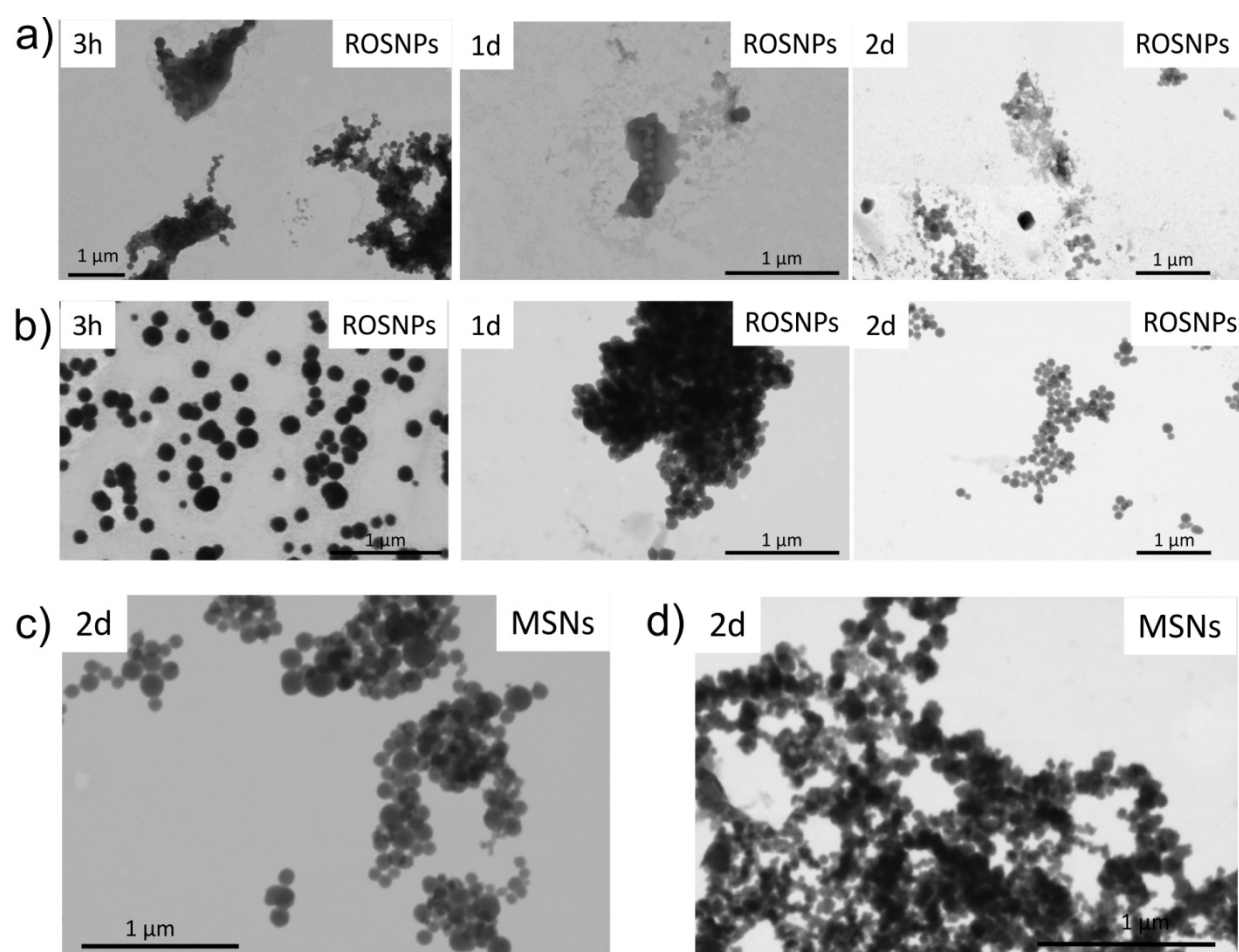


Figure 5.8: Breakability test on a dispersion of particles (0.1 mg·mL⁻¹). a) ROSNPs incubated for 3 h, 1 d and 2 d in a solution of KO₂ (10 mM). b) ROSNPs incubated for 3 h, 1 d and 2 d in milliQ water (control). c) MSN incubated 2 d in a solution of KO₂ (10 mM). d) MSN in incubated for 2 d in milliQ water (control). Scale bar = 1 μm.

5.4.2 Breakability with a photosensitizer (Rose Bengal)

As a good $^1\text{O}_2$ producer, Rose Bengal was therefore used to test the breakability of the particles. $0.1 \text{ mg}\cdot\text{mL}^{-1}$ of ROSNPs and MSNs were dispersed in a solution of Rose Bengal at 10^{-2} M in milliQ water. High concentration was tested to ensure the breakability of the particles but also to prove that high concentration of $^1\text{O}_2$ would not affect the MSN. Samples were irradiated under a Hg lamp for 4 h and then dropcasted on TEM grids before STEM analysis. Control experiments were also performed by keeping the dispersion of ROSNPs and MSN in the dark. As shown in **Figure 5.9**, both ROSNPs and MSN did not show any degradation without irradiation after 4 h of incubation showing the stability of the particles. MSN even incubated in a high concentrated solution of Rose Bengal, those generating huge amount of $^1\text{O}_2$ and under light irradiation, did not show any breaking during the exposure time. On the opposite, ROSNPs, treated in the same condition presented an advanced degradation rate as confirmed with the presence of light clouds around the nanoparticles.

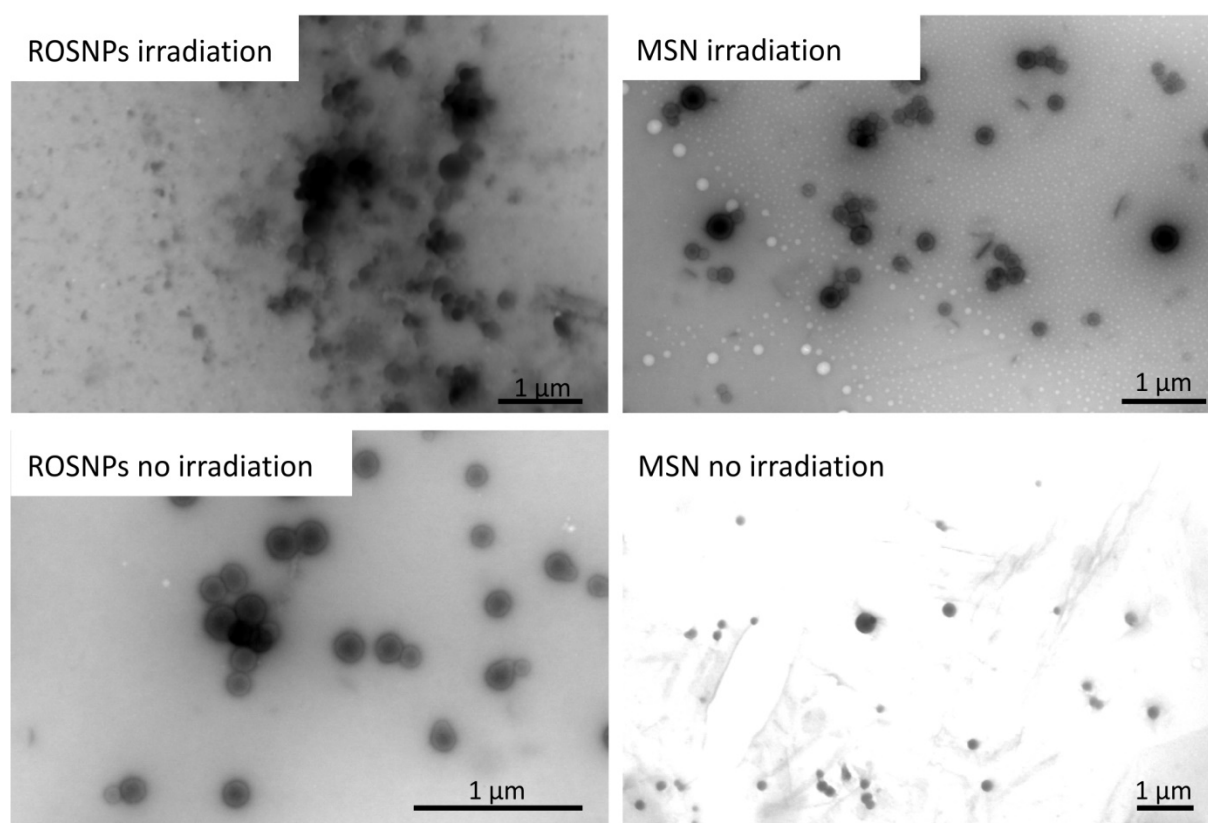


Figure 5.9: STEM micrographs of the breakability of particles incubated for 4 h at $0.1 \text{ mg}\cdot\text{mL}^{-1}$ in a 10^{-2} M solution of Rose Bengal. Images of ROSNPs with (top left) and without light irradiation (down left) and MSN with (top right) and without light irradiation (down right). Scale bar = $1 \mu\text{m}$.

The selective breakability of the ROSNPs in presence of Rose Bengal under light irradiation has been proven in a highly concentrated solution of the dye. As the Rose Bengal produces the singlet oxygen, its concentration in solution should directly influence the breakability of the ROSNPs. Thus, the breakable nanoparticles were incubated with different concentrations of the singlet oxygen producer (ranging from 10^{-2} to 10^{-5} M) and irradiated under Hg lamp for 4 h. As predicted, the different concentrations had an impact on the degradability behavior of the material (**Figure 5.10**). As already shown in (**Figure 5.9**), incubation at 10^{-2} M presented a really advanced breakability of the particles after only 4h of incubation. When the concentration is decreased to 10^{-3} M, efficient degradation still occurs. At 10^{-4} M, very light breaking was noticed compared to 10^{-5} M that did not show any destruction of the material.

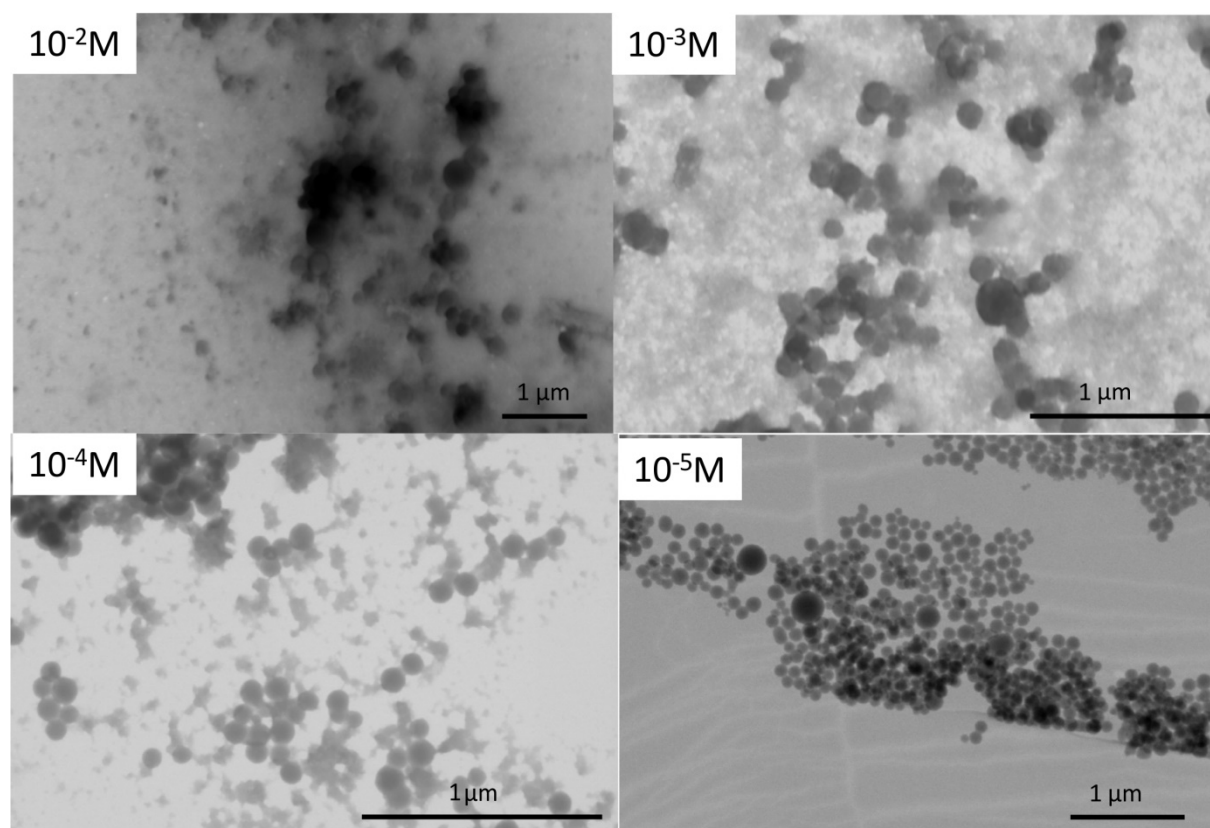


Figure 5.10: STEM analysis of a suspension of ROSNPs at $0.1 \text{ mg}\cdot\text{mL}^{-1}$, in presence of different concentrations of Rose Bengal in water (from 10^{-2} M to 10^{-5} M). All the samples were irradiated for 4h with an Hg lamp. Scale bar = $1 \mu\text{m}$.

5.4.3 Rose Bengal functionalization on the surface of ROSNPs

Rose Bengal presented interesting characteristics to generate singlet oxygen and therefore could be utilized as photosensitizer to break the ROSNPs. However, *in vitro*, only the ROS produced by the cells are able to break the particles and increasing the ROS level is an interesting initiative for photodynamic therapy and could enhanced the breakability kinetics of the ROSNPs. As shown in the introduction part, several examples already exist combining ROS-responsive linkers and photosensitizers to enhance locally the ROS production and thus increasing the breakability rate of the nanoparticles.^[35,37] Therefore, grafting of Rose Bengal directly on the surface of the ROSNPs could directly enhance the ROS production around the nanoparticles and increase the degradability rate. In this regard, Rose Bengal was first modified in order to link a spacer finishing with a carboxylic acid. The first step reaction is the esterification with 6-bromohexanoic acid (RBHA) followed by the activation of the carboxylic acid with *N*-hydrosuccinimide (RBHAOSu). The synthetic pathway is represented in **Figure 5.11.a** and was performed following the literature.^[43,44] Both excitation and emission spectrum measurements (**Figure 5.11.b and c**) presented a shift of 20 nm towards longer wavelengths after grafting of the hexanoic acid moiety.

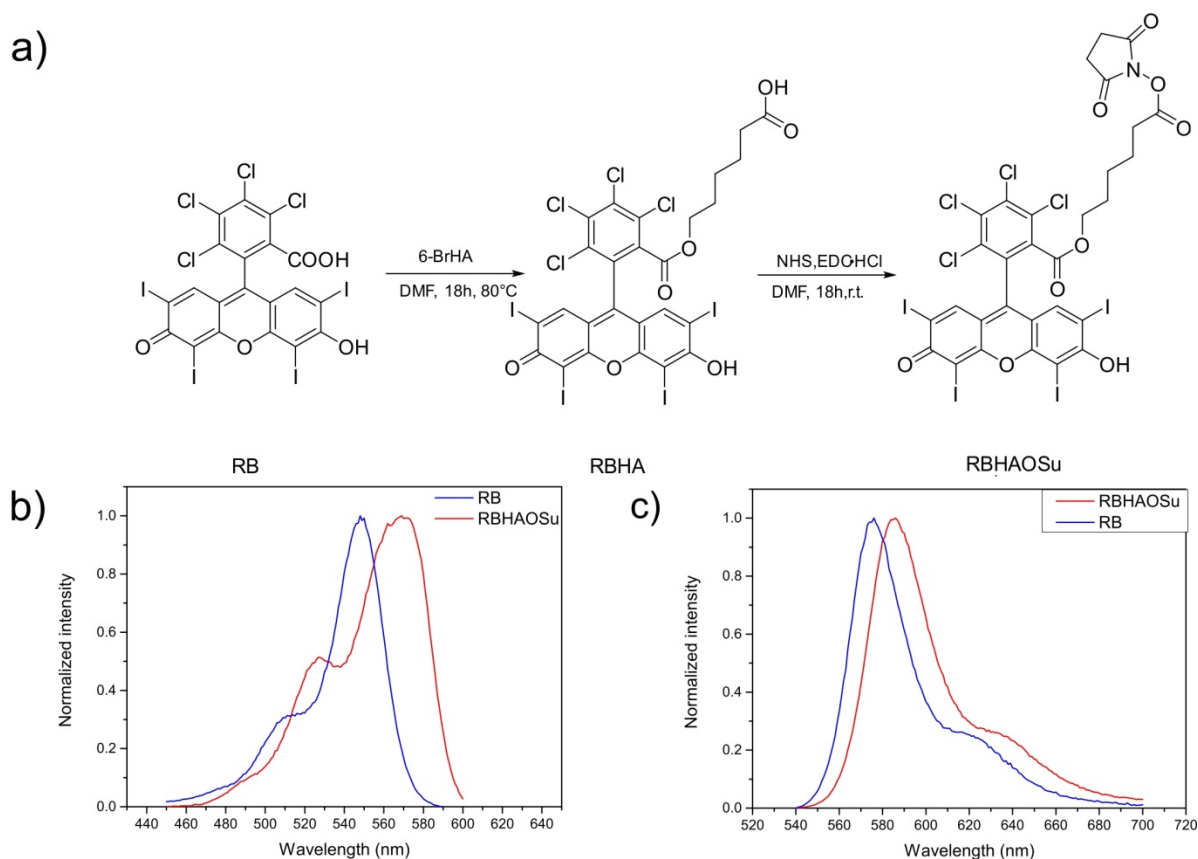


Figure 5.11: a) Synthetic pathway of RBHAOSu. b) Excitation spectrum and c) emission spectrum of RB (blue) and RBHAOSu (red) performed in EtOH. $\lambda_{em} = 610$ nm $\lambda_{exc} = 515$ nm.

The ROSNPs were then functionalized overnight by mixing in one pot, the nanoparticles, APTES and RBHAOSu in presence of triethylamine as a basic catalyst. The particles (ROSNPs-RBout) were then centrifuged and washed thoroughly with ethanol until to obtain a clear supernatant. Comparison was also performed by synthesizing Rose Bengal-doped ROSNPs by adding during the synthesis of the ROSNPs, a mixture of APTES and RBHAOSu (ROSNPs-RBin). The particles were then dried and TGA analysis was performed to determine the functionalization degree of ROSNPs-RBout and ROSNPs-RBin (**Figure 5.12**). As already shown previously, pristine ROSNPs presented a weight loss of 24 % due to the presence of the organic linker. After grafting, weight losses were more significant due to the presence of APTES and the different amounts of Rose Bengal attached. ROSNPs-RBout and ROSNPs-RBin presented weight losses of 34 % and 43% corresponding to functionalizations of 10 % and 19 % respectively.

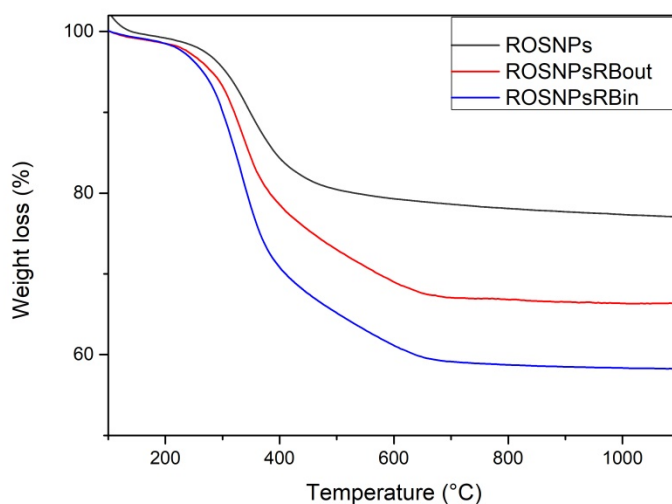


Figure 5.12: TGA Thermogram of ROSNPs and ROSNPsRB. Pristine ROSNPs presented a weight loss of 24 % corresponding to the organic linker. On the other side, ROSNPsRBout (red) and ROSNPsRBin (blue) showed a weight loss of 34 and 43 % respectively due to the efficient grafting of the photosensitizer.

A breakability test was again performed by dispersing ROSNPs-RBout and ROSNPs-RBin in milliQ water following the same conditions as previously described. **Figure 5.13.a** presents a TEM image of ROSNPs-RBout after incubation. Interestingly, the particles presented degradability only within the pores and on the particles surface. After breaking of the linker close to the photosensitizers, the dye was then released within the media and therefore was not close enough to the particles to induce an improved breaking. However, the doping of the Rose Bengal within the framework of the ROSNPs led to a complete destruction

of the particles with the same conditions as it can be observed on the STEM image (**Figure 5.13.b**)

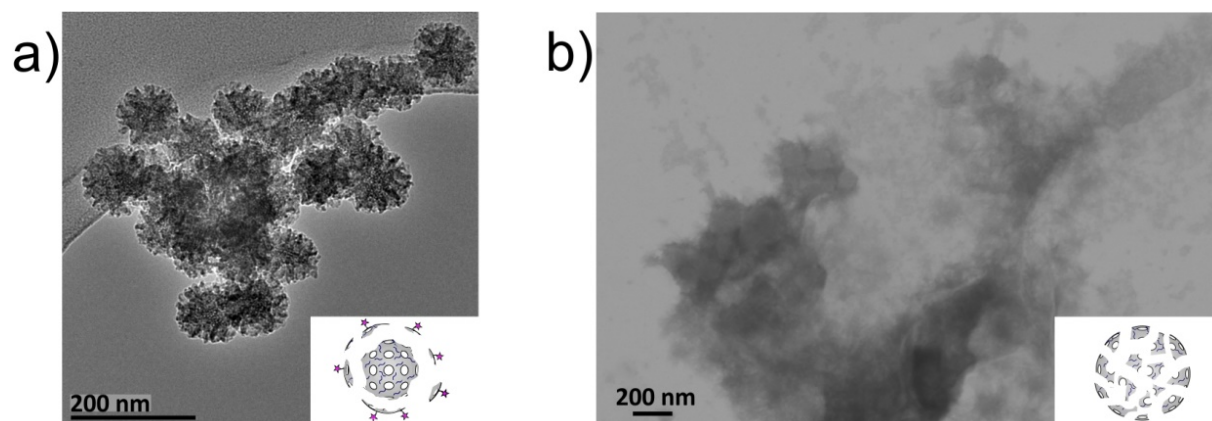


Figure 5.13: a) TEM image of ROSNPs-RBout and b) STEM image of ROSNPs-RBin. Scale bars = 200 nm.

5.5 *In vitro* experiments

Complex systems such as the biological environment require a lot of investigations for the understanding of cell-nanoparticles interactions. Cell type and nanoparticles present different behaviors depending on their association. Therefore, a material that would enter efficiently in one cell line would not necessarily present the same efficiency towards another cell line, mostly if the comparison is performed between a healthy and a cancer cell line. For instance, Vilaça *et al.* studied the internalization of zeolites within MCF-10, Hs578t and HMEC cells and demonstrated that cancer cells presented a higher permeability and therefore a faster internalization of nanomaterials.^[45] Intracellular characteristics also render stimuli-responsive materials interesting for the delivery of therapeutics within cancer cells. As explained previously, compared to other stimuli, ROS-responsive materials presented a better tumor specific approach where the ROS production in cancer is higher (up to 100 μM) compare to normal cells (2 nM).^[22] More importantly, ROS production is also cell line dependent and concentration can vary between tumor lines. Xu *et al.* studied four different prostate cancer cell lines (PC3, DU145, 22RV1, and LNCaP) and all presented different ROS concentrations.^[28] Thus would therefore modify the breakability kinetics of the different ROS-responsive nanomaterials. In this case, the *in vitro* behavior of the ROSNPs was study in four different cell lines, cancerous and healthy, from different organs. HeLa cells, coming from cervix cancer, are the oldest and most used human cells for *in vitro* studies. Huh-7, already presented in Chapter 2, are human hepatocellular carcinoma cells. Glioma C6, are rats glioblastoma cells. Finally, Hdfa are human dermal fibroblasts.

5.5.1 Cytotoxicity

Cytotoxicity of the ROSNPs was then studied in the four different cell lines with an Alamar blue assay. It is a metabolic activity test that relies on the reduction of rezasurin in resorufin within the cells. Resazurin presents a strong absorbance at 570 nm while its reduced form is shifted to 600 nm. Measurement of the absorbance and thanks to their additive properties, it is then possible to determine the concentration of the reduced form. Comparing this value to the control with only cells, it is then possible to have approximately a cell viability percentage. The metabolic activity assay was performed after 3, 24, and 48 h of incubation with the ROSNPs at two different concentrations (50 and 100 $\mu\text{g}\cdot\text{mL}^{-1}$). As shown in **Figure 5.14**, the new material did not show any cytotoxicity towards the cell lines tested up to 100 $\mu\text{g}\cdot\text{mL}^{-1}$ and 48 h of incubation. Their non-cytotoxicity renders them suitable for the safe delivery of molecules.

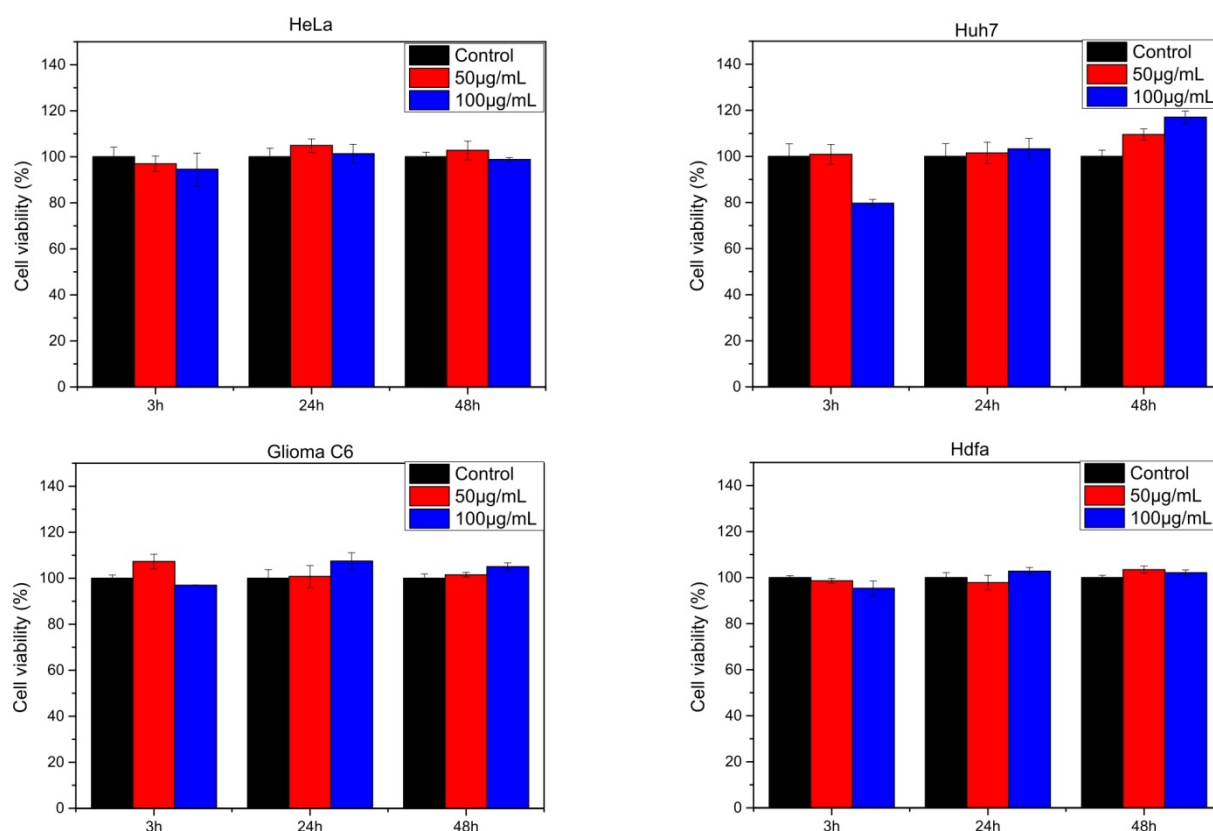


Figure 5.14: Metabolic activity performed with an Alamar Blue assay on four different cell lines (HeLa, Huh-7, Glioma C6 and Hdfa) after 3, 24 and 48 h with different concentrations of ROSNPs (50 and 100 $\mu\text{g}\cdot\text{mL}^{-1}$).

5.5.2 Synthesis of FITC-ROS NPs

Synthesis of ROS NPs was performed by adding *in-situ*, a mixture of pre-reacted fluorescein isothiocyanate (FITC) with APTES. Such procedure gives the opportunity to have the dye, not only on the surface of the pores, but also within the silica framework. Dye incorporation allows the intracellular tracking of the nanoparticles. Photophysical characterization of the dye were performed and presented the characteristic peaks of fluorescein with a maximum excitation band at 494 nm and a maximum emission at 521 nm. **(Figure 5.15).**

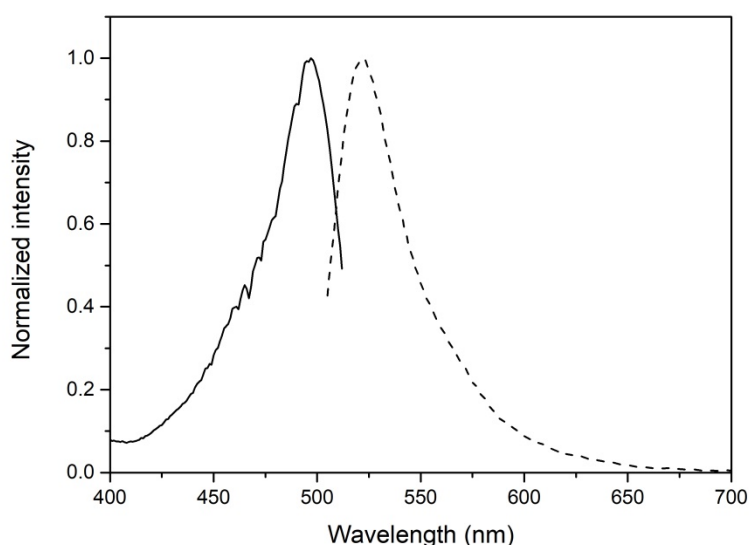


Figure 5.15: Photophysical characterization of the FITC-ROS NPs. The full line represents the excitation profile while the dashed line corresponds to the emission spectrum. $\lambda_{exc}= 495$ nm $\lambda_{em}= 522$ nm.

5.5.3 Cellular uptake followed by confocal microscopy

The efficient cellular internalization was then studied by confocal laser scanning microscopy (CLSM). FITC-ROS NPs ($50 \mu\text{g}\cdot\text{mL}^{-1}$) were incubated with the different cell lines for 3, 24 and 48 h. The cells were then fixed and the nuclei were stained with Hoechst 33342. Confocal micrographs in HeLa (**Figure 5.16**), Huh-7 (**Figure 5.17**), Glioma C6 (**Figure 5.18**) and Hdfa (**Figure 5.19**) showed different behavior between the cell lines and the nanoparticles. HeLa and Huh-7 cells seemed to internalize the ROS NPs in the same manner, while Glioma C6 presented a very high cellular uptake. However, Hdfa did not internalize efficiently the ROS NPs even after 48 h of incubation. Z-stacking analysis on cells incubated for 24 h and stained with Alexa Fluor® 647 Phalloidin (f-actin staining) demonstrated the internalization of the nanoparticles within the cells as it can be observed with the diffusion of the yellow signal (corresponding to the ROS NPs) through the y-z and z-x axes.

5.6 Conclusion

The synthesis of a new kind of stimuli-responsive mesoporous silica nanoparticles was demonstrated. The particles demonstrated interesting breakability properties upon reaction of the thioketal linker with singlet oxygen. The material was then doped with a photosensitizer, able to produce large amount of singlet oxygen, which allows a spatiotemporal breaking of the nanocarrier upon light exposure. Finally, preliminary *in vitro* experiments were performed and did not show any cytotoxicity in the cell lines tested, but interestingly presented also different cellular uptake behaviors.

5.7 Materials and Methods

5.7.1 Chemicals

All commercial solvents and reagents were used as received from, without further purification. Tetraethyl orthosilicate (TEOS), (3-aminopropyl)triethoxysilane (APTES), fluorescein isothiocyanate (FITC, mixed isomers), N-hydrosuccinimide, triethylamine (TEA), 3-mercaptopropyltriethoxysilane, paraformaldehyde (PFA), Rose Bengal, Triton X-100, 6-bromohexanoic acid, N-(3-Dimethylaminopropyl)-N'-ethylcarbodiimide hydrochloride, Bovine Serum Albumine (BSA), Fluoromont aqueous mounting medium, and all solvents were purchased from Sigma Aldrich and used as such. Potassium superoxide (KO₂) was brought from Alfa Aesar. Cetyltrimethylammonium bromide (CTAB) was purchased from Acros Organics. 2,2 diethoxypropane was purchased from TCI. Alamar Blue was purchased from Thermo Fisher. Dulbecco's Modified Eagle's Medium (DMEM), Phosphate Buffered Saline 7.4 (PBS), Fetal Bovine Serum (FBS), penicillin, streptomycin and L-glutamine 200 mM were purchased from Gibco (Life Technologies). Hoechst 33342, and Alexa Fluor® 647 Phalloidin were purchased from Invitrogen. HeLa, Huh-7, Glioma C6 and Hdfa cells were obtained from ATCC/LGC Standards GmbH (Wesel, Germany) and cultivated according to the provider's protocol.

5.7.2 Synthesis of the linker: 4,4,14,14-tetraethoxy-9,9-dimethyl-3,15-dioxo-8,10-dithia-4,14-disilaheptadecane (ROS-linker)

3-mercaptopropyltriethoxysilane (5.68 mL, 23.5 mmol) and 2,2 diethoxypropane (1.89 mL, 11.7 mmol) were mixed together in a round bottom flask connected to a condenser. Then a few drops of methane sulfonic acid were added and the solution was stirred for 4 h at 100 °C.

Then the solution was cooled at room temperature and the yellowish solution was characterized by ^1H and ^{13}C NMR and ESI-TOF mass spectroscopy.

^1H NMR (400 MHz, CDCl_3): 3.81 ppm (q, 12H), 2.62 ppm (t, 4H), 1.69 ppm (m, 4H), 1.58 ppm (s, 6H), 1.22 ppm (t, 18H) and 0.74 ppm (t, 4H).

^{13}C NMR (400 MHz, CDCl_3): 58.44 ppm ($-\text{O}-\text{CH}_2-\text{CH}_3$), 55.61 ppm (S-C-S), 33.37 ppm ($\text{CH}_2-\text{CH}_2-\text{S}$), 31.26 ppm ($\text{CH}_3-\text{C}-\text{S}$), 23.24 ppm ($\text{CH}_2-\text{CH}_2-\text{CH}_2$), 18.37 ppm ($\text{CH}_3-\text{CH}_2-\text{O}$), 10.58 ppm (Si- CH_2-CH_2)

ESI TOF: m/z calculated for $\text{C}_{21}\text{H}_{48}\text{NaO}_6\text{S}_2\text{Si}_2$: 538.24 , found $[\text{M}+\text{H}]^+ = 539.23$

5.7.3 Synthesis of the ROS breakable nanoparticles (ROSNPs)

In a flask, CTAB (250 mg, 0.685 mmol) was dissolved in a solution of distilled water (110 mL), EtOH (10 mL) and NaOH (2 M, 0.875 mL) that was heated to 80 C and stirred vigorously. In another flask, TEOS (0.875 mL, 3.91 mmol) and the ROS linker (0.390 mL, 0.72 mmol) were dissolved in 5 mL of EtOH. Once the temperature of the CTAB solution had stabilized, the solution containing the silane sources was added dropwise. After 6 h, the solution was cooled at r.t. and the particles, recovered and washed by means of sonication/centrifugation (20 min at 40 krcf) cycles. The CTAB was then removed by refluxing the ROSNPs in acidic EtOH (50 mL, 20 μL of HCl) overnight. The particles were then washed again 3 times by means of sonication/centrifugation cycles with EtOH before drying.

5.7.4 Synthesis of FITC doped ROS breakable nanoparticles (FITC-ROSNPs)

2.5 mg of FITC were dissolved in EtOH (5 mL) before adding APTES (6 μL). In another flask CTAB (250 mg) was dissolved in a mixture of 110 mL of distilled H_2O , 875 μL of NaOH (2M, 1.75 mmol) and 10 mL of EtOH. The mixture was then heat up to 80 °C at 800 rpm. In another flask, 875 μL of TEOS (3.91 mmol) and 390 μL of BTSPD (0.84 mmol) were dissolved in in the FITC/APTES solution. Once the temperature was stabilized at 80 °C, the silane solution was added to the aqueous solution and the mixture was stirred at 800 rpm for 6 h. The resulted nanoparticles were then cooled down at r.t. and centrifuged (30 krcf for 20 min), and washed 3 times by means of sonication/centrifugation cycles with EtOH. The CTAB was then removed by refluxing the FITC-ROSNPs in acidic EtOH (50 mL, 20 μL of HCl) overnight. The particles were then washed again 3 times by means of sonication/centrifugation cycles with EtOH before drying.

5.7.5 Breakability test with potassium superoxide (KO_2)

0.1 mg·mL⁻¹ of ROSNPs were dispersed in milliQ H₂O. Then KO_2 was added to the solution in order to reach a final concentration of 10 mM. Particles were then incubated for 3, 24 and 48 h and aliquots were then taken a deposit on a TEM grid for STEM analysis. Negative control experiments were performed without KO_2 and with non breakable MSNs with and without KO_2 .

5.7.6 Breakability test with Rose Bengal

0.1 mg·mL⁻¹ of ROSNPs were dispersed in a solution of Rose Bengal (concentrations ranging from 10⁻² M to 10⁻⁵ M) in water. The sample was then irradiated with a Hg lamp for 4 h and aliquots were taken and dropcasted on a TEM grids for STEM analysis. Negative control experiments were performed by keeping the solution in the dark and with non breakable MSNs with and without light irradiation.

5.7.7 Synthesis of Rose Bengal ω -carboxypentyl Ester (RBHA)

The synthesis was made by modifying a procedure recently reported in the literature.^[44] Rose Bengal (521 mg, 0.53 mmol) was dissolved in DMF (5 mL), and 6-bromohexanoic acid (313 mg, 1.60 mmol) was added. This solution was stirred and heated for 7h at 80°C. DMF was then distilled off under vacuum and the crude product was stirred overnight in presence of diethyl ether. After filtration and thorough diethyl ether washing, the residue was stirred overnight with water, to remove the excess of remaining Rose Bengal. After filtration, the product was recrystallized in ethanol, resulting to a dark red powder.

¹H NMR (400 MHz, DMSO-*d*₆): 3.86 (t, 2H), 2.02 (m, 2H), 1.25 (m, 2H) 1.09 (m, 2H) 0.92 (m, 2H).

5.7.8 Synthesis of Rose Bengal-NHS ester (RBHAOSu)

The synthesis was made by modifying a procedure recently reported in the literature.^[45] A solution of hexanoic acid ester of Rose Bengal (RBHA) (183 mg, 0.17 mmol) and N-hydrosuccinimide (39 mg, 0.34 mmol) in 8 mL DMF was treated with 64 mg of N-(3-Dimethylaminopropyl)-N'-ethylcarbodiimide hydrochloride, and the mixture was stirred at room temperature overnight. DMF was removed under vacuum. The resulting red oil was dissolved in 100 mL of chloroform. The resulting mixture was transferred to a separatory

funnel and washed four times with 100 mL of distilled water and dried with Na₂SO₄ and the chloroform removed under vacuum. The resulting red oil was dissolved in 10 mL of chloroform and precipitated upon of 150 mL of anhydrous ether. The final solid was filtered by gravity and air dried. The final product was used without any further purification.

¹H NMR (400 MHz, DMSO-*d*₆): 3.86 (t, 2H), 2.97 (m, 4H), 1.39 (t, 2H), 1.11 (m, 2H), 1.03 (m, 2H) 0.94 (t, 2H).

5.7.9 Grafting of RBHAOSu on the ROSNPs (ROSNPs-RBout)

20 mg of ROSNPs were dispersed in 4 mL of EtOH. After that, 0.2 mg of RBHAOSu, 5 μL of APTES and a few drops of TEA were added to the dispersion and stirred overnight in the dark. After that, the particles were centrifuged and washed thoroughly by means of sonication/centrifugation cycles with EtOH until to have clear supernatants. The particles were finally air dried.

5.7.10 Synthesis of Rose Bengal-doped ROSNPs (ROSNPs-RBin)

2.5 mg of RBHAOSu were dissolved in EtOH (5 mL) before adding APTES (6 μL). In another flask CTAB (250 mg) was dissolved in a mixture of 110 mL of distilled H₂O, 875 μL of NaOH (2 M, 1.75 mmol) and 10 mL of EtOH. The mixture was then heat up to 80 °C at 800 rpm. In another flask, 875 μL of TEOS (3.91 mmol) and 390 μL of BTSPD (0.84 mmol) were dissolved in in the RBHAOSu/APTES solution. Once the temperature was stabilized at 80 °C, the silane solution was added to the aqueous solution and the mixture was stirred at 800 rpm for 6h. The resulted nanoparticles were then cooled down at r.t. and centrifuged (30 krcf for 20 min), and washed 3 times by means of sonication/centrifugation cycles with EtOH. The CTAB was then removed by refluxing the ROSNPs-RBin in acidic EtOH (50 mL, 20 μL of HCl) overnight. The particles were then washed again 3 times by means of sonication/centrifugation cycles with EtOH before drying.

5.7.11 Breakability test with the grafted Rose Bengal ROS-NPs

0.1 mg·mL⁻¹ of ROSNPs-RBin and ROSNPs-RBout were dispersed in a solution of Rose Bengal (10⁻⁴ M) in water. The sample was then irradiated with a Hg lamp for 4 h and aliquots were taken and dropcasted on a TEM grids for STEM analysis.

5.7.12 Cell culture experiments

HeLa, Huh-7, Glioma C6 and Hdfa cells were cultured in culture medium (CM) containing 88% Dulbecco's Modified Eagle Medium (DMEM), 10% Fetal Bovine Serum (FBS), 1% Penicillin-Streptomycin and 1% L-Glutamine 200 mM at 37°C under 5% of CO₂ atmosphere and let grown until reaching 80 to 90 % confluency. Then, cells were washed twice with Phosphate Buffer Solution (PBS) and treated with trypsin to detach them from the flask surface. Cells were split every 2-3 days.

5.7.13 Cell viability

1.5×10^4 cells were seeded in 24 well plates and allowed to grow for 24 h. The cells were then incubated with ROSNPs in CM (50, 100 $\mu\text{g}\cdot\text{mL}^{-1}$). After 3, 24 and 48 h, 100 μL of Alamar Blue were added in each well plate and let incubate for 2 to 4 h. Then the culture media were transferred to a 96 well plates and the absorbance of each well plates was measured at 570 nm and 600 nm with a microplate reader. Each samples were triplicate.

5.7.14 Confocal experiments

30 000 cells were seeded onto glass cover slips in a 24 well plate and allowed to adhere and grow for 24 h. The cells were then incubated with FITC-ROSNPs in CM (40 $\mu\text{g}/\text{mL}$). After 3, 24 and 48 h, the cells were washed 5 times with PBS and fixed with 4 % PFA for 15 min. The cells were then washed again 3 times with PBS. In order to visualize the nuclear region, the samples were then stained with Hoechst 33342 and washed 3 times with PBS. The glass cover slips were mounted and fixed on a glass microscope slide with Fluoromont aqueous mounting medium for confocal microscope analysis. For Z-stacking experiments, cells were prepared as previously explained for the cellular uptake and incubated with FITC-ROSNPs under the same conditions. After 24 h of incubation, cells were washed 5 times with PBS and fixed with 4 wt. % PFA for 15 min. Cells were then washed with PBS and kept in Triton X-100 (0.1 % in PBS) for 10 min and afterwards in 1% bovine serum albumin (BSA) in PBS for 20 min. The cell layer on glass cover slip was stained with Phalloidin Alexa Fluor[®] 647 for F-actin/membrane staining, for 20 min in the dark at room temperature, and washed twice with PBS. The nuclear region was stained with Hoechst 33342 for 5 min and washed 3 times with PBS. The cover slips were mounted onto glass slides for confocal microscopy measurements. The excitation wavelength for Hoechst 33342 and FITC (grafted on the particles surface)

were 355 and 488 nm respectively, while with Alexa Fluor[®] 647 Phalloidin was excited at 650 nm.

5.7.15 Instruments

SEM images were recorded with a FEI Quanta FEG 250 instrument (FEI corporate, Hillsboro, Oregon, USA) with an acceleration voltage of 20 kV. The sample is prepared by drop-casting a dispersion of particles in EtOH onto a glass cover slip, subsequently sputter coated with Au (Emitech K575X peltier cooled) for 60 s at 60 mA prior to fixation on an Al support. TEM samples of particles were analyzed on a JEOL JEM-2100 instrument at an acceleration voltage of 120 kV. Ethanolic suspensions of the materials (0.1 mg/mL) were drop-casted onto Formvar coated Cu grids (400 mesh) and dried overnight prior to visualization. XPS analysis was performed using a K-AlphaTM+ X-ray Photoelectron Spectrometer (XPS) System (Thermo Scientific). Monochromatic Al K alpha X-rays were used (15 keV, 72 W, 200 mm spot diameter). Spectra were measured using a pass energy of 200 eV for survey spectra and 50 eV for core level spectra. The analyzed samples were prepared by drop-casting an ethanolic dispersion (0.1 mg/mL) of the particles onto a glass coverslip precoated with Au (Emitech K575X peltier cooled) for 3 min at 60 mA. TGA analyses were conducted on a Perkin Elmer TGA4000 Instrument machine under nitrogen atmosphere. The samples (0.1-2 mg) were kept at 100°C for 30 min for stabilization, then heated from 100 to 750°C at a speed of 10°C/min, before being held at this temperature for further 30 min before cooling. The analyses were performed under a gas flow of N₂ at 60 mL/min. DLS and ZP measurements were conducted on a Delsa Nano C Particle Analyzer (Beckman Coulter, Brea, CA, USA; operative wavelength 655 nm). All DLS measurements of the nanoparticles were conducted in water (0.1 mg/mL), and the Contin algorithm was used to supply the hydrodynamic diameters as intensity and volume distributions. ZP analyses were performed in PBS (pH 7.4). Porosimetry analyses of the samples were performed using a Micrometrics porosimeter (model ASAP-2020). The samples were degassed at 80 °C for 6 h and N₂ adsorption/desorption measurement was performed at -196 °C. The surface areas and pore volume were calculated by BET method and the pore size distribution was calculated by DFT methods. The surface area was calculated by Brunauer-Emmett-Teller (BET) method in the relative pressure range p/p_0 0.06-0.3.^[46] The pore size distribution and pore volume were calculated by density functional theory (DFT) method on the adsorption branch using a slit-based model. The total pore volume was estimated at p/p_0 0.989. The small-angle X-ray

scattering set-up comprised the SAXSess mc² instrument from Anton Paar GmbH (Graz, Austria), containing a slit collimation system, and the PW3830 laboratory X-ray generator (40 kV, 50 mA) with a long-fine focus sealed X-ray tube (CuK α wavelength of $\lambda = 0.1542$ nm) from PANalytical. Detection was performed with the 2D imaging-plate reader Cyclone® by Perkin Elmer. Measurements were performed on powder sample for 5 min and the data collected up to a scattering vector q value of 7 nm^{-1} , where $q = (4 \pi/\lambda) \sin(\theta/2)$ and 2θ the scattering angle. The 2D data were converted to 1D data and background-corrected by using SAXSQuant software (Anton Paar GmbH). Absorbance spectra were measured on a Shimadzu UV-3600 spectrophotometer double-beam UV-VIS-NIR spectrometer and baseline corrected. Steady-state emission spectra were recorded on a Horiba Jobin–Yvon IBH FL-322 Fluorolog 3 spectrometer equipped with a 450 W xenon arc lamp, double-grating excitation, and emission monochromators (2.1 nm mm^{-1} of dispersion; $1200 \text{ grooves mm}^{-1}$) and a TBX-04 single photon-counting detector. Emission spectra were corrected for source intensity (lamp and grating) and emission spectral response (detector and grating) by standard correction curves. Confocal imaging was performed with a Zeiss LSM 710 confocal microscope system equipped with a 63x magnification, numerical aperture 1.3 of Zeiss LCI Plan-NEOFLUAR water immersion objective lens (Zeiss GmbH, Germany). The excitation wavelength for Hoechst 33342 and FITC were 355 and 488 nm respectively, while with Phalloidin Alexa Fluor® 647 was excited at 650 nm. 96 well plates samples were analyzed using a Victor-X5 2030 Multilabel from Perkin Elmer. Absorbance was measured in 96 well plates using a filter at $\lambda = 570 \text{ nm}$. ¹H and ¹³C NMR spectrum were recorded on a Brücker 400 MHz.

5.8 References

- [1] M. Vallet-Regi, A. Rámila, R. P. del Real, J. Pérez-Pariente, *Chemistry of Materials* **2001**, *13*, 308–311.
- [2] C. Argyo, V. Weiss, C. Bräuchle, T. Bein, *Chemistry of Materials* **2013**, *26*, 435–451.
- [3] Lu Jie, Liong Monty, Li Zongxi, Zink Jeffrey I., Tamanoi Fuyuhiko, *Small* **2010**, *6*, 1794–1805.
- [4] Tang Fangqiong, Li Linlin, Chen Dong, *Advanced Materials* **2012**, *24*, 1504–1534.
- [5] S. Mura, J. Nicolas, P. Couvreur, *Nature Materials* **2013**, *12*, 991–1003.
- [6] H. Yan, C. Teh, S. Sreejith, L. Zhu, A. Kwok, W. Fang, X. Ma, K. T. Nguyen, V. Korzh, Y. Zhao, *Angewandte Chemie International Edition* **2012**, *51*, 8373–8377.
- [7] Z. S. Al-Ahmady, W. T. Al-Jamal, J. V. Bossche, T. T. Bui, A. F. Drake, A. J. Mason, K. Kostarelos, *ACS Nano* **2012**, *6*, 9335–9346.
- [8] E. Ruiz-Hernández, A. Baeza, M. Vallet-Regí, *ACS Nano* **2011**, *5*, 1259–1266.

- [9] T. D. Nguyen, Y. Liu, S. Saha, K. C.-F. Leung, J. F. Stoddart, J. I. Zink, *Journal of the American Chemical Society* **2007**, *129*, 626–634.
- [10] K. C.-F. Leung, T. D. Nguyen, J. F. Stoddart, J. I. Zink, *Chemistry of Materials* **2006**, *18*, 5919–5928.
- [11] H. Meng, M. Xue, T. Xia, Y.-L. Zhao, F. Tamanoi, J. F. Stoddart, J. I. Zink, A. E. Nel, *Journal of the American Chemical Society* **2010**, *132*, 12690–12697.
- [12] J. Lu, Z. Li, J. I. Zink, F. Tamanoi, *Nanomedicine: Nanotechnology, Biology and Medicine* **2012**, *8*, 212–220.
- [13] R. Kumar, I. Roy, T. Y. Ohulchanskyy, L. A. Vathy, E. J. Bergey, M. Sajjad, P. N. Prasad, *ACS Nano* **2010**, *4*, 699–708.
- [14] L. Maggini, I. Cabrera, A. Ruiz-Carretero, E. A. Prasetyanto, E. Robinet, L. D. Cola, *Nanoscale* **2016**, *8*, 7240–7247.
- [15] J. Croissant, X. Cattoën, M. W. C. Man, A. Gallud, L. Raehm, P. Trens, M. Maynadier, J.-O. Durand, *Advanced Materials* **2014**, *26*, 6174–6180.
- [16] P. Huang, Y. Chen, H. Lin, L. Yu, L. Zhang, L. Wang, Y. Zhu, J. Shi, *Biomaterials* **2017**, *125*, 23–37.
- [17] K. Möller, T. Bein, *Chemistry of Materials* **2017**, *29*, 371–388.
- [18] L. Maggini, L. Travaglini, I. Cabrera, P. Castro-Hartmann, L. De Cola, *Chemistry – A European Journal* **2016**, *22*, 3697–3703.
- [19] J.G. Croissant, Y. Fatieiev, K. Julfakyan, J. Lu, A.-H. Emwas, D.H. Anjum, H. Omar, F. Tamanoi, J.I. Zink, N.M. Khashab, *Chemistry – A European Journal* **2016**, *22*, 14806–14811.
- [20] J. Croissant, X. Cattoën, M. W. C. Man, A. Gallud, L. Raehm, P. Trens, M. Maynadier, J.-O. Durand, *Advanced Materials* **2014**, *26*, 6174–6180.
- [21] J. Zhu, Y. Niu, Y. Li, Y. Gong, H. Shi, Q. Huo, Y. Liu, Q. Xu, *Journal of Material Chemistry B* **2017**, *5*, 1339–1352.
- [22] T. P. Szatrowski, C. F. Nathan, *Cancer Research* **1991**, *51*, 794–798.
- [23] F. Q. Schafer, G. R. Buettner, *Free Radical Biology and Medicine* **2001**, *30*, 1191–1212.
- [24] D. S. Wilson, G. Dalmaso, L. Wang, S. V. Sitaraman, D. Merlin, N. Murthy, *Nature Materials* **2010**, *9*, 923–928.
- [25] J. Kountouras, D. Chatzopoulos, C. Zavos, *Hepatology* **2001**, *48*, 743–751.
- [26] D. Trachootham, J. Alexandre, P. Huang, *Nature Reviews Drug Discovery* **2009**, *8*, 579.
- [27] M. Nishikawa, *Cancer Letters* **2008**, *266*, 53–59.
- [28] X. Xu, P. E. Saw, W. Tao, Y. Li, X. Ji, S. Bhasin, Y. Liu, D. Ayyash, J. Rasmussen, M. Huo, *et al.*, *Advanced Materials* **2017**, *29*, 1700141.
- [29] D. Shao, M. Li, Z. Wang, X. Zheng, Y.-H. Lao, Z. Chang, F. Zhang, M. Lu, J. Yue, H. Hu, *et al.*, *Advanced Materials* **2018**, *30*, 1801198.
- [30] D. E. J. G. J. Dolmans, D. Fukumura, R. K. Jain, *Nature Reviews Cancer* **2003**, *3*, 380–387.
- [31] P. Agostinis, K. Berg, K. A. Cengel, T. H. Foster, A. W. Girotti, S. O. Gollnick, S. M. Hahn, M. R. Hamblin, A. Juzeniene, D. Kessel, *et al.*, *CA: A Cancer Journal for Clinicians* **2011**, *61*, 250–281.
- [32] R. R. Allison, C. H. Sibata, *Photodiagnosis and Photodynamic Therapy* **2010**, *7*, 61–75.
- [33] A. Gorman, J. Killoran, C. O’Shea, T. Kenna, W. M. Gallagher, D. F. O’Shea, *Journal of the American Chemical Society* **2004**, *126*, 10619–10631.

- [34] E. Gandin, Y. Lion, A. V. de Vorst, *Photochemistry and Photobiology* **1983**, *37*, 271–278.
- [35] P. Han, S. Li, W. Cao, Y. Li, Z. Sun, Z. Wang, H. Xu, *Journal of Material Chemistry B* **2013**, *1*, 740–743.
- [36] Y. Tian, J. Zheng, X. Tang, Q. Ren, Y. Wang, W. Yang, *Particle & Particle Systems Characterization* **2015**, *32*, 547–551.
- [37] C. Qian, P. Feng, J. Yu, Y. Chen, Q. Hu, W. Sun, X. Xiao, X. Hu, A. Bellotti, Q.-D. Shen, *et al.*, *Angewandte Chemie International Edition* **2017**, *56*, 2588–2593.
- [38] J. Wang, Y. Yu, K. Lu, M. Yang, Y. Li, X. Zhou, Z. Sun, *International Journal of Nanomedicine* **2017**, *12*, 809–825.
- [39] S. E. Lehman, A. S. Morris, P. S. Mueller, A. K. Salem, V. H. Grassian, S. C. Larsen, *Environmental Science: Nano* **2016**, *3*, 56–66.
- [40] T. Xia, M. Kovoichich, J. Brant, M. Hotze, J. Sempf, T. Oberley, C. Sioutas, J. I. Yeh, M. R. Wiesner, A. E. Nel, *Nano Letters* **2006**, *6*, 1794–1807.
- [41] G. Saravanakumar, J. Kim, W. J. Kim, *Advanced Science* **2017**, *4*, 1600124.
- [42] W. Stöber, A. Fink, E. Bohn, *Journal of Colloid and Interface Science* **1968**, *26*, 62–69.
- [43] N. Sugita, K. Kawabata, K. Sasaki, I. Sakata, S. Umemura, *Bioconjugate Chemistry* **2007**, *18*, 866–873.
- [44] K. A. Conlon, M. Berrios, *Journal of Photochemistry and Photobiology B: Biology* **2001**, *65*, 22–28.
- [45] N. Vilaça, R. Totovao, E. A. Prasetyanto, V. Miranda-Gonçalves, F. Morais-Santos, R. Fernandes, F. Figueiredo, M. Bañobre-López, A. M. Fonseca, L. D. Cola, *et al.*, *Journal of Material Chemistry B* **2018**, *6*, 469–476.
- [46] S. Brunauer, P. H. Emmett, E. Teller, *Journal of the American Chemical Society* **1938**, *60*, 309–319.

Chapter 6

Instrumental techniques

Abstract

This chapter presents the most important instrumental techniques employed to achieve this thesis for both material characterizations and *in vitro* studies. Electronic and confocal microscopy will be presented in a first part and then a short explanation of UV Visible and fluorescence spectrometers will be made. Finally, material characterization techniques as dynamic light scattering, zeta potential and thermogravimetric analysis will be introduced in a last part.

6.1 SEM

Since their development in the early 50's, scanning electron microscopes (SEM) have been used extensively in science comforting hypothesis and opening new areas of study.^[1] This technique is based on the use of electrons to acquire high resolved images thanks to a high-energy electron beam. It allows morphological characterizations of materials by generating a range of signals on the surface of a selected area, creating then a 2-dimensional image. Conventional SEM permits a 500000x magnification leading to a final resolution of less than 10 nm. Due to the characteristic ionization energies for each atom, SEM are also able to quantitatively analyze chemical composition of materials on selected areas by Energy dispersive X-ray analysis mode.

Display images of nanometer sized objects require specific components. The electron beam is generated by a tungsten hairpin filament (thermionic-based emission). This electron source, placed on the top of the column, is heated up to 2500°C where the energy of the weakest bounded electrons exceeds the work function of the material, thus allowing for the electron emission. Directly below the source, an anode is placed for the acceleration of the electron down to the electron beam and presents a voltage that can be modulated from 1 to 40 kV. An electron beam is then formed and guided through several condenser and focusing lenses that apply a repulsive electric field, focusing it through a small aperture. The sample is finally touched by the electron beam and diverse signal can be recorded from the reflected electrons. Among them, secondary electrons, which are commonly used for showing morphology and topology, result from the excitation of an electron in a sample by the incident electron beam. It migrates then to the surface and escaped from the sample. Due to the very low energy, only secondary electrons near the surface can leave the sample and produce the output signal. The volume in which secondary electrons are produced is relatively small, which leads to a high axial resolution (a few nm). The final image is thus a map of the secondary electron density depending on the properties of the sample. X-ray photons are used for elemental analysis of the surface of the material and come from the excited electrons of specific orbitals that returns to their ground state, yielding to photons of energies characteristic for each elements allowing a chemical composition mapping of the material. A schematic representation of a SEM is represented in **Figure 6.1**.

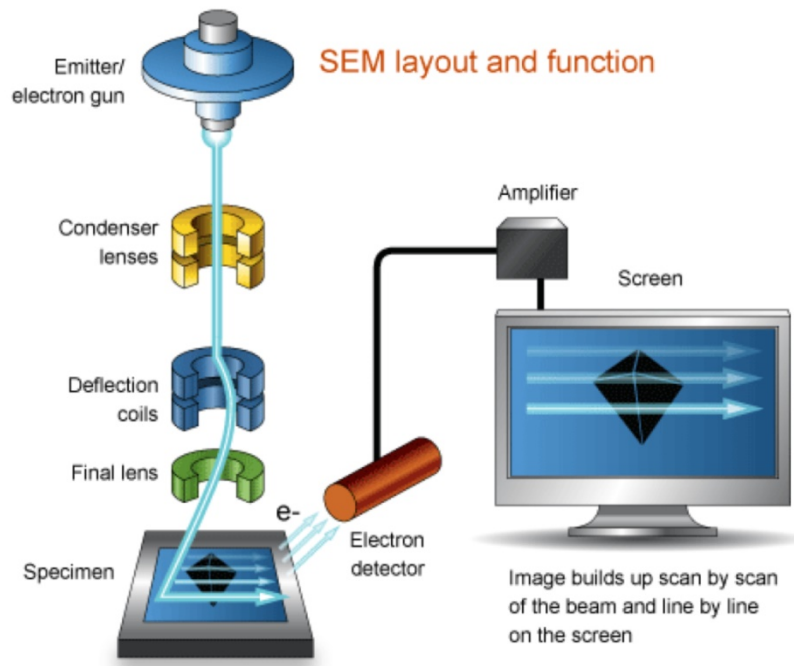


Figure 6.1: Schematic representation of a scanning electron microscope set up.

6.2 TEM

At the difference of SEM that use secondary electrons which are scattered from the surface of the sample, transmission electron microscopy instead produces his images through electrons that are transmitted through the sample. The material is illuminated with high energetic electrons within high vacuum and the electron beam points directly towards the detector and the sample is placed between them. Electrons that are not stopped by the sample pass through the TEM grid and reach the detector creating a bright image while the electrons that are stopped by the samples form black areas. Interaction and scattering of electrons by the sample can then be easily visualized by forming a range of intensity between the white and the black. Due to the high voltage necessary for the transmission of the electron, TEM possess a better resolution compare to SEM reaching a magnification of 10000000x. Even though the electron beam is similar compare to the SEM, TEM electrons reached a higher speed thanks to an increased voltage generally ranging from 80 to 400 kV.^[2]

The condenser lens forms the beam and is located before the object allowing the opening of the aperture, focusing the light and thus controlling the electron beam diameter depending on the desired magnification. After passing the specimen, the electron beam reaches the objective lens, generating the first intermediate image of the sample, therefore determining the quality of the resulted image. The image is then inverted and magnified

thanks to the intermediate lens creating an intermediate image, which is finally collected in the projector lens, forming the final image and translating the final image onto a screen. A schematic representation is presented in **Figure 6.2**.

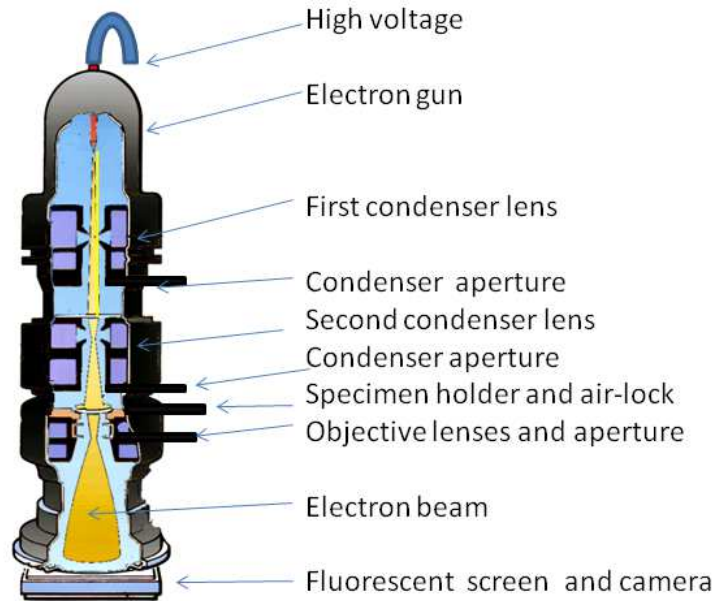


Figure 6.2: Transmission electron microscope representation with the electron beam represented in yellow. Image taken from www.wikipedia.org.

6.3 Confocal laser scanning microscope

Confocal laser scanning microscope (CLSM) was developed in the 60's by Marvin Minsky, who wanted to study the connections between brain cells in 3 dimensions and therefore becomes one of the most used tool for bioimaging.^[3] Compare to conventional optical epifluorescence microscopes, confocal microscopy allows the removal of out-of-focus light that resulted from the photons scattered from the sample. This improvement, related to the incorporation of pinholes that are placed before the sample and just before the photomultiplier. Such features brings a spatial control of the depth, the elimination of background signal, the visualization of several luminescent probes at the same time but further offers the possibility to collect several optical sections from thick samples permitting a 3D reconstruction of an image. A schematic representation of a traditional CLSM is represented in **Figure 6.3**.^[4]

The light is emitted from lasers of specific wavelength, passes through a first pinhole and is further reflected until reaching a galvanometer that offers the possibility of precise scanning in the x and y axis. At the difference with traditional epifluorescence microscopes, the signal received is obtained pixel by pixel and line by line. The beam is then reflected

towards the sample thanks to a dichroic mirror and goes through an objective to finally reach the sample. The photons emitted by the laser beam excite the fluorophores at specific wavelength leading to the passage from the ground state to an excited state. During relaxation, photons of higher wavelengths are emitted from the samples and passes through the dichroic mirror. The beam is then guided towards the detector pinhole that will block the photons that are out-of-focus. The resulting signal hit a diffraction grating separating the coming light to the different photomultiplier detectors that enhance the signal. The image is further processed by a computer and lead to an apparition of a final image. Changing the focus on the Z-axis allows the scanning of a different focal plane, allowing scanning of several optical slices before creating a 3D picture. Such technique is called a Z-stacking experiment.

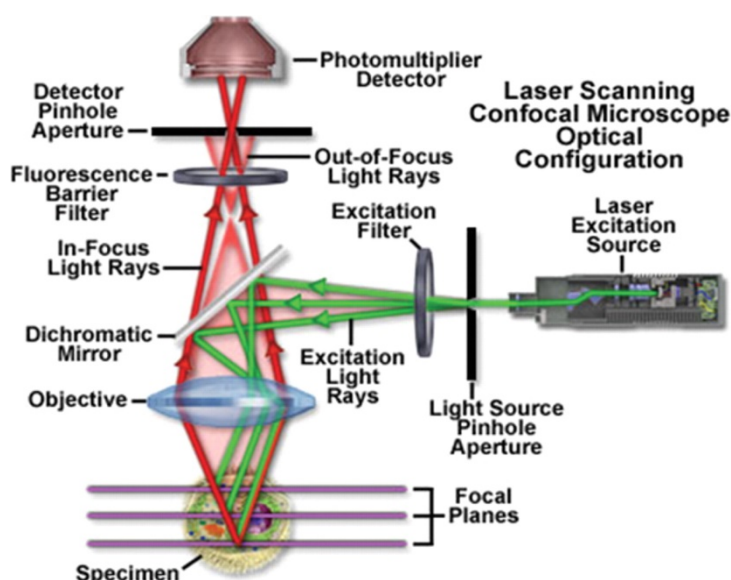


Figure 6.3: Confocal microscope set up with the different components and the light pathway. Image taken from reference 4.

The scan speed can be modified, which can increase the signal-to-noise ratio resulting to a better contrast and better resolution. Unfortunately, this could lead to a photobleaching of the dye after long term exposure. Such parameters are then important to control in order to obtain the best quality picture possible.

6.4 UV-Vis Spectroscopy

The quantification of absorbed light by a sample can be done by optical techniques such as UV-Vis spectroscopy. When a sample is exposed to a light beam, it absorbed photons at specific wavelength (λ). This absorbance can be defined by the equation:

$$A_s(\lambda) = -\log\left(\frac{I_s}{I_0}\right)$$

With I_s the light intensity going through the sample and I_0 the intensity of the incident light before reaching the sample. The absorbance follows a rule considering the length (l , in cm) of the light that passes through a solution, the concentration of the molecule (c in mol·L⁻¹) and the molar absorption coefficient (ϵ in L·mol⁻¹·cm⁻¹). This rule, as called Beer-Lambert law can be expressed as:

$$A_s(\lambda) = -\log\left(\frac{I_s}{I_0}\right) = \epsilon(\lambda) \cdot l \cdot c$$

Figure 6.4 shows a schematic representation of a UV-Vis instrument as well as the different components.^[5] It is generally composed of a lamp (the light source) that emits through a monochromator (diffraction grating or prism) to select specific wavelengths, a sample holder and a detector that will acquire the photons. It can be either a simple or double beam. For double beam measurements, the light is split in two before going through the sample. The first beam is used as a reference and will go through a cuvette filled with the solvent. It will be considered as 100 % of transmission intensity (0 absorbance). The second beam will pass through the sample of interest.

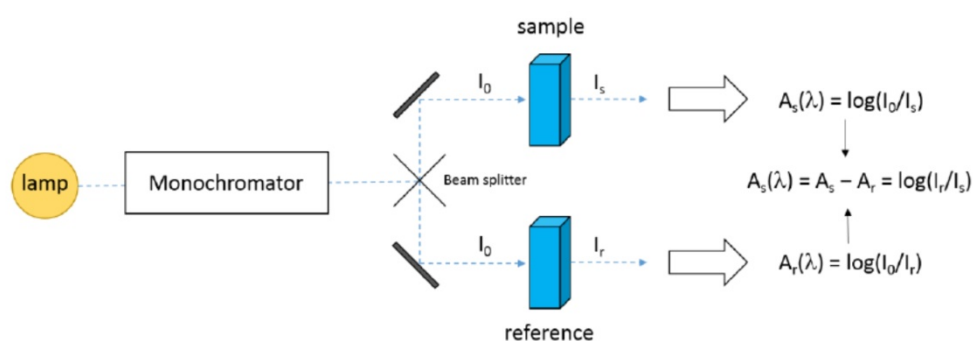


Figure 6.4: Schematic representation of a UV-Vis instrument. Image taken from reference 5.

6.5 Fluorescence spectroscopy

Photophysical properties of molecules or nanoparticles can be characterized by fluorescent spectroscopy by recording emission and excitation spectra. The emission spectrum in particular, is the wavelength distribution of the emission measured at a single constant excitation wavelength, while the excitation spectrum is the dependence of the emission intensity in the scanned excitation wavelength window, measured at a single emission wavelength. Such properties are analyzed with spectrofluorometers that are composed of a lamp (excitation source), a dual grating monochromator and a reference detector. In order to avoid the detection of the light source, the detection of the photons are placed at 90° compare to the incident light, passing then

through a second monochromator, and finally reach the photomultiplier amplifying the detected signal. Both source intensity and detector contained correction factors that are including during the measurements.

6.6 Dynamic Light Scattering (DLS)

Size of nanoparticles in dispersion is an important parameter to control in various applications. Characterization of such feature can be performed by Dynamic Light Scattering (DLS). Particles in suspension are in Brownian motion and collide with solvent molecules creating diffusion through the medium that can be further correlated to the particle size thanks to the Stokes-Einstein equation that is presented below:

$$D = \frac{k_b T}{3\pi\eta_0 d}$$

Where D is the diffusion coefficient, k_b the Boltzman's constant; T the absolute temperature; η_0 the viscosity and d the hydrodynamic diameter of the sample to measure.

D will be therefore very small for large particles, due to their low motion in the media while it will be higher for small particles, which will move rapidly within the sample. Such diffusion coefficient can be then measured in order to determine the size of a particle in a specific media. As an example, in presence of particles, the light is scattered in all the

directions when they are hit by a laser beam. The observed scattered light provides from scattered elements and results in an intensity of the scattered light from each element. When particles are in motion, the fluctuation in time of the light intensity will be observable due to the different positions that will take the material. In Brownian motion, the light intensity resulting from the scattered beam fluctuates according to the size of the particles and can be therefore analyzed using an autocorrelation function (ACF) (**Figure 6.6**).

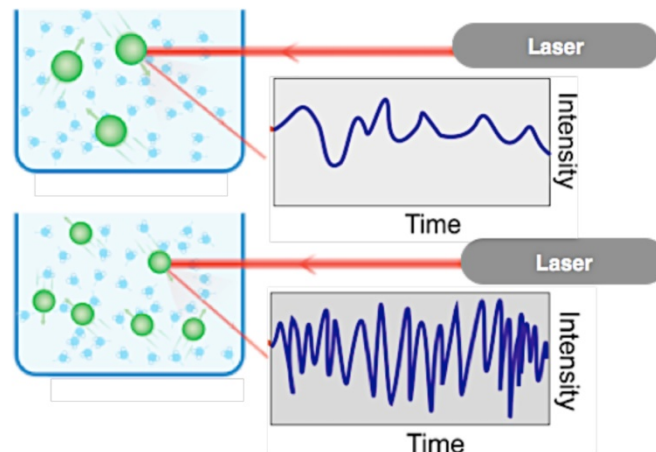


Figure 6.6: Intensity fluctuations of scattered laser resulting from a dispersion of big (top) and small (bottom) particles.

ACF decays rapidly with a large decay function for small particles due to their rapid motion and rapid intensity fluctuations while bigger particles present a smaller decay constant. This function can then be used to find the diffusion coefficient and after applying the Stokes-Einstein equation, the particle size. The result is then given as a statistical distribution that can be analyzed as scattering intensity, volume or number of particles. Intensity distribution is usually the most reliable parameter and corresponds to the raw data while volume and number distributions results from software calculations.

6.7 Zeta Potential

The electric surface charge of materials can be determined by Zeta Potential analysis which is illustrated in **Figure 6.7**. In aqueous media, charged nanoparticles are surrounded by a high concentration of counter-ions to maintain electric stability. The surface charge combined with its oppositely charged layer are called together the electrical double layer. In solution, a Brownian motion is applied resulting to a movement of the Stern layer and a part of the diffuse layer. The interface in between the moving and static ions in the diffused layer is called the slipping plane, which versus from a point far away from the particle, defines the Zeta Potential.

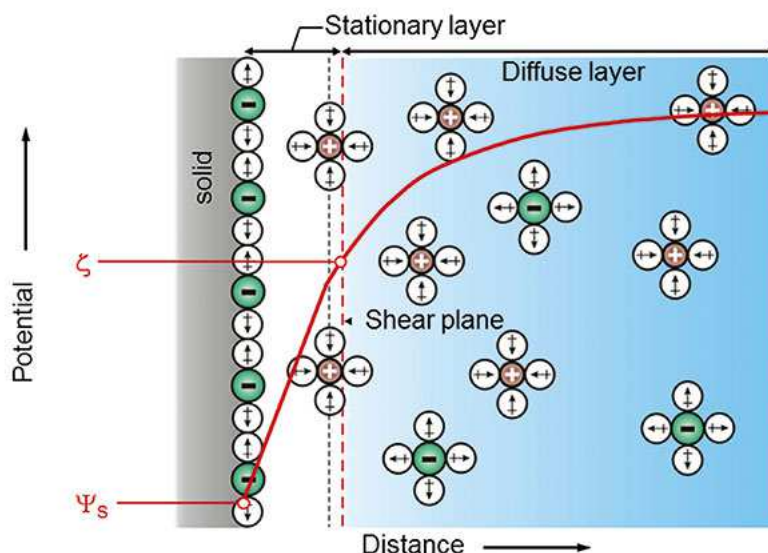


Figure 6.7: Representation of a Zeta Potential measurement at the interface between the material and the diffuse layer. Image taken from the Anton Paar website. <https://wiki.anton-paar.com/en/zeta-potential/>

The measurement is performed with particle in solution, placed in a cell containing two gold electrodes. The application of a voltage on the electrodes moves the particles towards the electrode of the opposite charge and allows the calculation of the particle velocity depending of the voltage applied. A laser beam is then going through the sample while the particles are getting towards one of the electrode. The resulted scattered light intensity result from the particle speed and can therefore be calculated at multiple voltages, leading to the final value so-called Zeta Potential.

6.8 TGA

Thermogravimetric analysis (TGA) is a technique used to measure mass changes in a chemical compound as a function of the temperature under a controlled atmosphere. In a TGA process, the sample is placed within the furnace and weighted before analysis. The temperature of the sample, placed on an internal balance, gradually increases within the furnace. As the temperature increases, the loss of volatile compound as well as the combustion of organic compounds induce a mass loss that is measured. However, it is not the case for physical changes, such as melting. The obtained thermogram represents the mass of the sample as a function of the temperature or time. The mass loss illustrates thermal transitions in the compound, such as loss of solvent and plasticisers in polymers, water of hydration in inorganic materials and, eventually, decomposition of the compound. All this description is illustrated in **Figure 6.8**.

6.9 References

- [1] J. J. Bozzola, in *ELS*, American Cancer Society, **2001**.
- [2] D. B. Williams, C. B. Carter, *Transmission Electron Microscopy: A Textbook for Materials Science*, Springer US, **2009**.
- [3] M. Minsky, *Scanning* **1988**, *10*, 128–138.
- [4] R. Ahmadov, T. Vanorio, G. Mavko, *The Leading Edge* **2009**, *28*, 18–23.
- [5] “Molecular Fluorescence: Principles and Applications, 2nd Edition,” can be found under [https://www.wiley.com/en-us/Molecular+Fluorescence%3A+Principles +and+Applications%2C+2nd+Edition-p-9783527328376](https://www.wiley.com/en-us/Molecular+Fluorescence%3A+Principles+and+Applications%2C+2nd+Edition-p-9783527328376), **n.d.**

General conclusions and Perspectives

With the rising of new technologies and their potential biomedical applications, researchers have focused on the development of safe and effective tools. Among the various types of nanomaterials, mesoporous silica nanoparticles, thanks to their versatile properties, biocompatibility and ease of functionalization, have attracted a lot of attention for the delivery of specific molecules within cancer cells. Despite all their advantages that makes them a powerful tool as drug delivery systems, their bioaccumulation and slow degradability hinder their clinical translation, especially for cancer treatment, where frequent injections are required.

This thesis focused on the development and applications of breakable mesoporous silica nanoparticles, which contains within the framework, stimuli-responsive linkers able to be cleaved, leading to a breaking of the particles in pieces tackling the bioaccumulation of silica by allowing excretion through the kidneys.

Chapter 1 was a general introduction about nanomaterials for biomedical applications, centering our focus then on silica nanoparticles and their tuning possibilities for delivery of specific molecules ranging from small drugs to big proteins. Finally, the introduction of organic moieties within the silica framework was introduced, starting with the pioneer work of Inagaki with the synthesis of periodic mesoporous organo-silica nanoparticles following with the insertion of stimuli-responsive linkers allowing specific release of molecules and adding breakability properties.

Chapter 2 presented the synthesis of 12 nm pore organo-hybrid mesoporous silica nanoparticles, which contain disulfide bridges. Those linkers were able to respond towards glutathione (GSH), which is present at about 2-10 mM within the cells, promoting the breaking of the particles. The material was further functionalized with 3-(aminopropyl)triethoxysilane (APTES) to electrostatically interact with a PLK1 siRNA. A loading of $182 \mu\text{g}\cdot\text{mg}^{-1}$ was recorded by UV-Visible spectroscopy and was further coated with jetPEI[®] improving the cellular uptake and protecting the siRNA. Both *in vitro* and *in vivo* experiments were performed in hepatocellular carcinoma Huh-7 cells demonstrating the

efficient release of the siRNA and the breaking of the material within the cells. Despite all the results obtained, there are still experiments that can be performed in both the understanding and optimization of the material. First, the loading of the material could be improved with the use of different amines grafted on the surface of the materials. The bioaccumulation of the nanomaterial towards the liver has also to be tested thanks to the EPR effect. This accumulation can be therefore improved by the grafting of targeting ligands on the surface of the nanoparticles such as antibodies against glypican-3 or epidermal growth factors that are overexpressed on this type of cells.

Chapter 3 presented the same particles to load a peptide for the crop industry. The peptide, known to be toxic for the insects were loaded within the material in order to improve their uptake by larvae. The loaded material was then tested on the larvae. Unfortunately, the system did not show any improvement compared to the bare peptide. Another strategy was to encapsulate the peptide within nanocapsules. The particles have then been sent to a company for further tests.

Chapter 4 focuses on the synthesis of 50 nm disulfide doped breakable silica nanoparticles for the intracellular pharmacokinetic studies of release of Doxorubicin. The particles were loaded with Doxorubicin and the efficient release was followed *in vitro* in U87 glioblastoma cells and compared to Caelyx[®], the commercially available liposomal form of Doxorubicin. In order to improve the material and to apply these particles *in vivo* for brain delivery, their ability to cross the blood brain barrier (BBB). To improve the crossing, the particles could be further functionalized with glucose moieties. Moreover, early leakage of the Doxorubicin could also be observed and therefore, clogging of the pores with stimuli responsive ligands could be an option.

Chapter 5 described the synthesis and characterization of Reactive Oxygen Species responsive silica nanoparticles. The material was further functionalized with a photosensitizer Rose Bengal, enhancing the breakability properties of the material upon light irradiation. Preliminary *in vitro* experiments demonstrated no cytotoxicity and efficient cellular uptake in several cell lines tested. As further experiments, the quenching of singlet oxygen has to be tested as well as the amount of reactive oxygen necessary to break the particles. *In vitro*, as the concentration of ROS in cell line dependent, the breakability properties of the material have to be tested and the nanoparticles could also be loaded with an active prodrug.

Acknowledgments

This is probably one of the most important part of this thesis. A way to thank all the people involved in this long path even though those short words cannot express all the gratitude I have for them.

My first words are for my supervisor, Prof. Luisa De Cola. You offered me the opportunity to join your group for my Master and gave me the possibility to continue for my PhD a few months after. The project you let me work on was exactly what I was looking for, an interdisciplinary topic where I could work and discuss with people from totally different backgrounds. I have learned so much during the five years I spent here, and also met so many wonderful people. You did not only teach me science, but you also opened my eyes to the world. Thanks to you, I met extraordinary people from all around the world.

I would like also to express my gratitude to the jury members who kindly accepted to judge this thesis: Prof. Emanuela Licandro, Prof. Isabela Neves, Prof Plinio Innocenzi and Prof. Michael Sailor.

This work could not have been done without the help of external collaborators having expertise in various different fields. I would like also to thank them for their help and fruitful advices. First our collaborators in IHU and the Clinique de la souris in Strasbourg: Dr. Eric Robinet, Dr. François Duong, Antonio Savano, Prof. Tania Sorg-Guss, Dr. Ghina Alame Bouabout...Then our collaborator from the Luxembourg Insitute of Health; Dr. Valérie Palissot. Dr. Fides Benfatti, from Syngenta®. Dr. Eline Bartolami and Prof. Stephan Matile from the University of Geneva and finally our colleagues in Dresden, the Dr. Kritee Pant and Dr. Stephan Hölger.

Then I would like to thank Laura, the one who taught me the basis, making me discover the nanoworld during my first internship here.

Ingrid, my second mom, I do not even know how I could thank you. You helped and taught me so much during my master thesis but also once you were gone. Your advices and comments were always precious for me. I came here as a kid and thanks to your smile and constant happiness, it help me to improve and keep smiling even when the science was not

working. I am glad that I have been your student. I wish you all the best for the future with your family!

Eko, your daily supervision really helped me during the first years of my PhD. I do not know how you manage to supervise so many things at the same time. Your ideas really made you a unique and unforgettable person in this lab.

Leana, you have always been more than patient with me, thanks a lot for all the discussion, fruitful advices that helped me a lot. You are sometimes tough with us but I do know that it is for our own good.

To the best mates “Les monsieurs” (Alberto, John, Ricardo and Youssef). Guys I do not know how I could thank you. I should write an entire book just for you guys! During those last years, you did not become only colleagues, but friends that now I consider like my brothers... Alberto, mon frère, meeting and working with you was probably one of the best thing that could have happened to me during this thesis. Your support always helped me to go through all the difficulties. Youssef, tu es le gars sûr! Toujours là quand on a besoin de toi! Je ne sais même pas comment te remercier pour tous les services que tu m’as rendus! Je me sens même stupide à chaque fois que je te demande quelque chose parce que tu ne demandes jamais rien en retour... John, both of us have started more or less at the same time and we will finish together. Thanks for your constant support during these 3 years, I will miss sharing my office with you as well as I will miss our discussions (serious or not). Ricardo, le tcha begueheeeeeeeich, tu m’as tellement fait rire avec tes débilités ces dernières années! C’est vrai que t’es grave relou parfois mais on a tous besoin de quelqu’un comme toi dans notre vie, rien que pour rendre le sourire! Merci pour l’aide que tu m’as apporté, même si on doit s’avouer qu’une partie de ta thèse est quand même la mienne haha !

Simone, you are probably one of the smartest guy I ever met in my life. It seems that you know everything, and you are really careful to each details of an experiment. You have always found the right way to do things, and the lab started already to miss you. We were lucky to have you around.

Charles, ou chef comme tu portes si bien ce surnom. Tu es le genre de personne avec qui on aime travailler et qui est toujours prêt à rendre service. Tu m’as fait refaire de la chimie orga et j’ai pris conscience que j’avais beaucoup oubliée dans ce domaine. Ta culture scientifique m’impressionne tous les jours et je sais que tu iras très loin!

Dedy, the master of the biolab! Thanks for all the knowledge you shared with me at the beginning of the PhD. You are the one who taught me how to take care of the biolab, how to use the confocal, well I learned a lot from you.

Serena, le sourire de ce laboratoire, ton départ à laisser un grand vide ici! Tu vois toujours les choses du bon côté et tu sais profiter de la vie! Je t'avais promis qu'on se verrait à Palermo et c'est chose faite maintenant! Merci à toi pour toutes ces années de bonne humeur!

Giuseppe, how can you invest yourself so much in what you do? You are an example of what motivation means! You have so many passions between science with your channel, flying and now also climbing... I really do not know how you can do everything at the same time.

Etienne = smile, motivation, never gives up. If I would have to choose 3 criteria that define you, it would be those ones.

Mariel, la mapachita del grupo, muchas gracias por todo. I wish I could have improved more my Spanish, but I am not giving up, I will keep learning. Keep spreading your good vibes all around you!

Matteo, Cintia, Camilla and Martina, your stays here were way too short, but I did appreciate each moment I spent with you. It is not possible to not get attached to people like you, each of you are unique. I am glad that I had the opportunity to meet you.

Kasia, thank you for your help and kindness during your short stay. It was a real pleasure to work with you. We share the same point of view and had so many ideas in such a short time. I wish we could have worked more together!

Alessandra, Lucrezia and Silvia, the three Erasmus! Thanks a lot for all the good times, those crazy nights out. I wish you a good luck for the end of your Master thesis and for the future. Thanks a lot also to your Italian friends, Fede, Giulia, Lorenzo and all the others...

Noujoud, mon étudiante en Master. Un grand merci à toi aussi! J'aurai souhaité être un meilleur encadrant pour toi... Je te souhaite évidemment le meilleur.

Claire, comment pourrais-je te remercier pour toute l'aide que tu m'as apporté? Toutes ces galères avec les commandes n'auraient jamais été réglées sans toi... Tu es sans aucun doute la meilleure secrétaire qu'on puisse espérer avoir, toujours à te plier en quatre pour pouvoir nous aider. Tu es aussi par ailleurs une mère formidable!

Ines and Alessandro, the engineers taking care of everything... Thanks for your help, making sure that everything works well and that we do not miss anything. Taking care of such a lab is not an easy task...

Thank you also to all the members of the De Cola group that I had the opportunity to meet, Mari Carmen, Rémi, Etienne B., Chien Wei, Valentina, Alexa, Becky, Brian, Pierre, Loïc, Nadia, Amparo, Damiano, Frank, Stephan, Veronika, Angélique, Hiroki, Sarah, Simon,

Sourav, Letitia, Elena, Marina, Pengkun. And also the master students; Yevhen, Quentin, Joachim, Tommaso and Matteo Bartolini...

On ne peut pas espérer que la science marche sans une équipe qui gère l'institut. Un grand merci à Muriel, Fabien, Fabienne, Nathalie, Jean-Louis, Thierry, Philippe, Vincent pour tout ce qu'ils font au quotidien afin que cet institut puisse fonctionner....

Parfois, il arrive que certaines manips requièrent des instruments ou des compétences spécifiques qui ne sont pas de notre ressort. Pour ça, il est utile de pouvoir discuter afin de trouver des solutions avec des personnes d'autres laboratoires ayant des connaissances complètement différentes et pouvant peut être nous aider. Je voudrais donc remercier Oussama, Marc-Antoine, Vuk, Elise, Régis, Jean-Baptiste et Reynald pour toutes ces discussions instructives (ou non ^^).

Une mention spéciale quand même pour Nicolas. Un grand merci pour ta patience, ton aide m'a été précieuse. Je ne fais même pas partie de ton équipe et pourtant tu m'as consacré tellement de temps à m'expliquer des choses qui pour toi, devait sûrement être logique.

Aussi, je ne peux pas écrire de remerciements sans citer Dr.Alexandre Specht. Tu as été le premier à m'accorder une place dans ton laboratoire afin que je puisse découvrir réellement ce qu'était la paillasse. Un grand merci aussi à Sébastien, pour ton aide et les discussions.

During this PhD, I had also the opportunity to do a summer school in mini invasive surgery and entrepreneurship. This event allowed me to meet a wonderful interdisciplinary team (surgeons, doctors and engineers) and I spent an amazing week with them. I would like especially thank the TEAM 2, Francesca, Stelios, Claudio, Alina, Brian, Gene for the amazing teamwork we created in one week but also Francesco, Ludovica and many others.

Having colleagues that you can consider as friends is something very special. The De Cola team is not only a working group, but a group of friends always ready to help each other when needed. And this kind of relationship goes above the work in the lab, leading us to special events, parties, climbing, cinema, concerts... However, some other people out of work played also an important role during this thesis by cheering me up and for all the good times I spent. It is also an opportunity to thank them for their support.

Valentine et Charlotte, mes supers colocs! Vous n'imaginez même pas à quel point emménager avec vous a été une bouffée d'oxygène pour moi. Je regrette seulement ne pas avoir passé plus de temps avec vous... Vous êtes toutes les deux formidables et je suis certain que vous irez très très loin!

Najet, la meuuuuf haha! Merci pour toutes ces années, toujours présente depuis la L1 et là pour encore longtemps! Je ne peux même plus compter le nombre de fois où j'ai eu un fou rire à cause de tes conneries! Ton aide et ton soutien m'ont été précieux pendant toutes ces années.

Juline, ton soutien aussi m'a été précieux dans certains moments très difficiles! J'ai passé énormément de bons moments avec toi que ce soit à Rome, au Bunny's ou tout simplement nos soirées Netflix... Tout ça va me manquer.

Jerem, tu t'es exilé sur Amiens mais chacun de tes retours sur Strasbourg est synonyme de fous rires. Tu arrives toujours à nous faire rire, souvent sans faire exprès.

Laura, comme tu saoules haha! Merci pour ton aide, tes explications en bio m'ont été très utiles.

Yann, Kévin et Steph, les potos geeks! Chacun a suivi une voie différente et nos squats se font de plus en plus rares, mais ils ont toujours été une partie de rigolade avec toujours les mêmes petites habitudes.

Sezer, mon pote! Plus de 20 ans d'amitié et toujours là! Certes, c'est toujours une galère pour se voir, mais on arrive à trouver le temps et à chaque fois c'est un vrai plaisir.

La prof Cathy et les potes du basket, Manu, Brice, Thomas, Gauthier, Amaury, Carlos, Maxime, Veronika, Pegah, Lalah, Fred, Lansiné, Bill, Léon, Emilie, Kasia, Orora, Jim et tous les autres... Jouer avec vous ces dernières années a été une vraie partie de plaisir et un moyen de se vider la tête de temps en temps. Le SUAPS va me manquer...

Je voudrais à présent remercier ma mère, pour tous les sacrifices qu'elle a fait durant toutes ces années afin de me permettre d'en arriver là. Son soutien infaillible m'a aidé à traverser toutes ces épreuves et a fait de moi, une grande partie de la personne que je suis aujourd'hui.

Finalement, ces derniers remerciements seront pour mon père, qui m'a quitté juste avant le début de cette thèse... J'aurais aimé que tu sois là pour voir ce que j'ai accompli ces trois dernières années. Les choses n'ont pas toujours été faciles entre nous, mais tu m'as aidé à comprendre pourquoi et comment faire les bons choix. Tu m'as toujours laissé prendre mes propres décisions, sans jamais douter de moi, et m'a apporté un grand soutien à chacune d'entre elles. J'espère juste que tu es fier de là où tu es...

Dr. Mike Dentinger

2b rue de Molsheim – 67000 Strasbourg

March 29th 1991, Strasbourg (France)

Phone: +33(0)699395297

E-mail: mikedentinger@gmail.com mdentinger@unistra.fr

LinkedIn : <https://www.linkedin.com/in/mike-dentinger-1625a3108/>



Professional experiences

- | | | |
|-----------|--|---------------------------------|
| 2019 | Research Scientist
Institut de Science et d'Ingénierie Supramoléculaires (ISIS), Prof. Luisa De Cola | <i>Université de Strasbourg</i> |
| 2015-2018 | PhD student
Institut de Science et d'Ingénierie Supramoléculaires (ISIS), Prof. Luisa De Cola
“Breakable nanoparticles for the <i>in vitro</i> and <i>in vivo</i> delivery of biomolecules”
Synthesis and development of breakable organo-hybrid mesoporous silica nanoparticles aimed for the delivery of siRNA towards hepatocellular carcinoma. (ARC grant “Thera-HCC” N° IHU201301187) | <i>Université de Strasbourg</i> |
| 2014-2015 | Master internship (9 months)
ISIS, Prof. Luisa De Cola
“Influence of the breakable mesoporous silica nanoparticles functionalization in their physicochemical properties and behavior” Laboratory supervisor: Dr. Ingrid Cabrera-Puig
Understanding the breakability properties of newly developed mesoporous silica nanoparticles after functionalization with specific targeting moieties (folic acid and antibodies).
“Bioconjugated Nanozeolites: a New Vector for Hepatocarcinoma (Huh-7) Cells” Laboratory Supervisor: Dr. Laura Maggini
Development of antibody functionalized zeolites for the specific targeting of Hepatocarcinoma cells (Huh-7). | <i>Université de Strasbourg</i> |
| 2013 | Voluntary internship (2 months)
Faculté de Pharmacie, Dr. Alexandre Specht
“Synthesis of two photon uncaging systems”
Synthesis of nitro-bisphenyl uncaging systems for the biorthogonal delivery of neurotransmitters. | <i>Université de Strasbourg</i> |

Skills

- Synthesize and characterize of **porous materials** for **medical applications**.
- Synthesize and characterize of **small organic molecules**.
- Analyze data through various **characterization techniques**, i.e. SAXS, XPS, TEM / SEM / STEM / EDX, DLS, ZP, TGA, Fluorometry, UV-Vis-NIR, NMR and FTIR spectroscopies, CLSM.
- Loading and delivery of sensitive molecules such as **siRNA, DNA, peptides...**
- Be responsible of a **biolab** and **confocal microscope** (LSM Zeiss 710).
- Able to perform **in vitro experiments** (cytotoxicity, imaging, flow cytometry...).
- Undertaking **various projects** as team member and **collaborating** with **international scientists** / groups and from different fields (biologist, medical doctors, engineers...).
- Oral communication skills expressed with **several presentations** of the research results at various international meetings and congresses through oral and poster presentations.
- Have set up a project for the **fictive creation of a biomedical start-up** with an international team composed of chemists, medical doctors and engineers (B.E.S.T. course 2017) as well as the discovery of **mini-invasive surgery**.
- **Manage several students** (in the lab: helping several master students in their experiments. Presenting our activities to very young students). Manage a basketball class (around 60 students).

Education

- | | |
|------|---|
| 2018 | PhD in Chemistry , Université de Strasbourg, France |
| 2015 | Master in Chemistry-Biology , Université de Strasbourg, France |
| 2013 | Bachelor in Chemistry , Université de Strasbourg, France |

Softwares and languages

Office, ChemBiodraw, Zotero, Origin, MestRenova,
French (mother tongue) English (fluent) – German, Italian and Spanish (basic notions)

Papers, communications and awards

Patents:

L. De Cola, **M. Dentinger**, V. Giglio, L. Maggini, Disintegrable porous organometaloxide nanoparticles and uses thereof as vehicle for controlled delivery of siRNA. PCT/EP2018/055829, March 2018.

Papers:

M. Dentinger[‡], V. Giglio[‡], L. Maggini, L. Travaglini, I. Cabrera, A. Insuasty, C. Thumann, F. Duong, E. Robinet, T. Baumert, L. De Cola, "Breakable large pore mesoporous silica nanoparticles for efficient siRNA delivery reducing liver cancer growth *in vivo*". To be submitted.

M. Dentinger, K. Pant, S. Meister, J. Pufe, J. Pietzsch, and H. Stephan, L. De Cola, "*in vivo* fate of ⁶⁴Cu coupled breakable mesoporous silica nanoparticles for PET imaging". Manuscript in preparation.

M. Dentinger, C. Lochenie, L. De Cola, "Reactive Oxygen Species breakable silica nanoparticles". Manuscript in preparation.

R. Totovao, N. Brandão-Vilaça, **M. Dentinger**, E.A. Prasetyanto, F. Baltazar, I.C. Neves, L. De Cola, "pH-Responsive breakable porous nanoparticles for drug delivery towards breast cancer cells". To be submitted.

Oral and poster communications:

M. Dentinger, V. Giglio, L. Maggini, L. Travaglini, I. Cabrera, A. Insuasty, E. Robinet, T. Baumert, L. De Cola, "Breakable large pore mesoporous silica nanoparticles for efficient siRNA delivery", **E-MRS, June 2018** (Strasbourg, FR), *oral presentation*.

M. Dentinger, V. Giglio, L. Maggini, L. Travaglini, I. Cabrera, A. Insuasty, E. Robinet, T. Baumert, L. De Cola, "Breakable large pore mesoporous silica nanoparticles for efficient siRNA delivery", **Hybrid Materials, March 2017** (Lisbon, P), *oral presentation*.

M. Dentinger, V. Giglio, L. Maggini, L. Travaglini, I. Cabrera, A. Insuasty, E. Robinet, T. Baumert, L. De Cola, "Breakable large pore mesoporous silica nanoparticles for efficient siRNA delivery", **Doctoral day in Chemistry, Université de Strasbourg, November 2016** (Strasbourg, FR), *oral presentation*.

M. Dentinger, A. Insuasty, E. Prasetyanto, L. De Cola, "Breakable silica nanoparticles for the *in vitro* delivery of biomolecules", **Biointerfaces international, August 2016** (Zürich, CH), *poster presentation*.

M. Dentinger, A. Insuasty, E. Prasetyanto, L. De Cola, "Breakable silica nanoparticles for the *in-vitro* delivery of biomolecules", **Forum Biochem 2016 – Meeting Academia-Industry, June 2016** (Illkirch, FR), *oral and poster presentations*.

M. Dentinger, I. Cabrera-Puig, R. Totovao, E. Robinet, L. De Cola, "Characterization and *in vitro* behavior of functionalized breakable mesoporous silica nanoparticles", **E-WISPOC 2016, January 2016** (Bressanone, IT), *oral and poster presentations*.

Awards:

"**Best Design/Prototype**" at the B.E.S.T. Innovation Course 2016 organized by IRCAD/IHU Strasbourg.

"**Naturalia & Biologia 2016**" subvention for the participation to an international scientific conference

"**Best Presentation Price**" awarded from the E-WISPOC 2016 conference

Participation to other congresses:

Business Engineering and Surgical Technologies (B.E.S.T.) 2017, IRCAD/IHU Strasbourg, France.

10th ISMSC-2015, the International Symposium on Macrocyclic and Supramolecular Chemistry Strasbourg, France (organized by Prof. Luisa De Cola).

Interests

Sports (basketball, climbing, football)
Cinema and music
Travelling

Breakable silica nanoparticles for the *in vitro* and *in vivo* delivery of biomolecules

Résumé

Le travail de recherche de cette thèse se concentre sur le développement de nanoparticules de silice organo-hybrides pour des applications en nanomédecine et agroalimentaire. Ces nanoconteneurs de silice, comportant des liens disulfures, sont capables de se briser en petits fragments en présence du milieu réductif intracellulaire. Des nanoparticules présentant de larges pores ont été synthétisées pour la livraison d'un siRNA PLK1 pour le traitement du carcinome hépatocellulaire et ont démontré des résultats prometteurs *in vitro* et *in vivo*. Ces particules ont été également utilisées pour charger un peptide cytotoxique, souvent utilisé comme pesticide dans l'industrie agroalimentaire. Les nanoparticules cassables ont ensuite été miniaturisées pour le relargage d'agents thérapeutiques dans des glioblastomes humains. Le système présentait un relargage plus rapide comparé à la forme liposomale actuellement sur le marché. Enfin, des nanoparticules contenant des liens répondant aux réactifs dérivés de l'oxygène ont été développées et ont démontré une fragmentation importante en présence d'oxygène singulet.

Mots clés : Nanomédecine, nanoparticules de silice, matériaux stimuli-responsive.

Résumé en anglais

The research work presented throughout this thesis focuses on the development of organo-hybrid mesoporous silica nanoparticles for their applications in nanomedicine and crop industry. Disulfide-doped silica nanocarriers, able to break down in small pieces in presence of the intracellular reductive environment have been tailored. A large pore stimuli-responsive system was developed to deliver a PLK1 siRNA within hepatocellular carcinoma cells demonstrating promising results both *in vitro* and *in vivo*. The particles were further used to deliver a venom peptide, often utilized as pesticide in the crop industry. The breakable nanocarriers were further miniaturized for the delivery of chemotherapeutic agents within human glioblastoma cells. The system presented a faster delivery compared to the commercially available liposomal form. Finally, Reactive-Oxygen-Species-responsive mesoporous silica nanoparticles were developed and demonstrated fast breakability upon incubation with singlet oxygen.

Keywords: Nanomedicine, silica nanoparticles, stimuli-responsive materials